

Phase Field Modeling of Dynamic Brittle Fracture

vom Fachbereich Maschinenbau und Verfahrenstechnik
der Technischen Universität Kaiserslautern
zur Verleihung des akademischen Grades
Doktor-Ingenieur (Dr.-Ing.)
genehmigte Dissertation

von
M.Sc. Alexander Schlüter
aus Koblenz

Hauptreferentin:	JP Dr.-Ing. Charlotte Kuhn
Korreferenten:	Prof. Dr.-Ing. Ralf Müller Prof. Tarek I. Zohdi
Vorsitzende:	JP Dr.-Ing. Kristin de Payrebrune
Dekan:	Prof. Dr.-Ing. Jörg Seewig

Tag der Einreichung: 09.11.2017

Tag der mündlichen Prüfung: 27.02.2018

Kaiserslautern, 2018

D 386

Herausgeber

Lehrstuhl für Technische Mechanik
Technische Universität Kaiserslautern
Gottlieb-Daimler-Straße
Postfach 3049
67653 Kaiserslautern

© Alexander Schlüter

Ich danke der „Prof. Dr. Hans Georg und Liselotte Hahn Stiftung“ für die finanzielle Unterstützung bei der Drucklegung.

Druck

Technische Universität Kaiserslautern
Hauptabteilung 5/ Bau-Technik-Energie
Abteilung 5.6 Foto-Repro-Druck

Alle Rechte vorbehalten, auch das des auszugsweisen Nachdrucks, der auszugsweisen oder vollständigen Wiedergabe (Photographie, Mikroskopie), der Speicherung in Datenverarbeitungsanlagen und das der Übersetzung.

ISBN 978-3-942695-17-6

Vorwort

Die vorliegende Arbeit entstand während meiner Tätigkeit als wissenschaftlicher Mitarbeiter am Lehrstuhl für Technische Mechanik der Technischen Universität Kaiserslautern.

Zuerst möchte ich mich bei JP. Dr.-Ing. Charlotte Kuhn sowie bei Prof. Dr.-Ing. Ralf Müller für die Ermöglichung dieser Arbeit und die hervorragende Betreuung bedanken. Ich habe die Zusammenarbeit mit euch immer sehr genossen. Außerdem danke ich Herrn Prof. Tarek I. Zohdi für die Möglichkeit einige Monate an seinem Institut an der UC Berkeley zu arbeiten und für die Übernahme eines der Korreferate. Genauso danke ich JP Dr.-Ing. Kristin de Payrebrune für die Übernahme des Vorsitzes.

Prof. Dr. Christina Trautmann und Dr. Marilena Tomut danke ich für die angenehme und konstruktive Zusammenarbeit während meiner Besuche bei der GSI in Darmstadt.

Den vielen Mitgliedern der IRTG 2057 möchte ich ebenfalls für die außergewöhnliche gemeinsame Erfahrung in einem internationalen Graduiertenkolleg danken. Mein besonderer Dank gilt hier den Kollegen am Institut von Prof. Tarek I. Zohdi für ihre Gastfreundlichkeit während meiner Auslandsaufenthalte.

Allen meinen Kollegen am LTM danke ich für das tolle Arbeitsklima, ihre Hilfsbereitschaft und die schöne Zeit in Kaiserslautern zu der auch zahlreiche außeruniversitäre Aktivitäten gehörten. An dieser Stelle gilt mein Dank auch den Mitarbeitern der AWP für die gemeinsamen Erlebnisse.

Meiner Familie und meinen Freunden danke ich für ihre Unterstützung während meiner gesamten Ausbildung. Besonders meiner Freundin Natalie Knecht möchte ich für ihre nicht enden wollende Geduld – gerade in den letzten Zügen dieser Arbeit – danken.

Kurzfassung

Unter einem Bruch versteht man, wie in Gross and Seelig (2011) beschrieben, die vollständige oder teilweise Trennung eines ursprünglich unbeschädigten Körpers. Das Forschungsgebiet der Bruchmechanik widmet sich der Studie solcher Bruch- oder Rissprozesse und beinhaltet eine große Anzahl von Untergebieten. Die vorliegende Arbeit nähert sich der Thematik aus kontinuumsmechanischer Sicht, wobei die Wurzeln des betrachteten Modells für Rissausbreitung in der Arbeit von Griffith (1921) zu finden sind. A. A. Griffith hat mit seiner Arbeit die energetische Sichtweise auf die Rissausbreitung begründet. Er postulierte, dass die Energie, die zur Schaffung neuer Rissoberflächen notwendig ist, vom betrachteten Körper als mechanische Energie bereitgestellt werden muss. Diese Idee wurde in der Variationsformulierung des Sprödbruchs nach Francfort and Marigo (1998) verallgemeinert und erlaubt prinzipiell die Vorhersage von nahezu beliebig komplizierter Rissausbreitung. Im Allgemeinen sind dazu jedoch numerische Methoden notwendig. Motiviert durch die Tatsache, dass die direkte numerische Implementierung der Variationsformulierung für Sprödbruch mit einigen Schwierigkeiten verbunden ist, hat Bourdin (1998) eine regularisierte Version vorgestellt. In dieser Variante wird der Riss durch ein zusätzliches skalares Feld, den Ordnungsparameter, dargestellt. Der Wert dieses Parameters variiert kontinuierlich von einem Wert, der gebrochenes Material repräsentiert, zu einem anderen Wert, der intaktes Material anzeigt. Die regularisierte Variationsformulierung für Sprödbruch hat viele strukturelle Gemeinsamkeiten mit sogenannten Phasenfeldmodellen. Die ersten Phasenfeldmodelle wurden tatsächlich dazu genutzt um Phasenumwandlungen, wie sie beispielsweise in Erstarrungsprozessen auftreten, zu beschreiben. Hier repräsentiert der Ordnungsparameter verschiedene Phasen des betrachteten Materials. Mit dieser Sichtweise kann auch der Sprödbruch als eine Phasenumwandlung von unbeschädigtem zu gebrochenem Material verstanden werden. Konsequenterweise wird dann der Ordnungsparameter als Phasenfeld bezeichnet.

Die vorliegende Arbeit widmet sich einem Phasenfeldmodell für dynamischen Sprödbruch. Das heißt die Massenträgheit des Materials wird im Gegensatz zum ursprünglichen quasi-statischen Modell berücksichtigt. Weiterhin werden ausschließlich spröde Materialien wie Keramiken und gehärteter Stahl betrachtet.

Dazu werden nach einer Zusammenfassung der benötigten kontinuumsmechanischen Grundlagen einige wichtige Ergebnisse der dynamischen linearen Bruchmechanik vorgestellt. Dies dient im Wesentlichen zwei Zwecken. Zum Ersten werden notwendige Grundlagen für das diskutierte Phasenfeldmodell erläutert und zweitens werden einige charakteristische Eigenschaften des dynamischen Sprödbruchs erklärt, die zur Bewertung der Ergebnisse der nachfolgenden numerischen Simulationen genutzt werden. Im Anschluss folgt die Diskussion der regularisierten Modellierung von Rissen sowie die Einführung der sogenannten Phasenfeldformulierung des dynamischen Sprödbruchproblems im Rahmen des Hamiltonschen Variationsprinzips. Die beschreibenden, gekoppelten Feldgleichungen bestehen aus der klassischen Bewegungsgleichung und der Evolutionsgleichung für das Phasenfeld. Diese Gleichungen folgen als notwendige Bedingungen aus dem oben genannten Variationsprinzip. Um auch thermomechanische Probleme betrachten zu können, werden diese Beziehungen durch eine zusätzliche Feldgleichung, die lokale Energiebilanz, ergänzt. Das resultierende System aus gekoppelten, partiellen Differentialgleichungen beschreibt den thermoelastischen Bruchprozess nahezu vollständig. Dennoch sind einige Modifikationen notwendig, um das Verhalten von Rissen physikalisch korrekt wiederzugeben. Zum Beispiel wird die Irreversibilität der Rissausbreitung durch das Aufbringen von entsprechenden homogenen Dirichlet-Randbedingungen für das Phasenfeld am Riss implementiert. Weiterhin werden zwei etablierte Methoden zur Modellierung der Zug-Druck-Asymmetrie von Rissen und Rissausbreitung diskutiert und analysiert. Es wird gezeigt, dass die spektrale Zerlegung der Verzerrungsenergiegedichte nach Miehe et al. (2010b) ebenso wie die volumetrisch-deviatorische Zerlegung nach Amor et al. (2009) eine wesentliche Verbesserung des Modells unter Drucklast darstellen. Zusätzlich werden deutliche Unterschiede zwischen den beiden Ansätzen, besonders unter Scherbelastung, hervorgehoben. Im Anschluss wird die Auswirkung der Wahl der Degradationsfunktion auf das modellierte konstitutive Materialverhalten untersucht. Die Degradationsfunktion modelliert im gebrochenen Material den Steifigkeitsverlust und beeinflusst damit wesentlich das konstitutive Materialverhalten bis zur Rissbildung. Eine allgemeine kubische Degradationsfunktion, wie sie in Borden (2012) vorgestellt ist, wird in einem vereinfachten eindimensionalen Problem betrachtet. Es zeigt sich, dass die kubische Degradationsfunktion so eingestellt werden kann, dass das Materialverhalten bis zum Bruch ein sprödes Materialverhalten besser wiedergibt als dies bei der häufig verwendeten quadratischen Degradationsfunktion der Fall ist. Ein weiterer wichtiger Schwerpunkt dieser Arbeit ist die Untersuchung von Konfigurationskräften, welche auf regularisierte Risspitzen wirken. Die Analyse verdeutlicht die enge Verbindung des Phasenfeldmodells zu Griffiths Theorie und illustriert die Möglichkeiten, die sich bei der Auswertung von Phasenfeldsimulationen von dynamischen Sprödbruch durch das Berechnen der entsprechenden

Konfigurationskräfte bieten.

Danach werden einige numerische Strategien zum Lösen des gekoppelten thermoelastischen Phasenfeldproblems eingeführt. Alle vorgestellten Methoden nutzen die räumliche Diskretisierung mit standardmäßigen finiten Elementen mit linearen Ansatzfunktionen. Der übergeordnete Algorithmus kann entweder gestaffelt oder monolithisch sein. Während im gestaffelten Algorithmus das gekoppelte Problem in drei entkoppelte Teilprobleme zerlegt wird, die sukzessive gelöst werden, wird im monolithischen Algorithmus das vollständige Problem in einem Schritt gelöst. Die Simulation von zwei Testproblemen zeigt, dass eine gestaffelte Lösungsstrategie mit expliziter Zeitintegration der Bewegungsgleichung und eine monolithische Strategie mit Zeitintegration durch ein modifiziertes Newmark-Verfahren am effizientesten arbeiten.

Darauf aufbauend werden anschließend mehrere numerische Experimente durchgeführt, um die Fähigkeiten des diskutierten Phasenfeldmodells zur Beschreibung von dynamischen Bruchphänomenen zu demonstrieren. Die Analyse von stationären Rissen zeigt die Fähigkeit der Zug-Druck-Modifikationen zur akkuraten Beschreibung der Randbedingungen am Riss. Gleichzeitig werden aber auch Schwachpunkte dieser Ansätze herausgearbeitet. Zusätzlich wird die Rissbildung durch dynamische Effekte, wie etwa der Reflektion von elastischen Wellen an den Rändern der betrachteten Struktur, in zuvor unbeschädigtem Material untersucht. Anhand der Rissbildung im Kerbgrund einer Kompaktzugprobe wird ein Vergleich zwischen den Ergebnissen des dynamischen Modells und eines quasi-statischen Modells durchgeführt und wesentliche Unterschiede im berechneten Rissverhalten werden diskutiert. Im weiteren Verlauf der Arbeit wird der Fokus auf die Analyse der maximal erreichbaren Rissgeschwindigkeiten im dynamischen Phasenfeldmodell gelegt. Die Simulationen ergeben, dass die maximal erreichbare Rissgeschwindigkeit vom Modus der Risspitzenöffnung abhängig ist. Die erreichten Geschwindigkeiten sind in guter Übereinstimmung mit analytischen Ergebnissen und Experimenten. Die Analyse dynamischer Rissverzweigung zeigt, dass die Konfigurationskräfte, welche auf ein Risspitzenkontrollvolumen wirken, die riss-treibenden energetischen Mechanismen nur dann repräsentieren, wenn eine einzige Risspitze im betrachteten Kontrollvolumen enthalten ist. Ist dies der Fall, zeigt die Auswertung der Konfigurationskräfte die enge Verbindung des Phasenfeldmodells mit der Griffith-Bedingung für Risswachstum.

Abschließend werden zwei Anwendungsbeispiele des betrachteten Phasenfeldmodells zur Beschreibung von thermoelastischen Bruchproblemen präsentiert. Zuerst wird das Laserschneiden von Keramiken untersucht, während sich das zweite Beispiel der Modellierung von Versagen in Strukturen in Hochleistungsteilchenbeschleunigeranlagen widmet, die Schwerionenbestrahlung ausgesetzt sind. In beiden Anwendungsbeispielen wird die Temperatur als zusätzliches Feld berücksichtigt.

Abstract

Fracture is understood as the complete or partial separation of an originally undamaged body, see Gross and Seelig (2011). The field of fracture mechanics is devoted to the study of such processes and includes a variety of sub-branches. This work approaches the subject from a continuum mechanics point of view, meaning that the analyzed body is assumed to be a continuous set of contiguous material particles. The origins of the considered model for fracture lie in the work of Griffith (1921). A. A. Griffith was the first to formulate an energetic criterion that allowed to predict the onset of crack propagation. The idea of Griffith has been generalized by the variational formulation of brittle fracture by Francfort and Marigo (1998) which – in principle – enables the prediction of crack propagation of almost arbitrary complexity. Nonetheless, a numerical solution is required in order to determine the crack evolution. Motivated by the fact that the numerical solution of the original variational formulation of brittle fracture faces severe difficulties, Bourdin (1998) presented a regularized version. In this case, the crack is represented by an additional scalar field variable – the order parameter – that continuously varies from a value indicating broken material to another value that represents undamaged material. The structure of the regularized version of the variational formulation of brittle fracture closely resembles so-called phase field models. Originally, phase field models were used to model phase transformations such as they occur for example during solidification processes or during the austenite-martensite transformation in steels. In such scenarios, the order parameter indicates the different phases of the regarded continuum. Analogously, fracturing may also be considered as a phase transformation from undamaged to broken material and consequently the order parameter may be referred to as a phase field.

The present work addresses a phase field model for dynamic brittle fracture, i.e. inertial effects are accounted for and only brittle materials such as ceramics and hardened steel are considered. After the required background information on continuum mechanics is stated, the reader is introduced to some fundamental results of dynamic linear elastic fracture mechanics. This serves two purposes. Firstly, the foundations of the model such as the Griffith condition are introduced.

Secondly, features of dynamic fracturing such as theoretical crack speed limits are discussed which serve as benchmarks for the evaluation of the performance of the phase field model in subsequent numerical simulations.

Afterwards, the regularized representation of cracks is presented and the dynamic phase field fracture problem is stated in the framework of Hamilton's variational principle. The governing field equations which are the equation of motion and a phase field evolution equation follow as necessary conditions from the variational principle. They are complemented by the local energy balance which provides a third field equation. The resulting set of coupled partial differential equations implicitly governs the evolution of all three primary fields, i.e. the displacements, the phase field and the temperature. Thus, the whole thermoelastic fracture process is treated in a unified framework. Nonetheless, certain additions and modifications are necessary to capture physically sound crack behaviour. The irreversibility of fracturing is implemented by prescribing adequate homogeneous Dirichlet boundary conditions for the phase field at the crack. Secondly, two established approaches to model the tension-compression asymmetry of fracturing are discussed and analyzed. It is shown that the spectral decomposition of the strain energy density by Miehe et al. (2010b) as well as the volumetric-deviatoric formulation of Amor et al. (2009) provide a substantial improvement in compressive load states. Furthermore, fundamental differences between both approaches are highlighted in particular in shear load states. In this situation, the spectral decomposition predicts a higher resistance to crack nucleation in undamaged material and furthermore retains a residual stiffness to a sliding motion of crack faces. This makes the spectral approach less suited to model crack propagation under in-plane shear loading of the crack tip. Next, the effect of the choice of the degradation function on the modelled constitutive material behaviour is studied. The degradation function implements the loss of stiffness of the material in broken material and significantly impacts the local constitutive behaviour of the material up to fracture. A general cubic degradation function of the type originally proposed in Borden (2012) is considered in a simplified analytic scenario. It is found that the general cubic degradation function can be set up such that the material behaviour up to fracture matches brittle material behaviour better than the common quadratic degradation function. Another contribution of this work, is the consideration of configurational forces as a means to highlight the connection of the phase field model to the Griffith condition and to enhance the post-processing of dynamic phase field fracture simulations. It is demonstrated that a generalized configurational force balance which is evaluated for a control volume containing a single crack tip is closely related to the Griffith condition for crack propagation.

In the following, several numerical solution strategies for the solution of the coupled thermoelastic phase field problem are introduced. All presented methods

rely on a spatial discretization of the partial differential equations by means of standard finite elements with linear shape functions. The overall algorithm can be either a staggered or a monolithic solution strategy. In the staggered algorithm, the coupled problem is decomposed into three decoupled subproblems that are solved successively, whereas in the monolithic case the solution of the full problem is obtained in a single step. Benchmark problems reveal that a staggered strategy with explicit time integration of the equation of motion and a monolithic solution strategy with implicit time integration by a modified Newmark scheme perform best.

Subsequently, a number of numerical experiments is conducted that demonstrate the model's capability to accurately capture features of dynamic fracture. The analysis of stationary cracks displays the ability of the tension-compression asymmetry implementations to accurately model the crack boundary conditions but also reveals certain shortcomings of these modifications. Crack nucleation in previously undamaged bodies due to dynamic effects such as wave reflection at the body's boundaries is also investigated and it is shown that the phase field model at hand is able to govern such fracture scenarios. A comparison to the performance of a quasi-static phase field model for brittle fracture is conducted as well, taking as an example the crack nucleation in the notch ground of a compact tension specimen. In this case, critical differences between the dynamic and quasi-static formulations are discussed. Furthermore, the crack tip trajectory obtained from a phase field simulation is compared to an analytical solution for a relatively simple crack nucleation scenario. The simulation is found to be in agreement with the analytical prediction. In the following part the focus is shifted towards analyzing the maximum obtainable crack speeds in the phase field model. Depending on the mode of crack tip loading, the phase field model predicts different crack speed limits that are in agreement with analytical results and experimental investigations. For symmetric tensile crack tip loading, so-called Mode I, the maximum crack speed in the simulations is the Rayleigh wave speed if the directional instability of such a crack is removed by introducing a weak strip of reduced fracture resistance into the material. For Mode II it is necessary to prescribe the crack path as well and crack speeds above the characteristic wave speed of equivoluminal waves can be obtained. The analysis of a dynamic crack branching scenario reveals that the configurational forces evaluated on a crack tip control volume can only accurately represent the energetic driving forces on the crack tip if only a single crack tip is contained in the control volume. If this is the case, the analysis of the configurational forces verifies the close connection of the present phase field model to the Griffith condition of crack growth.

Lastly, two applications of the phase field model at hand to thermoelastic fracture problems are presented. Firstly, the laser-cutting of ceramic substrates is

studied and secondly the failure of structures that are subject to intense heavy-ion beams in high-power particle accelerator facilities is considered. Only in these two case studies, the temperature is included as an additional field.

Contents

1	Introduction	17
1.1	Motivation and Background	17
1.2	Objectives and Overview	20
2	Continuum Mechanics	23
2.1	Kinematics	23
2.1.1	Small Deformation Theory	25
2.2	Stress	27
2.3	Balance Laws	29
2.3.1	Conservation of Mass	29
2.3.2	Balance of Linear Momentum	29
2.3.3	Balance of Angular Momentum	30
2.3.4	Balance of Energy and Caloric Equation of State	31
2.3.5	Conservative Systems	33
2.3.6	Second Law of Thermodynamics and Helmholtz Free Energy	33
2.4	Wave Propagation	36
2.5	Hamilton's Principle	37
3	Dynamic Linear Elastic Fracture Mechanics	41
3.1	Basic Assumptions	41
3.2	Asymptotic Fields	43
3.3	Energy Concepts	45
3.4	Crack Speed Limits	50
3.5	Dynamic Crack Branching	53
3.6	Configurational Forces in Dynamic Linear Elastic Fracture Mechanics	55
3.7	The Variational Formulation of Brittle Fracture	57
4	A Phase Field Model of Dynamic Brittle Fracture	61
4.1	Regularized Representation of Cracks and Fracture Energy	61

4.2	Derivation of the Field Equations from Hamilton's Principle	64
4.3	Irreversibility	68
4.4	Tension-Compression Asymmetry of Fracturing	69
4.4.1	Volumetric-Deviatoric Decomposition of the Strain Energy Density	72
4.4.2	Spectral Decomposition of the Strain Energy Density	73
4.4.3	Discussion of the Asymmetry Formulations	75
4.5	Dimensional Analysis	77
4.6	Analytic Results	81
4.6.1	1D Bar	81
4.6.2	Configurational Forces	91
5	Performance of Numerical Solution Strategies	99
6	Simulations of Dynamic Brittle Fracture	113
6.1	Stationary Cracks and the Effect of the Tension-Compression Asymmetry Formulations	114
6.1.1	Quasi-Static Load	114
6.1.2	Wave Interaction with a Phase Field Crack	120
6.2	Crack Nucleation	121
6.2.1	1D-Hopkinson Wire	122
6.2.2	2D-Crack Nucleation Hopkinson Plate	125
6.2.3	Crack Nucleation in a CT Specimen	130
6.2.4	Crack Initiation in an Infinite Elastic Body	136
6.3	Crack Speed Limits and Intersonic Fracture	139
6.4	Dynamic Crack Branching	146
7	Application to Thermoelastic Fracture Problems	155
7.1	Laser-Cutting of Ceramic Substrates	155
7.1.1	Modelling of the Laser Beam	156
7.1.2	Simulation of Laser-Cutting of Ceramic Substrates by a Controlled Fracture Technique	157
7.2	Phase Field Modelling of Thermal Fracture in the Context of Irradiation Damage	163
7.2.1	Fracturing of a Cylinder	164
7.2.2	Fracturing of a Disc	167
8	Conclusion and Outlook	171

A	Notation and Mathematical Preliminaries	177
B	Finite Element Implementation	181
B.1	Spatial Discretization and Linearization	181
B.2	Isoparametric Concept and Numerical Quadrature	190
B.3	Staggered Solution Strategy	192
B.4	Monolithic Solution Strategy	194
B.5	Time Integration	195
B.6	Implementation of the Irreversibility Constraint	199
B.7	Computation of the Crack Tip Position and of the Crack Velocity .	200
B.8	Finite Element Discretization of the Configurational Force Balance	201
	Bibliography	203

1 Introduction

1.1 Motivation and Background

Fracture is referred to as the complete or partial separation of a previously connected solid body by applying stress loads that are large enough to overcome the cohesive strength of the material. Since fracturing is a central concern in many industrial applications as well as it is a major aspect of natural phenomena such as earthquakes, engineers and scientists have devoted a considerable effort to the study of cracks and crack propagation. A major objective in the design of technical devices and facilities, for example, is to prevent structural failure of critical components due to fracture. Oftentimes, fracturing of key components can lead to immediate and catastrophic consequences. In other cases, fracturing may be a desired part of a technological process. An illustrative example for such an application is the hydraulic fracturing technology, where rock is fractured by a pressurized fluid in order to increase the stimulation rate of natural gas and oil. Furthermore, a number of very efficient manufacturing techniques deliberately induce fracture to separate a workpiece. A natural phenomenon that involves fracturing is the separation of the earth crust during an earthquake. In this research field, a better understanding of the fracture process might enable the development and improvement of early warning systems.

The primary motivation for the original studies of fracturing was indeed the failure of technical structures due to fracture which could not be explained by the available mechanical theories at the time. In particular, the theoretical works of Griffith (1921) and Irwin (1957) established the field that is today known as fracture mechanics. These early contributions enabled the engineer to estimate whether an existing crack in brittle material such as hardened steel and ceramics was likely to propagate or not. Furthermore, Griffith (1921) founded the basis of the theoretical understanding of fracturing as an energy driven process. He stated that the energy needed to separate the material – and thus to form the new surfaces – needs to be supplied by the body as mechanical energy. Griffith and Irwin considered only quasi-static situations meaning that they neglected the inertia of the material. Such an approach is suitable as long as the load is applied slowly

compared to a time scale given by the ratio of a characteristic length of the problem and a characteristic wave speed. In addition, crack propagation needs to be slowly compared to a characteristic wave speed of the material as well. Oftentimes such conditions are not prevalent and dynamic effects have to be taken into account. For example, if a load is applied rapidly, the material resists the applied load not only by means of its stiffness but also by its mass inertia. Consequently, the loading is radiated into the body as an elastic wave and thus it affects different locations of the body at different times, cf. Freund (1990). Furthermore, inertial loads may cause a dynamic overshoot of the fields at a crack tip until they eventually decay to their limiting equilibrium value. Another dynamic effect arises at the crack tip of a fast moving crack. Here, the inertia of the material on either side of the crack resists an opening of the crack and thus counteracts fast crack propagation. The extension of the classical theories of brittle fracture to the dynamic situation has been driven by a number of scientists and excellent overviews on the topic can be found in the literature, e.g. in Freund (1990), Broberg (1999) and Gross and Seelig (2011). Experimental work on the topic of dynamic fracture is available e.g. in Kalthoff and Winkler (1987), Kalthoff (2000), Ravi-Chandar and Knauss (1984a,b,c,d), Sharon et al. (1995), Sharon and Fineberg (1996, 1999) and Rosakis et al. (2000).

In science and engineering, experimental methods are still the most trusted approach to verify theories and designs. Nonetheless, experiments are often time consuming and expensive resulting in a search for alternative approaches to analyze physical processes like fracture. The applicability of the analytic results for dynamic fracture to real world engineering problems is limited since such solutions do not exist for general loading and geometric configurations. The high effort of experimental methods as well as the limited applicability of analytic solutions motivate the development of numerical approaches that make use of the increasing capacities of modern computers in order to solve more complex problems. In structural mechanics the finite element method (FEM) has become the predominant numerical tool for the evaluation of loaded continuous bodies. However, the implementation of material separation and particular fracture into a finite element scheme is still an ongoing topic of research. General material separation can for example be handled by the particle finite element method, e.g. in Sabel et al. (2014), whereas common approaches to model brittle fracture may be divided into two general classes: discrete and diffusive models of fracture. The extended finite element method, e.g. in Moës et al. (1999), the virtual crack closure technique by Krueger (2004), the inter element crack method by Xu and Needleman (1994) as well as element deletion methods all fall into the first category and model the crack as a discontinuity in the mechanical fields or by a modification of the finite element mesh. A comparative study of these strategies can be found in Song et al. (2008). Such discrete strategies generally require the tracking of the crack path in order

to apply the correct boundary conditions at the crack faces. Thus, especially in 3D situations and when phenomena such as crack branching are to be considered the algorithmic treatment is complex.

In contrast to the discrete models, diffusive approaches to fracture introduce an additional field, the order parameter, into the model that controls the stiffness of the material. This order parameter varies smoothly from a value indicating undamaged material to another value indicating broken material and thus represents the crack in a continuous manner. Hence, in a diffusive fracture model the representation of the crack is not mesh-based but field-based. The idea of a diffusive or regularized approach to solve brittle fracture problems numerically originated with Bourdin (1998), who made the generalization of the Griffith theory by Francfort and Marigo (1998) accessible to a numerical solution. Since then the approach has caught the interest of a large number of researchers like Miehe et al. (2010a), Miehe et al. (2010b), Kuhn and Müller (2010a) and Borden et al. (2012). The term ‘phase field models of fracture’ is often used in the literature to characterize these diffusive fracture models because of their formal similarity to the original diffusive interface models for phase transformation processes like solidification, e.g. in Boettinger et al. (2002), austenit-martensit transformation in steels, e.g. in Schmitt et al. (2014), or general microstructure evolution, e.g. in Moelans et al. (2008). In this classic context, the order parameter, which is referred to as the phase field, indeed indicates different phases of a material. Analogously to real phase transformation processes, crack growth may be considered as a phase transition from the undamaged to the broken state in phase field models of fracture. A major advantage of the phase field models of fracture is that the evolution of the phase field follows implicitly from the solution of a set of partial differential equations, and thus the whole fracture process is described in a uniform framework. Furthermore, since the order parameter and all other fields vary smoothly in the vicinity of the crack, no jump discontinuities need to be treated. Consequently, the algorithmic treatment is straightforward and can be handled by standard multi-field finite element methods. An extension to the 3D situation and the prediction of complex crack patterns such as crack branching and the merging of cracks also does not require any specific algorithmic treatment which is considered to be another advantage of the approach.

Recently the original quasi-static model has also been extended to the dynamic case, where inertial effects are accounted for, e.g. in Bourdin et al. (2011), Borden (2012), Borden et al. (2012), Hofacker and Miehe (2012, 2013), Schlüter et al. (2014b,a), Steinke et al. (2016) or Li et al. (2016). These works show that also in the dynamic case, the phase field approach is a versatile tool to model complex features of brittle fracture.

1.2 Objectives and Overview

As mentioned in the previous section, the phase field approach is a powerful tool that can handle even complicated fracture phenomena within an apparently simple framework. Nonetheless, a profound understanding of the model is required in order to be able to interpret the obtained results correctly. Furthermore, in the dynamic case the phase field model needs to be verified in comparison to experimental data and analytical results in order to increase the trust in this new approach. Once the capabilities of the model are verified, the proper analysis of the results of phase field simulations of dynamic brittle fracture have the potential to provide insights into fracture phenomena that are only partly understood up until now such as dynamic crack branching or intersonic fracture. Additionally, the application of the approach to engineering problems is another topic that has rarely been addressed in the literature so far. The treatment of complex engineering problems also requires the development of efficient numerical solution strategies for the dynamic phase field fracture problem.

The goal of this thesis is to thoroughly investigate the phase field approach to dynamic brittle fracture with respect to these aspects. At first, the required fundamentals of continuum mechanics are introduced in Chapter 2. In particular the small deformation theory, which serves as a framework for the formulation of the phase field model is presented. Subsequently, Chapter 3 summarizes some aspects of the theory of dynamic fracture mechanics which are required to assess the numerical simulations in consecutive chapters. At the end of this part, the variational formulation of brittle fracture is presented, which is the foundation of the present phase field formulation.

Chapter 4 contains the first important contributions of this work. Here, Hamilton's variational principle is applied to state the dynamic phase field fracture problem in a way that is consistent with the variational formulation of brittle fracture. This derivation is performed for a general thermoelastic setting, such that thermal effects can also be considered. The reader is made familiar with the regularized representation of cracks and certain aspects of the phase field model such as the modelling of the irreversibility of fracturing. A particular focus lies on the modelling of the tension-compression asymmetry with regard to the crack boundary conditions as well as with regard to the different material strength in tension and compression. Two formulations that are common in the literature are discussed and compared to each other. Furthermore, analytic results are obtained for an 1D-bar under quasi-static conditions which illustrate the significance of the choice of the degradation function for the modelled constitutive material behaviour and the effective material strength. The consideration of configurational forces in the present phase field model also highlights its connection to the Griffith criterion

and to the variational formulation of brittle fracture.

A main strength of the phase field approach to dynamic brittle fracture is its straightforward numerical implementation. Nonetheless, the computational effort can become relatively high which is why it is of interest to develop efficient numerical solution strategies. A contribution of this work that is related to this topic is the presentation and analysis of different finite element implementations of the considered phase field model in Chapter 5. Different staggered and monolithic solution strategies are presented and discussed. A thorough assessment of the different strategies in two benchmark problems follows.

A major part of this work follows in Chapter 6, where the capabilities of the phase field approach to capture dynamic brittle fracture are demonstrated by several numerical simulations. The analysis of stationary cracks sheds light on the effect of the tension-compression asymmetry implementations and also displays how the model governs wave interaction with cracks. Crack nucleation in undamaged material is a special feature of phase field models for fracture which is discussed for situations in which elastic wave propagation has substantial impact on the expected results. The analysis of crack nucleation in the notch ground of a compact tension specimen highlights the differences between quasi-static and dynamic phase field formulations of brittle fracture. To conclude this passage, a comparison of a crack tip trajectory obtained from a phase field simulation to an analytic solution is made. In the subsequent part, the ability of the phase field model to predict crack speed limits in accordance with theory and experiments is investigated. A particular focus lies on the effect of the mode of crack opening on the maximum obtainable crack speed. Lastly, dynamic crack branching of a crack that is subjected to a symmetric tensile load is analyzed. In this example, configurational forces are employed as a post-processing tool.

The last chapter presents two examples of applications of the present phase field model to engineering problems. At the beginning, simulations of laser cutting of ceramics by employing a thermoelastic formulation of the present phase field model are presented. The subsequent section considers structural failure triggered by heavy-ion beams that hit the investigated solid.

2 Continuum Mechanics

In this work, dynamic fracturing is studied in the framework of continuum mechanics. Therefore, feasible length and time scales are assumed to be much larger than the characteristic length of the atomic spacing and the characteristic times of atomic bond vibrations. Typically, these limiting scales are of the order of a few angstroms ($1\text{\AA} = 10^{-10}$ m) and a few femtoseconds (1 femtosecond = 10^{-15} s). The continuous body of interest \mathcal{B} is idealized as a composition of particles $\mathcal{P} \in \mathcal{B}$. The particles themselves represent a large number of molecules but are small enough compared to the size of the solid \mathcal{B} to be assumed to be points in physical space.

In addition to the theoretical basics that are outlined in this chapter, the interested reader is referred to the many excellent textbooks on continuum mechanics such as e.g. Holzapfel (2000), Gurtin (1981), Sadd (2009) and Becker and Gross (2002). Information on the notation that is utilized in this work and a number of required mathematical preliminaries can be found in Appendix A.

2.1 Kinematics

Consider the body \mathcal{B} to be embedded in the three-dimensional Euclidean space \mathbb{E}^3 at a specific point in time t . Due to the motion, \mathcal{B} occupies a sequence of regions Ω_0, \dots, Ω . Typically, the region $\Omega_0 \subset \mathbb{E}^3$ that is occupied at a reference time t_0 is called the reference configuration of \mathcal{B} , whereas the region that is occupied at the current time t is denoted as the current configuration Ω of \mathcal{B} , see Fig. 2.1.

By introducing a reference frame of right-handed, rectangular coordinate axes with orthonormal basis vectors \mathbf{e}_i at a fixed origin \mathcal{O} , the particle \mathcal{P} may be identified by its position in the reference configuration $\mathbf{X} = X_i \mathbf{e}_i$. Its coordinates in the current configuration are referred to as $\mathbf{x} = x_i \mathbf{e}_i$. Differential operators that contain derivatives with respect to the material coordinates \mathbf{X} are typically denoted as ‘Div’ and ‘Grad’ in contrast to the ‘div’ and ‘grad’ that is used for operators with derivatives with respect to the spatial coordinates \mathbf{x} . The motion χ maps the position of particles in the reference configuration to their position in

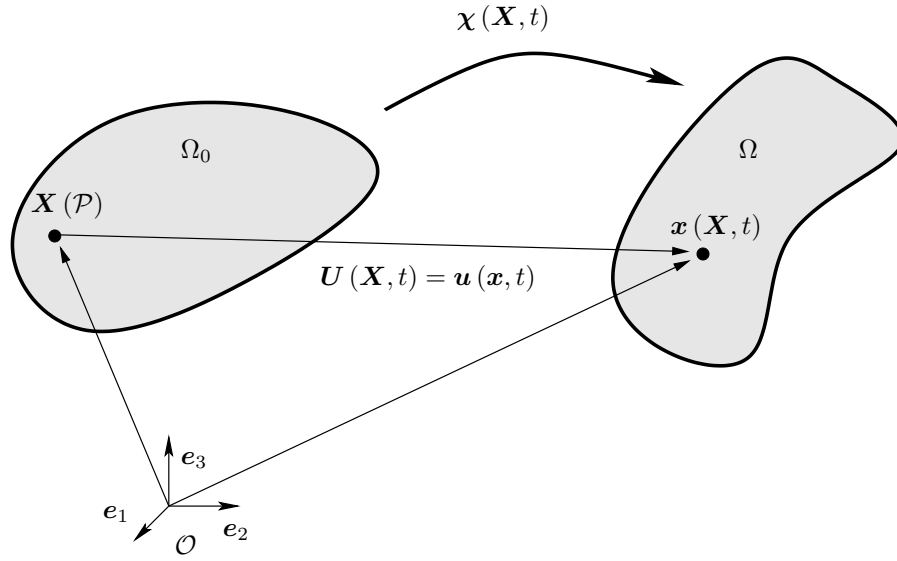


Figure 2.1: Motion of a continuum.

the current configuration, i.e.

$$\mathbf{x} = \boldsymbol{\chi}(\mathbf{X}, t) \quad (2.1)$$

and is assumed to be locally uniquely invertible, i.e.

$$\mathbf{X} = \boldsymbol{\chi}^{-1}(\mathbf{x}, t). \quad (2.2)$$

The motion and the inverse motion can be used to define the displacement of \mathcal{P} as a function of its coordinates in the reference configuration $\mathbf{U}(\mathbf{X}, t)$ or equivalently as a function of its coordinates in the current configuration $\mathbf{u}(\mathbf{x}, t)$, i.e.

$$\mathbf{U}(\mathbf{X}, t) = \boldsymbol{\chi}(\mathbf{X}, t) - \mathbf{X} = \mathbf{x} - \boldsymbol{\chi}^{-1}(\mathbf{x}, t) = \mathbf{u}(\mathbf{x}, t). \quad (2.3)$$

The material gradient of the motion $\boldsymbol{\chi}(\mathbf{X}, t)$ is denoted as the deformation gradient

$$\mathbf{F} = \frac{\partial \boldsymbol{\chi}(\mathbf{X}, t)}{\partial \mathbf{X}} = \frac{\partial \mathbf{x}}{\partial \mathbf{X}} \quad (2.4)$$

and linearly maps infinitesimally small line elements $d\mathbf{X}$ of the reference configuration onto the corresponding line elements $d\mathbf{x}$ in the current configuration, i.e.

$$d\mathbf{x} = \mathbf{F}d\mathbf{X}. \quad (2.5)$$

The inverse linear map is defined as

$$\mathbf{F}^{-1} = \frac{\partial \boldsymbol{\chi}^{-1}(\mathbf{x}, t)}{\partial \mathbf{x}} = \frac{\partial \mathbf{X}}{\partial \mathbf{x}}. \quad (2.6)$$

The deformation gradient can be uniquely decomposed into a proper orthogonal rotation tensor \mathbf{R} and a symmetric positive definite right stretch tensor \mathbf{A} or left stretch tensor \mathbf{B} , so that

$$\mathbf{F} = \mathbf{R}\mathbf{A} = \mathbf{B}\mathbf{R}. \quad (2.7)$$

In addition to the introduced quantities, strain measures are required that quantify the deformation at a certain point in order to define constitutive relations later on. The definition of strain is, unlike e.g. the definition of the displacement, based on a strain concept. Consequently, a number of strain measures are available in the literature. A common measure defined in the reference configuration is the Green-Lagrange strain tensor

$$\mathbf{E} = \frac{1}{2} (\mathbf{F}^T \mathbf{F} - \mathbf{1}) = \frac{1}{2} \left(\text{Grad}\mathbf{U} + (\text{Grad}\mathbf{U})^T + (\text{Grad}\mathbf{U})^T \text{Grad}\mathbf{U} \right), \quad (2.8)$$

in which $\mathbf{1}$ is the second order identity tensor, which operates on line elements in the reference configuration to express the change of the squared length of these line elements, i.e.

$$d\mathbf{x} \cdot d\mathbf{x} - d\mathbf{X} \cdot d\mathbf{X} = d\mathbf{X} \cdot 2\mathbf{E}d\mathbf{X}. \quad (2.9)$$

Similarly the Euler-Almansi strain tensor

$$\boldsymbol{\gamma} = \frac{1}{2} (\mathbf{1} - \mathbf{F}^{-T} \mathbf{F}^{-1}) = \frac{1}{2} \left(\text{grad}\mathbf{u} + (\text{grad}\mathbf{u})^T - (\text{grad}\mathbf{u})^T \text{grad}\mathbf{u} \right) \quad (2.10)$$

is a strain measure operating on line elements in the current configuration that expresses the change of squared lengths of these line elements, i.e.

$$d\mathbf{x} \cdot d\mathbf{x} - d\mathbf{X} \cdot d\mathbf{X} = d\mathbf{x} \cdot 2\boldsymbol{\epsilon}d\mathbf{x}. \quad (2.11)$$

2.1.1 Small Deformation Theory

In this work, brittle materials such as hardened steel, glass and ceramics are considered. These materials undergo only small stretches in the elastic range, i.e. $\mathbf{A} \approx \mathbf{1}$ and $\mathbf{B} \approx \mathbf{1}$. If the magnitude of the rotations is negligible as well, $\mathbf{R} \approx \mathbf{1}$, the displacement gradient is also small, i.e. $|\frac{\partial U_i}{\partial X_j}| \ll 1$. In addition to a small displacement gradient, the displacements themselves are assumed to fulfill $|\mathbf{u}| \ll 1$. This justifies that – except for the definition of the displacement field $\mathbf{u}(\mathbf{x}, t)$ – in the small deformation theory no distinction between the current and the reference configurations is made, i.e.

$$\Omega \approx \Omega_0, \quad \mathbf{x} \approx \mathbf{X}, \quad \frac{\partial(*)}{\partial \mathbf{X}} \approx \frac{\partial(*)}{\partial \mathbf{x}} \quad (2.12)$$

for any field (*). The above assumptions imply that the quadratic terms in (2.8) and (2.10) can be neglected. Under these circumstances the Green-Lagrange strain tensor is identical to the Euler-Almansi strain tensor, i.e.

$$\mathbf{E} \approx \boldsymbol{\gamma} \approx \frac{1}{2} \left(\text{grad} \mathbf{u} + (\text{grad} \mathbf{u})^T \right). \quad (2.13)$$

The quantity

$$\boldsymbol{\varepsilon} = \frac{1}{2} \left(\text{grad} \mathbf{u} + (\text{grad} \mathbf{u})^T \right) \quad (2.14)$$

is referred to as the linearized strain tensor. From this point on the small deformation theory is employed. The trace of the linearized strain tensor is equal to the volume change of an infinitesimal volume element dV in the small deformation theory

$$\text{tr}(\boldsymbol{\varepsilon}) = \varepsilon_{kk} = \varepsilon_V = \lim_{dV \rightarrow 0} \frac{dv - dV}{dV}, \quad (2.15)$$

which is also referred to as the volume dilatation. Based on this, the linearized strain tensor in an n -dimensional setting can be decomposed into a volumetric or spherical part and a deviatoric part as

$$\boldsymbol{\varepsilon} = \frac{\text{tr}(\boldsymbol{\varepsilon})}{n} \mathbf{1} + \mathbf{e}. \quad (2.16)$$

Alternatively, an eigenvalue decomposition of the strain tensor, such that

$$\boldsymbol{\varepsilon} = \sum_{i=1}^n \varepsilon_i \mathbf{n}_i \otimes \mathbf{n}_i, \quad (2.17)$$

where ε_i is the i -th eigenvalue of $\boldsymbol{\varepsilon}$ and \mathbf{n}_i is the associated normalized eigenvector, may be employed. The decompositions (2.16) and (2.17) enable the formulation of constitutive laws with specific characteristics which will be utilized in Section 4.4. The velocity of a specific particle

$$\dot{\mathbf{u}} = \frac{d\mathbf{u}}{dt} = \frac{\partial \mathbf{u}}{\partial t} \quad (2.18)$$

represents the rate at which a particle moves through physical space, where the last identity is only true within a small deformation framework. Similarly, the acceleration is

$$\ddot{\mathbf{u}} = \frac{d^2 \mathbf{u}}{dt^2} = \frac{\partial^2 \mathbf{u}}{\partial t^2}. \quad (2.19)$$

Hence, although it is assumed that the particles do not change their position in physical space in the small deformation theory, each particle is still associated with a velocity and acceleration. From a purely mathematical point of view, however, the displacement field can be understood as a time dependent vector field on a fixed domain. Thus, unlike in the case of a finite deformation theory, the interpretation of \mathbf{u} as a displacement in physical space is separated from the mathematical model.

2.2 Stress

The notion of stress is a fundamental concept of continuum mechanics. Consider the configuration Ω of a body \mathcal{B} that is subjected to external tractions \mathbf{t}^* on the part $\partial\Omega_t$ of the boundary. Neither distributed volume forces nor resultant couples are considered in this work. The body may also be subjected to Dirichlet type boundary conditions \mathbf{u}^* on $\partial\Omega_u$. Presume the body is cut into two pieces where

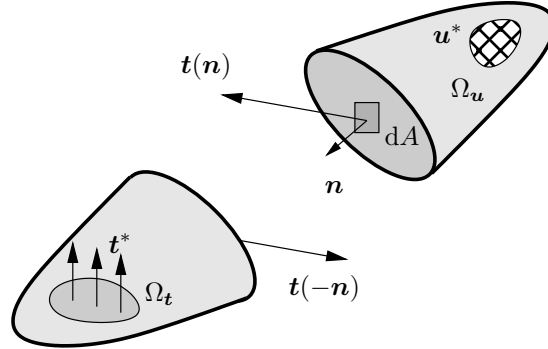


Figure 2.2: The traction vector.

$\mathbf{n}(\mathbf{x})$ is the normal vector at the interface, see Fig. 2.2. Let $d\mathbf{f}$ denote the force acting on an infinitesimally small surface element of size dA of the interface, i.e. the force that is transmitted to the other part of the body. The traction vector $\mathbf{t}(\mathbf{x}, t, \mathbf{n})$ relates $d\mathbf{f}$ and dA through

$$d\mathbf{f} = \mathbf{t}dA. \quad (2.20)$$

By means of Cauchy's theorem

$$\mathbf{t}(\mathbf{x}, t, \mathbf{n}) = \boldsymbol{\sigma}^T(\mathbf{x}, t) \mathbf{n} \quad (2.21)$$

the unique second-order tensor $\boldsymbol{\sigma}$ - the Cauchy stress tensor- is defined which linearly maps any normal $\mathbf{n}(\mathbf{x})$ onto the corresponding current stress vector at that particular location. The superscript $(*)^T$ indicates the transpose of a second-order tensor. The stress vector can be decomposed in a part that is parallel to the normal vector

$$\mathbf{t}_{\parallel} = (\mathbf{n} \cdot \mathbf{t}) \mathbf{n} \quad (2.22)$$

and a part

$$\mathbf{t}_{\perp} = \mathbf{t} - (\mathbf{n} \cdot \mathbf{t}) \mathbf{n} \quad (2.23)$$

that is perpendicular to \mathbf{n} and thus tangent to the surface element dA . The so-called normal stress is the magnitude of \mathbf{t}_{\parallel} , i.e.

$$\sigma = \sqrt{\mathbf{t}_{\parallel} \cdot \mathbf{t}_{\parallel}}, \quad (2.24)$$

whereas the total shear stress acting on ds is

$$\tau_s = \sqrt{\mathbf{t}_\perp \cdot \mathbf{t}_\perp}. \quad (2.25)$$

The components of the stress tensor in a cartesian reference frame can be determined by evaluating the normal and shear stress at a point \mathbf{x} for three cuts with linearly independent associated normal vectors. A practical choice is to align these cuts perpendicularly to the basis vectors in the orthonormal coordinate system $\{\mathbf{e}_1, \mathbf{e}_2, \mathbf{e}_3\}$. The respective traction vectors may be represented by their

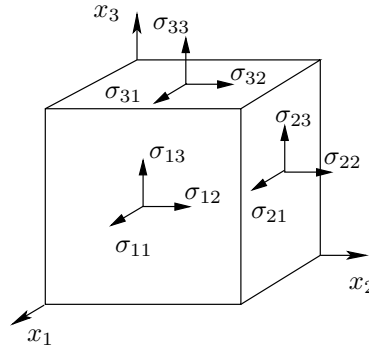


Figure 2.3: Stress components at an infinitesimally small volume element.

components in this coordinate system as

$$\mathbf{t}_i = \begin{bmatrix} \sigma_{i1} \\ \sigma_{i2} \\ \sigma_{i3} \end{bmatrix}, \quad i \in \{1, 2, 3\}, \quad (2.26)$$

see Fig. 2.2, which allows to express the stress tensor as

$$\boldsymbol{\sigma} = [\mathbf{t}_1, \mathbf{t}_2, \mathbf{t}_3]^T = \begin{bmatrix} \sigma_{11} & \sigma_{12} & \sigma_{13} \\ \sigma_{21} & \sigma_{22} & \sigma_{23} \\ \sigma_{31} & \sigma_{32} & \sigma_{33} \end{bmatrix}, \quad (2.27)$$

where the first index i of each component σ_{ij} indicates the direction $\mathbf{e}_i \parallel \mathbf{n}$ of the cutting plane with the associated traction vector \mathbf{t}_i and the second index j represents the direction \mathbf{e}_j in which the respective stress component acts.

2.3 Balance Laws

In continuum mechanics, the physical behaviour of the regarded body is often postulated by so-called balance laws.

As an exception to the notation that is introduced in Appendix A concerning boldface and normal letters, let $A(t) = \int_R a(\mathbf{x}, t) \, dR$ be a tensor-valued function that characterizes the state of the particles in a region $R \subseteq \Omega$. The smooth field $a(\mathbf{x}, t)$ may represent a tensor quantity, i.e. a scalar, vector or higher order tensor. The operators used below have to be interpreted accordingly. A balance law postulates a change of $A(t)$ to obey

$$\dot{A} = \frac{d}{dt} \int_R a(\mathbf{x}, t) \, dV = \int_{\partial R} \mathbf{q}^a \cdot \mathbf{n} \, dA + \int_R r^a + s^a \, dV, \quad (2.28)$$

where \mathbf{q}^a is the Cauchy flux of $a(\mathbf{x}, t)$ across the boundary ∂R , r^a is the internal production of $a(\mathbf{x}, t)$ and s^a is the supply of the quantity $a(\mathbf{x}, t)$ provided by external sources. Equation (2.28) is referred to as a master balance law. Similarly, one can postulate a master inequality law by replacing the equality with an inequality

$$\dot{A} = \frac{d}{dt} \int_R a(\mathbf{x}, t) \, dV \geq \int_{\partial R} \mathbf{q}^a \cdot \mathbf{n} \, dA + \int_R r^a + s^a \, dV. \quad (2.29)$$

2.3.1 Conservation of Mass

Consider a closed system $R \subseteq \Omega$, i.e. no mass can cross ∂R , and let the mass per unit volume inside R be described by the density $\rho(\mathbf{x}, t)$. Mass cannot be destroyed or produced in classical mechanics, which yields $r^\rho = 0$ and $s^\rho = 0$. Since the small deformation theory is applied, the region R is also independent on t , and thus integration over R and differentiation w.r.t. time commute. Consequently, it is

$$\dot{m} = \frac{d}{dt} \int_R \rho(\mathbf{x}, t) \, dV = \int_R \frac{\partial \rho(\mathbf{x}, t)}{\partial t} \, dV = 0 \quad (2.30)$$

for the mass m in R . This relation needs to hold for all admissible closed (sub-) systems R which yields the local form of the mass continuity equation for small deformations

$$\dot{\rho} = \frac{\partial \rho(\mathbf{x}, t)}{\partial t} = 0. \quad (2.31)$$

2.3.2 Balance of Linear Momentum

The linear momentum of R is defined as

$$\mathbf{L}(t) = \int_R \mathbf{p} \, dV = \int_R \rho \mathbf{u} \, dV. \quad (2.32)$$

Following Newton's principles of motion, the balance of linear momentum

$$\dot{\mathbf{L}} = \frac{d}{dt} \int_R \rho \dot{\mathbf{u}} \, dV = \mathbf{F}^{ext} \quad (2.33)$$

is postulated, where

$$\mathbf{F}^{ext} = \int_{\partial R} \mathbf{t} \, dA \quad (2.34)$$

is the resultant external force acting on R if external volume forces are neglected. With (2.34) and Cauchy's theorem (2.21), the global balance of linear momentum (2.33) reads

$$\frac{d}{dt} \int_R \rho \dot{\mathbf{u}} \, dV = \int_{\partial R} \boldsymbol{\sigma}^T \mathbf{n} \, dA. \quad (2.35)$$

An equivalent local form can be derived using the local mass balance (2.31) as

$$\rho \ddot{\mathbf{u}} = \operatorname{div} \boldsymbol{\sigma}^T. \quad (2.36)$$

The local form of the balance of linear momentum (2.36) is also referred to as the equation of motion.

2.3.3 Balance of Angular Momentum

The angular momentum of R is

$$\mathbf{J}(t) = \int_R \mathbf{r}(\mathbf{x}) \times (\rho \dot{\mathbf{u}}) \, dV, \quad \mathbf{r}(\mathbf{x}) = \mathbf{x} - \mathbf{x}_0, \quad (2.37)$$

where \mathbf{x}_0 is a reference position and ' \times ' denotes the cross product of two vectors. Neglecting distributed resulting couples, a balance of angular momentum is postulated as

$$\dot{\mathbf{J}} = \frac{d}{dt} \int_R \mathbf{r} \times (\rho \dot{\mathbf{u}}) \, dV = \int_{\partial R} \mathbf{r} \times \mathbf{t} \, dA. \quad (2.38)$$

By means of the balance of linear momentum (2.36), the conservation of mass (2.31), Cauchy's theorem (2.21) and the divergence theorem (A.11) it follows the symmetry of the Cauchy stress tensor

$$\boldsymbol{\sigma} = \boldsymbol{\sigma}^T. \quad (2.39)$$

2.3.4 Balance of Energy and Caloric Equation of State

The kinetic energy inside R is

$$\mathcal{K} = \int_R k \, dV \quad \text{with} \quad k = \frac{1}{2} \rho \dot{\mathbf{u}} \cdot \dot{\mathbf{u}}. \quad (2.40)$$

Furthermore, the power of external forces is defined as

$$\mathcal{P}^{\text{ext}} = \int_{\partial R} \mathbf{t} \cdot \dot{\mathbf{u}} \, dA \quad (2.41)$$

and can be reformulated by means of the balance of the conservation of mass (2.31), linear momentum (2.36), the divergence theorem (A.11), the symmetry of the stress tensor (2.39) and Cauchy's theorem (2.21) to

$$\mathcal{P}^{\text{ext}} = \int_R (\boldsymbol{\sigma} : \dot{\boldsymbol{\varepsilon}} + \rho \ddot{\mathbf{u}} \cdot \dot{\mathbf{u}}) \, dV = \mathcal{P}^{\text{int}} + \frac{d\mathcal{K}}{dt}, \quad \text{with} \quad \mathcal{P}^{\text{int}} = \int_R \boldsymbol{\sigma} : \dot{\boldsymbol{\varepsilon}} \, dV. \quad (2.42)$$

Thus, the balance of mechanical energy

$$\frac{d\mathcal{K}}{dt} + \mathcal{P}^{\text{int}} = \mathcal{P}^{\text{ext}} \quad (2.43)$$

is a direct consequence of these relations. The quantity

$$\boldsymbol{\sigma} : \dot{\boldsymbol{\varepsilon}} = \frac{d}{dt} \int_{t_0}^t \boldsymbol{\sigma} : \frac{\partial \boldsymbol{\varepsilon}}{\partial t} \, dt = \frac{d}{dt} \int_{\boldsymbol{\varepsilon}(\mathbf{x}, t_0)}^{\boldsymbol{\varepsilon}(\mathbf{x}, t)} \boldsymbol{\sigma} : d\boldsymbol{\varepsilon} = \frac{dw^{\text{int}}}{dt} \quad (2.44)$$

is referred to as the stress power density, where

$$w^{\text{int}} = \int_{\boldsymbol{\varepsilon}(\mathbf{x}, t_0)}^{\boldsymbol{\varepsilon}(\mathbf{x}, t)} \boldsymbol{\sigma} : d\boldsymbol{\varepsilon} \quad (2.45)$$

is denoted as the stress work density. If the stress work density is only dependent on the current deformation $\boldsymbol{\varepsilon}$ and not on the deformation history or other fields, the work increment $dw^{\text{int}} = \boldsymbol{\sigma} : d\boldsymbol{\varepsilon}$ is the total differential of the potential

$$\psi^e(\boldsymbol{\varepsilon}) = w^{\text{int}}, \quad (2.46)$$

which is denoted as the strain energy density, i.e.

$$d\psi^e = \boldsymbol{\sigma} : d\boldsymbol{\varepsilon}. \quad (2.47)$$

The internal energy

$$\mathcal{E}(t) = \int_R e \, dV \quad (2.48)$$

represents the sum of all microscopic forms of energy in R . Its rate is equal to the stress power plus the thermal power

$$\mathcal{Q} = - \int_{\partial R} \mathbf{q}^\theta \cdot \mathbf{n} \, dA + \int_R s^\theta \, dV \quad (2.49)$$

currently applied to R , i.e.

$$\frac{d\mathcal{E}}{dt} = \mathcal{P}^{\text{int}} + \mathcal{Q}. \quad (2.50)$$

By substituting (2.43) into (2.50), the balance of energy

$$\frac{d\mathcal{K}}{dt} + \frac{d\mathcal{E}}{dt} = \mathcal{P}^{\text{ext}} + \mathcal{Q} \quad (2.51)$$

is obtained, which is also referred to as the first law of thermodynamics. The local form of the balance of thermal energy (2.50) can be derived by means of the divergence theorem (A.11) as

$$\dot{e} = \boldsymbol{\sigma} : \dot{\boldsymbol{\varepsilon}} - \text{div} \mathbf{q}^\theta + s^\theta. \quad (2.52)$$

In addition to the energy balance (2.52), it is necessary to establish a constitutive law that relates the internal energy e to measurable fields. For solids that sustain only small deformations, the internal energy is typically regarded as a function of the temperature only, i.e. $e = e(\theta)$, see e.g. Sadd (2009). Under these assumptions, the caloric equation of state is

$$de = \frac{\partial e}{\partial \theta} d\theta. \quad (2.53)$$

The material property

$$c_\theta^* = \frac{\partial e}{\partial \theta} \quad (2.54)$$

is denoted as the specific heat capacity at constant volume. It is the energy required to produce a unit increase in temperature of a unit volume of the body keeping the volume fixed. From (2.53) follows

$$de = c_\theta^* d\theta. \quad (2.55)$$

In the literature, the specific heat capacity is often given as the energy required to produce a unit increase of the temperature of a unit mass of the body keeping the volume fixed c_θ . Hence, it is also

$$de = \rho c_\theta d\theta. \quad (2.56)$$

2.3.5 Conservative Systems

Suppose the power of external forces for a purely mechanical system can be expressed as

$$\mathcal{P}^{\text{ext}} = -\frac{d\Pi^{\text{ext}}(t)}{dt} \quad (2.57)$$

and the stress power as

$$\frac{d\mathcal{P}^{\text{int}}}{dt} = \frac{d\Pi^{\text{int}}(t)}{dt}, \quad (2.58)$$

where the external potential energy Π^{ext} and the internal potential energy

$$\Pi^{\text{int}} = \int_R \psi^e dV \quad (2.59)$$

are scalar-valued functions. By (2.51) and $\mathcal{Q} = 0$ it is found that

$$\dot{\Pi} + \dot{\mathcal{K}} = \dot{\Pi}^{\text{int}} + \dot{\Pi}^{\text{ext}} + \dot{\mathcal{K}} = 0, \quad (2.60)$$

i.e. the sum of potential and the kinetic energy is conserved for a conservative dynamical process.

2.3.6 Second Law of Thermodynamics and Helmholtz Free Energy

The balance of energy (2.51) and (2.52) governs the energy transfer in a physical process but does not account for the direction of energy transfer. Nonetheless, in real processes a certain direction of energy transfer is often observed, e.g. heat always flows from the warmer region to the colder region of a body. This directional aspect is described by a thermodynamic state variable, the entropy $\eta(\mathbf{x}, t)$. The second law of thermodynamics postulates that the production of entropy is always positive, i.e.

$$\int_R r^\eta dR = \frac{d}{dt} \int_R \eta dV + \int_{\partial R} \mathbf{q}^\eta \cdot \mathbf{n} dA - \int_R s^\eta dV \geq 0, \quad (2.61)$$

where \mathbf{q}^η is the flux of entropy across the boundary ∂R and s^η is the entropy supply per unit volume from external sources. Furthermore, the relations

$$\mathbf{q}^\eta = \frac{\mathbf{q}^\theta}{\theta}, \quad s^\eta = \frac{s^\theta}{\theta} \quad (2.62)$$

are postulated, where $\theta(\mathbf{x}, t) > 0$ is the absolute temperature. With relation (2.62), the second law of thermodynamics in the global form reads

$$\frac{d}{dt} \int_R \eta dV + \int_{\partial R} \frac{\mathbf{q}^\theta}{\theta} \cdot \mathbf{n} dA - \int_R \frac{s^\theta}{\theta} dV \geq 0 \quad (2.63)$$

and by means of the divergence theorem (A.11), the local form of the second law

$$\theta\dot{\eta} + \operatorname{div}\mathbf{q}^\theta - \frac{1}{\theta}\mathbf{q}^\theta \cdot \operatorname{grad}\theta - s^\theta \geq 0 \quad (2.64)$$

is derived. The external heat supply s^θ can be eliminated by (2.52) to obtain

$$\boldsymbol{\sigma} : \dot{\boldsymbol{\varepsilon}} - \dot{e} + \theta\dot{\eta} - \frac{1}{\theta}\mathbf{q}^\theta \cdot \operatorname{grad}\theta \geq 0. \quad (2.65)$$

Considering heat conduction only, i.e. the last term in the above equation, and keeping in mind that the entropy production of such a pure heat conduction process should be non-negative results in

$$-\frac{1}{\theta}\mathbf{q}^\theta \cdot \operatorname{grad}\theta \geq 0, \quad (2.66)$$

which is the heat conduction inequality. A constitutive assumption for the heat flow under isotropic conditions that agrees with (2.66) is the well known Fourier's law of heat conduction

$$\mathbf{q}_\theta = -\kappa \operatorname{grad}\theta, \quad (2.67)$$

where $\kappa > 0$ is the thermal conductivity. The requirement (2.66) in conjunction with (2.65) leads to a stricter form of the second law of thermodynamics

$$\boldsymbol{\sigma} : \dot{\boldsymbol{\varepsilon}} - \dot{e} + \theta\dot{\eta} \geq 0. \quad (2.68)$$

Introducing the Helmholtz free energy per unit reference volume as

$$\psi^h = e - \theta\eta \quad (2.69)$$

and making use of (2.68) results in the form

$$\boldsymbol{\sigma} : \dot{\boldsymbol{\varepsilon}} - \dot{\psi}^h - \eta\dot{\theta} \geq 0 \quad (2.70)$$

of the so-called Clausius-Planck inequality. Suppose the Helmholtz free energy is a function of the strain $\boldsymbol{\varepsilon}$ and the temperature θ i.e.

$$\psi^h = \psi^h(\boldsymbol{\varepsilon}, \theta). \quad (2.71)$$

Then

$$\boldsymbol{\sigma} : \dot{\boldsymbol{\varepsilon}} - \frac{\partial\psi^h}{\partial\boldsymbol{\varepsilon}} : \dot{\boldsymbol{\varepsilon}} - \frac{\partial\psi^h}{\partial\theta}\dot{\theta} - \eta\dot{\theta} \geq 0 \quad (2.72)$$

which gives two constitutive laws

$$\boldsymbol{\sigma} = \frac{\partial\psi^h}{\partial\boldsymbol{\varepsilon}} \quad (2.73)$$

and

$$\text{and } \eta = -\frac{\partial \psi^h}{\partial \theta}. \quad (2.74)$$

By defining the free energy $\psi^h(\boldsymbol{\varepsilon}, \theta)$, the constitutive relations for the stress and the entropy are determined. Under small strain assumptions, the strain of a thermoelastic solid may be additionally decomposed as

$$\boldsymbol{\varepsilon} = \boldsymbol{\varepsilon}^e + \boldsymbol{\varepsilon}^\theta. \quad (2.75)$$

The first term on the right-hand side, $\boldsymbol{\varepsilon}^e$, denotes the elastic strain due to internal forces $\boldsymbol{\sigma}$, whereas $\boldsymbol{\varepsilon}^\theta$ is the strain that is caused by a temperature change relative to a reference temperature θ_0 . The strain due to thermal loads is assumed to be purely volumetric and isotropic, i.e.

$$\boldsymbol{\varepsilon}^\theta = \alpha_T (\theta - \theta_0) \mathbf{1}, \quad (2.76)$$

where α_T is the coefficient of thermal expansion of the material. Eventually, the free energy of the thermoelastic body is stated as

$$\psi^h = \psi^e(\boldsymbol{\varepsilon}, \theta) + \psi^\theta(\theta) = \frac{1}{2} \boldsymbol{\varepsilon}^e : (\mathbb{C} : \boldsymbol{\varepsilon}^e) + \psi^\theta(\theta), \quad (2.77)$$

where strain energy density ψ^e is the potential of the stress for fixed θ and

$$\mathbb{C} = [\lambda \delta_{ij} \delta_{kl} + \mu (\delta_{ik} \delta_{jl} + \delta_{il} \delta_{jk})] \mathbf{e}_i \otimes \mathbf{e}_j \otimes \mathbf{e}_k \otimes \mathbf{e}_l \quad (2.78)$$

is the fourth-order elasticity tensor for isotropic linear elastic material. The parameters λ and μ are the Lamé parameters. Equations (2.73) yield

$$\boldsymbol{\sigma} = \mathbb{C} : \boldsymbol{\varepsilon}^e \quad (2.79)$$

and

$$\eta = \alpha_T \text{tr}(\boldsymbol{\sigma}) - \frac{\partial \psi^\theta}{\partial \theta}. \quad (2.80)$$

Equivalent representations of the strain energy density are

$$\psi^e = \frac{1}{2} \boldsymbol{\sigma} : \boldsymbol{\varepsilon}^e, \quad (2.81)$$

$$\psi^e = \frac{1}{2} \lambda \text{tr}(\boldsymbol{\varepsilon}^e)^2 + \mu (\boldsymbol{\varepsilon}^e : \boldsymbol{\varepsilon}^e) \quad (2.82)$$

and

$$\psi^e = \frac{1}{2} K \text{tr}(\boldsymbol{\varepsilon}^e)^2 + \mu (\mathbf{e}^e : \mathbf{e}^e), \quad (2.83)$$

where

$$K_n = \lambda + \frac{2}{n}\mu \quad (2.84)$$

is the n -dimensional bulk modulus. For plane strain problems, the expressions of the free energy density and the constitutive law (2.80) can be used as well, except that $n = 2$. Often, the Young's modulus

$$E = \frac{\mu(3\lambda + 2\mu)}{\lambda + \mu} \quad (2.85)$$

and the Poisson's ratio

$$\nu = \frac{\lambda}{2(\lambda + \mu)} \quad (2.86)$$

are used as an alternative to the elasticity parameters λ , μ and K_n .

2.4 Wave Propagation

By substituting the kinematic relation (2.14) and the constitutive law (2.79) into (2.36) the relation

$$(\lambda + \mu) \nabla (\nabla \cdot \mathbf{u}) + \mu \Delta \mathbf{u} + \alpha_T n K_n \nabla \theta = \rho \ddot{\mathbf{u}} \quad (2.87)$$

is obtained, where

$$\Delta(*) = \frac{\partial^2(*)}{\partial x_i \partial x_i} = \nabla \cdot \nabla (*). \quad (2.88)$$

is the Laplace operator. Assuming isothermal conditions ($\theta = \text{const.}$) and making use of the identity $\nabla \times (\nabla \times \mathbf{u}) = \nabla(\nabla \cdot \mathbf{u}) - \Delta \mathbf{u}$ yields Navier's equation

$$c_d^2 \nabla (\nabla \cdot \mathbf{u}) - c_s^2 \nabla \times (\nabla \times \mathbf{u}) = \ddot{\mathbf{u}}, \quad (2.89)$$

where

$$c_d = \sqrt{\frac{\lambda + 2\mu}{\rho}} \quad \text{and} \quad c_s = \sqrt{\frac{\mu}{\rho}}. \quad (2.90)$$

Taking the divergence of each term in (2.89) results in

$$c_d^2 \Delta (\nabla \cdot \mathbf{u}) = \frac{\partial^2 (\nabla \cdot \mathbf{u})}{\partial t^2}. \quad (2.91)$$

Thus, the dilatation $\nabla \cdot \mathbf{u}$ obeys the wave equation, with the characteristic wave speed c_d . By operating on each term of (2.89) with the curl operator $\nabla \times (*)$ the relation

$$c_s^2 \Delta (\nabla \times \mathbf{u}) = \frac{\partial^2 (\nabla \times \mathbf{u})}{\partial t^2} \quad (2.92)$$

is obtained which shows that the rotation vector $\nabla \times \mathbf{u}$ obeys the wave equation with wave speed c_s . Apart from dilatational and shear waves, surface waves also play an important role for dynamic fracture problems. Surface waves are propagated over the bounding surface of a solid body and their amplitude decreases rapidly inside of the body. It can be shown that the motion of such a wave is two-dimensional and that their wave speed c_r the so called Rayleigh wave speed is a root of the Rayleigh function

$$R(c_r) = 4\sqrt{1 - \left(\frac{c_r}{c_d}\right)^2} \sqrt{1 - \left(\frac{c_r}{c_s}\right)^2} - \left[2 - \left(\frac{c_r}{c_s}\right)^2\right]^2 = 0, \quad (2.93)$$

see Gross and Seelig (2011) and Love (1944). According to Rahman and Micheli (2006) the Rayleigh wave speed can be approximated by

$$c_r \approx \frac{0.87 + 1.12\nu}{1 + \nu} c_s, \quad (2.94)$$

which is used to compute c_r in this work. Poisson's ratio ν is related to the Lamé parameters through

$$\nu = \frac{\lambda}{2(\lambda + \mu)}. \quad (2.95)$$

2.5 Hamilton's Principle

Hamilton's principle allows to state the behaviour of a physical system in a way that is equivalent to the balance laws from Section 2.3. However, the principle also allows useful generalizations of these laws as for the dynamic phase field fracture model considered in this work. Motivated by his previous work in optics, W. R. Hamilton stated the variational principle today known as Hamilton's principle for dynamic systems of particles in Hamilton (1835). Since then, the principle has also widely been used in continuum mechanics. An introduction to the application of Hamilton's principle to continuum mechanics can be found in Reddy (1989).

In order to be able to formulate Hamilton's principle, the concepts of *admissible* and *comparison* fields are introduced in the following. A field ϕ , subject to Dirichlet boundary conditions on $\partial\Omega_\phi \subseteq \partial\Omega$ as well as Neumann boundary conditions on $\partial\Omega_{\nabla\phi} \subseteq \partial\Omega$, that represents some physical quantity is called *admissible* if it is C^2 on $\Omega \times [t_1, t_2]$, where t_1 and $t_2 > t_1$ are fixed times at which the value of the field ϕ is prescribed. A *comparison* field is an admissible field of the form

$$\phi^*(\mathbf{x}, t, \epsilon) = \phi(\mathbf{x}, t) + \epsilon\eta_\phi(\mathbf{x}, t), \quad (2.96)$$

where η_ϕ is an arbitrary scalar field that obeys $\eta_\phi(\mathbf{x}, t_1) = 0$, $\eta_\phi(\mathbf{x}, t_2) = 0$, is C^2 on $\Omega \times [t_1, t_2]$ and vanishes on $\partial\Omega_\phi$. The quantity ϵ is a scalar parameter.

The kinetic and potential energies of the body may be considered as functions of multiple comparison fields ϕ_k^* and their derivatives, i.e.

$$\mathcal{K}^*(\epsilon) = \mathcal{K}(\phi_1^*, \phi_2^*, \dots, \nabla\phi_1^*, \nabla\phi_2^*, \dots, \dot{\phi}_1^*, \dot{\phi}_2^*, \dots), \quad (2.97)$$

$$\Pi^*(\epsilon) = \Pi_i^*(\epsilon) + \Pi_i^*(\epsilon) = \Pi(\phi_1^*, \phi_2^*, \dots, \nabla\phi_1^*, \nabla\phi_2^*, \dots, \dot{\phi}_1^*, \dot{\phi}_2^*, \dots). \quad (2.98)$$

Furthermore, the notation

$$\delta(*) = \left. \frac{\partial(*)}{\partial\epsilon} \right|_{\epsilon=0} \quad (2.99)$$

of the variation of $(*)$ is introduced. Non-conservative generalized forces Q that are work-conjugate to ϕ may be included in Hamilton's principle by expressing their virtual work as

$$\delta W = Q\delta\phi, \quad (2.100)$$

which is a slight violation of the notation (2.99) that nonetheless is common in the literature. Eventually Hamilton's principle can be stated as follows:

Among admissible fields, the actual fields of a system fulfill

$$\left[\int_{t_1}^{t_2} \delta(\mathcal{K} - \Pi) + \delta W \right] dt = 0. \quad (2.101)$$

This statement is a postulate on the behaviour of the considered system much as the balance laws that were considered in Section 2.3. The quantity

$$L = \int_{\Omega} \mathcal{L} dV = \mathcal{K} - \Pi \quad (2.102)$$

is referred to as the Lagrangian, whereas

$$\mathcal{L} = \mathcal{L}(\phi_1, \phi_2, \dots) \quad (2.103)$$

is the Lagrangian density. The equations that govern the evolution of the local fields ϕ_k follow from (2.101) as necessary conditions. The prerequisite for their derivation are the fundamental Lemmas of variational calculus, which are presented in Reddy (1989) as:

Lemma 1: *Let \mathcal{W} be an inner product space and consider a C^0 field $\mathbf{g} : \Omega \times [t_1, t_2] \rightarrow \mathcal{W}$. If the equation*

$$\int_{t_1}^{t_2} \int_{\Omega} \mathbf{g} \cdot \mathbf{w} dV dt = 0 \quad (2.104)$$

holds for every C^∞ field $\mathbf{w} : \Omega \times [t_1, t_2]$ that vanishes at time t_1 and at time t_2 then $\mathbf{g} = \mathbf{0}$ on $\Omega \times [t_1, t_2]$.

Lemma 2: Suppose that $\partial\Omega$ consists of complementary regular sub-surfaces $\partial\Omega_\phi$ and $\partial\Omega_{\nabla\phi}$. Let \mathcal{W} be an inner product space, and consider a function $\mathbf{g} : \partial\Omega_{\nabla\phi} \times [t_1, t_2] \rightarrow \mathcal{W}$ that is piecewise regular and continuous in time. If the equation

$$\int_{t_1}^{t_2} \int_{\partial\Omega} \mathbf{g} \cdot \mathbf{w} \, dA \, dt = 0 \quad (2.105)$$

holds for every C^∞ field $\mathbf{w} : \Omega \times [t_1, t_2]$ that vanishes at time t_1 , at time t_2 , and on the part of the boundary $\partial\Omega_\phi \subseteq \partial\Omega$, then $\mathbf{g} = \mathbf{0}$ on $\partial\Omega_{\nabla\phi} \times [t_1, t_2]$.

3 Dynamic Linear Elastic Fracture Mechanics

This chapter gives an introduction to the analysis of dynamic fracture of brittle materials within the framework of continuum mechanics and discusses some experimental findings on the topic. Further details can be found in textbooks on fracture mechanics such as Gross and Seelig (2011) and Freund (1990), as well as in the cited literature.

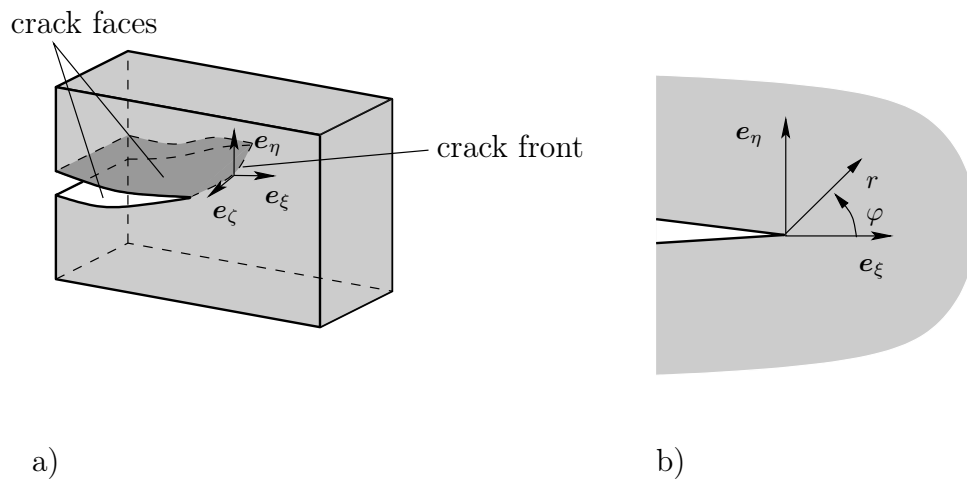


Figure 3.1: Illustration of a) a crack in three dimensions and b) crack tip vicinity in a two dimensional setting. Here, r and ϕ represent the radial and angular coordinates.

3.1 Basic Assumptions

From a continuum mechanics point of view, cracks can be interpreted as cuts inside a continuous body. The boundaries on opposite sides of the crack are referred to as the *crack faces*, which together form the *crack surface*, see Fig. 3.1 a). The crack ends at the *crack front* or *crack tip* in 2D. In the reference configuration,

the crack faces occupy the same surface – or line in a two-dimensional setting – in the physical space. Imagine a crack whose crack front is a smooth curve with no corners or cusps. Furthermore, a local coordinate system, where the ζ -axis is locally parallel to the crack front and the ξ -axis is tangent to the crack surface as depicted in Fig. 3.1 a) and b), is introduced. The mechanical fields are essentially two-dimensional for points that are close to the crack front compared to the radius of curvature of the crack front, the distance to the boundaries and the distance to possible wavefronts since the dependence on the radial coordinate r dominates the fields in this case, see Fig. 3.1 b). This results in the fields being insensitive to a variation of the ζ -coordinate, see Irwin (1960). Consequently, the displacement field near the crack tip \mathbf{u}^{tip} can be resolved into three distinct two-dimensional fields as

$$\mathbf{u}^{\text{tip}} = \mathbf{u}^I(r, \varphi) + \mathbf{u}^{II}(r, \varphi) + u^{III}(r, \varphi)\mathbf{e}_\zeta, \quad (3.1)$$

where the components \mathbf{u}^I , \mathbf{u}^{II} and u^{III} are classified based on the different modes of crack opening as shown in Fig. 3.1. Mode I, i.e. the component \mathbf{u}^I , refers to

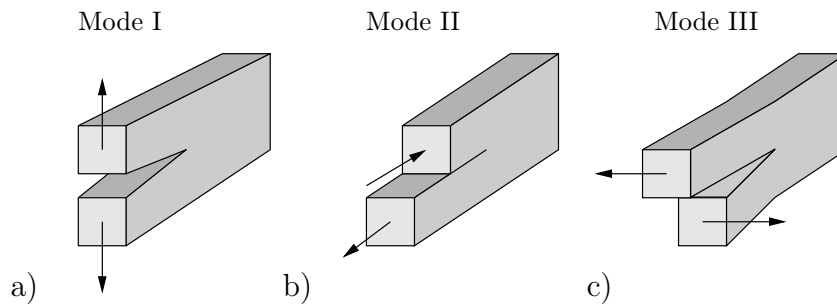


Figure 3.2: Crack opening modes.

symmetric crack opening orthogonal to the local crack surface. In contrast, the in-plane shearing Mode II described by \mathbf{u}^{II} is a sliding motion of the crack faces perpendicular to the crack front. Finally, the antiplane shearing Mode III given by u^{III} describes a sliding motion of the crack faces parallel to the crack front.

In this work, cracks are considered to be of the same size as a typical length-scale of the regarded body. Thus, material features that are small compared to the considered macroscopic scale, e.g. micro cracks, inclusions, pores or dislocations in the crystal lattice of the material are not modelled explicitly. Furthermore, a number of processes that accompany fracturing, such as the breaking of material bonds, cannot be described in a straightforward manner by a continuum model. For a continuum model to still be a justified idealization, these processes need to be restricted to a negligibly small region around the crack front (crack tip in 2D) which is called the process zone. This assumption holds true for most brittle materials and metals. In addition to the presumption of a small process zone, it

is also required that the whole body can be assumed to be composed of linear elastic material that only undergoes small deformations and displacements. This requires the zone in which inelastic, e.g. plastic, material behaviour is present to be of negligible size as well.

For the scope of this work, the breaking of the material bonds during fracturing is assumed to be irreversible, i.e. a restoration of the material cohesion is not possible after the material has separated. A further feature of cracks that is fundamental to modelling fracture is the impenetrability of the crack faces, which is discussed in detail in Section 4.4.

3.2 Asymptotic Fields

By means of asymptotic analysis, the fields near a moving crack tip corresponding to bounded total mechanical energy can be derived, as described in Freund (1990). The asymptotic expressions for the fields are only valid for points that are close to the crack tip compared to any other length-scale of the regarded body. Still, since non-linear effects are assumed to be restricted to a small region around the crack tip, the asymptotic linear elastic fields provide a reasonably accurate description of the mechanical state at the crack tip. Therefore, they allow to predict the behaviour of real brittle materials if the assumptions mentioned above apply.

Often, only the dominant (as $r \rightarrow 0$) components of the asymptotic fields are considered. For a Mode I deformation of a straight crack the singular term of the asymptotic expansion of the stress field is given in the subsonic speed regime, meaning for crack velocities v smaller than the shear wave speed c_s , in the ξ - η - ζ reference frame by

$$\sigma_{ij}^I \approx \frac{K_I(t)}{\sqrt{2\pi r}} \Sigma_{ij}^I(\varphi, v), \quad \text{with} \quad \Sigma_{ij}^I = \frac{V_{ij}^I(\varphi, v)}{R(v)}, \quad i, j \in \{\xi, \eta\}, \quad (3.2)$$

where $V_{ij}^I(\varphi, v)$ is a universal function of the crack speed v and φ see e.g. Freund (1990) for details. The asymptotic particle velocities corresponding to the stress field (3.2) have a similar structure, i.e.

$$\dot{u}_\xi^I = \frac{K_I(t)U_\xi^I(\varphi, v)}{\mu R(v)\sqrt{2\pi r}}, \quad \dot{u}_\eta^I = \frac{K_I(t)U_\eta^I(\varphi, v)}{\mu R(v)\sqrt{2\pi r}}. \quad (3.3)$$

Analogously, for the Mode II case the structure is

$$\sigma_{ij}^{II} \approx \frac{K_{II}(t)}{\sqrt{2\pi r}} \Sigma_{ij}^{II}(\varphi, v), \quad \text{with} \quad \Sigma_{ij}^{II} = \frac{V_{ij}^{II}(\varphi, v)}{R(v)}, \quad i, j \in \{\xi, \eta\}, \quad (3.4)$$

and

$$\dot{u}_{\xi}^{II} = \frac{K_{II}(t)U_{\xi}^{II}(\varphi, v)}{\mu R(v)\sqrt{2\pi r}}, \quad \dot{u}_{\eta}^{II} = \frac{K_{II}(t)U_{\eta}^{II}(\varphi, v)}{\mu R(v)\sqrt{2\pi r}}. \quad (3.5)$$

Lastly, the asymptotic analysis of a Mode III loaded crack yields the corresponding near-tip stress field as

$$\sigma_{i\zeta}^{III} \approx \frac{K_{III}(t)}{\sqrt{2\pi r}} \Sigma_{i\zeta}(\varphi, v), \quad i, j \in \{\xi, \eta\} \quad (3.6)$$

and the associated particle velocity as

$$\dot{u}_{\zeta} \approx \frac{K_{III}(t)}{\sqrt{2\pi r}} U_{\zeta}^{III}(\varphi, v). \quad (3.7)$$

Thus, apart from the scalar multipliers $K_I(t)$, $K_{II}(t)$ and $K_{III}(t)$ the crack tip fields are determined for a given crack speed v by the universal functions V_{ij}^I , V_{ij}^{II} , $\Sigma_{i\zeta}$, U_i^I , U_i^{II} , U_{ζ}^{III} . The multipliers quantify the intensity of the crack tip field which motivates the term *stress intensity factors* (SIFs). The region in which the stress of the body is dominated by the singular expressions (3.2), (3.4) and (3.6) is referred to as the K -dominant zone in which the stress for general crack tip opening, i.e. a combination of all modes, is determined by

$$\sigma_{ij} \approx \frac{K_I(t)}{\sqrt{2\pi r}} \Sigma_{ij}^I(\varphi, v) + \frac{K_{II}(t)}{\sqrt{2\pi r}} \Sigma_{ij}^{II}(\varphi, v) + \frac{K_{III}(t)}{\sqrt{2\pi r}} \Sigma_{ij}^{III}(\varphi, v). \quad (3.8)$$

The stress distribution is singular at the crack tip for all three modes of crack opening which is a consequence of assuming that the body is made of linear elastic material. This idealization is justified by the assumption of small scale yielding, i.e. excess stresses are relieved by plastic deformation in a region of negligible size compared to the K -dominant region. Based on the concept that the asymptotic fields determine the material separation in the process zone, a condition for crack propagation may be formulated as

$$F(K_I, K_{II}, K_{III}) = 0. \quad (3.9)$$

An important result for the fields $\phi(\mathbf{x}, t)$ near a moving crack tip with current position \mathbf{z} can be obtained if the $\boldsymbol{\xi}$ -coordinate system is considered to move with the crack tip, i.e. the transformation $\phi(\mathbf{x}, t) = \phi(\boldsymbol{\xi}, t)$, where $\boldsymbol{\xi} = \mathbf{x} - \mathbf{z}$ is introduced. The material time derivative of ϕ is

$$\left. \frac{\partial \phi}{\partial t} \right|_{\mathbf{x}} = \left. \frac{\partial \phi}{\partial t} \right|_{\boldsymbol{\xi}} - \nabla \phi \cdot \mathbf{v}, \quad (3.10)$$

with the crack speed

$$\mathbf{v} = \frac{dz}{dt}. \quad (3.11)$$

For fields ϕ that show high gradients in the vicinity of cracks, the time derivative in the moving reference frame is negligible compared to the convective second term on the right-hand side of (3.10) and thus

$$\left. \frac{\partial \phi}{\partial t} \right|_{\mathbf{x}} \approx -\nabla \phi \cdot \mathbf{v}, \quad (3.12)$$

which is referred to as the ‘transport condition of the singularity’, see Ehrlacher (1981). In particular,

$$-\dot{\mathbf{u}} \approx (\text{grad} \mathbf{u}) \mathbf{v} \quad \text{and} \quad -\ddot{\mathbf{u}} \approx (\text{grad} \dot{\mathbf{u}}) \mathbf{v} \quad (3.13)$$

which also implies the relation

$$\dot{k} = \rho \ddot{\mathbf{u}} \cdot \dot{\mathbf{u}} \approx -\nabla k \cdot \mathbf{v} \quad (3.14)$$

for the kinetic energy density $k = \frac{1}{2} \rho \dot{\mathbf{u}} \cdot \dot{\mathbf{u}}$.

3.3 Energy Concepts

The importance of energy concepts in fracture mechanics has first been recognized by Griffith (1921). He reasoned that crack propagation requires the creation of new surfaces with their associated surface energies and concluded that this energy has to be provided by the body as mechanical energy in order for a crack to grow. When inertial effects are neglected, the negative rate of change of the potential energy of a body with respect to a crack advance is called the *energy release rate* which can be interpreted as a generalized force that is work-conjugated to the amount of crack advance. Atkinson and Eshelby (1968) proposed that in the dynamic case the energy release rate should be the same as for quasi-static growth with the potential energy replaced by the total mechanical energy. An integral expression for the dynamic energy release rate was derived by Kostrov and Nikitin (1970) for general material behaviour and by Freund (1972) for linear elastodynamics. Following Griffith’s idea, the energy that is required to separate the material and thus to create the fracture surfaces Γ is included in the energy balance (2.51), i.e.

$$\dot{\mathcal{K}} + \dot{\mathcal{E}} + \dot{\Gamma} = \mathcal{P}^{ext} + \mathcal{Q}. \quad (3.15)$$

As mentioned before, fracturing is assumed to be irreversible in this work. Hence, the rate of the fracture energy is required to be non-negative, i.e. $\dot{\Gamma} \geq 0$. Since

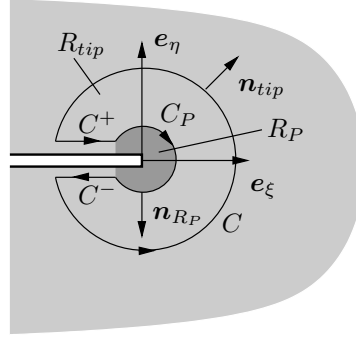


Figure 3.3: Illustration of the near-tip region.

the fracture process itself, including the breaking of material bonds and other phenomena that are not described by the continuum model, takes place in the process zone, it is reasonable to split the energy balance into separate parts for the process zone and the remainder of the body as described in Gross and Seelig (2011), i.e.

$$\begin{aligned} \text{process zone: } \dot{\Gamma} &= -\mathcal{P}', \\ \text{remainder of the body: } \dot{\mathcal{E}} + \dot{\mathcal{K}} &= \mathcal{P}^{ext} + \mathcal{Q} + \mathcal{P}', \end{aligned} \quad (3.16)$$

where $-\mathcal{P}'$ describes the energy transport into the process zone. The transformation of energy into fracture energy occurs only in the process zone and cannot be described directly by means of continuum mechanics. Consequently, the focus is on the energy balance for the remainder of the body (3.16)₂ except for the definition of the fracture resistance or specific fracture energy that describes the amount of energy that is required to create a crack surface increment dA , i.e.

$$\mathcal{G}_c = \frac{d\Gamma}{dA}. \quad (3.17)$$

In order to compute the energy flux into the process zone \mathcal{P}' , the setup in Fig. 3.3 is considered. The control volume $R_{tip} \subseteq \Omega$ is bounded by the curves (2D) or surfaces (3D) C , $C^+(t)$, $C^-(t)$ and $C_P(t)$. The boundary C is stationary, the crack faces $C^+(t)$ and $C^-(t)$ are traction-free and the boundary of the process zone C_P moves with the crack speed \mathbf{v} . The energy balance (3.16)₂ for R_{tip} yields by means of the transport theorem (A.13)

$$\begin{aligned} & \int_{R_{tip}} (\dot{e} + \dot{k}) \, dV + \int_{C_P} (e + k) \mathbf{n}_{tip} \cdot \mathbf{v} \, dA \\ &= \int_C \boldsymbol{\sigma} \mathbf{n}_{tip} \cdot \dot{\mathbf{u}} \, dA - \int_C \mathbf{q}^\theta \cdot \mathbf{n}_{tip} \, dA + \int_{R_{tip}} s^\theta \, dV + \mathcal{P}', \end{aligned} \quad (3.18)$$

which with the local energy balance (2.52), the equation of motion (2.36), the identity $\boldsymbol{\sigma} : \dot{\boldsymbol{\varepsilon}} = \text{div}(\boldsymbol{\sigma}\dot{\mathbf{u}}) - \text{div}\boldsymbol{\sigma} \cdot \dot{\mathbf{u}}$, and the divergence theorem (A.11) results in

$$\int_{C_P} (\boldsymbol{\sigma}\dot{\mathbf{u}} - \mathbf{q}^\theta) \cdot \mathbf{n}_{tip} \, dA + \int_{C_P} (e + k) \mathbf{n}_{tip} \cdot \mathbf{v} \, dA = \mathcal{P}'. \quad (3.19)$$

Hence, the energy flow into the process zone is

$$-\mathcal{P}' = \int_{C_P} (\boldsymbol{\sigma}\dot{\mathbf{u}} - \mathbf{q}^\theta) \cdot \mathbf{n}_{R_P} \, dA + \int_{C_P} (e + k) \mathbf{n}_{R_P} \cdot \mathbf{v} \, dA. \quad (3.20)$$

Considering a purely mechanical system, this simplifies to

$$-\mathcal{P}' = F(C_P) = \int_{C_P} [\boldsymbol{\sigma}\dot{\mathbf{u}} + (\psi^e + k) \mathbf{v}] \cdot \mathbf{n}_{R_P} \, dA. \quad (3.21)$$

In general, the value of F is not independent from the chosen contour. In order to illustrate this fact, consider two contours C_1 and C_2 of the same type as C_P with C_2 enclosing C_1 and C_P . These new contours also define control volumes R_1 and R_2 with their boundaries consisting of the traction-free crack faces, the contour C_1 or C_2 respectively and C_P . By denoting the outward normal vectors as \mathbf{n}_1 and \mathbf{n}_2 respectively, the difference between $F(C_2)$ and $F(C_1)$ becomes

$$\begin{aligned} F(C_2) - F(C_1) &= \int_{C_2} [\boldsymbol{\sigma}\dot{\mathbf{u}} + (\psi^e + k) \mathbf{v}] \cdot \mathbf{n}_2 \, dA - \int_{C_1} [\boldsymbol{\sigma}\dot{\mathbf{u}} + (\psi^e + k) \mathbf{v}] \cdot \mathbf{n}_1 \, dA \\ &= \int_{C_{12}} [\boldsymbol{\sigma}\dot{\mathbf{u}} + (\psi^e + k) \mathbf{v}] \cdot \mathbf{n}_{12} \, dA \end{aligned} \quad (3.22)$$

with C_{12} being the boundary of the control volume R_{12} that is composed of C_1 , C_2 and the crack face segments in between and has the outward normal vector \mathbf{n}_{12} . By means of the divergence theorem it is

$$F(C_2) - F(C_1) = \int_{R_{12}} \text{div}(\boldsymbol{\sigma}\dot{\mathbf{u}} + (\psi^e + k) \mathbf{v}) \, dV \quad (3.23)$$

$$= \int_{R_{12}} \left[\dot{\psi}^e + \dot{k} + \nabla\psi^e \cdot \mathbf{v} + \nabla k \cdot \mathbf{v} \right] \, dV, \quad (3.24)$$

which is in general non-zero. In the vicinity of the crack tip, however, (3.12) applies for k and ψ^e and consequently the integral is indeed path independent. The *dynamic energy release rate* is defined as the rate of mechanical energy flow out of the body and into the process zone per unit crack advance, see Freund (1990). Thus, it is

$$\mathcal{G} = \lim_{C_1 \rightarrow 0} \left[\frac{1}{v} \int_{C_1} ((\psi^e + k) \mathbf{n}_1 \cdot \mathbf{v} + (\boldsymbol{\sigma}\dot{\mathbf{u}}) \cdot \mathbf{n}_1) \, dA \right], \quad (3.25)$$

where the limit $C_1 \rightarrow 0$ should be understood as any contour C_1 that is at least small enough to be completely embedded in the K -dominant zone in a way that (3.12) applies. A domain-independent expression of the energy release rate can be obtained by substituting (3.25) into (3.22) and using the notation $C = C_2$ which yields

$$\mathcal{G} = \frac{1}{v} \left[\int_C [\boldsymbol{\sigma} \dot{\mathbf{u}} + (\psi^e + k) \mathbf{v}] \cdot \mathbf{n}_R \, dA - \int_{R_{tip}} \operatorname{div} [(\psi^e + k) \mathbf{v} + \boldsymbol{\sigma} \dot{\mathbf{u}}] \, dV \right]. \quad (3.26)$$

The integrand of the second integral appears to be singular but indeed has a finite value as described in Nakamura et al. (1985). Thus, in contrast to equilibrium fracture mechanics, the crack tip integral is not path-independent but is complemented by a domain integral, i.e. it is a domain independent quantity. It can be shown that the dynamic energy release rate is related to the stress intensity factors by

$$\mathcal{G} = \frac{1 - \nu^2}{E} [A_I(v)K_I^2 + A_{II}(v)K_{II}^2] + \frac{1}{2\mu} A_{III}(v)K_{III}^2, \quad (3.27)$$

where A_I , A_{II} and A_{III} are universal functions of the crack velocity v , see e.g. Freund (1990) for details.

The expressions for the energy release rate (3.25) and (3.26) as well as the asymptotic crack tip fields from Section 3.6, follow from the a priori assumption of a crack motion with speed \mathbf{v} . In principle, it is possible to solve the governing field equations for this specified motion in order to compute \mathcal{G} and the SIFs. In order to be able to actually predict the motion of a crack, however, the field equations must be complemented by a *crack growth criterion* which is an additional physical postulate on the material behaviour. Typically, such a criterion states that the crack grows if a parameter defining the mechanical state of the crack front (or crack tip) like the energy release rate or the SIF is equal to some material parameter defining the resistance of the material. In linear elastic fracture mechanics, the most common formulations are Irwin's critical stress intensity factor criterion (3.9) and Griffith's critical energy release rate criterion which may be stated as:

A crack grows in such a way that the dynamic energy release rate \mathcal{G} is always equal to the specific fracture energy \mathcal{G}_c , i.e.

$$\mathcal{G} = \mathcal{G}_c \quad \text{during crack growth.} \quad (3.28)$$

The specific fracture energy \mathcal{G}_c has to be determined in experiments and may depend on the crack length, the crack velocity, the temperature or other physical quantities. In this work, however, it is assumed to be constant.

As mentioned in Freund (1990), in the simplest situation of two dimensional deformation, the energy release rate may be considered as a function of the current crack tip position $\mathbf{z}(t)$, the crack velocity $\dot{\mathbf{z}} = \mathbf{v}$, the time t , the loading history, the geometrical configuration of the regarded body, and the material parameters. Thus, (3.28) can be written as

$$\mathcal{G}(\mathbf{z}, \dot{\mathbf{z}}, t, \text{loading, configuration, material parameters}) = \mathcal{G}_c. \quad (3.29)$$

Equation (3.29) is a first order ordinary differential equation for the crack tip position $\mathbf{z}(t)$ which is called the *equation of motion of the crack tip* in analogy to the ordinary differential equations that describe the motion of particles.

Consider a body with a straight crack that grows under plane strain Mode I deformation in x_1 -direction in an infinite elastic medium. The equation of motion of the crack tip by means of (3.27) and (3.28) is

$$\frac{1 - \nu^2}{E} A_I(\dot{z}_1) K_I^2(t, z_1, \dot{z}_1) = \mathcal{G}_c. \quad (3.30)$$

Equation (3.30) allows to describe the motion of a crack tip if the dependence of the stress intensity factor on its arguments is known. As shown in Burridge (1976), the stress intensity factor for the considered situation and for general crack face loading has the form

$$K_I(t, z_1, \dot{z}_1) = k(\dot{z}_1) K_I(t, z_1, 0), \quad (3.31)$$

where the universal function $k(v)$ of the crack speed can be approximated by

$$k(v) \approx \frac{1 - \frac{v}{c_r}}{\alpha_d}, \quad \text{with} \quad \alpha_d = \sqrt{1 - \frac{v^2}{c_d^2}}. \quad (3.32)$$

The quantity $K_I(t, z_1, 0)$ is the SIF for a stationary crack of the same size and subject to the same crack face loading. For time independent loading with general spatial distribution along the crack faces the relation (3.31) simplifies to

$$K_I(z_1, \dot{z}_1) = k(\dot{z}_1) K_I(z_1, 0), \quad (3.33)$$

where $K_I(z_1, 0)$ is the equilibrium stress intensity factor for the specified time independent loading and instant crack tip position z_1 as described in Freund (1990). With the approximation

$$A_I(\dot{z}_1) k(\dot{z}_1)^2 \approx 1 - \frac{\dot{z}_1}{c_r}, \quad (3.34)$$

which is accurate over the whole range of velocities $0 < \dot{z}_1 < c_r$, the equation of motion of the crack tip (3.30) becomes

$$\frac{E \mathcal{G}_c}{(1 - \nu^2) K_I(t, z_1, 0)^2} = 1 - \frac{\dot{z}_1}{c_r}. \quad (3.35)$$

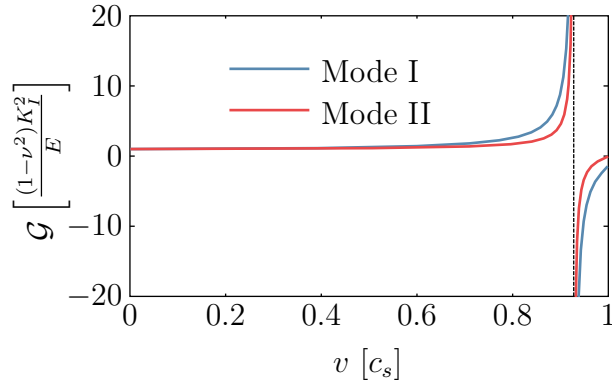


Figure 3.4: Energy release rates in the subsonic crack speed regime. The Rayleigh wave speed is indicated by the vertical black line.

From (3.35) it can be concluded that the upper limit for the crack speed under pure Mode I deformation is the Rayleigh wave speed since $\dot{z}_1 \rightarrow c_r$ as $K_I \rightarrow \infty$. Furthermore, the separation of a cohesionless interface, i.e. crack growth with no energy absorption $\mathcal{G}_c = 0$, occurs at the Rayleigh wave speed.

3.4 Crack Speed Limits

Unlike to equilibrium fracture mechanics, inertial effects limit admissible crack tip velocities in a dynamic setting. Material particles have to be separated from each other at the crack tip of a fast running crack. The inertia of these material particles results in a resistance to crack propagation. An overview of theoretically admissible crack speed regimes is given in Broberg (1989), where the criterion that defines admissible velocity fields is a non-negative energy release rate \mathcal{G} , i.e. energy is required to flow into the process zone in order for crack growth to be possible. Crack velocities $v < c_s$ are referred to as subsonic, whereas velocities $v > c_d$ are called supersonic velocities. Crack growth at the intermediate speed, $c_s < v < c_d$, is denoted as transsonic or intersonic crack speed. The energy release rates for the subsonic case for Mode I and Mode II can be computed by (3.27) for a given K_I . In Fig. 3.4, it can be observed that the energy release rate for Mode I and Mode II is only non-negative for sub Rayleigh wave speeds. Therefore, a Mode I or Mode II crack cannot propagate in the subsonic super Rayleigh speed regime, $c_r < v < c_s$.

The intersonic speed regime is more cumbersome to analyze and only an excerpt of the results is given here. It is mentioned in Broberg (1989) that a Barenblatt-type process zone, see Barenblatt (1962), needs to be considered in this case. By means of this approach, it turns out that for a Mode II deformation, \mathcal{G} is indeed positive in the intersonic speed regime. Thus, Mode II crack propagation is, in

principle, possible for $c_s \leq v \leq c_d$. The stress singularity for intersonic Mode II fracture, which is of the order $r^{-\gamma}$, $\gamma < 0.5$, is weaker than the singularity for the subsonic case $r^{-\frac{1}{2}}$. An exception to this is the case of crack propagation at a speed of $v = \sqrt{2}c_s$ for which the singularity is also of order $r^{-\frac{1}{2}}$. Hence, \mathcal{G} is maximal for this particular crack speed and one can argue that this should be a preferred crack speed in the intersonic speed regime. An interesting feature of intersonic Mode II crack growth is the appearance of a wave front that lags behind the crack tip and propagates at the speed of equivoluminal waves. The angle of the wave front relative to the crack plane is given by

$$\sin \theta_s = \frac{c_s}{v}, \quad \frac{\pi}{2} < \theta_s < \pi. \quad (3.36)$$

For the intersonic Mode I situation it turns out, that the formally computed energy release rate \mathcal{G} is negative independently of the exact value of the crack speed, see Broberg (1989). Consequently, Mode I propagation in the intersonic speed regime is not possible. Although not treated in this work, for completeness the truly supersonic case, $v > c_d$ is mentioned. In this case, the material in which the crack advances has no prior information on the crack. That is, the material might be completely stress-free. For such crack growth to occur, a moving traction load must be invoked on the crack tip which supplies enough energy for material separation. This has for example been achieved by means of a laser in Curran et al. (1970).

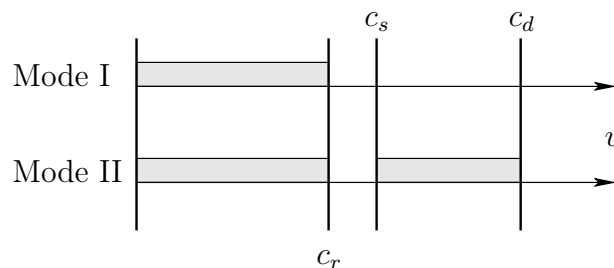


Figure 3.5: Admissible crack speeds (grey shaded regions) for Mode I and Mode II.

The theoretically admissible crack tip velocities for Mode I and Mode II are summarized in Fig. 3.5. Nevertheless, experiments show that in reality Mode I crack velocities rarely exceed $0.6c_r$ even for the most brittle materials, see e.g. Ravi-Chandar and Knauss (1984c). This can be explained by a dynamic instability that occurs above a critical crack velocity of $v_c \approx 0.4c_r$. The instability manifests in the occurrence of a number of micro-branches which is accompanied by a change in the structure of the crack surface, acoustic emission and oscillations of the crack speed, see e.g. Fineberg et al. (1992), Gross et al. (1993), Sharon et al. (1995)

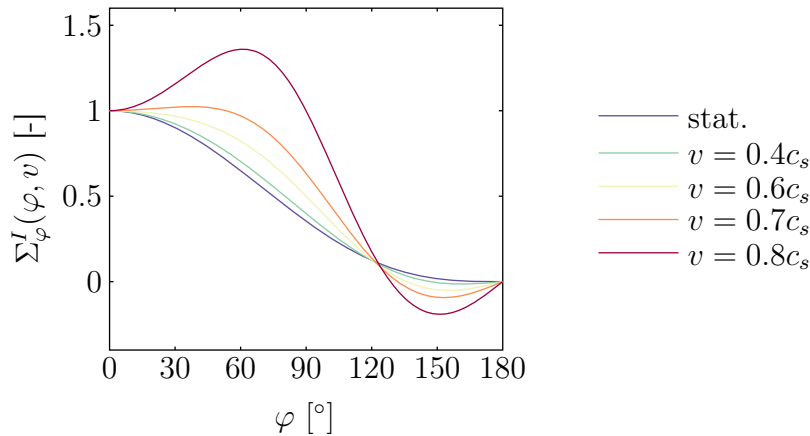


Figure 3.6: Angular distribution of the asymptotic hoop stress σ_φ for a Mode I crack at different crack speeds.

and Sharon and Fineberg (1999). Multiple micro-branches increase the energy consumption of the crack per unit of ‘macroscopic’ crack advance and thereby limit the crack speed to less than $0.6c_r$. According to this explanation the crack tip should grow at a speed close to c_r if only one micro-branch is propagating or if the directional instability is removed. This hypothesis has actually been confirmed in the high-resolution measurements presented in Sharon and Fineberg (1999). They detected that the crack speed indeed exceeded $0.9c_r$ for short time intervals. In the experiments done by Washabaugh and Knauss (1994) the directional instability has been suppressed by directing the crack along manufactured weak planes in the specimens. The measured crack velocities asymptotically approached c_r for vanishing bond strength of the weak plane. The directional instability of Mode I cracks at high crack speeds may also be illustrated by considering the velocity dependence of the asymptotic fields (3.2). The angular distribution of the hoop stress

$$\sigma_\varphi = \frac{\sigma_{11} + \sigma_{22}}{2} - \frac{\sigma_{11} - \sigma_{22}}{2} \cos(2\varphi) - \sigma_{12} \sin(2\varphi) \quad (3.37)$$

is critically dependent on v , see Fig. 3.6. For crack speeds $v > 0.6c_s$ the maximum hoop stress shifts from $\varphi = 0^\circ$ to $\varphi \approx 60^\circ$, thus promoting micro crack formation at an angle to the macroscopic crack tip.

Directional instability is also an issue for Mode II cracks which have the tendency to immediately kink so that further crack propagation happens under Mode I conditions at the crack tip. Thus, when studying intersonic crack growth of Mode II cracks, it is necessary to restrict the crack path to stay in Mode II. Such a constraint is not purely academical since there are real world problems that impose a preferred direction of crack propagation. A natural event that can be associated with this situation is fracturing along a fault in the earth crust during an

earthquake. Indeed, by analyzing the seismic data recorded during crustal earthquakes Archuleta and Day (1980) came to the conclusion that a shear fracture can propagate at $v > c_s$ along a weak plane, i.e. a preexisting fault in this case. Similar observations were made for the 2002 Denali earthquake, where intersonic rupture speeds were recorded. This event has been reproduced on a laboratory scale by Mello et al. (2014).

In experiments or simulations, it is necessary to artificially introduce a weak plane in an otherwise homogeneous material in order to prevent the kinking of the crack. This weak plane has to have the same elastic properties as the bulk material but a significantly lower resistance to fracture. By doing so, the theories of dynamic linear-elastic fracture mechanics predicting the above mentioned crack speed limits still apply. The first experimental evidence for intersonic crack growth along a weak plane was provided by Rosakis et al. (2000). Rosakis and his coworkers studied Mode II fracture in a photoelastic brittle polyester and reported crack speeds above c_s . The directional instability of Mode I cracks and intersonic crack propagation of Mode II cracks will be further discussed by means of numerical simulations in Section 6.3.

3.5 Dynamic Crack Branching

Another dynamic crack growth phenomenon that has been extensively studied is branching of a fast moving Mode I crack in brittle materials. A comparative study of several branching criteria that were correlated to experimental data can be found e.g. in Ramulu and Kobayashi (1985). Dynamic crack branching is still not completely understood and, while the previously mentioned instability can explain this phenomenon to some extent, some features, like branching at crack speeds smaller than the instability threshold v_c , cannot be explained. Thus, no generally accepted explanation for dynamic crack branching and no reliable branching criterion exist, see Gross and Seelig (2011). Nonetheless, the reasoning that supports the dynamic instability theory is: if the energy flow into the process zone is large enough to support more than one macroscopic crack tip, the directional instability of a fast running Mode I crack may eventually cause macroscopic crack branching, see e.g. Sharon and Fineberg (1999). Experimental results reported in Kobayashi et al. (1972) show that the SIF indeed exceeded the fracture toughness right before branching occurs. By means of (3.27) this statement can be extended to the energy release rate, which assumes a critical value prior to crack branching. Thus, a sufficient energy release rate may be considered as a necessary condition for macroscopic branching. In the literature it is often assumed that branching occurs if the energy release rate exceeds the specific fracture energy to a certain

degree, i.e. a crack is able to branch if

$$\frac{\mathcal{G}}{\mathcal{G}_c} \geq m, \quad (3.38)$$

where m is a constant multiplier that is in general larger than two, see e.g. Kobayashi et al. (1972) and Ramulu and Kobayashi (1985).

Apart from experimental work on the dynamic instability and branching of Mode I cracks, efforts have been made to describe crack branching by analytical methods as well. Early attempts to analytically predict the critical velocity for branching considered the asymptotic stress fields at the crack tip of a single fast moving crack as derived in Yoffe (1951) and Freund (1990). The argument was that a single stress quantity that is decisive for the direction of crack propagation, such as the hoop or principal stress, attains a maximum at an angle to the original crack path. However, none of these approaches considered whether the resulting branched state was energetically possible as pointed out in Adda-Bedia (2005). Motivated by the work of Eshelby (1999), Adda-Bedia and his coworkers addressed this fact by considering a growth criterion for the branched state, i.e. bifurcation is not predicted directly but the necessary energetic prerequisites for the propagation of two macroscopic crack branches are determined. In Adda-Bedia (2004) bifurcation of a Mode III crack is studied by applying a branching criterion based on the balance between the energy flow into each propagating tip and the increase of surface energy due to this propagation of the branched configuration. It is shown that the minimum velocity at which a Mode III crack might branch is $v_c^{III} = 0.39c_s$. By analogy to the exact solutions for the Mode III case, a critical branching velocity, which is only weakly dependent on the Poisson ratio and can be assumed to be $v_c^I = 0.52c_s$, has been derived in Adda-Bedia (2005) for the Mode I case. This critical velocity agrees reasonably well with numerical phase field simulations of brittle fracture under in-plane loading as reported in Henry and Levine (2004). The work of Katzav et al. (2007) follows the approach of Adda-Bedia (2005) to analyze the branching instability for a fast Mode I crack. Apart from the prediction of a critical branching velocity of $v_c^I \approx 0.46c_s$, the focus of the study of Katzav et al. (2007) is on calculating the post-branching crack paths. An interesting feature of this analytical solution is the determination of an initial branching angle of $\sim 27^\circ$ followed by a curved extension described by a single curvature parameter that is consistent with the experimental results from Sharon and Fineberg (1996, 1999). Dynamic crack branching is studied by means of numerical simulations in Section 6.4 of this work.

3.6 Configurational Forces in Dynamic Linear Elastic Fracture Mechanics

The development of the concept of configurational forces, sometimes also referred to as material forces in the literature, started with Eshelby (1951) and has since been extended and applied to various fields, see e.g. the textbooks of Gurtin (2000), Kienzler and Herrmann (2000) and Maugin (1993, 2010). Configurational forces represent the change of the total energy of a body with respect to certain quantities that characterize the material configuration, i.e. the size and shape of cracks or the position of an inclusion. In this section, the concept of configurational forces is introduced in the context of dynamic linear elastic fracture mechanics. Consider the Lagrangian density, c.f. (2.103), of a homogeneous linear elastic solid under isothermal conditions to be of the form

$$\mathcal{L}(\mathbf{u}, \dot{\mathbf{u}}, \boldsymbol{\varepsilon}) = k(\dot{\mathbf{u}}) - \psi^e(\boldsymbol{\varepsilon}). \quad (3.39)$$

A configurational force balance related to a material translation, i.e. a translation in the reference configuration, of the considered defect can be derived by computing the gradient of the Lagrangian density as discussed in Kienzler and Herrmann (2000). The negative of the gradient of \mathcal{L} is

$$-\nabla \mathcal{L}(\dot{\mathbf{u}}, \boldsymbol{\varepsilon}) = \left(\frac{\partial \psi^e}{\partial \varepsilon_{ij}} \varepsilon_{ij,k} - \frac{\partial k}{\partial \dot{u}_i} \dot{u}_{i,k} \right) \mathbf{e}_k, \quad (3.40)$$

which by means of the identity

$$\frac{\partial \psi^e}{\partial \varepsilon_{ij}} \varepsilon_{ij,k} = (u_{j,k} \sigma_{ji})_{,i} - u_{i,k} \sigma_{ij,j}, \quad (3.41)$$

the equation of motion (2.36), and the definition of the linear momentum per unit volume

$$\mathbf{p} = \rho \dot{\mathbf{u}} = \frac{\partial k}{\partial \dot{u}_k} \mathbf{e}_k \quad (3.42)$$

can be recast into the form

$$-\nabla \mathcal{L} = \left((u_{j,k} \sigma_{ji})_{,i} - u_{i,k} \dot{p}_i - p_i \dot{u}_{i,k} \right) \mathbf{e}_k. \quad (3.43)$$

Eventually, by means of

$$-\nabla \mathcal{L} = -(\mathcal{L} \delta_{ki})_{,i} \mathbf{e}_k, \quad (3.44)$$

it is

$$\operatorname{div} \boldsymbol{\Sigma}^{\mathcal{L}} - \dot{\mathbf{p}}^{\mathcal{L}} = \mathbf{0}. \quad (3.45)$$

Here, the dynamic Eshelby stress tensor

$$\boldsymbol{\Sigma}^{\mathcal{L}} = ((\psi^e - k)\delta_{ij} - u_{k,i}\sigma_{kj}) \mathbf{e}_i \otimes \mathbf{e}_j, \quad (3.46)$$

has been introduced. The expression

$$\mathbf{p}^{\mathcal{L}} = -u_{i,k}p_i \mathbf{e}_k = -(\text{grad}\mathbf{u})^T \mathbf{p} \quad (3.47)$$

denotes the so-called pseudo-momentum, see e.g. Maugin and Trimarco (1992). By means of the divergence theorem (A.11)₃ an integral form of (3.45) can be derived. Assume that R is a regular bounded subset of Ω with outward normal vector \mathbf{n}_R . Integration of (3.45) over the domain R results in

$$\mathbf{G}_R^{\mathcal{L}} + \mathfrak{P}_R^{\mathcal{L}} = \mathbf{0}, \quad (3.48)$$

with

$$\mathbf{G}_R^{\mathcal{L}} = \int_{\partial R} \boldsymbol{\Sigma}^{\mathcal{L}} \mathbf{n}_R \, dA, \quad \text{and} \quad \mathfrak{P}_R^{\mathcal{L}} = - \int_R \dot{\mathbf{p}}^{\mathcal{L}} \, dV. \quad (3.49)$$

By means of the identity $2\nabla k = 2\rho(\text{grad}\dot{\mathbf{u}})^T \dot{\mathbf{u}}$, the local balance law (3.45) can be written in a form that already resembles the energy release rate (3.26), i.e.

$$\text{div}((\psi^e + k)\mathbf{1} - (\text{grad}\mathbf{u})^T \boldsymbol{\sigma}) - (\text{grad}\dot{\mathbf{u}})^T \rho \dot{\mathbf{u}} + \rho(\text{grad}\mathbf{u})^T \ddot{\mathbf{u}} = \mathbf{0}, \quad (3.50)$$

which may be reformulated as

$$\text{div}\boldsymbol{\Sigma}^{\mathcal{H}} - (\text{grad}\dot{\mathbf{u}})^T \rho \dot{\mathbf{u}} + \rho(\text{grad}\mathbf{u})^T \ddot{\mathbf{u}} = \mathbf{0}, \quad (3.51)$$

where

$$\boldsymbol{\Sigma}^{\mathcal{H}} = ((\psi^e + k)\delta_{ij} - u_{k,i}\sigma_{kj}) \mathbf{e}_i \otimes \mathbf{e}_j. \quad (3.52)$$

Integration of (3.51) over an arbitrary regular bounded region R that does not contain a crack tip or any other defect yields

$$\mathbf{G}_R^{\mathcal{H}} + \mathcal{P}_R^{\mathcal{H}} = \mathbf{0}, \quad (3.53)$$

where

$$\mathbf{G}_R^{\mathcal{H}} = \int_{\partial R} \boldsymbol{\Sigma}^{\mathcal{H}} \mathbf{n}_R \, dA, \quad \mathcal{P}_R^{\mathcal{H}} = \int_R \left(-(\text{grad}\dot{\mathbf{u}})^T \rho \dot{\mathbf{u}} + \rho(\text{grad}\mathbf{u})^T \ddot{\mathbf{u}} \right) \, dV. \quad (3.54)$$

By integration of (3.51) over a subdomain R_{tip} as depicted in Fig. 3.3, it is, for traction free crack faces and by means of the divergence theorem

$$\begin{aligned} \int_C ((\psi^e + k)\mathbf{1} - (\text{grad}\mathbf{u})^T \boldsymbol{\sigma}) \cdot \mathbf{n}_{tip} \, dA + \int_{C_P} ((\psi^e + k)\mathbf{1} - (\text{grad}\mathbf{u})^T \boldsymbol{\sigma}) \cdot \mathbf{n}_{tip} \, dA \\ + \int_{R_{tip}} \left(-(\text{grad}\dot{\mathbf{u}})^T \rho \dot{\mathbf{u}} + \rho(\text{grad}\mathbf{u})^T \ddot{\mathbf{u}} \right) \, dV = \mathbf{0}. \end{aligned} \quad (3.55)$$

Taking the dot product of each term with the crack tip velocity, recalling (3.12) and making use of $\mathbf{n}_{tip} = -\mathbf{n}_{R_P}$ on C_P results in

$$\begin{aligned} \int_C ((\psi^e + k)\mathbf{1} - (\text{grad}\mathbf{u})^T \boldsymbol{\sigma}) \mathbf{n}_{tip} \, dA \cdot \mathbf{v} - \underbrace{\int_{C_P} ((\psi^e + k)\mathbf{1} - (\text{grad}\mathbf{u})^T \boldsymbol{\sigma}) \mathbf{n}_{R_P} \, dA \cdot \mathbf{v}}_{\mathcal{G}_v} \\ + \int_{R_{tip}} \left(-(\text{grad}\dot{\mathbf{u}})^T \rho \dot{\mathbf{u}} + \rho (\text{grad}\mathbf{u})^T \ddot{\mathbf{u}} \right) \, dV \cdot \mathbf{v} = \mathbf{0}. \end{aligned} \quad (3.56)$$

The relation of the resulting configurational forces to the energy release rate is

$$\mathcal{G} = (\mathbf{G}_{tip}^{\mathcal{H}} + \mathbf{P}_{tip}^{\mathcal{H}}) \cdot \mathbf{e}_v \quad (3.57)$$

with

$$\mathbf{G}_{tip}^{\mathcal{H}} = \int_C \boldsymbol{\Sigma}^{\mathcal{H}} \mathbf{n}_{tip} \, dA, \quad \mathbf{P}_{tip}^{\mathcal{H}} = \int_{R_{tip}} \left(-(\text{grad}\dot{\mathbf{u}})^T \rho \dot{\mathbf{u}} + \rho (\text{grad}\mathbf{u})^T \ddot{\mathbf{u}} \right) \, dV \quad (3.58)$$

and \mathbf{e}_v the normalized current direction of \mathbf{v} . As in (3.26), it appears that the energy release rate in the dynamic case is not a path-independent quantity but may be expressed as the sum of a path (surface) integral and a domain integral, similar to (3.26).

3.7 The Variational Formulation of Brittle Fracture

The original Griffith criterion encounters difficulties when complex crack evolutions are considered. One reason for this is that the computation of the energy release rate of a (virtual) crack advance a priori assumes a certain direction of crack propagation which is not known in general. In an attempt to overcome this limitation, a number of criteria have been proposed that aim to determine the direction of crack propagation. The principle of local symmetry states that cracks grow in a way that in-plane shear stresses vanish in the vicinity of the crack tip and has originally been proposed in Goldstein and Salganik (1974). Alternative approaches are the maximum hoop stress criterion of Erdogan and Sih (1963) and the maximum energy release rate criterion of Wu (1978). A crack growth criterion in conjunction with a criterion that determines the direction of crack growth might be a cumbersome but suitable postulate that describes crack initiation and the subsequent crack growth for a preexisting crack. However, if the nucleation of new cracks in pristine material and features such as crack branching are to be included

as well, even more criteria are required. Instead of pursuing this line of thought, a different approach – a generalized formulation of the Griffith criterion – originated with the work of Ambrosio and Braides (1995) for the stationary crack case and Francfort and Marigo (1998) for crack evolution under quasi-static conditions. The work of Francfort and Marigo (1998) also introduced the term *variational formulation of brittle fracture*. Francfort and Marigo regarded an n -dimensional elastic body Ω under isothermal conditions with a smooth boundary $\partial\Omega$. An important feature of the variational formulation of brittle fracture is that the crack sets \mathcal{S} are allowed to grow discontinuously, i.e. cracks can also nucleate in previously undamaged material. In principle all closed subdomains of $\bar{\Omega} = \Omega \cup \partial\Omega$ whose dimensions are not greater than $n - 1$ are considered as possible crack sets, whereby only the $n - 1$ case is treated in this work. Furthermore, an admissible crack set $\mathcal{S}(t)$ needs to fulfill the irreversibility constraint

$$\mathcal{S}(s) \subset \mathcal{S}(t) \quad \text{for all } s < t. \quad (3.59)$$

Following Griffith's idea, the fracture energy that is associated with a crack set is expressed as

$$\Gamma(\mathcal{S}) = \mathcal{G}_c \mathcal{H}(\mathcal{S}), \quad (3.60)$$

where $\mathcal{H}(\mathcal{S})$ denotes the surface measure of \mathcal{S} . The strain energy which is stored in Ω is

$$\tilde{E}^e(\mathcal{S}, \mathbf{u}) = \int_{\Omega \setminus \mathcal{S}} \frac{1}{2} \boldsymbol{\varepsilon}(\mathbf{u}) : (\mathbb{C} : \boldsymbol{\varepsilon}(\mathbf{u})) \, dV. \quad (3.61)$$

Only Dirichlet boundary conditions

$$\mathbf{u}(\mathbf{x}, t) = \mathbf{u}^*(\mathbf{x}, t) \quad \text{on } \partial\Omega_{\mathbf{u}} \setminus \mathcal{S}(t), \quad (3.62)$$

i.e. on the part of the boundary that has not yet debonded, are considered, whereas traction boundary conditions and volume forces are not treated by the original formulation. The fracture criterion defined by the variational formulation of brittle fracture is:

The true displacement \mathbf{u} and the true crack set $\mathcal{S}(t)$ are global minimizers of

$$\tilde{E}(\mathcal{S}, \mathbf{u}) = \tilde{E}^e(\mathcal{S}, \mathbf{u}) + \Gamma(\mathcal{S}). \quad (3.63)$$

The functional (3.63) closely resembles the Mumford-Shah potential, see Mumford and Shah (1989), which is encountered in image segmentation. This analogy provides a mathematical justification for a reformulation of the variational formulation of brittle fracture that was originally proposed by Bourdin (1998), see also Section 4. Furthermore, the postulate (3.63) has the form of a free discontinuity

problem that is connected to the idea of the Griffith criterion (3.28). To illustrate this connection, consider a body with an initial crack \mathcal{S} under quasi-static and isothermal conditions that is subject to conservative external loads. The energy release for a (virtual) crack advance $\delta\mathcal{S}$ is $-\mathcal{G}\delta\mathcal{S} = \delta_{\mathcal{S}}\Pi$ and the change of surface energy is $\mathcal{G}_c\delta\mathcal{S} = \delta_{\mathcal{S}}\Gamma$, see Gross and Seelig (2011). Thus, the Griffith criterion (3.28) may be restated as

$$\mathcal{G}\delta\mathcal{S} = \mathcal{G}_c\delta\mathcal{S} \quad \Leftrightarrow \quad \delta_{\mathcal{S}}(\Pi + \Gamma) = 0. \quad (3.64)$$

Except for the exclusion of conservative external forces, the postulate of the variational formulation (3.63) is more general than (3.64), since it also considers non-incremental, general crack growth along arbitrary pathes. In fact, the Griffith postulate in the form of (3.64) may be considered a necessary condition for local minimality of \tilde{E} , see Francfort and Marigo (2005). As elaborated in Kuhn (2013), a main advantage of the variational formulation is that all possible features of crack growth such as branching, kinking and the nucleation of new cracks is solely triggered by a single postulate on crack growth.

The existence of global minimizers $(\mathcal{S}, \mathbf{u})$ of \tilde{E} is investigated for linearly increasing displacement loads in Maso and Toader (2002) and Francfort and Larsen (2003) for the antiplane shear case and for the case of planar elasticity in Chambolle (2003). As pointed out in Francfort and Marigo (1998), Francfort and Marigo (2005), Francfort (2006) and Bourdin et al. (2008), global minimizers of \tilde{E} cannot exist in the presence of traction loads and volume forces. As a remedy, it has been argued that it may be sufficient to soften up the postulate and to search for local minimizers of \tilde{E} as the correct crack sets and displacement fields instead. Nonetheless, this approach is faced with difficulties in crack nucleation scenarios, since the purely elastic solution without cracks is always a local minimizer of \tilde{E} . The difficulty can be overcome by replacing the Griffith surface energy with a cohesive surface energy as introduced by Barenblatt (1962). In this case, the purely elastic solution stops to be a local minimum at a certain load level. A combination of a Barenblatt type cohesive fracture energy and a local minimum of \tilde{E} has been proposed as an extension of the variational formulation of brittle fracture that allows for traction loads and volume forces in Francfort and Marigo (2005) and Francfort (2006).

For a dynamic setting, Bourdin et al. (2011) proposed a model based on two principles:

- *The displacements should follow from the solution of the elastodynamic problem, i.e. as a solution of Navier's equation (2.89).*
- *The crack set should be a local minimizer of \tilde{E} consistent with the irreversibility constraint (3.59) for the instantaneous displacement field.*

Thus, as long as the elastic fields near the crack are such that the crack would grow under quasi-static conditions it should also grow if the near tip field is due to elastodynamics. As mentioned in Bourdin et al. (2011), making the dynamic criterion mathematically precise is more difficult than in the quasi-static case where the crack growth criterion is basically a comparison between the instantaneous strain energy release and the increase in fracture energy due to a crack set increment $\Delta\mathcal{S}$. Extending the criterion to the dynamic case is not straightforward since in this situation crack growth does not necessarily lead to an instantaneous release of strain energy. Furthermore, the immediate effect on the kinetic energy is unclear. In Larsen et al. (2010), the two principles for the extension of the variational formulation of brittle fracture to the dynamic case mentioned in Bourdin et al. (2011) are complemented by a third requirement, i.e. an energy balance similar to (3.15) should be adhered to it. For the antiplane-shear case, i.e. Mode III, Larsen et al. (2010) were able to show that solutions of a regularized formulation of the dynamic variational formulation of brittle fracture exist and that these solutions indeed fulfill the required energy balance. In the conclusion of their work, Larsen and his coworkers raised the interesting question whether the behaviour of the dynamic regularized formulation in the quasi-static limit is really the same as for regularized quasi-static formulation of the variational formulation of brittle fracture proposed by Francfort and Marigo (1998) or whether there are situations in which they differ. This question is further investigated in Li et al. (2016) by means of numerical simulations.

4 A Phase Field Model of Dynamic Brittle Fracture

This chapter introduces a phase field description of dynamic fracture in brittle materials. The model is based on the variational formulation of dynamic brittle fracture that has been presented in the previous Section 3.7.

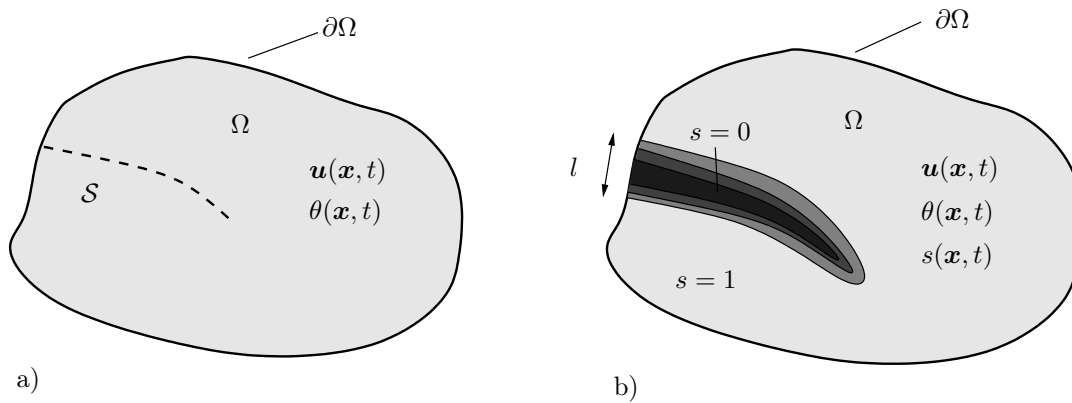


Figure 4.1: a) Body with internal discontinuities (sharp cracks) S and b) approximation of internal discontinuities by an order parameter field $s(\mathbf{x}, t)$.

4.1 Regularized Representation of Cracks and Fracture Energy

Though the variational formulation of brittle fracture is a powerful postulate that allows to describe all fracture phenomena in a unified framework, a numerical implementation is necessary to handle more complex scenarios. The main difficulty in numerically solving the variational fracture problem is that the energetic change due to an infinite number of arbitrary crack set evolutions needs to be taken into account. This means that all possible crack set configurations including the

associated crack face boundary conditions and the associated surface energy need to be represented. This difficulty can be faced by exploiting the similarity of the energy functional (3.63) to the Mumford-Shah functional from the field of image segmentation, see Mumford and Shah (1989). A regularized representation of the Mumford-Shah functional has been presented in Ambrosio and Tortorelli (1990), which motivates to formulate a regularized version of \tilde{E} in an analogous manner, as has been proposed in Bourdin (1998) and Bourdin and Chambolle (2000). The idea is that an additional scalar field $s(\mathbf{x}, t)$ is introduced to indicate cracks. This field varies continuously from $s(\mathbf{x}, t) = 0$ when \mathbf{x} is part of the crack set \mathcal{S} to $s(\mathbf{x}, t) = 1.0$ if \mathbf{x} is sufficiently far away from the crack set, see Fig. 4.1. By means of the smooth representation of cracks through s , a regularized approximation of the energy functional (3.63)

$$E_l(\boldsymbol{\varepsilon}^e(\nabla \mathbf{u}, \theta), s, \nabla s) = \int_{\Omega} (\psi^e(\nabla \mathbf{u}, s, \theta) + \psi^s(\nabla s, s)) \, dV \quad (4.1)$$

is defined. The strain energy density is decomposed into positive, i.e. crack driving, and negative, i.e. not crack driving, components ψ_+^e and ψ_-^e , respectively, as

$$\psi^e = g(s)\psi_+^e + \psi_-^e, \quad E^e = \int_{\Omega} \psi^e \, dV, \quad (4.2)$$

whereas the fracture energy density and total fracture energy are given by

$$\psi^s = \mathcal{G}_c \gamma^s, \quad \gamma^s = \frac{1}{2c_w} \left(\frac{w(s)}{4l} + l|\nabla s|^2 \right), \quad E^s = \int_{\Omega} \psi^s \, dV. \quad (4.3)$$

The degradation function $g(s) : [0, 1] \rightarrow [0, \infty)$ models the loss of stiffness in broken material. It is required to be a monotonously increasing function that satisfies

$$g(0) = 0, \quad g(1) = 1, \quad g'(0) = 0, \quad g'(1) > 0, \quad (4.4)$$

see Borden (2012). The first two constraints define the limits in the broken $s = 0$ state with no remaining material stiffness and the undamaged state $s = 1$ which is associated with the full stiffness of the material. The third property guarantees that $s \rightarrow 0$ as $\psi_+^e \rightarrow \infty$ and eliminates the crack driving force for $s = 0$, whereas the fourth requirement makes certain that the phase field will evolve from a homogeneously undamaged state where $s = 1$ everywhere, see Borden (2012). The normalization constant c_w of the surface energy density γ^s must be chosen in a way that the integral $\int \gamma^s \, dV$ converges to the correct surface measure as $l \rightarrow 0$, cf. (3.60). Several approaches of the order parameter potential $w(s)$ exist in the literature, such as double well potentials of the type

$$w(s) = 16s^2(1 - s^2) \quad (4.5)$$

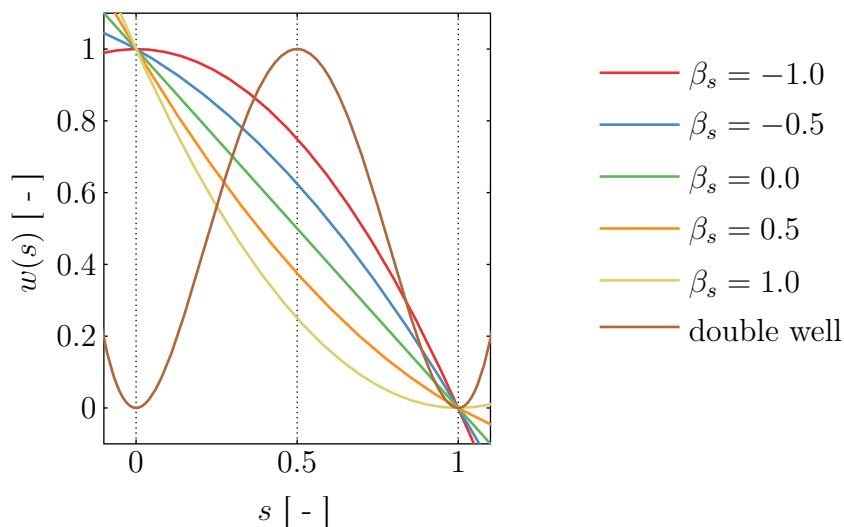


Figure 4.2: Different choices of the order parameter potential.

and monotonous functions

$$w(s) = (1 + \beta_s s)(1 - s), \quad \beta_s \in [-1, 1], \quad (4.6)$$

see Fig. 4.2. A double well function like it is employed in Aranson et al. (2000), Karma et al. (2001) and Eastgate et al. (2002), naturally models the irreversibility of fracturing since an energy barrier, i.e. a local maximum of $w(s)$, exists between the undamaged state $s = 1$ and the completely fractured state $s = 0$, see Fig. 4.2. However, in the unloaded case $\psi_+^e = 0$, the fractured state assumes the same total energy as the undamaged state, which leads to an unphysical widening of cracks for large time scales.

Concerning monotonous functions of the type (4.6), $\beta_s = -1$ is the most common choice. Nonetheless, also a linear function with $\beta_s = 0$ is used in the literature, see e.g. Bourdin et al. (2014) and Hossain et al. (2014). The monotonous potentials do not model the irreversibility of fracturing and need to be complemented by an irreversibility constraint, which is discussed in Section 4.3. Nonetheless, the monotonous function with $\beta_s = -1$ is chosen in this work because there exists an energetic difference between the fractured and the undamaged solution in the unloaded state. Thus, unphysical crack widening is prohibited by the monotonous formulation. The normalization constant is required to be $c_w = 0.5$ in this case and the fracture energy density is

$$\psi^s = \mathcal{G}_c \left(\frac{(1-s)^2}{4l} + l|\nabla s|^2 \right). \quad (4.7)$$

The first term in (4.7) vanishes in undamaged material $s = 1$ and is maximal in fully broken material $s = 0$. According to the considerations made in Section 3.7

the fracture energy is to be minimized for a given load state in order to find the correct crack set. Consequently, the first term prevents large regions where $s = 0$, i.e. excessively wide cracks. The second term in (4.7) includes the gradient of s and describes the fracture energy stored in the transition zone between broken $s = 0$ and unbroken material $s = 1$. This term impedes the formation of many narrow cracks, since this would mean a large number of energetically unfavourable transition zones. The internal length l weights the two terms and thereby controls the typical width of the regularized crack, see Fig. 4.1 b).

The original expression of the strain energy density

$$\psi_+^e = \frac{1}{2} \boldsymbol{\varepsilon}^e : (\mathbb{C} : \boldsymbol{\varepsilon}^e), \quad \psi_-^e = 0, \quad (4.8)$$

combined with a degradation function satisfying the conditions stated in (4.4) has been shown to converge to the variational formulation of brittle fracture from Section 3.7 by Bourdin (1998) for the Mode III case, in the sense that minimizers (\mathbf{u}, s) of the regularized energy functional (4.1) converge to minimizers $(\mathbf{u}, \mathcal{S})$ of (3.63) as $l \rightarrow 0$. In this context, convergence of s to the crack set \mathcal{S} should be understood such that the zero set of s converges to \mathcal{S} . The proof provided by Bourdin (1998), is a direct application of the results of Ambrosio and Tortorelli (1990) who have shown convergence of a regularized functional to the previously mentioned Mumford-Shah functional. A similar proof for the case of general deformation can be found in Chambolle (2004).

4.2 Derivation of the Field Equations from Hamilton's Principle

As described in Section 2.5, the governing field equations of a dynamic system can be derived from Hamilton's principle if the Lagrangian of the system is known. This section illustrates how Hamilton's principle can be applied to formulate the dynamic regularized fracture problem in a way that is consistent with the requirements on a dynamic version of the variational formulation of brittle fracture, see the last paragraph of Section 3.7.

Consider the configuration Ω a thermoelastic body subject to small deformations and small displacements as described in Section 2. Cracks are represented in a regularized way by means of an additional order parameter as described in Section 4.1. The parts of the boundary $\partial\Omega$ where Dirichlet boundary conditions are to be fulfilled for the primary fields are referred to as $\partial\Omega_{\mathbf{u}}$, $\partial\Omega_{\theta}$ and $\partial\Omega_s$, whereas the parts of the boundary where Neumann boundary conditions are specified are denoted as $\partial\Omega_t$, $\partial\Omega_{\mathbf{q}^\theta}$ and $\partial\Omega_{\nabla s}$. It is $\partial\Omega = \partial\Omega_{\mathbf{u}} \cup \partial\Omega_t = \partial\Omega_{\theta} \cup \partial\Omega_{\mathbf{q}^\theta} = \partial\Omega_s \cup \partial\Omega_{\nabla s}$.

The Dirichlet boundary conditions on $\partial\Omega$ are

$$\begin{aligned} \mathbf{u}(\mathbf{x}, t) &= \mathbf{u}^*(\mathbf{x}, t) & \text{on } \partial\Omega_{\mathbf{u}}, \\ \theta(\mathbf{x}, t) &= \theta^*(\mathbf{x}, t) & \text{on } \partial\Omega_{\theta}, \\ s(\mathbf{x}, t) &= s^*(\mathbf{x}, t) & \text{on } \partial\Omega_s \end{aligned} \quad (4.9)$$

and the Neumann boundary conditions are defined as

$$\begin{aligned} \boldsymbol{\sigma}(\mathbf{x}, t)\mathbf{n}(\mathbf{x}, t) &= \mathbf{t}^*(\mathbf{x}, t) & \text{on } \partial\Omega_{\mathbf{t}}, \\ \mathbf{q}_{\theta}(\mathbf{x}, t) \cdot \mathbf{n}(\mathbf{x}, t) &= \mathbf{q}_{\theta}^*(\mathbf{x}, t) \cdot \mathbf{n}(\mathbf{x}, t) & \text{on } \partial\Omega_{\mathbf{q}_{\theta}}, \\ \nabla s(\mathbf{x}, t) \cdot \mathbf{n}(\mathbf{x}, t) &= 0 & \text{on } \partial\Omega_{\nabla s}. \end{aligned} \quad (4.10)$$

The applied traction \mathbf{t}^* may be of non-conservative nature. Furthermore, it is necessary to provide initial conditions

$$\begin{aligned} \mathbf{u}(\mathbf{x}, t_0) &= \mathbf{u}_0(\mathbf{x}), & \dot{\mathbf{u}}(\mathbf{x}, t_0) &= \mathbf{v}_0(\mathbf{x}), \\ \theta(\mathbf{x}, t_0) &= \theta_0(\mathbf{x}), \\ s(\mathbf{x}, t_0) &= s_0(\mathbf{x}) \end{aligned} \quad (4.11)$$

at time t_0 in Ω . The initial conditions for the order parameter $s_0(\mathbf{x})$ can be used to describe an initial crack set. Since the immediate effect of crack propagation on the kinetic energy is unclear, \mathcal{K} is assumed not to be directly affected by s . Consequently, \mathcal{K} is given by (2.40). As pointed out in Section 3.7, the displacements should follow from elastodynamics while the crack evolution should be determined by the minimization of E_l in a regularized formulation of the variational approach to dynamic brittle fracture. A formulation that is consistent with these requirements can be obtained from Hamilton's principle, cf. Section 2.5. The respective postulate on the mechanical behaviour and on the crack evolution is:

Among admissible displacements and order parameter fields, the actual displacement field \mathbf{u} and the order parameter field s at the current temperature θ , fulfill

$$\int_{t_1}^{t_2} \left[\delta(\mathcal{K} - E_l) + \int_{\partial\Omega_{\mathbf{t}}} (\mathbf{t}^* \cdot \delta\mathbf{u}) \, dA \right] dt = 0, \quad (4.12)$$

where the variation $\delta()$ is performed for the fields \mathbf{u} and s only and the times $t_2 > t_1$ specify the regarded time interval $t \in [t_1, t_2]$.*

As mentioned in Section 2.5, such a postulate may be used to derive the strong form of the governing field equations which is shown in the following paragraphs.

The statement (4.12) is reformulated by means of the interchangeability of the domain integrals and the variation operation as

$$\int_{t_1}^{t_2} \left[\int_{\Omega} \delta \mathcal{L} \, dV + \int_{\partial \Omega_t} (\mathbf{t}^* \cdot \delta \mathbf{u}) \, dA \right] dt = 0, \quad (4.13)$$

with the Lagrangian density of the problem

$$\mathcal{L}(\dot{\mathbf{u}}, \nabla \mathbf{u}, s, \nabla s, \theta) = k(\dot{\mathbf{u}}) - \psi^e(\mathbf{u}, \nabla \mathbf{u}, s, \theta) - \psi^s(s, \nabla s). \quad (4.14)$$

By performing the variation $\delta(\ast)$ only for the fields \mathbf{u} and s it is

$$\delta \mathcal{L} = \frac{\partial \mathcal{L}}{\partial \dot{\mathbf{u}}} \cdot \delta \dot{\mathbf{u}} + \frac{\partial \mathcal{L}}{\partial \nabla \mathbf{u}} : \nabla \delta \mathbf{u} + \frac{\partial \mathcal{L}}{\partial s} \delta s + \frac{\partial \mathcal{L}}{\partial \nabla s} \cdot \nabla \delta s. \quad (4.15)$$

Employing the product rule, (4.15) yields

$$\begin{aligned} \delta \mathcal{L} &= \frac{d}{dt} \left(\frac{\partial \mathcal{L}}{\partial \dot{\mathbf{u}}} \cdot \delta \mathbf{u} \right) - \frac{d}{dt} \frac{\partial \mathcal{L}}{\partial \dot{\mathbf{u}}} \cdot \delta \mathbf{u} - \operatorname{div} \left(\frac{\partial \mathcal{L}}{\partial \nabla \mathbf{u}} \right) \cdot \delta \mathbf{u} + \operatorname{div} \left(\left(\frac{\partial \mathcal{L}}{\partial \nabla \mathbf{u}} \right)^T \delta \mathbf{u} \right) \\ &+ \frac{\partial \mathcal{L}}{\partial s} \delta s - \operatorname{div} \left(\frac{\partial \mathcal{L}}{\partial \nabla s} \right) \delta s + \operatorname{div} \left(\frac{\partial \mathcal{L}}{\partial \nabla s} \delta s \right). \end{aligned} \quad (4.16)$$

Subsequent integration over the time interval $[t_1, t_2]$ and the domain Ω as well as application of the divergence theorem (A.11) results in

$$\begin{aligned} \int_{t_1}^{t_2} \int_{\Omega} \delta \mathcal{L} \, dV \, dt &= \int_{t_1}^{t_2} \int_{\Omega} \left(\left[-\frac{d}{dt} \frac{\partial \mathcal{L}}{\partial \dot{\mathbf{u}}} - \operatorname{div} \left(\frac{\partial \mathcal{L}}{\partial \nabla \mathbf{u}} \right) \right] \cdot \delta \mathbf{u} \right. \\ &+ \left. \left[\frac{\partial \mathcal{L}}{\partial s} - \operatorname{div} \left(\frac{\partial \mathcal{L}}{\partial \nabla s} \right) \right] \delta s \right) dV \, dt \\ &+ \int_{t_1}^{t_2} \int_{\partial \Omega} \left[\frac{\partial \mathcal{L}}{\partial \nabla s} \cdot \mathbf{n} \right] \delta s \, dA \, dt + \int_{t_1}^{t_2} \int_{\partial \Omega} \left[\left(\frac{\partial \mathcal{L}}{\partial \nabla \mathbf{u}} \right)^T \mathbf{n} \right] \cdot \delta \mathbf{u} \, dA \, dt \\ &+ \int_{\Omega} \left[\frac{\partial \mathcal{L}}{\partial \dot{\mathbf{u}}} \cdot \delta \mathbf{u} \right] dV \Big|_{t_1}^{t_2}. \end{aligned} \quad (4.17)$$

Since the domain Ω is not time-dependent in a small deformation setting, it is possible to exchange the order of the integration with respect to time and the integration over Ω . Thus, the last term in (4.17)

$$\int_{\Omega} \left[\frac{\partial \mathcal{L}}{\partial \dot{\mathbf{u}}} \cdot \delta \mathbf{u} \right] \Big|_{t_1}^{t_2} dV = 0, \quad (4.18)$$

vanishes if

$$\delta \mathbf{u}(\mathbf{x}, t_1) = \delta \mathbf{u}(\mathbf{x}, t_2) = \mathbf{0} \quad (4.19)$$

is recalled, cf. Section 2.5. According to the fundamental Lemmas of variational calculus (2.104) and (2.105), the bracket terms representing volume contributions and surface contributions respectively must vanish independently for each field. This yields the Euler-Lagrange equations of the variational principle (4.12)

$$\frac{d}{dt} \frac{\partial \mathcal{L}}{\partial \dot{\mathbf{u}}} + \operatorname{div} \left(\frac{\partial \mathcal{L}}{\partial \nabla \mathbf{u}} \right) = \mathbf{0}, \quad (4.20)$$

$$\frac{\partial \mathcal{L}}{\partial s} - \operatorname{div} \left(\frac{\partial \mathcal{L}}{\partial \nabla s} \right) = 0, \quad (4.21)$$

$$\frac{\partial \mathcal{L}}{\partial \nabla s} \cdot \mathbf{n} = 0 \quad \text{on } \partial \Omega_{\nabla s}, \quad (4.22)$$

and

$$\left(\frac{\partial \mathcal{L}}{\partial \nabla \mathbf{u}} \right)^T \mathbf{n} + \mathbf{t}^* = \mathbf{0} \quad \text{on } \partial \Omega_t. \quad (4.23)$$

Evaluation of (4.20) gives the equation of motion

$$\rho \ddot{\mathbf{u}} = \operatorname{div} \boldsymbol{\sigma}, \quad (4.24)$$

with the constitutive law

$$\boldsymbol{\sigma} = \frac{\partial \psi^e(\boldsymbol{\varepsilon}, s, \theta)}{\partial \boldsymbol{\varepsilon}}, \quad (4.25)$$

whereas (4.21) provides the evolution equation for the crack field

$$g'(s) \psi_+^e - \mathcal{G}_c \left[2l \Delta s + \frac{1-s}{2l} \right] = 0. \quad (4.26)$$

It appears that crack growth is only controlled by the 'positive' part of the strain energy density ψ_+^e which allows to model certain physical features of fracturing. This topic is elaborated in Section 4.4. The last two Euler-Lagrange equations (4.22) and (4.23) are the Neumann boundary conditions for the order parameter

$$\nabla s \cdot \mathbf{n} = 0 \quad \text{on } \partial \Omega_{\nabla s} \quad (4.27)$$

and the stress

$$\boldsymbol{\sigma} \mathbf{n} = \mathbf{t}^* \quad \text{on } \partial \Omega_t. \quad (4.28)$$

The temperature field is governed by the balance of energy (2.52) and does affect the stress and strain states by means of (2.75) and (2.79)₁. Additionally, an evolution of the crack field influences the stress work term in (2.52) and thereby affects

the temperature distribution. Further coupling effects occur, if the heat flux \mathbf{q}^θ is assumed to be influenced by cracks. In Kuhn and Müller (2009) the formulation

$$\mathbf{q}^\theta(s, \theta) = -(\beta^\theta(g(s) - 1) + 1)\kappa\nabla\theta, \quad \beta^\theta \in [0, 1], \quad (4.29)$$

with a quadratic degradation function $g(s)$ has been used successfully to model isolating ($\beta^\theta = 1$) and perfectly conducting ($\beta^\theta = 0$) cracks. Eventually, the balance of energy (2.52), the caloric equation of state (2.56) and the constitutive law (4.29) yield a field equation for the temperature as

$$\rho c_\theta \dot{\theta} = \boldsymbol{\sigma} : \dot{\boldsymbol{\varepsilon}} - \operatorname{div} \mathbf{q}^\theta + s^\theta, \quad (4.30)$$

that is coupled to the displacement field \mathbf{u} as well as to the order parameter s . In this work, cracks are assumed to be conducting whenever thermoelastic material is considered, i.e. $\beta^\theta = 0$.

The present set of equations (4.24), (4.26) and (4.30) can be interpreted in two ways, see e.g. Li et al. (2016). First, the approach may be considered as a regularized approximation of the variational approach discussed in Section 3.7. Alternatively, the regularized representation may be regarded as a genuine model of fracture on its own. In the latter case, the field $s(\mathbf{x}, t)$ is referred to as a phase field and the model is called a phase field model for dynamic brittle fracture.

4.3 Irreversibility

For the scope of this work, fracturing is assumed to be an irreversible process meaning that the material cohesion between particles cannot be reestablished once the particles have been separated. However, this constraint is not incorporated in the variational principle (4.12) and has to be stated separately. As mentioned in Section 4.2, the zero set of the order parameter $\Omega_{s=0}(t) \subset \Omega$ may be interpreted as the crack set \mathcal{S} of the variational formulation of brittle fracture. Accordingly, the irreversibility constraint (3.59) is modelled by imposing the Dirichlet type constraint

$$s = s^* = 0 \quad \text{in } \Omega_{s=0} \quad \text{for all } t \geq t_0. \quad (4.31)$$

A second approach to define the irreversibility constraint that goes hand in hand with a damage like interpretation of s , is

$$\dot{s} \leq 0, \quad (4.32)$$

as proposed for example in Miehe et al. (2010b). Both formulations yield an overall thermodynamically consistent formulation of the phase field fracture model that complies with the second law of thermodynamics, cf. Section 2.3.6, as is mentioned in Kuhn (2013). In this work (4.31) is used to enforce the irreversibility of fracturing.

4.4 Tension-Compression Asymmetry of Fracturing

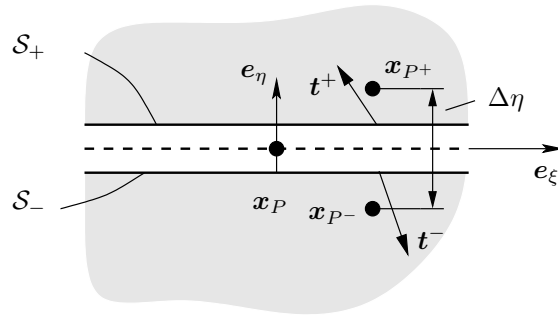


Figure 4.3: Section of a crack.

The decomposition of the strain energy density into positive and negative parts by (4.2) has two objectives. The first motive is to model the crack boundary conditions and in particular the contact between crack faces during crack closure, i.e. the impenetrability of the crack faces. Secondly, since crack growth requires the stretching of material bonds until the material cohesion is eventually gone, it is reasonable to increase the material resistance to fracturing or to prohibit fracturing completely in purely compressive load states. The different behaviour of cracks in tensile and compressive situations is referred to as the *tension-compression asymmetry of fracturing*, cf. Strobl et al. (2016). The purpose of this section is to present and discuss ways in which this phenomenon can be implemented into a phase field model for brittle fracture.

At first, crack closure is considered for the classical description of cracks, see Fig. 4.1 a), within the framework of standard linear elasticity. Consider a section of the crack as depicted in Fig. 4.3, where the crack's orientation is described by the tangential direction \mathbf{e}_ξ and the outward normal of the lower crack face \mathbf{e}_η . For illustrative purposes, a slit remains between the two crack faces although they occupy the same location in the reference configuration. For a given traction \mathbf{t}^- at the lower crack face it is $\mathbf{t}^- = \boldsymbol{\sigma} \mathbf{e}_\eta$ by means of the Cauchy relation (2.21). Similarly, at the upper crack face it is $\mathbf{t}^+ = -\boldsymbol{\sigma} \mathbf{e}_\eta$ for a given traction load.

It is essential to decide whether a crack is closed in order to specify the correct boundary traction on the crack faces. Thus, as a preliminary step, a crack closure criterion needs to be established. In a small deformation setting, significant changes of the topology at the crack do not occur. Under these circumstances, the contact constraint can be described similar to the node-to-node contact constraints

proposed in Wriggers (2006) as

$$(\mathbf{u}^+(\mathbf{x}_P) - \mathbf{u}^-(\mathbf{x}_P)) \cdot \mathbf{e}_\eta \geq 0. \quad (4.33)$$

Crack closure at a certain point \mathbf{x}_P implies that the contact constraint (4.33) is fulfilled identically, i.e.

$$u_\eta^+(\mathbf{x}_P) = u_\eta^-(\mathbf{x}_P) \quad (4.34)$$

if the crack is closed. Consequently, u_η is also continuous across the crack. Consider two points \mathbf{x}_{P+} and \mathbf{x}_{P-} on opposite sides of the crack that are very close to the crack face but are separated by $\Delta\eta$ in the reference configuration, see Fig. 4.3. For a closed crack it can be assumed that the difference between the thermally induced displacements and the total displacements in η -direction is non-positive, meaning that the material is compressed or strain-free in η -direction

$$u_\eta^+(\mathbf{x}_{P-}) - u_\eta^-(\mathbf{x}_{P+}) - \int_0^{\Delta\eta} \alpha_T(\theta - \theta_0) d\tilde{\eta} \leq 0 \quad (4.35)$$

and in the limit

$$\varepsilon_{\eta\eta}^e = \lim_{\Delta\eta \rightarrow 0} \frac{u_\eta^+(\mathbf{x}_{P-}) - u_\eta^-(\mathbf{x}_{P+}) - \int_0^{\Delta\eta} \alpha_T(\theta - \theta_0) d\tilde{\eta}}{\Delta\eta} \leq 0, \quad (4.36)$$

if the crack is closed. A crack closure criterion based on (4.34) cannot directly be utilized in a phase field model for fracture since the displacement field at \mathbf{x}_P is single valued in a phase field representation of the crack. The form (4.36), however, is suitable for a phase field formulation, because a strain $\varepsilon_{\eta\eta}^e$ can be defined at \mathbf{x}_P .

For an open crack, the crack faces are assumed to be traction free $\mathbf{t}^\pm = \mathbf{0}$, i.e. there is no external load at the crack faces. Thus, the Cauchy theorem yields $\sigma_{\eta\eta} = 0$ and $\sigma_{\eta\xi} = 0$ on either crack face, while $\sigma_{\xi\xi}$ should be unaffected by the presence of the crack. On the other hand, if the crack is closed it is $\mathbf{t}^- = -\mathbf{t}^+$. In this case, the normal stress in η -direction on either crack face is the same, i.e. $\sigma_{\eta\eta} < 0$. The in-plane shear stress ($\sigma_{\xi\eta}$) transmission capability of the crack, however, requires a constitutive assumption. In this work, it is assumed that there is no friction and no adhesion between the crack faces which requires $\sigma_{\eta\xi} = 0$. The treatment of the crack boundary conditions with no external crack face loading may therefore be summarized as

$$\begin{aligned} \varepsilon_{\eta\eta}^e(\mathbf{x}_P, t) \geq 0, & \Rightarrow \text{open crack at } \mathbf{x}_P & \Rightarrow \sigma_{\eta\eta} = \sigma_{\eta\xi} = 0 \\ \varepsilon_{\eta\eta}^e(\mathbf{x}_P, t) < 0, & \Rightarrow \text{closed crack at } \mathbf{x}_P & \Rightarrow \sigma_{\eta\eta} < 0, \sigma_{\eta\xi} = 0. \end{aligned} \quad (4.37)$$

The implementation of the crack boundary conditions (4.37) into a phase field model can be achieved by degrading only the zero-stress components mentioned above, i.e.

$$\begin{aligned} \sigma_{\eta\eta}(s, \boldsymbol{\varepsilon}) &= g(s)\tilde{\sigma}_{\eta\eta}(\boldsymbol{\varepsilon}), & \sigma_{\xi\eta}(s, \boldsymbol{\varepsilon}) &= g(s)\tilde{\sigma}_{\xi\eta}(\boldsymbol{\varepsilon}) && \text{for an open crack,} \\ \sigma_{\eta\eta}(s, \boldsymbol{\varepsilon}) &= \tilde{\sigma}_{\eta\eta}(\boldsymbol{\varepsilon}), & \sigma_{\xi\eta}(s, \boldsymbol{\varepsilon}) &= g(s)\tilde{\sigma}_{\xi\eta}(\boldsymbol{\varepsilon}) && \text{for a closed crack,} \end{aligned} \quad (4.38)$$

where $\tilde{\sigma}_{ij} = \mathbb{C}_{ijkl}\varepsilon_{kl}^e$ is the trial stress response of a completely undamaged material at a given ε_{kl}^e . An implementation of the crack boundary conditions according to (4.38) has been originally proposed in Strobl and Seelig (2015) and Strobl and Seelig (2016). The approach has been shown to be superior to other formulations in handling the boundary conditions at cracks realistically but requires a more sophisticated formulation than other methods. First of all, the crack orientation at a certain point must be determined. Potentially, this can be handled by setting

$$\mathbf{e}_\eta = -\frac{\nabla s}{|\nabla s|}, \quad (4.39)$$

so that the crack orientation does not necessarily have to be known a priori. Nevertheless, as mentioned in Strobl and Seelig (2015), such an approach can only be utilized at a distance away from the crack tip where the direction of ∇s is well behaved. Furthermore, it is not possible to stick to the variational formulation described in Section 4.2. In a strictly variational approach the decomposition (4.2) governs the asymmetric boundary conditions at the crack via the modification of the constitutive law (4.25) as well as the asymmetric resistance to crack propagation, see ψ_+^e in (4.26). Thus, it would be necessary to perform the decomposition (4.2) also at the crack tip in order to determine the crack driving ψ_+^e in (4.25) which involves difficulties as mentioned above. Furthermore, no decomposition of the strain energy density is available in undamaged material, because the computation of \mathbf{e}_η relies on the existence of a gradient ∇s . Thus, the tension-compression asymmetry cannot be modelled for crack nucleation scenarios by such an approach. Due to these difficulties, the treatment of crack boundary conditions according to (4.38) is complemented in Strobl and Seelig (2016) by a separate crack driving force D_s that substitutes ψ_+^e in the evolution equation (4.26). This breaks the variational character of the phase field problem which in turn increases the computational cost for the numerical solution of the problem.

The most common ways to handle the tension-compression asymmetry of fracturing in phase field models are the volumetric-deviatoric decomposition of the

strain energy density (VDD) by Amor et al. (2009) and the spectral decomposition (SD) introduced by Miehe et al. (2010b). Both formulations are variationally consistent and impose a decomposition of the strain energy density and the stress that is independent of the crack orientation. This comes at the cost of not predicting the crack boundary conditions as accurate as the advanced formulations presented in Strobl and Seelig (2016).

4.4.1 Volumetric-Deviatoric Decomposition of the Strain Energy Density

The fundamental assumption of the model of Amor et al. (2009) is that the elastic part of the volume dilatation

$$\varepsilon_V^e = \text{tr}(\boldsymbol{\varepsilon}^e) \quad (4.40)$$

is negative at the crack if the crack is closed. Assuming that there is a crack at \boldsymbol{x}_P , the respective crack closure criterion is

$$\begin{aligned} \text{tr}(\boldsymbol{\varepsilon}^e(\boldsymbol{x}_P, t)) \geq 0, & \Rightarrow \text{open crack at } \boldsymbol{x}_P, \\ \text{tr}(\boldsymbol{\varepsilon}^e(\boldsymbol{x}_P, t)) < 0, & \Rightarrow \text{closed crack at } \boldsymbol{x}_P, \end{aligned} \quad (4.41)$$

which is also illustrated in Fig. 4.4. As $\text{tr}(\boldsymbol{\varepsilon}^e)$ is invariant to a change of the coordinate system, knowledge of the crack orientation is not required. However, a positive dilatation does not automatically imply that $\varepsilon_{\eta\eta}^e > 0$. If a sufficiently large $\varepsilon_{\xi\xi}^e > |\varepsilon_{\eta\eta}^e|$ exists, the crack might be closed ($\varepsilon_{\eta\eta}^e < 0$) even though $\text{tr}(\boldsymbol{\varepsilon}^e)$ would still be positive. The constitutive relation at the crack is given by (4.25)

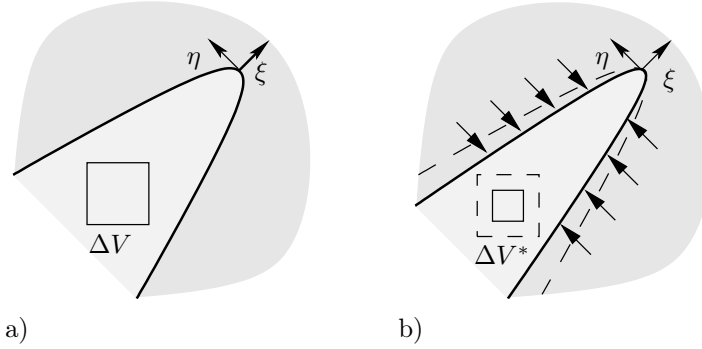


Figure 4.4: a) Open crack and b) closed crack with negative dilatation ε_v .

and is consequently determined by the formulation of the strain energy (4.2). From a physical standpoint, crack opening and sliding of the crack faces should not cause any surface traction nor a stress response at the crack, see (4.38), while

compression of a closed crack should. Associating opening, sliding and compression of the crack faces with positive volumetric, deviatoric and negative volumetric strain states respectively motivates the formulation of the strain energy density in the form (4.2) as

$$\begin{aligned}\psi_+^e &= \frac{K}{2} \langle \text{tr}(\boldsymbol{\varepsilon}^e) \rangle_+^2 + \mu (\mathbf{e}^e : \mathbf{e}^e), \\ \psi_-^e &= \frac{K}{2} \langle \text{tr}(\boldsymbol{\varepsilon}^e) \rangle_-^2,\end{aligned}\tag{4.42}$$

where

$$\langle x \rangle_- = \begin{cases} x & \text{if } x < 0 \\ 0 & \text{else} \end{cases}\tag{4.43}$$

and

$$\langle x \rangle_+ = \begin{cases} x & \text{if } x \geq 0 \\ 0 & \text{else} . \end{cases}\tag{4.44}$$

The associated constitutive law follows from (4.25) as

$$\boldsymbol{\sigma} = \frac{\partial \psi^e}{\partial \boldsymbol{\varepsilon}} = K \langle \text{tr}(\boldsymbol{\varepsilon}^e) \rangle_- \mathbf{1} + g(s) [K \langle \text{tr}(\boldsymbol{\varepsilon}^e) \rangle_+ \mathbf{1} + 2\mu \mathbf{e}^e].\tag{4.45}$$

For uniaxial compression perpendicular to the crack faces, i.e. $\sigma_{\eta\eta} < 0$ it can be verified from (4.45) that it is indeed $\text{tr}(\boldsymbol{\varepsilon}^e) < 0$. Thus, crack closure is predicted correctly under these circumstances.

Just as a positive volumetric deformation does not necessarily imply that the crack actually opens, i.e. that $\boldsymbol{\varepsilon}_{\eta\eta}^e > 0$, an isochoric deviatoric deformation \mathbf{e} does not necessarily represent a simple shear sliding motion of the crack faces. However, a simple shear sliding motion of the crack faces is accompanied by a purely deviatoric deformation which justifies the VDD formulation as an adequate model to describe Mode II fracture.

The crack driving part of the strain energy density ψ_+^e is also referred to as the ‘positive’ part of the strain energy density. It enters the phase field evolution equation (4.26) as a driving source term, and thus decides which load states cause crack propagation and crack nucleation.

4.4.2 Spectral Decomposition of the Strain Energy Density

The second popular approach to improve the phase field model’s behaviour in compressive load states and for crack closure is the spectral decomposition (SD)

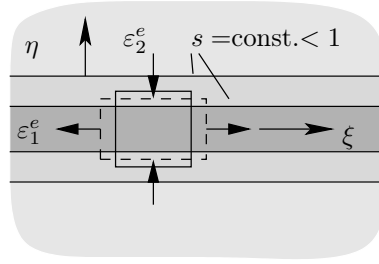


Figure 4.5: Detection of crack closure.

originally proposed by Miehe et al. (2010a). Miehe and his coworkers propose a mixed criterion for the detection of crack closure which also does not require any information on the crack orientation. The previously discussed dilatation criterion is used in conjunction with an approach that relies on the spectral decomposition of the elastic part of the linearized strain tensor

$$\boldsymbol{\varepsilon}^e = \sum_{i=1}^n \varepsilon_i^e \mathbf{n}_i \otimes \mathbf{n}_i, \quad (4.46)$$

where ε_i^e is the i -th eigenvalue of $\boldsymbol{\varepsilon}^e$ and \mathbf{n}_i is the associated normalized eigenvector. In this approach, negative eigenvalues are assumed to also indicate crack closure.

The strain energy density for the SD formulation is given by (4.2), with

$$\begin{aligned} \psi_+^e &= \frac{\lambda}{2} \langle \text{tr}(\boldsymbol{\varepsilon}^e) \rangle_+^2 + \mu (\boldsymbol{\varepsilon}_+^e : \boldsymbol{\varepsilon}_+^e), \\ \psi_-^e &= \frac{\lambda}{2} \langle \text{tr}(\boldsymbol{\varepsilon}^e) \rangle_-^2 + \mu (\boldsymbol{\varepsilon}_-^e : \boldsymbol{\varepsilon}_-^e), \end{aligned} \quad (4.47)$$

where

$$\boldsymbol{\varepsilon}_-^e = \sum_{i=1}^n \langle \varepsilon_i^e \rangle_- \mathbf{n}_i \otimes \mathbf{n}_i, \quad (4.48)$$

and

$$\boldsymbol{\varepsilon}_+^e = \sum_{i=1}^n \langle \varepsilon_i^e \rangle_+ \mathbf{n}_i \otimes \mathbf{n}_i. \quad (4.49)$$

The first term in ψ_-^e and ψ_+^e reveals that the dilatation criterion is still utilized for the component $\frac{\lambda}{2} \text{tr}(\boldsymbol{\varepsilon}^e)^2$. For the remainder of the strain energy density, however, the sign of the eigenvalues is employed as an indicator for crack closure, see (4.47). The constitutive law derived from (4.25) is given by

$$\boldsymbol{\sigma} = \frac{\partial \psi^e}{\partial \boldsymbol{\varepsilon}} = g(s) [\lambda \langle \text{tr}(\boldsymbol{\varepsilon}^e) \rangle_+ \mathbf{1} + 2\mu \boldsymbol{\varepsilon}_+^e] + [\lambda \langle \text{tr}(\boldsymbol{\varepsilon}^e) \rangle_- \mathbf{1} + 2\mu \boldsymbol{\varepsilon}_-^e]. \quad (4.50)$$

Since the model partly shares the crack closure criterion of the VDD formulation, it also keeps the previously mentioned weaknesses. Nonetheless, some of the negative effects are diminished, which can be illustrated as follows. Consider a configuration in which one principal strain ε_1^e is positive and the associated eigenvector \mathbf{n}_1 is aligned with the crack direction. The other principal strain, which is identical to $\varepsilon_{\eta\eta}^e$, is negative and therefore the crack would be closed, see Fig. 4.5. The VDD formulation fully degrades all stress components in a situation like this if $|\varepsilon_1^e| > |\varepsilon_2^e|$, i.e. if $\text{tr}(\boldsymbol{\varepsilon}^e) > 0$. In case of the SD formulation, not all stress components are degraded to the full extent, since the contribution of the negative principal strain ε_2^e in the second bracket of (4.50) is not affected by $g(s)$.

In contrast to the VDD model, the SD formulation has a weak point in treating Mode II fracture. Consider a plane strain simple shear sliding motion of the crack faces of a crack segment as depicted in Fig. 4.5 under isothermal conditions. The displacement field is given as $\mathbf{u} = 2c_0\eta\mathbf{e}_\xi$ and $c_0 \neq 0$ is a constant. The strain in this case is purely deviatoric, i.e.

$$\boldsymbol{\varepsilon}^e = \mathbf{e}^e = c_0\mathbf{e}_\xi \otimes \mathbf{e}_\eta + c_0 \mathbf{e}_\eta \otimes \mathbf{e}_\xi \quad (4.51)$$

and $\text{tr}(\boldsymbol{\varepsilon}^e) = 0$. The eigenvalues of the strain tensor are

$$\varepsilon_1^e = +c_0, \quad \varepsilon_2^e = -c_0. \quad (4.52)$$

Assuming that no friction and no adhesion is present between the crack faces, the sliding motion should not cause a stress response, i.e. $\boldsymbol{\sigma} = \mathbf{0}$ for $s = 0$. This is true for VDD, see (4.45), but not for the SD formulation. In the latter case, the stress resulting from such a deformation is

$$\boldsymbol{\sigma} = 2\mu c_0 (g(s)\mathbf{n}_1 \otimes \mathbf{n}_1 - \mathbf{n}_2 \otimes \mathbf{n}_2) \neq \mathbf{0}. \quad (4.53)$$

Consequently, the SD approach will result in unphysically stiff structural behaviour for sliding motions of the crack faces.

4.4.3 Discussion of the Asymmetry Formulations

From a physical point of view, the two tension-compression asymmetry formulations presented in the previous sections provide a substantial improvement over the original formulation (4.2). Although some aspects have been discussed above, the resulting sharp interface fracture model remains unclear, see Li et al. (2016). This means that no proof of the convergence of the energy functional (4.1) to a discrete energy functional similar to (3.63) as $l \rightarrow 0$ is available and thus it is not known which physical process is modelled exactly by such modifications. The performance of the VDD and SD approaches in numerical finite element simulations

of fracture has been discussed in Ambati et al. (2015). Ambati and his coworkers pointed out that the discontinuous decomposition of the strain fields is nonlinearly dependent on the strain state in both formulations, which results in a significant computational effort. In Ambati et al. (2015) it is argued that the computational effort of the SD formulation is higher ($\sim 12\%$ in one benchmark) than that of the VDD formulation because of the larger number of required computational operations. The authors of Ambati et al. (2015) also advocated a hybrid formulation that significantly outperformed the VDD as well as the SD formulation.

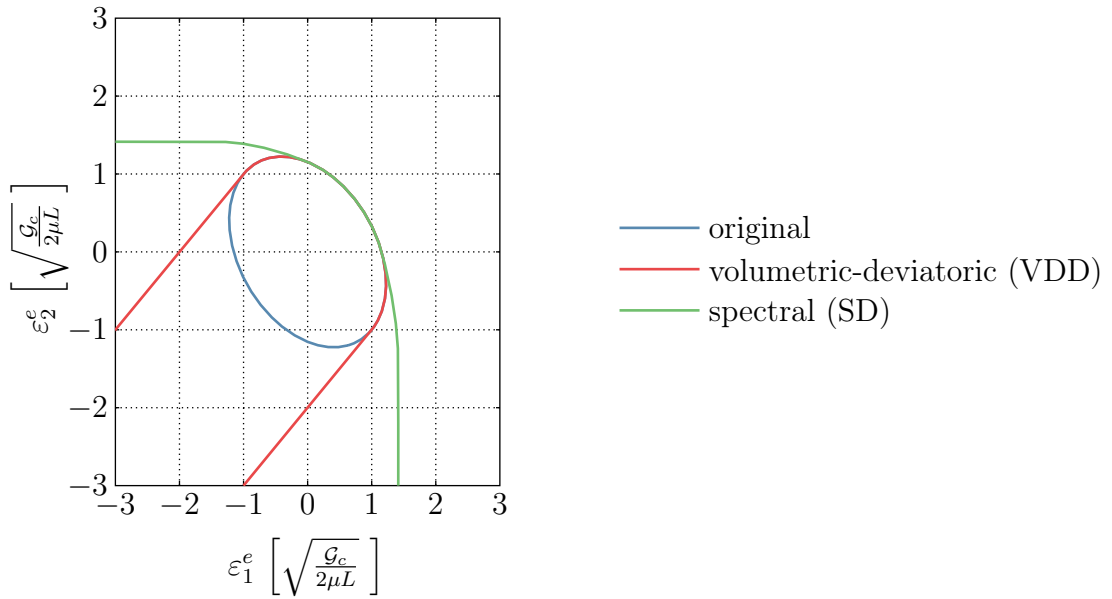


Figure 4.6: Isolines of $\psi_+^e = \psi^c = 1.0G_c/L$ for the different formulations of the strain energy density and different biaxial strain load.

In order to enhance the understanding of the effects that the choice of the asymmetry formulations has on the model's behaviour, the positive part of the strain energy density ψ_+^e is studied in more detail. As ψ_+^e is the crack driving force in the phase field evolution equation (4.26), an analysis of this term allows to gain insight in the effective material strength modelled by the two considered formulations (4.42) and (4.47) under a biaxial strain load. A biaxial elastic plane strain state is determined by the two principal elastic strains, cf. (2.17). The formulations of the positive part of the strain energy are given by (4.42) and (4.47), whereas the unmodified, original formulation is determined by (4.8). It is assumed that the undamaged material will fail at a critical load corresponding to

a driving force of ψ^c . Consequently, the relation

$$\psi_+^e(\varepsilon_1^e, \varepsilon_2^e) = \psi^c \quad (4.54)$$

implicitly describes a curve in the ε_1^e - ε_2^e -plane that determines the strength of the material for a given strain state. These graphs are plotted in Fig. 4.6 for the two tension-compression formulations as well as for the original formulation. One can observe that in biaxial expansion $\varepsilon_1^e > 0, \varepsilon_2^e > 0$, all models predict the same effective strength meaning that the material will fail at the same load level ($\varepsilon_1^e > 0, \varepsilon_2^e > 0$). Under pure shear strain $\varepsilon_1^e/\varepsilon_2^e = -1$, the VDD formulation still agrees with the unmodified formulation with respect to the bearable load level, while the SD approach predicts failure at considerably higher absolute strain levels. Thus, the material resistance to shear loading will be enhanced for SD. As soon as a negative volumetric strain is present, i.e. $\varepsilon_1^e + \varepsilon_2^e < 0$, VDD also results in a higher material resistance than the original formulation. However, a large enough deviatoric strain still allows for failure even if $\varepsilon_1^e < 0$ and $\varepsilon_2^e < 0$. For $\text{tr}(\boldsymbol{\varepsilon}^e) < 0$ (4.54) reduces to

$$\frac{\mu}{2}(\varepsilon_1^e - \varepsilon_2^e)^2 = \psi^c, \quad (4.55)$$

in the VDD case which can be rearranged to get the equation of the bounding curves as

$$\varepsilon_2^e = \varepsilon_1^e \pm \sqrt{\frac{2\psi^c}{\mu}} \quad \text{for } \text{tr}(\boldsymbol{\varepsilon}^e) < 0. \quad (4.56)$$

The SD approach yields even larger bearable strains in the compressive region. As soon as the volumetric strain is negative, failure can only be obtained if one of the principle strains is large enough, i.e. if

$$\varepsilon_1^e \geq \sqrt{\frac{\psi^c}{\mu}} \quad \text{or} \quad \varepsilon_2^e \geq \sqrt{\frac{\psi^c}{\mu}}. \quad (4.57)$$

Consequently, the bounding curve is given by the vertical and the horizontal line segments respectively for $\text{tr}(\boldsymbol{\varepsilon}^e) < 0$, see the green line in Fig. 4.6.

4.5 Dimensional Analysis

In order to decrease the number of free parameters in the subsequent analysis and the simulations that follow in later chapters, the governing equations that were derived in Section 4.2 are expressed in a non-dimensional format by means of

- the characteristic length-scale L of the problem,

- the density ρ ,
- the Lamé parameter 2μ ,
- the specific fracture energy \mathcal{G}_c and
- the specific heat capacity c_θ .

The normalization procedure is motivated by the one-dimensional coupled problem

$$\begin{aligned} \frac{2\mu}{\rho} \frac{\partial}{\partial x} \left[g(s) \left\langle \frac{\partial u}{\partial x} - \alpha_T (\theta - \theta_0) \right\rangle_+ + \left\langle \frac{\partial u}{\partial x} - \alpha_T (\theta - \theta_0) \right\rangle_- \right] &= \frac{\partial^2 u}{\partial t^2}, \\ g'(s) \frac{1}{2} 2\mu \left\langle \frac{\partial u}{\partial x} - \alpha_T (\theta - \theta_0) \right\rangle_+^2 - \mathcal{G}_c \left[2l \frac{\partial^2 s}{\partial x^2} - \frac{1-s}{2l} \right] &= 0, \\ \rho c_\theta \dot{\theta} = 2\mu \left[g(s) \left\langle \frac{\partial u}{\partial x} - \alpha_T (\theta - \theta_0) \right\rangle_+ + \left\langle \frac{\partial u}{\partial x} - \alpha_T (\theta - \theta_0) \right\rangle_- \right] \frac{\partial^2 u}{\partial x \partial t} + \kappa \frac{\partial^2 \theta}{\partial x^2} + s^\theta. \end{aligned} \quad (4.58)$$

The introduction of the dimensionless fields $\bar{\mathbf{u}}$ and $\bar{\theta}$,

$$\begin{aligned} \mathbf{u} &= \bar{\mathbf{u}} u_{ref}, \quad \text{where } u_{ref} = \sqrt{\frac{\mathcal{G}_c L}{2\mu}}, \\ \theta &= \bar{\theta} \theta_{ref}, \quad \text{where } \theta_{ref} = \frac{\mathcal{G}_c}{\rho c_\theta L}, \end{aligned} \quad (4.59)$$

as well as scaling spatial dimensions by L

$$\bar{\mathbf{x}} = \frac{\mathbf{x}}{L}, \quad \bar{l} = \frac{l}{L}, \quad (4.60)$$

and the time by the time scale T

$$\bar{t} = \frac{t}{T} \quad (4.61)$$

yield the non-dimensional set of equations

$$\begin{aligned} \frac{2\mu T^2}{L^2 \rho} \frac{\partial}{\partial \bar{x}} \left[g(s) \left\langle \frac{\partial \bar{u}}{\partial \bar{x}} - \bar{\alpha}_T (\bar{\theta} - \bar{\theta}_0) \right\rangle_+ + \left\langle \frac{\partial \bar{u}}{\partial \bar{x}} - \bar{\alpha}_T (\bar{\theta} - \bar{\theta}_0) \right\rangle_- \right] &= \frac{\partial^2 \bar{u}}{\partial \bar{t}^2}, \\ g'(s) \frac{1}{2} \left\langle \frac{\partial \bar{u}}{\partial \bar{x}} - \bar{\alpha}_T (\bar{\theta} - \bar{\theta}_0) \right\rangle_+^2 - \left[2\bar{l} \frac{\partial^2 s}{\partial \bar{x}^2} - \frac{1-s}{2\bar{l}} \right] &= 0, \\ \frac{\partial \bar{\theta}}{\partial \bar{t}} = 2\mu \left[g(s) \left\langle \frac{\partial \bar{u}}{\partial \bar{x}} - \bar{\alpha}_T (\bar{\theta} - \bar{\theta}_0) \right\rangle_+ + \left\langle \frac{\partial \bar{u}}{\partial \bar{x}} - \bar{\alpha}_T (\bar{\theta} - \bar{\theta}_0) \right\rangle_- \right] \frac{\partial^2 \bar{u}}{\partial \bar{x} \partial \bar{t}} + \bar{\kappa} \frac{\partial \bar{\theta}}{\partial \bar{x}^2} + \bar{s}^\theta, \end{aligned} \quad (4.62)$$

where the non-dimensional coefficient of thermal expansion and the non-dimensional heat conductivity are given by

$$\begin{aligned}\bar{\alpha}_T &= \frac{\alpha_T}{\alpha_{T,\text{ref}}}, & \alpha_{T,\text{ref}} &= \sqrt{\frac{\rho^2 c_\theta^2 L}{\mathcal{G}_c 2\mu}}, \\ \bar{\kappa} &= \frac{\kappa}{\kappa_{\text{ref}}}, & \kappa_{\text{ref}} &= \frac{\rho c_\theta L^2}{T}\end{aligned}\quad (4.63)$$

and the normalized heat source is

$$\bar{s}^\theta = \frac{s^\theta}{s_{\text{ref}}^\theta}, \quad s_{\text{ref}}^\theta = \frac{\mathcal{G}_c}{LT}. \quad (4.64)$$

Equation (4.62)₁ suggests to introduce the time scale as

$$T = \frac{L}{c}, \quad (4.65)$$

where

$$c = \sqrt{\frac{2\mu}{\rho}} \quad (4.66)$$

is the characteristic wave speed of the 1D-problem. The differential operations with respect to the non-dimensional coordinates $\bar{\mathbf{x}}$ and time \bar{t} follow from the scaling (4.60) and (4.61) as

$$\frac{\partial(*)}{\partial x} = \frac{1}{L} \frac{\partial(*)}{\partial \bar{x}}, \quad \frac{\partial(*)}{\partial t} = \frac{1}{T} \frac{\partial(*)}{\partial \bar{t}} = \frac{1}{T} \overset{\circ}{\partial}(*). \quad (4.67)$$

An analog definition of the non-dimensional differential operators

$$\text{grad}(*) = \frac{1}{L} \bar{\text{grad}}(*), \quad \text{div}(*) = \frac{1}{L} \bar{\text{div}}(*), \quad \Delta(*) = \frac{1}{L^2} \bar{\Delta}(*), \quad (4.68)$$

allows to reformulate the equations governing fracture in a non-dimensional fashion as

$$\overset{\circ}{\mathbf{u}} = \bar{\text{div}} \bar{\boldsymbol{\sigma}}, \quad (4.69)$$

$$g'(s) \bar{\psi}_+^e - \left[2l \bar{\Delta} s - \frac{1-s}{2l} \right] = 0, \quad (4.70)$$

$$\overset{\circ}{\bar{\theta}} = \bar{\boldsymbol{\sigma}} : \overset{\circ}{\bar{\boldsymbol{\varepsilon}}} + \bar{\kappa} \bar{\text{grad}} \bar{\theta} + \bar{r}^\theta. \quad (4.71)$$

The normalized representation of derived quantities follows from the scaling of the primary fields (4.59) as well as the definition of the non-dimensional differential operators. The respective relations for the infinitesimal strain tensor, the stress

tensor, the positive part of the strain energy density, and the heat flux are given as

$$\boldsymbol{\varepsilon} = \bar{\boldsymbol{\varepsilon}}\varepsilon_{\text{ref}} \quad \boldsymbol{\varepsilon}^e = \bar{\boldsymbol{\varepsilon}}^e\varepsilon_{\text{ref}}, \quad \text{where} \quad \varepsilon_{\text{ref}} = \sqrt{\frac{\mathcal{G}_c}{2\mu L}}, \quad (4.72)$$

$$\boldsymbol{\sigma} = \bar{\boldsymbol{\sigma}}\sigma_{\text{ref}}, \quad \text{where} \quad \sigma_{\text{ref}} = \sqrt{\frac{2\mu\mathcal{G}_c}{L}}, \quad (4.73)$$

$$\psi_+^e = \bar{\psi}_+^e\psi_{+,\text{ref}}^e, \quad \text{where} \quad \psi_{+,\text{ref}}^e = \frac{\mathcal{G}_c}{L}, \quad (4.74)$$

and

$$\mathbf{q}^\theta = \bar{\mathbf{q}}^\theta q_{\text{ref}}^\theta, \quad \text{where} \quad q_{\text{ref}}^\theta = \frac{\mathcal{G}_c}{T} \quad (4.75)$$

respectively. By scaling the elastic parameters with 2μ , i.e.

$$\bar{\mu} = \frac{\mu}{2\mu} = \frac{1}{2}, \quad \bar{\lambda} = \frac{\lambda}{2\mu}, \quad (4.76)$$

one can also derive the non-dimensional expressions for the wave speeds

$$c_s = \sqrt{\frac{\bar{\mu}}{\rho}} = \sqrt{\frac{1}{2}}c = \bar{c}_s c = \bar{c}_s \frac{L}{T} \quad (4.77)$$

and

$$c_d = \sqrt{\frac{\bar{\lambda} + 2\bar{\mu}}{\rho}} = \sqrt{\bar{\lambda} + 1}c = \bar{c}_d c = \bar{c}_d \frac{L}{T}. \quad (4.78)$$

Note, that material velocities, meaning changes of a position \mathbf{x} with respect to time, such as the wave speed, are scaled differently, i.e. as $\dot{\mathbf{x}} \sim L/T$, than rates of the displacement $\dot{\mathbf{u}} \sim u_{\text{ref}}/T$. This results from the fact that while the physical interpretations of c_s and $\dot{\mathbf{u}}$ are the same, i.e. both represent the rate of change of a position with respect to time, the displacement \mathbf{u} is decoupled from the actual position of the associated particle \mathbf{x} in the mathematical model and is treated as an independent field within the small deformation theory. In dynamics one often tries to judge whether a loading speed $\dot{\mathbf{u}}$ is high or low compared to the wave speed. Nonetheless, such a comparison relies on the interpretation of the displacements as a translation in physical space. Nevertheless, this connection is not a feature of the mathematical formulation of the problem such as it would be in a finite deformation theory. If one wants to specify a velocity ratio as

$$r = \frac{|\dot{\mathbf{u}}|}{c} \quad (4.79)$$

the associated non-dimensional rate is, by means of (4.67) and (4.65),

$$\left| \overset{\circ}{\mathbf{u}} \right| = r \frac{L}{u_{\text{ref}}}. \quad (4.80)$$

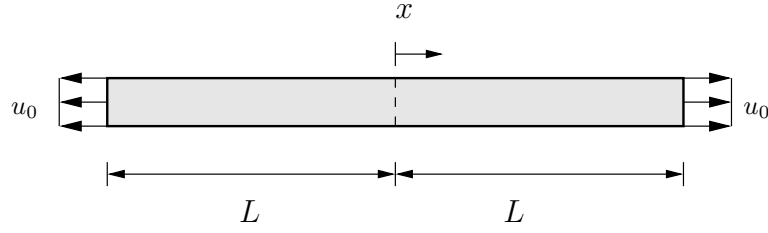


Figure 4.7: One dimensional bar subject to a displacement load u_0 .

4.6 Analytic Results

In this Section, analytic results are presented that shed light on several features of the present phase field model for dynamic brittle fracture and improve the understanding of the numerical simulations that are discussed in the subsequent chapters.

4.6.1 1D Bar

Interesting results concerning the constitutive behaviour of the material in the phase field model and crack nucleation can be obtained by considering a 1D bar that is subjected to tensile loading under quasi-static and isothermal conditions, as depicted in Fig. 4.7. The discussion of this quasi-static case are also relevant for the dynamic model as the numerical simulations in Chapter 6 reveal.

The analysis of this problem follows the approach discussed in Kuhn (2013) and Kuhn et al. (2015) as well as some aspects presented in Borden (2012). For the given scenario, the governing set of equations reduce to

$$\frac{d\sigma}{dx} = 0, \quad \text{where} \quad \sigma = g(s)2\mu \frac{du}{dx} \quad (4.81)$$

$$g'(s)\mu \left(\frac{du}{dx}\right)^2 - \mathcal{G}_c \left[\frac{1-s}{2l} + 2l \frac{d^2s}{dx^2} \right] = 0 \quad (4.82)$$

Furthermore, the phase field is assumed to take on a spatially constant value at the boundaries, meaning that $s'(\pm L) = 0$.

Homogeneous Solution

To begin with, a homogeneous solution of the coupled problem is searched for. This signifies that all spatial derivatives of the phase field s are set to zero and it is

$$\frac{du}{dx} = \frac{u_0}{L} = \varepsilon_0. \quad (4.83)$$

Such a situation can be expected away from cracks in pristine material. Relation (4.82) results in

$$g'(s)\mu \left(\frac{u_0}{L}\right)^2 - \mathcal{G}_c \left[\frac{1-s}{2l}\right] = 0. \quad (4.84)$$

It becomes apparent, that the homogeneous solution s_h of (4.84) and consequently also the stress σ_h are critically dependent on the choice of the degradation function $g(s)$. In this work, the degradation function is chosen to be of the form

$$g(s) = a(s^3 - s^2) + 3s^2 - 2s^3 + \eta_s, \quad (4.85)$$

where $a > 1$ is the slope of the degradation function at $s = 1$, as proposed in Borden (2012). A choice of $a > 0$ guarantees the fourth constraint in (4.4). Figure 4.8 displays such degradation functions for values of $a = 0$, $a = 0.5$ and $a = 2$. In the latter case, $g(s)$ reduces to the quadratic form

$$g(s) = s^2 + \eta_s, \quad (4.86)$$

which is a common formulation in the literature. The parameter $\eta_s \ll 1$ provides

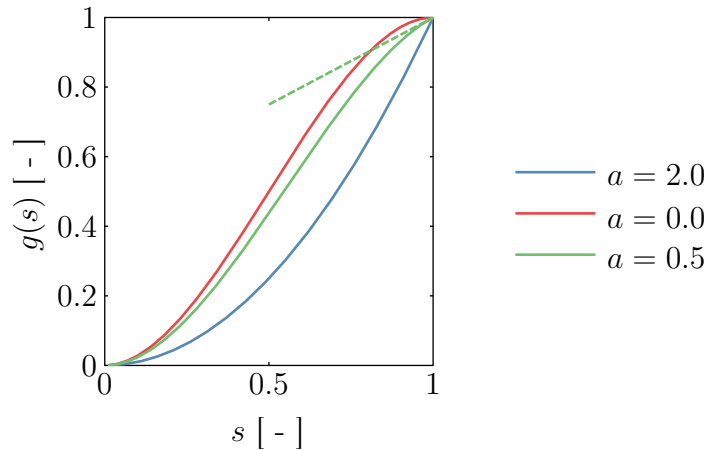


Figure 4.8: Different choices of the degradation function. The dashed green line indicates the slope $g'(1) = 0.5$.

a small residual stiffness in the completely broken state. The introduction of this residual stiffness stems from the original quasi-static phase field fracture models. In the quasi-static case, it is necessary to ensure positive definiteness of the tangent matrix in numerical simulations by a small auxiliary stiffness. In a dynamic setting, this has been found to be unnecessary and thus, in this work, the parameter is set to zero unless otherwise mentioned. For a general degradation function of the type (4.85), equation (4.84) has the solutions

$$s_{h,a} = \frac{\mathcal{G}_c + (6 - 2a)l\varepsilon_0^2 2\mu}{2l\varepsilon_0^2 2\mu(6 - 3a)} \pm \frac{\sqrt{(\mathcal{G}_c + (6 - 2a)l\varepsilon_0^2 2\mu)^2 + 4\mathcal{G}_c(3a - 6)l\varepsilon_0^2 2\mu}}{2l\varepsilon_0^2 2\mu(6 - 3a)}, \quad (4.87)$$

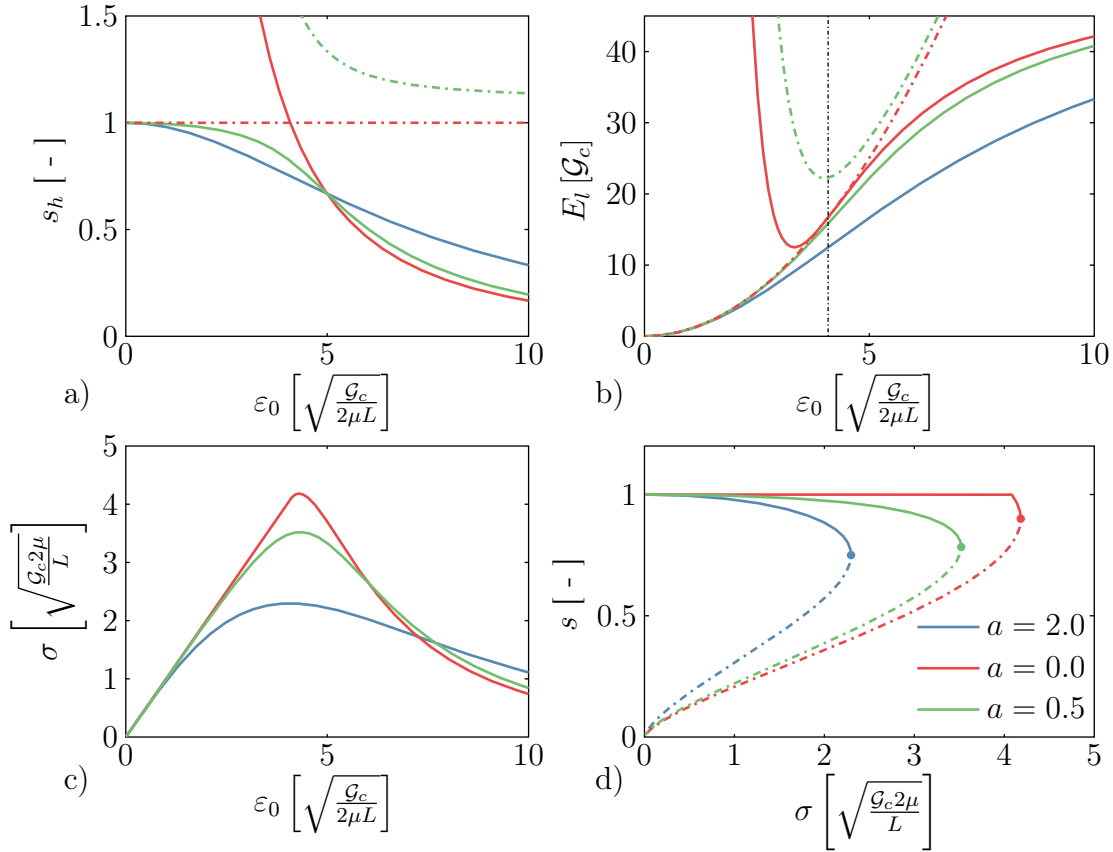


Figure 4.9: Homogeneous solution of the 1D bar problem for different choices of the degradation function. a) Homogeneous solution of the phase field ε_h vs. s_h , b) E_l vs. ε_h , c) stress vs. strain graph and d) phase field s_h vs. applied stress σ_h . The second solution for the cubic cases is indicated by the dashed-dotted lines in a) and b), whereas the dashed-dotted line in d) indicates supercritical loading. The vertical dashed black line in b) shows $\tilde{\varepsilon}$. The length-scale parameter is set to $l = 0.01L$

which are displayed in Fig. 4.9 a) for $a = 0$, $a = 0.5$ and $a = 2$. In the special case of $a = 2$, there is a unique and admissible solution, meaning that $s_h \leq 1$,

$$s_{h,a=2} = \frac{\mathcal{G}_c}{4l\mu\varepsilon_0^2 + \mathcal{G}_c}, \quad (4.88)$$

which monotonously approaches zero as the load ε_0 is increased. Furthermore, for this choice of a , significant changes of the phase field can be observed at relatively small loads.

For $a = 0$ the solution (4.87) has two branches. The first branch $s_{h,a=0} = 1$ is admissible in the whole regime of loads ε_0 . The other branch is described by

$$s_{h,a=0} = \frac{\mathcal{G}_c}{6l\varepsilon_0^2\mu}. \quad (4.89)$$

Since $s_h \leq 1$ has to hold for any admissible solution, this branch is constrained to

$$\varepsilon_0 \geq \tilde{\varepsilon} = \sqrt{\frac{\mathcal{G}_c}{12l\mu}}. \quad (4.90)$$

Thus, for $\varepsilon_0 > \tilde{\varepsilon}$ there are two admissible solutions: the purely elastic solution $s_{h,a=0} = 1$ and a homogeneous solution with degraded stiffness (4.89). The question arises which of the two possible branches is the correct energy minimizing solution for $\varepsilon_0 > \tilde{\varepsilon}$. To answer this, it is illustrative to consider the sum of elastic and fracture energy (4.1) as depicted in Fig. 4.9 b). Initially, the branch $s_{h,a=0} = 1$ is the energetically favourable solution, i.e. the branch with the lower total energy. However, just as the second branch of the solution becomes admissible at $\varepsilon_0 = \tilde{\varepsilon}$, the associated energies of the two branches as well as their slopes $\frac{\partial E_l}{\partial \varepsilon_0}$ are exactly the same. For $\varepsilon_0 > \tilde{\varepsilon}$ the second branch of the solution given by (4.89) is indeed the energy minimizing solution. Consequently, the correct solution for the whole load regime might be summarized as

$$s_{h,a=0} = \begin{cases} 1, & \text{for } \varepsilon_0 \leq \tilde{\varepsilon}, \\ \frac{\mathcal{G}_c}{6l\varepsilon_0^2 2\mu}, & \text{for } \varepsilon_0 > \tilde{\varepsilon}. \end{cases} \quad (4.91)$$

The fact that the value and the slope of the energies are identical at a load level, where the correct solution switches from one branch of (4.87) to another can lead to difficulties in numerical algorithms. In order to overcome this difficulty, the algorithm has to trigger the switch of the solution branches, as for example reported in Kuhn et al. (2015).

In the general case $0 < a < 2$, again two branches of the solution (4.87) exist of which only the branch with the minus sign in (4.87) is admissible for all ε_0 , see the green lines in Fig. 4.9 a). This solution is displayed as the solid green line in Fig. 4.9 a). It is very close to $s = 1$ at low load levels and approaches the second branch of $s_{h,a=0}$ for $\varepsilon_0 > \tilde{\varepsilon}$.

The homogeneous stress-strain response can be found by substituting the correct solutions s_h into the constitutive law (4.82)₂. The associated graphs are displayed in Fig. 4.9 c), for the quadratic case $a = 2$, for the combined solution (4.91) in case of $a = 0$ and the minus branch of (4.87) for the general case $a = 0.5$. All curves show an initial increase of the stress up to a maximum level at which the homogeneous stress response decreases again. However, nonlinear constitutive behaviour can be observed for the quadratic case even for low applied strains. Recalling that it is the intention of this work to model brittle materials, which show almost linear constitutive behaviour up to fracture, this is certainly a weak point of the quadratic formulation. The cubic formulations, in particular $a = 0$, cure

this weakness. Here, the material response is linear up to a point very close to the maximum stress response. Furthermore, it can be observed that the maximum stress increases for $a \rightarrow 0$. The critical strain level at which the maximum stress response appears, can be obtained from the necessary condition

$$\frac{\partial \sigma}{\partial \varepsilon_0} = 0. \quad (4.92)$$

For $a = 2$ the maximum stress, the associated strain and phase field values are

$$\varepsilon_c^* = \sqrt{\frac{\mathcal{G}_c}{2\mu 6l}}, \quad \sigma_c^* = \frac{9}{16} \sqrt{\frac{\mathcal{G}_c 2\mu}{6l}}, \quad s_c^* = \frac{3}{4}, \quad (4.93)$$

whereas for $a = 0$ it is

$$\varepsilon_c = \frac{5}{3} \sqrt{\frac{\mathcal{G}_c}{2\mu 15l}}, \quad \sigma_c = \frac{81}{50} \sqrt{\frac{\mathcal{G}_c 2\mu}{15l}}, \quad s_c = \frac{9}{10}, \quad (4.94)$$

cf. Kuhn et al. (2015).

Spatially Inhomogeneous Solution and Bifurcation

The spatially homogeneous solution of the 1D bar is stable for subcritical load levels $\varepsilon_0 \leq \varepsilon_c$, as mentioned in Kuhn et al. (2015) and shown for the quadratic case in Kuhn (2013). Nevertheless, stability cannot be guaranteed if the strain exceeds this level, see Kuhn (2013). In fact, the fracture field starts to localize for $\varepsilon_0 > \varepsilon_c$ and eventually a crack forms. For a quadratic degradation function, it is shown in Benallal and Marigo (2007), Amor et al. (2008) and Pham et al. (2011) that the stability point for a broader class of gradient damage models similar to the present phase field model lies only slightly above the critical load σ_c^* if $l \ll L$. Thus, the maximum stress response of the homogeneous solution may be interpreted as the strength of the modelled material. This opens an entirely different view on the length-scale l which initially may be considered as a purely numerical parameter that controls the width of phase field cracks. Nevertheless, l critically affects σ_c and σ_c^* , see (4.94) and (4.93), and thus can be interpreted as a material parameter that is related to measurable quantities such as the fracture toughness and the tensile strength of the material, see also Kuhn et al. (2015). In order to study the localization process in more detail, the procedure described in Hakim and Karma (2009), Kuhn (2013), and Kuhn et al. (2015) is followed to derive a spatially inhomogeneous solution of the 1D bar problem. The equations (4.82) can be combined to

$$\frac{g'(s)l\sigma^2}{\mathcal{G}_c 2\mu g^2(s)} + s - 4l^2 s_{,xx} - 1 = 0, \quad (4.95)$$

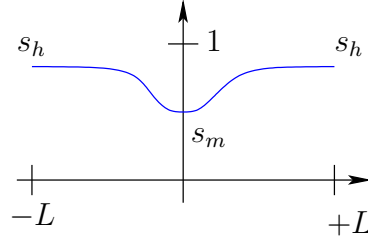


Figure 4.10: Spatially inhomogeneous solution of the 1-bar problem.

which is considered for $l \ll L$ for a given stress level $\sigma \leq \sigma_c$. The solution that is searched for is differentiable, symmetric $s(-x) = s(x)$, obeys $s'(0) = 0$ and is approximately spatially constant at the ends of the bar. The bounding value is the subcritical homogeneous solution at the specified stress level, i.e. $s'(\pm L) = 0$ and $s(\pm L) = s_h(\sigma)$. Such a function is depicted in Fig. 4.10, where $s_m = s(0)$ denotes the minimal value of the order parameter at the localization site $x = 0$. Equation (4.95) is integrated in a first step

$$\int_{s_m}^{s(x)} \left(\frac{g'(s)l\sigma^2}{\mathcal{G}_c 2\mu g^2(s)} + s - 4l^2 s_{,xx} - 1 \right) ds = 0. \quad (4.96)$$

By means of the identities

$$\frac{d}{ds} \left(\frac{1}{g(s)} \right) = -\frac{g'(s)}{g^2(s)}, \quad (4.97)$$

$$\frac{d}{ds} \left[\left(\frac{ds}{dx} \right)^2 \right] = 2 \frac{d}{ds} \left(\frac{ds}{dx} \right) \left(\frac{ds}{dx} \right) = 2 \frac{d}{dx} \left(\frac{ds}{dx} \right) = 2 \left(\frac{d^2 s}{dx^2} \right), \quad (4.98)$$

relation (4.96) yields

$$\underbrace{2l^2 (s_{,x})^2}_{V_{\text{kin}}(s,x)} + \underbrace{\frac{l\sigma^2}{\mathcal{G}_c 2\mu g(s)} - \frac{s^2}{2} + s}_{V_{\text{eff}}(s)} = \underbrace{\frac{l\sigma^2}{\mathcal{G}_c 2\mu g(s_m)} - \frac{s_m^2}{2} + s_m}_{V_{\text{eff}}(s_m)}, \quad (4.99)$$

which can be interpreted as a conservation law where V_{kin} is the kinetic energy of s and V_{eff} is the effective potential, see Kuhn (2013). If (4.99) is evaluated at $x = L$ then $V_{\text{kin}}(L) = 0$ and $s(L) = s_h$. The homogeneous solution of the phase field variable is known for the subcritical case for a given stress level, cf. the solid lines in Fig. 4.9 d). Consequently, s_m is the only unknown in (4.99) in this situation and can be determined as the root of the function

$$V_\sigma(s) = V_{\text{eff}}(s) - V_{\text{eff}}(s_h). \quad (4.100)$$

The localization process is described and analyzed in detail in Kuhn (2013) for the quadratic case ($a = 2$) and in Kuhn et al. (2015) for $a = 0.0$. The analysis presented here will be done for $a = 0.1$. As becomes apparent in Fig. 4.11 a)

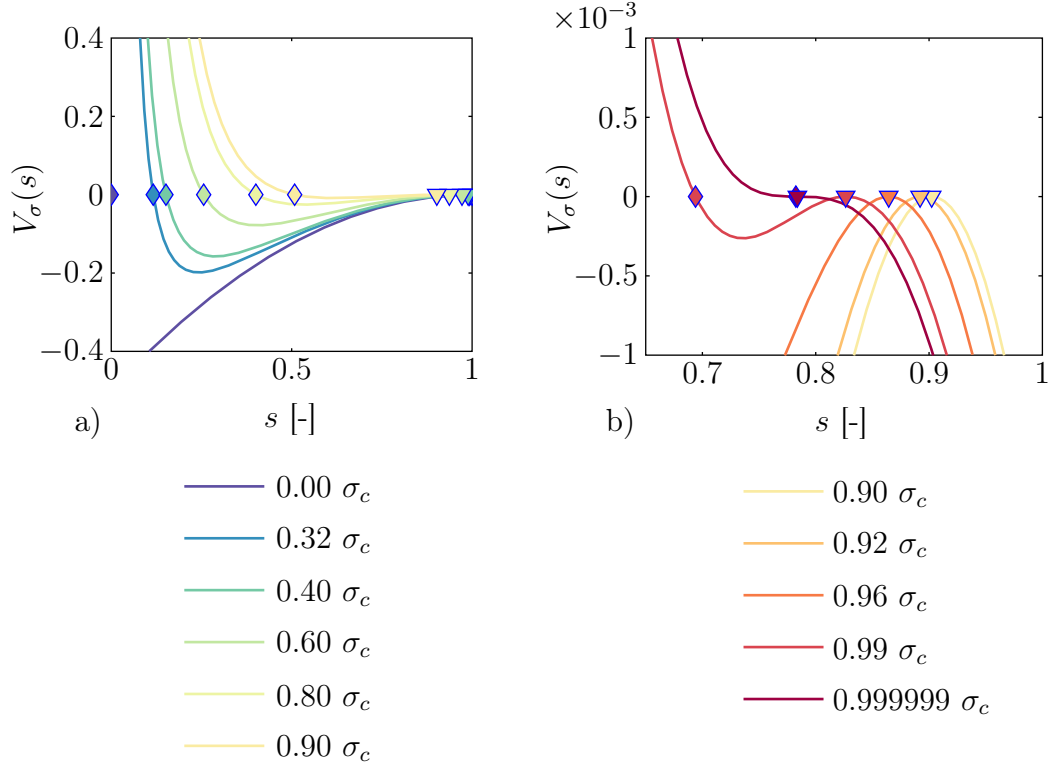


Figure 4.11: a) function V_σ for relatively low stress levels and b) magnified view of V_σ for high stress levels. The smaller root of V_σ for the respective stress levels is indicated by the diamond markers, whereas the larger root is displayed as the triangle markers. The length-scale parameter is set to $l = 0.01L$.

and b), V_σ generally has two roots. The first root corresponds to the homogeneous solution $s_{m1} = s_h(\sigma)$, marked by triangles in Fig. 4.11, which is admissible for the constraints introduced above. This solution s_{m1} is close to $s = 1$, see also the magnified section that is displayed Fig. 4.11 b). The value of s_{m1} decreases as $\sigma \rightarrow \sigma_c$ and it is a local maximum of V_σ , as can also be observed in Fig. 4.11 b). The second root s_{m2} , marked by the diamonds, corresponds to the truly inhomogeneous solution with $s(0) = s_{m2} < s_h(\sigma)$. The value of s_{m2} increases as $\sigma \rightarrow \sigma_c$. At the critical load state, the two solutions collapse and mark a saddle point of V_σ , see the purple line in Fig. 4.11 b). The unloaded state $\sigma = 0$ has to be treated separately as discussed in Kuhn (2013) and Kuhn et al. (2015). For $\sigma = 0$, $s_{m1} = 1$ is the only root of V_σ . Since $s_{m2} \rightarrow 0$ as $\sigma \rightarrow 0$, it is still reasonable to set $s_{m2} = 0$ in this case.

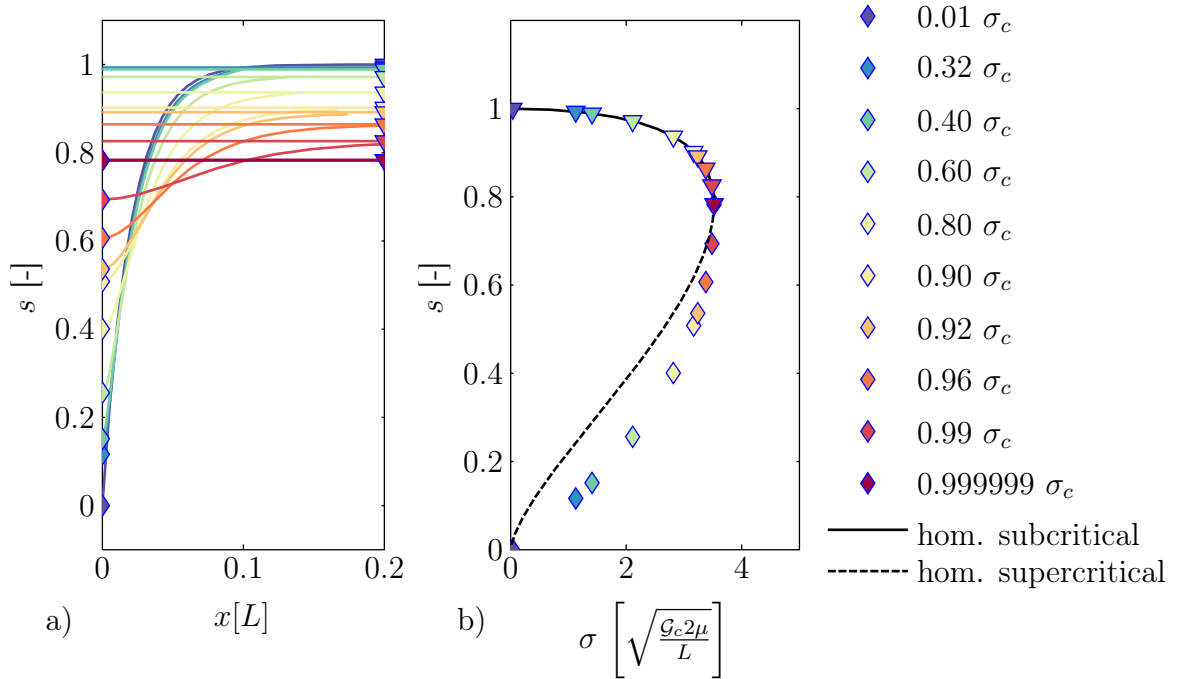


Figure 4.12: a) Homogeneous solution s_h and spatially inhomogeneous solution with minimal value of s_{m2} . b) Homogeneous solution σ_h vs. s_h and inhomogeneous solution σ vs. s_m . The length-scale parameter is set to $l = 0.01L$.

Now that the minimal value s_{m2} is known, the conservation law in the form (4.99) can be integrated to obtain the complete spatial distribution of the phase field as the inverse function of

$$x(s) = \text{sgn}(x) \int_{s_{m2}}^s \sqrt{\frac{2l^2}{V_{\text{eff}}(s_{m2}) - V_{\text{eff}}(\tilde{s})}} d\tilde{s}. \quad (4.101)$$

Figure 4.12 a) displays the computed inhomogeneous fracture fields for $x > 0$ as well as the associated spatially homogeneous solution. The roots of V_σ corresponding to the homogeneous solution s_{m1} (triangles) and the minimum value of the inhomogeneous solution s_{m2} (diamonds) are also marked in the figure. The fully broken solution can be found by substituting $\sigma = 0$ into (4.82) and solving the resulting problem

$$2ls_{,xx} + \frac{1-s}{2l} = 0 \quad (4.102)$$

subject to the constraints $s(0) = s_m(\sigma = 0) = 0$ and $s'(\pm L) = 0$. For $l \ll L$, the solution is

$$s(x) = 1 - \exp\left(-\frac{|x|}{2l}\right). \quad (4.103)$$

Suppose, that an undamaged bar $s = 1$ is subjected to an increasing displacement load u_0 . The corresponding solutions of the phase field are displayed in Fig. 4.12 a) for the respective stress level. Initially, the stress is subcritical and since the bar is undamaged the correct solution is the homogeneous solution. With increasing load, the constant level s_h will drop slightly as can be observed in Fig. 4.12 a). At a strain just above the maximum strain load ε_c , the homogeneous solution is unstable and the spatially inhomogeneous solution at the corresponding stress level becomes the correct solution. Thus, the phase field is now inhomogeneous with a minimum at $x = 0$, where the crack is assumed to appear. Simultaneously, the fracture field away from the localization point recovers and in the fully fractured state it is $s(\pm L) = 1$. The transition from the homogeneous solution is also displayed in Fig. 4.12 b). The solid black line represents the subcritical σ - s -relation which is given by the homogeneous solution. The triangles representing s_{m1} perfectly match the graph in this part. In the vicinity of the critical stress load, the homogeneous solution is unstable and transitions to the inhomogeneous solution displayed in Fig. 4.10. The dashed black line indicates the unattainable supercritical homogeneous solution. The diamonds mark the minimal value s_{m2} at the given load. As the displacement load increases, the stress level and s_{m2} decrease more and more until eventually the fully broken solution is obtained. As mentioned in Kuhn et al. (2015), this analysis shows that the nucleation of fracture in originally undamaged material corresponds to a localization of the fracture field, which initiates close to the maximum stress response σ_c of the spatially homogeneous solution. This observation justifies the interpretation of σ_c as the fracture stress of the phase field model.

Finite Element Simulation of Fracturing of a 1D bar

In order to study how the semi-analytical considerations presented in this section relate to the behaviour of the model in numerical simulations, finite element simulations of the 1D bar problem are performed. The finite element scheme for the dynamic problem is described in Appendix B. For the present example, however, a quasi-static formulation is applied, where the phase field evolution equation is complemented by a viscous term as advocated in Kuhn (2013), see (B.74). As also proposed in Kuhn (2013), an implicit Euler scheme is used for time integration and linear finite elements are used for spatial discretization. Furthermore, the original formulation of the strain energy density (4.8) is employed since compressive mechanical states do not occur. The setup, is the same as depicted in Fig. 4.7, where the regular mesh consists of 200 elements. The load is applied through a linearly increasing displacement load $u^*(t) = u_0 \cdot t$. The mobility parameter for the viscous

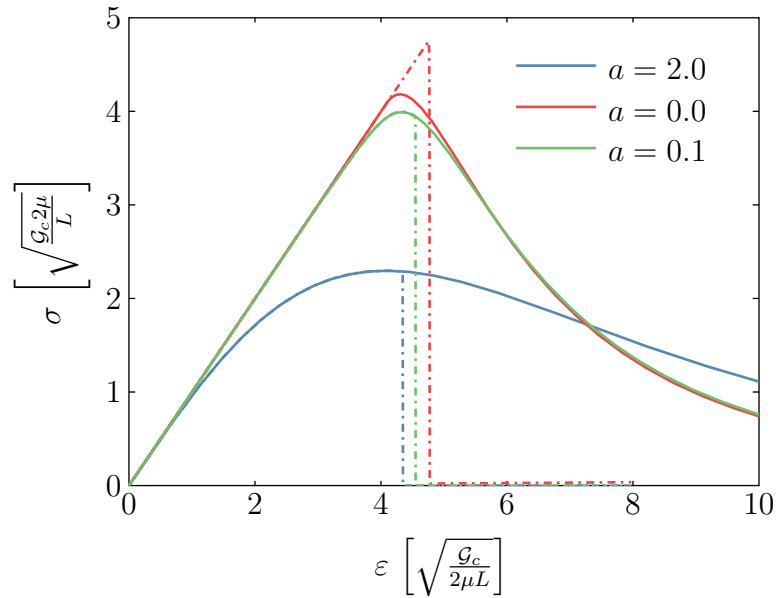


Figure 4.13: Stress strain relation of the 1D bar example for different choices of the degradation function. Homogeneous solution (solid lines) and finite element simulations (dashed-dotted lines). The length-scale parameter is set to $l = 0.01L$.

regularization is set to

$$M = 2 \cdot 10^5 u_0 \sqrt{\frac{2\mu L}{\mathcal{G}_c^3}}. \quad (4.104)$$

Crack growth is triggered to happen at $x = 0$ by reducing the fracture toughness of the center element by 0.01%.

Figure 4.13 shows the stress-strain graphs for the quadratic case $a = 2$ as well as for $a = 0.1$ and $a = 0$. In all simulations the stress increases to a critical value at which the homogeneous solution becomes unstable, the phase field localizes, and a crack forms abruptly which eventually causes the stress to drop to zero. In the quadratic case this happens just above the critical strain rate ε_c as expected. Up to ε_c , the simulation perfectly matches the analytic prediction, i.e. the homogeneous solution. However, an unwanted strongly nonlinear stress-strain relation can be observed for $a = 2$. The constitutive behaviour matches brittle material behaviour a lot better for $a = 0$. Nonetheless, the solution deviates from the analytical predictions and significantly overshoots the predicted maximum value. The reason for this is that the two solution branches of $s_{h,a=0}$ are hard to distinguish energetically at a load of $\varepsilon_0 = \tilde{\varepsilon}_0$ as mentioned before, see also Fig. 4.9. Furthermore, the solution needs to switch from the $s_h = 1$ branch to the branch given by (4.89) at $\tilde{\varepsilon}$, cf. (4.91). Thus, for a numerical scheme, it is very difficult to figure out

the correct solution. Consequently, the switch to the energy minimizing second branch at $\tilde{\varepsilon}$ is not predicted correctly by the finite element simulations but it is delayed. In Kuhn et al. (2015) a numerical perturbation of the fields in the first Newton iteration of each time step has been implemented to trigger a switch from the branch $s_h = 1$ to the branch $s_h < 1$ at $\varepsilon_0 = \tilde{\varepsilon}$. However, a small deviation from the correct solution could not be prevented. Hence, the effective material strength can hardly be estimated by σ_c , since the critical stress level also depends on the implementation and the numerical algorithm. The degradation function with $a = 0.1$ realizes the strong points of both previous formulations, and consequently justifies the fourth constraint in (4.4). Here, the material response is indeed practically linear up to a point very close to the maximum stress response and the numerical solution matches the analytical predictions perfectly. This is due to the fact that only one of the two possible branches of the solution is admissible for all applied displacements, i.e. a switch to another branch of the solution is unnecessary. Furthermore, the value of the phase field as well as the slope of the total energy differ for both branches at $\tilde{\varepsilon}$. Thus, the fracture behaviour that is obtained in simulations can be predicted by the analytic results and a strict upper limit of the bearable stress is given by σ_c as $a \rightarrow 0$. An argument justifying the quadratic formulation is that regions, where the phase field is distinctly different from one, usually only appear in limited parts of the considered body, e.g. close to crack or at stress concentrations, and do not significantly affect the overall response of the structure. A numerical example, where the effect of the degradation function on the global behaviour of a more complicated structure can be found in Section 6.16.

4.6.2 Configurational Forces

The energetic point of view of material changes, see Sections 3.6 and 4.2, links the concept of configurational forces to phase field models for fracture. Indeed, this connection has been investigated in Kuhn and Müller (2010b), Kuhn (2013) and Hakim and Karma (2009) for the quasi-static case. For the quasi-static situation, it has been shown that the configurational force components acting on a crack tip are related to well-known quantities of fracture mechanics such as the path-independent \mathcal{J} -integral, see Rice (1968), and the fracture resistance \mathcal{G}_c . In contrast to numerical strategies that rely on configurational forces in order to model crack propagation such as in Miehe and Gürses (2007) and Özenç et al. (2016), the evaluation of the configurational forces is not a necessity in phase field fracture models but configurational forces should rather be understood as a post-processing tool that enhances the understanding of the simulations. In this Section, the idea to consider configurational forces for a phase field fracture model from Kuhn and Müller (2010b) is extended to the dynamic case by following the approach

presented in Schlüter et al. (2017). A slightly different way to derive a meaningful configurational force balance for a dynamic phase field model for brittle fracture is outlined in Schlüter et al. (2016a).

Crack growth corresponds to a translation of the crack tip with respect to its coordinates \mathbf{z} in the reference configuration. As explained in Kienzler and Herrmann (2000), a configurational force balance law that captures the energy change due to a translation of the considered defect, in our case the crack tip, can be found by taking the gradient of the Lagrangian density. In the phase field model, the evolution of the phase field is governed by the variation of the Lagrangian density with respect to \mathbf{u} and s keeping θ fixed, see (4.13). Crack growth is determined by the formulation of the Lagrangian density but also by the irreversibility constraint (4.31). Accordingly, it follows that a configurational force balance law derived by taking the gradient of the Lagrangian density without incorporating the irreversibility constraint does only describe the fracture process as long as the load is high enough to sustain the cracks. In this situation the irreversibility constraint does not play a role. Nonetheless, the ‘gradient of the Lagrangian approach’ is still followed to derive a configurational force balance in this work, but the neglected irreversibility condition is discussed as part of the interpretation of the computational results in Section 6.4. In order to determine the energetic driving force on a particular crack tip, the Lagrangian density \mathcal{L} is considered to additionally be a function of the position of that crack tip \mathbf{z} and the gradient

$$-\nabla\mathcal{L}(\dot{\mathbf{u}}, \boldsymbol{\varepsilon}, s, \nabla s, \mathbf{z}) = \left(\frac{\partial\psi}{\partial s} s_{,k} + \frac{\partial\psi}{\partial s_{,i}} s_{,ik} + \frac{\partial\psi}{\partial \varepsilon_{ij}} \varepsilon_{ij,k} - \frac{\partial k}{\partial \dot{u}_i} \dot{u}_{i,k} - \frac{\partial \mathcal{L}}{\partial z_i} z_{i,k} \right) \mathbf{e}_k \quad (4.105)$$

is computed, neglecting the temperature field. Making use of the identities

$$\frac{\partial\psi}{\partial s_{,i}} s_{,ik} = \left(s_{,k} \frac{\partial\psi}{\partial s_{,i}} \right)_{,i} - \left(\frac{\partial\psi}{\partial s_{,i}} \right)_{,i} s_{,k} \quad (4.106)$$

and

$$\frac{\partial\psi}{\partial \varepsilon_{ij}} \varepsilon_{ij,k} = (u_{j,k} \sigma_{ji})_{,i} - u_{i,k} \sigma_{ij,j} \quad (4.107)$$

the components of equation (4.105) can be rewritten as

$$\begin{aligned} -\mathcal{L}_{,k} &= \frac{\partial\psi}{\partial s} s_{,k} + \left(s_{,k} \frac{\partial\psi}{\partial s_{,i}} \right)_{,i} - \left(\frac{\partial\psi}{\partial s_{,i}} \right)_{,i} s_{,k} \\ &+ (u_{j,k} \sigma_{ji})_{,i} - u_{i,k} \sigma_{ij,j} - \frac{\partial k}{\partial \dot{u}_i} \dot{u}_{i,k} - \frac{\partial \mathcal{L}}{\partial z_i} z_{i,k}. \end{aligned} \quad (4.108)$$

By means of the equation of motion (4.24), the evolution equation (4.26) and the linear momentum

$$\mathbf{p} = \frac{\partial k}{\partial \dot{u}_k} \mathbf{e}_k = \rho \dot{\mathbf{u}} \quad (4.109)$$

the relation

$$-\nabla \mathcal{L} = \left(\left(s_{,k} \frac{\partial \psi}{\partial s_{,i}} + u_{j,k} \sigma_{ji} \right)_{,i} - u_{i,k} \dot{p}_i - p_i \dot{u}_{i,k} - \frac{\partial \mathcal{L}}{\partial z_i} z_{i,k} \right) \mathbf{e}_k \quad (4.110)$$

is obtained, which with

$$-\nabla \mathcal{L} = -(\mathcal{L} \delta_{ki})_{,i} \mathbf{e}_k, \quad \delta_{ij} = \begin{cases} 1 & \text{if } i = j \\ 0 & \text{else} \end{cases} \quad (4.111)$$

can be recast in the form

$$\mathbf{g} = \text{div} \boldsymbol{\Sigma} - \dot{\mathbf{p}}. \quad (4.112)$$

Here, the configurational stress tensor

$$\boldsymbol{\Sigma} = \boldsymbol{\Sigma}^e + \boldsymbol{\Sigma}^s \quad (4.113)$$

consisting of the dynamic Eshelby stress tensor or elastic part of the configurational stress tensor

$$\boldsymbol{\Sigma}^e = ((\psi^e - k) \delta_{ij} - u_{k,i} \sigma_{kj}) \mathbf{e}_i \otimes \mathbf{e}_j, \quad (4.114)$$

and the cohesive configurational stress tensor

$$\boldsymbol{\Sigma}^s = \left(\psi^s \delta_{ij} - s_{,i} \frac{\partial \psi}{\partial s_{,j}} \right) \mathbf{e}_i \otimes \mathbf{e}_j \quad (4.115)$$

has been introduced. The pseudo-momentum

$$\mathbf{p} = -u_{i,k} p_i \mathbf{e}_k = -(\text{grad} \mathbf{u})^T \mathbf{p} \quad (4.116)$$

has already been introduced in (3.47), whereas the quantity

$$\mathbf{g} = -z_{i,k} \frac{\partial \mathcal{L}}{\partial z_i} \mathbf{e}_k \quad (4.117)$$

is the contribution of the state $[\dot{\mathbf{u}}(\mathbf{x}, t), \boldsymbol{\varepsilon}(\mathbf{x}, t), s(\mathbf{x}, t), \nabla s(\mathbf{x}, t)]$ to the energetic driving force that acts on the crack tip \mathbf{z} . Alternatively, \mathbf{g} might be interpreted as a measure of the change of \mathcal{L} at \mathbf{x} due to an infinitesimally small translation

of the crack tip \mathbf{z} . By integration over a subdomain R of Ω , a global form of the configurational force balance

$$\underbrace{\int_R \mathbf{g} \, dV}_{\mathbf{G}_R} = \underbrace{\int_R \operatorname{div} \boldsymbol{\Sigma}^e \, dV}_{\mathbf{G}_R^e} + \underbrace{\int_R \operatorname{div} \boldsymbol{\Sigma}^s \, dV}_{\mathbf{G}_R^s} - \underbrace{\int_R \dot{\mathbf{p}} \, dV}_{-\mathfrak{P}_R}, \quad (4.118)$$

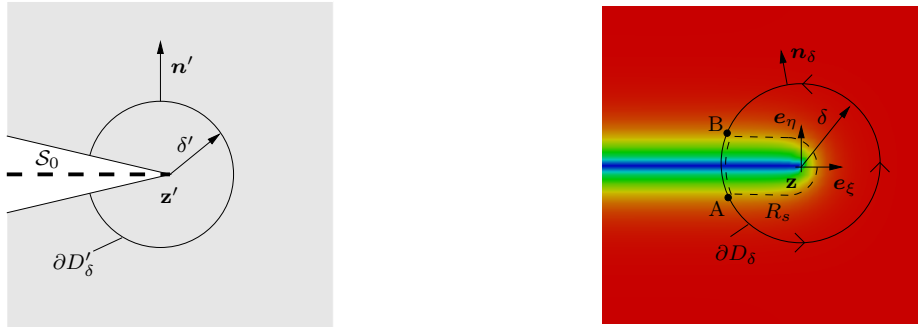
$$\mathbf{G}_R = \mathbf{G}_R^e + \mathbf{G}_R^s + \mathfrak{P}_R$$

is obtained. In contrast to \mathbf{g} , the quantity \mathbf{G}_R represents the configurational force on \mathbf{z} resulting from the states $[\dot{\mathbf{u}}(\mathbf{x}, t), \boldsymbol{\varepsilon}(\mathbf{x}, t), s(\mathbf{x}, t), \nabla s(\mathbf{x}, t)]$ of all particles \mathbf{x} inside R .

In the following the role of the derived configurational force balance as a means to highlight the connection between phase models for dynamic brittle fracture and Griffith's description of brittle fracture in the framework of dynamic linear elastic fracture mechanics (LEFM) is explained. To this end, a LEFM model of the crack tip and the region surrounding it, see Fig. 4.14 a), as well as the corresponding phase field representation, see Fig. 4.14 b), are considered. In order to evaluate the relevant energetic driving forces on a particular crack tip, suitable control volumes should at least contain all particles that constitute the near tip region but no additional crack tip or defect. A disc with radius δ that is centered around the crack tip \mathbf{z}

$$D_\delta(t) = \{\mathbf{x}(t) \in \Omega : \|\mathbf{x}(t) - \mathbf{z}(t)\| \leq \delta\} \quad (4.119)$$

is chosen as a control volume for the phase field problem and a ξ - η -coordinate system is introduced, where \mathbf{e}_ξ is tangential to the crack path at \mathbf{z} . The control volume for the respective LEFM problem, is bounded by the contour $\partial D'_\delta$ and the crack faces as displayed in Fig. 4.14 a). Presume that



a)

b)

Figure 4.14: a) Crack tip region of a problem formulated in the framework of linear elastic fracture mechanics (LEFM) and b) the associated phase field representation of the crack tip region.

A: the boundary conditions at the crack faces are adequately modeled by the constitutive law (4.25).

In that case,

B: the displacements \mathbf{u} in D_δ but outside the subset $R_s \subset D_\delta$ where the phase field is significantly different from $s = 1$ are assumed to be a good approximation of the displacements \mathbf{u}' that are obtained for the otherwise identical problem formulated in the framework of dynamic linear elastic fracture mechanics, see Fig. 4.14 a). The size of R_s depends on the length-scale parameter l which is assumed to be small compared to δ . Consequently, it is also $\partial D_{\delta, A \rightarrow B} \approx \partial D_\delta$.

Assumption B is motivated by the proofs of Γ -convergence for the quasi-static phase field model which establish a link between the global energies and their minimizers obtained in a free-discontinuity model on the one hand and a phase field model on the other hand, cf. Section 4.1. Additionally,

C: it is assumed that the fields in D_δ are smooth enough to allow the gradient and divergence operations.

With $2\nabla k = 2\rho(\text{grad}\dot{\mathbf{u}})^T \dot{\mathbf{u}}$ the identity

$$\begin{aligned} \mathbf{G}_{D_\delta}^e + \mathfrak{P}_{D_\delta} &= \int_{D_\delta} \text{div}((\psi^e + k))\mathbf{1} - (\text{grad}\mathbf{u})^T \boldsymbol{\sigma} \, dV \\ &\quad + \int_{D_\delta} (-\rho(\text{grad}\dot{\mathbf{u}})^T \dot{\mathbf{u}} + \rho(\text{grad}\mathbf{u})^T \ddot{\mathbf{u}}) \, dV \end{aligned} \quad (4.120)$$

is obtained which with the divergence theorem (A.11) yields

$$\begin{aligned} \mathbf{G}_{D_\delta}^e + \mathfrak{P}_{D_\delta} &= \int_{\partial D_\delta} ((\psi^e + k))\mathbf{1} - (\text{grad}\mathbf{u})^T \boldsymbol{\sigma} \, \mathbf{n} \, dA \\ &\quad + \int_{D_\delta} (-\rho(\text{grad}\dot{\mathbf{u}})^T \dot{\mathbf{u}} + \rho(\text{grad}\mathbf{u})^T \ddot{\mathbf{u}}) \, dV. \end{aligned} \quad (4.121)$$

Thus, by means of the assumptions A-C it is

$$\mathbf{G}_{D_\delta}^e + \mathfrak{P}_{D_\delta} \approx \mathbf{G}_{R_{\text{tip}}}^{\mathcal{H}} + \mathfrak{P}_{R_{\text{tip}}}^{\mathcal{H}}, \quad (4.122)$$

cf. (3.54), and eventually with the help of (3.57) a link between the configurational forces introduced above and the dynamic energy release rate as

$$(\mathbf{G}_{D_\delta}^e + \mathfrak{P}_{D_\delta}) \cdot \mathbf{e}_v \approx \mathcal{G} \quad (4.123)$$

is obtained. In order to derive an interpretation of the cohesive configurational stress the procedure described in Kuhn (2013) is followed. Firstly, the divergence theorem is applied to the second term on the right-hand side of (4.118), i.e.

$$\mathbf{G}_{D_\delta}^s = \int_{D_\delta} \operatorname{div} \boldsymbol{\Sigma}^s \, dV = \int_{\partial D_\delta} \boldsymbol{\Sigma}^s \mathbf{n}_\delta \, dA = \int_{\partial D_{\delta,A \rightarrow B}} \boldsymbol{\Sigma}^s \mathbf{n}_\delta \, dA + \int_{\partial D_{\delta,B \rightarrow A}} \boldsymbol{\Sigma}^s \mathbf{n}_\delta \, dA. \quad (4.124)$$

On the first segment $\boldsymbol{\Sigma}^s|_{\partial D_{\delta,A \rightarrow B}} = \mathbf{0}$ since $s \equiv 1$. If the second segment is sufficiently far away from the crack tip, i.e. assumption B is fulfilled and the crack is straight inside D_δ , it is reasonable to assume that the phase field has the same shape in η -direction as the 1D solution (4.103),

$$s(x_1, x_2)|_{\partial D_{\delta,B \rightarrow A}} = 1 - \exp\left(-\frac{|\eta|}{2l}\right). \quad (4.125)$$

Thus, it is

$$\boldsymbol{\Sigma}^s|_{\partial D_{\delta,B \rightarrow A}} = \begin{pmatrix} \psi^s & 0 \\ 0 & 0 \end{pmatrix} \quad (4.126)$$

with

$$\psi^s = \frac{\mathcal{G}_c}{2l} \exp\left(-\frac{|\eta|}{l}\right). \quad (4.127)$$

Eventually these considerations yield

$$\mathbf{G}_{D_\delta}^s = \int_{\partial D_{\delta,B \rightarrow A}} \boldsymbol{\Sigma}^s \mathbf{n} \, dA = \int_{\partial D_{\delta,B \rightarrow A}} \begin{pmatrix} -\psi^s \\ 0 \end{pmatrix} d\eta = \begin{pmatrix} -\mathcal{G}_c \\ 0 \end{pmatrix} = -\mathcal{G}_c \mathbf{e}_\xi. \quad (4.128)$$

Hence, with (4.123), (4.128), (4.118) and $\mathbf{e}_\xi \approx \mathbf{e}_v$ it is found that the configurational force balance applied to an appropriately small crack tip disc D_δ , in which the crack is approximately straight, in the form

$$\mathbf{G}_{D_\delta} \cdot \mathbf{e}_\xi = (\mathbf{G}_{D_\delta}^e + \mathfrak{B}_{D_\delta} + \mathbf{G}_{D_\delta}^s) \cdot \mathbf{e}_\xi = 0 \quad (4.129)$$

is closely related to the Griffith condition for crack growth (4.130)

$$\mathcal{G} = \mathcal{G}_c. \quad (4.130)$$

The Griffith condition is fulfilled if $\mathbf{G}_{D_\delta} \cdot \mathbf{e}_v = 0$, i.e. the crack driving forces $\mathbf{G}_{D_\delta}^e + \mathfrak{B}_{D_\delta}$ balance the cohesive configurational force $\mathbf{G}_{D_\delta}^s$ in the direction of crack growth.

In order to judge whether the size of the control volume D_δ is chosen large enough to comply with assumption B, a second tip disc control volume R with

radius $\delta_R > \delta$ and a third control volume $R_\delta = R \setminus D_\delta$ that does not include the crack tip, any other crack tip nor the regions dominated by the stress concentrations surrounding them are considered. It is

$$\int_R (\operatorname{div} \Sigma^e - \dot{\mathbf{p}}) \, dV = \int_{R_\delta} (\operatorname{div} \Sigma^e - \dot{\mathbf{p}}) \, dV + \int_{D_\delta} (\operatorname{div} \Sigma^e - \dot{\mathbf{p}}) \, dV. \quad (4.131)$$

The integral $\int_{R_\delta} (\operatorname{div} \Sigma^e - \dot{\mathbf{p}}) \, dV$ represents the crack-extending energetic driving force on \mathbf{z} that results from the states $[\mathbf{u}(\mathbf{x}, t), \boldsymbol{\varepsilon}(\mathbf{x}, t), s(\mathbf{x}, t)]$ of all \mathbf{x} inside R_δ , see (4.118). Since no stress concentration is located in R_δ , it is

$$\left| \int_{R_\delta} (\operatorname{div} \Sigma^e - \dot{\mathbf{p}}) \, dV \right| \ll \left| \int_{D_\delta} (\operatorname{div} \Sigma^e - \dot{\mathbf{p}}) \, dV \right|. \quad (4.132)$$

From (4.131) it follows

$$\mathbf{G}_R^e + \mathfrak{P}_R \approx \mathbf{G}_{D_\delta}^e + \mathfrak{P}_{D_\delta} \quad (4.133)$$

Equation (4.133) implies that the value of the above integral is insensitive to a further increase of the size of the control volume if the crack tip field is sufficiently contained in D_δ . Hence, δ is chosen large enough, if (4.133) is fulfilled for $\delta_R > \delta$.

5 Performance of Numerical Solution Strategies

As mentioned before, an analytical solution of the dynamic phase field fracture problem from Section 4.2 is only available for simplified situations such as the 1D-bar problem discussed in Section 4.6.1. This section presents and discusses a numerical strategy that allows to obtain a solution for more complicated scenarios. The phase field fracture problem is given by a set of coupled partial differential equations, consisting of the equation of motion (4.24), the phase field evolution equation (4.26) and the energy balance (4.30), the constitutive laws (4.25) and (4.29) as well as the boundary conditions (4.9), (4.10) and initial conditions (4.11) which fully governs the fracture process, i.e. the evolution of the phase field, the displacements and the temperature over time. This renders tracking of the crack pathes, as required by other methods, as unnecessary. Consequently, the numerical discretization of this set of equations is straightforward and can be handled with standard finite element methods, see textbooks on the topic like Zienkiewicz and Taylor (2000), Wriggers (2009) and Hughes (2000). Nonetheless, the advantages of the phase field also come with costs. Since the size of the transition zone l in which the phase field varies from broken to unbroken material has to be small relative to the dimensions of the considered body L , a very fine spatial discretization is required, at least locally, to resolve the associated high gradients properly. Furthermore, in dynamic simulations wave propagation needs to be treated adequately and hence reasonable time step sizes are small. This means that the computational effort for dynamic fracture phase field simulations can become relatively high. It is therefore of interest to find solution strategies that allow an efficient numerical treatment of the spatially discretized dynamic phase field fracture problem. In the literature, there are mainly two approaches. The first possibility is to solve the coupled equations simultaneously for the primary fields, i.e. the displacements, the phase field and the temperature. This so-called monolithic strategy promises to find the, up to a predefined tolerance, exact solution at each discrete time step. Here, implicit schemes have to be used and the computational effort per time step is comparatively large, because of the nonlinearity of the coupled system.

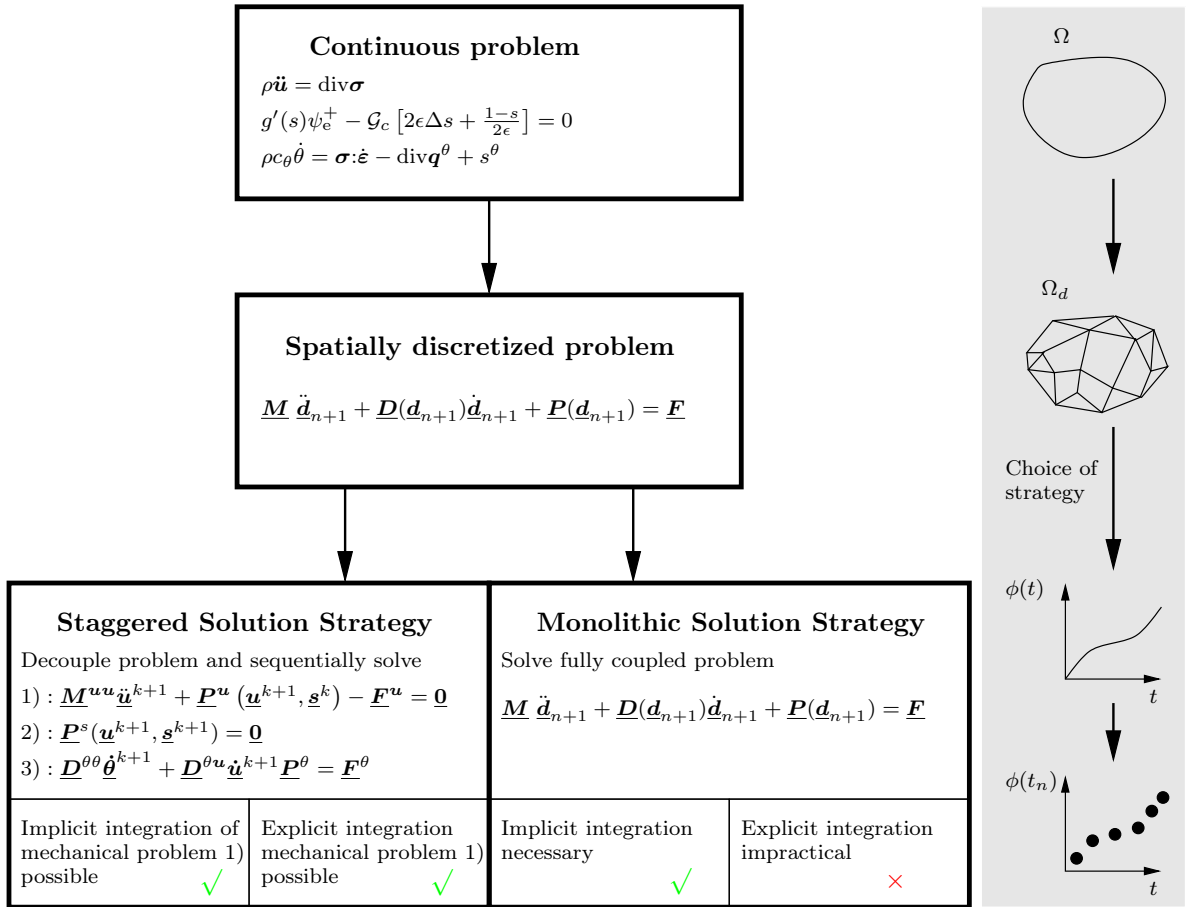


Figure 5.1: Overview of numerical solution strategies for the coupled phase field fracture problem.

Alternatively, staggered solution strategies can be used, as described in e.g. Hofacker and Miehe (2013) and Ambati et al. (2015) for the isothermal case. In these strategies, the problem is decoupled and solved in two steps. First, the equation of motion is solved keeping the phase field fixed and subsequently the evolution equation is solved for the phase field variable fixing the displacements. This way, nonlinearities that come from the coupling of the two fields are removed and consequently the subproblems can be treated more efficiently. However, the substeps of the staggered algorithm may have to be repeated several times in order to obtain convergence, i.e. a solution that is insensitive to further so-called ‘staggered iterations’. A criterion to judge convergence of the staggered algorithm in this sense is proposed in Ambati et al. (2015). Nevertheless, it is rather common to perform only one staggered iteration. For such a one-step staggered approach it is necessary to keep the time step comparatively small which might be required

anyway in dynamic simulations. Furthermore, the decoupling allows for efficient explicit time integration of the equation of motion which is not possible in the monolithic case. An overview of the mentioned numerical strategies is displayed in Fig. 5.1, whereas detailed information of the numerical implementation is summarized in appendix B. The presented algorithms are implemented into the finite element code FEAP, c.f. Taylor (2014).

In this chapter, the performance of three different monolithic and three different staggered strategies is analyzed by means of two benchmark problems as originally published in Schlüter et al. (2017). The six numerical solution strategies are investigated for isothermal conditions, i.e. the temperature is considered to be $\theta = \theta_0 \forall \mathbf{x} \in \Omega$ at all times. Furthermore, the SD formulation of the strain energy density (4.47) is employed. The considered strategies are

- S1: a monolithic strategy with a standard Newmark scheme ($\beta = 0.25$, $\gamma = 0.5$) for time integration and automatic time step control,
- S2: a monolithic strategy with a modified Newmark scheme ($\beta = 0.5$, $\gamma = 0.5$) and automatic time step control,
- S3: a monolithic strategy with the Euler scheme for time integration and automatic time step control,
- S4: a staggered strategy with implicit time integration of the equation of motion by the standard Newmark scheme ($\beta = 0.25$, $\gamma = 0.5$),
- S5: a staggered strategy with implicit time integration of the equation of motion by a modified Newmark scheme ($\beta = 0.5$, $\gamma = 0.5$),
- S6: a staggered strategy with explicit time integration of the equation of motion by the central difference scheme.

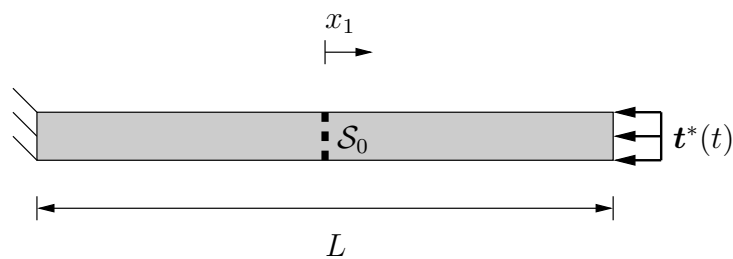


Figure 5.2: 1D-bar with an initial, center crack \mathcal{S}_0 . Fixed at the left boundary and subjected to pressure pulse on the right end.

The first benchmark problem considers a fractured 1D-bar with an initial crack as depicted in Fig. 5.2. The bar is constrained at its left end and subjected to a

pressure pulse at the right end. The governing set of field equation for the 1D-case is given by (4.58). Note that the isothermal case $\theta = \theta_0 = \text{const.}$ is considered and thus a solution of the heat equation is not necessary. The specimen is subjected to a sinusoidal pressure pulse $\mathbf{t}^*(t) = \sigma_0 Y(t) \mathbf{e}_x$ at its right end. The amplitude of the pulse is $\sigma_0 = -1.0 \sqrt{\frac{2\mu\mathcal{G}_c}{L}}$ and

$$Y(t) = \begin{cases} \sin^2\left(2\pi\frac{t}{t_e}\right) & \text{if } 0 \leq t \leq \frac{t_e}{2} \\ 0.0 & \text{if } t \geq \frac{t_e}{2} \end{cases}, \quad (5.1)$$

where $t_e = 0.25\frac{L}{c}$. The degradation function (4.85) with $a = 0.1$ is chosen for the numerical benchmarks presented in this section and the absolute value of the stress pulse is distinctly smaller than the critical stress

$$\sigma_c = \frac{81}{50} \sqrt{\frac{\mathcal{G}_c 2\mu}{15l}} \approx 4.18 \sqrt{\frac{2\mu\mathcal{G}_c}{L}}, \quad (5.2)$$

see (4.85), such that no further fracturing is expected even after reflection of the elastic wave at the boundaries. Before reflection of the original pulse at the left end of the bar, the analytic solution is

$$\sigma_{11}(x_1, t) = \begin{cases} \sigma_0 \sin^2\left(2\pi\frac{\xi}{t_e c}\right) & \text{if } 0 \leq \xi \leq \frac{t_e c}{2} \\ 0.0 & \text{else} \end{cases} \quad (5.3)$$

for $0 \leq t \leq \frac{L}{c}$ with $\xi = x_1 - \frac{L}{2} + ct$. The bar is discretized by 200 homogeneously distributed elements with linear shape functions, i.e. the element size is $h = 0.005L$. The length-scale parameter is $l = 0.01L$. The initial crack is modelled by defining respective initial conditions $s(x_1 = \frac{L}{2}, 0) = 0$ for both nodes of the center element. In this example, no automatic time step control is used for the monolithic schemes (S1, S2, S3) and only one iteration of the staggered schemes (S4, S5, S6) is performed. Time steps are chosen to be the CFL time step $1\Delta t_{cfl}$, cf. (B.93), for all schemes except for S6, the staggered strategy with explicit time integration, for which the time step is set to $0.5\Delta t_{cfl}$ in order to ensure stability. This numerical experiment is suited to judge the numerical dissipation involved in the solution strategies as well as their capability to accurately model the wave speed, because an analytic solution is available for comparison. Furthermore, because of the subcritical load, the focus is on analyzing the efficiency of the various schemes in handling the equation of motion (4.58)₁. Since the time step is relatively small and the phase field is not expected to change very much, the restriction

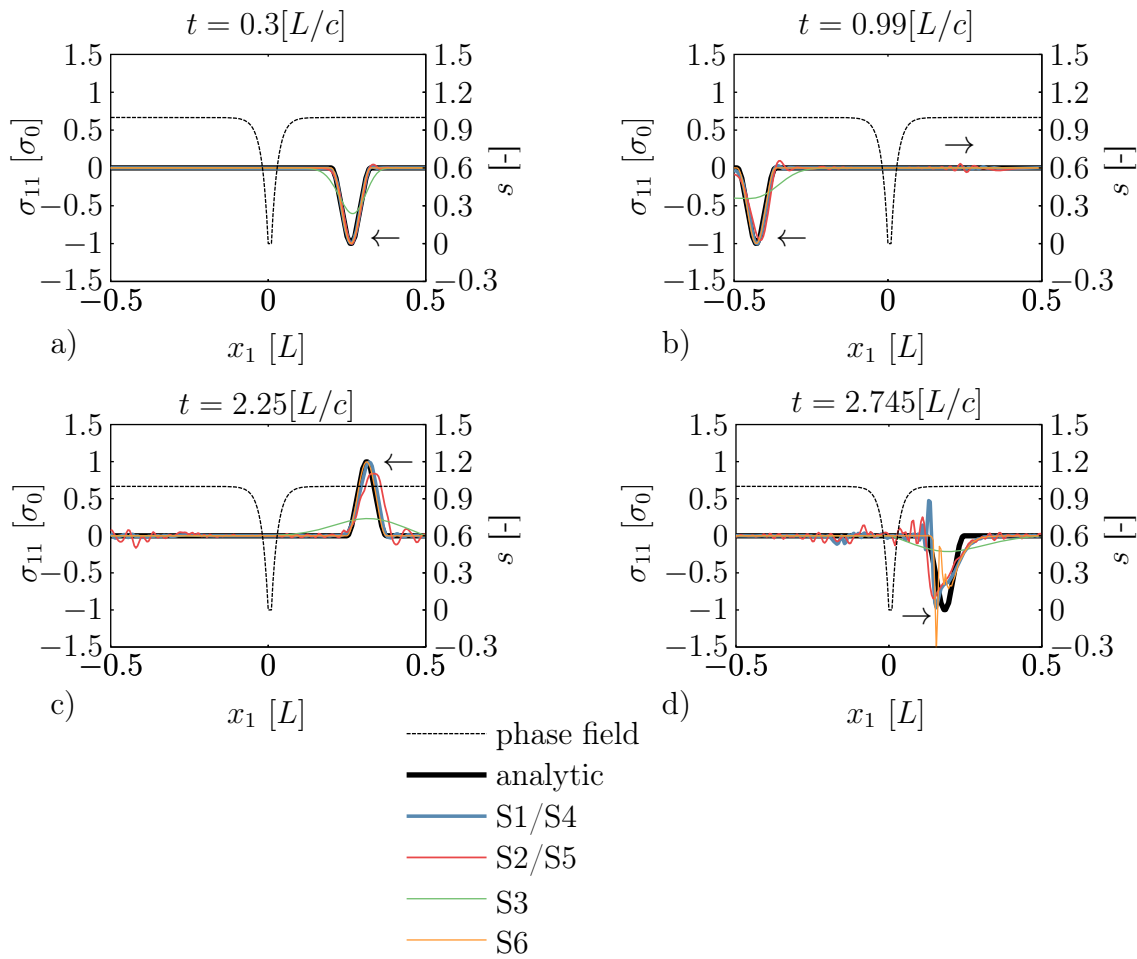


Figure 5.3: Stress σ_{11} at different times. Additionally, the crack field s is displayed as the dash-dotted line.

to only one staggered iteration (S4, S5) and the lack of the automatic time step control (S1, S2, S3) are regarded as acceptable. Of course, larger time steps can in principle be used for all solution strategies with implicit time integration of the equation of motion (S1-S5), which will be considered in a second numerical benchmark.

Fig. 5.3 shows snapshots of σ_{11} at different times. Initially, the numerical solutions all agree reasonably well with the analytic solution except for S3 for which the large amount of numerical dissipation of the Euler scheme becomes obvious, see Fig. 5.3 a). Furthermore, the staggered solution strategies S4, S5 yield virtually identical stress distributions compared to their monolithic counterparts at all times. The reason for this can be found in the fact that the phase field does not evolve at all no matter which solution strategy is chosen. This is to be

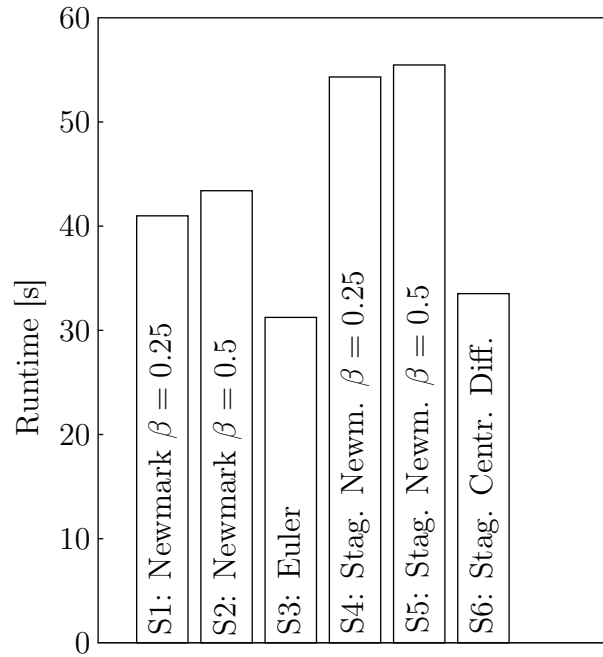


Figure 5.4: Runtimes for the 1D bar problem

expected because of the subcritical loading and it is the reason why S1/S4 and S2/S5, respectively, are not distinguished, i.e. only one graph of the phase field $s(x_1, t)$ is shown in the plots. One can also observe a slight amount of dissipation in the Newmark-strategies that manifests in a smeared out shape of the stress pulse compared to the analytic solution. This effect is larger in S2/S5 than in S1/S4. Furthermore, first oscillations appear for S2/S5 and S1/S4 where again the effect is more pronounced for S2/S5. The stress distribution computed by S6 matches the analytic solution almost perfectly.

Just before the reflection of the initial pulse at the left boundary, further differences become apparent, see Fig. 5.3 b). While the effects of numerical dissipation increase for S3, the strategies S2/S5 also deviate significantly from the analytic solution. The amplitude of the stress pulse decreases notably, but also the peak position does not match the analytic solution anymore. Thus, the wave speed is also not computed correctly. This is not the case for the standard Newmark scheme S1/S4.

Caused by the initial oscillations which result in a partly positive stress, the stress waves are not completely transmitted by the crack but the tensile parts are reflected. Again, S6 almost yields the exact analytical stress distribution. Subsequently, the pulse is reflected at the fixed left end and returns in positive x_1 -direction as a compressive wave. Consequently, there is again only minor interaction between the pulse and the crack in this stage of the simulation.

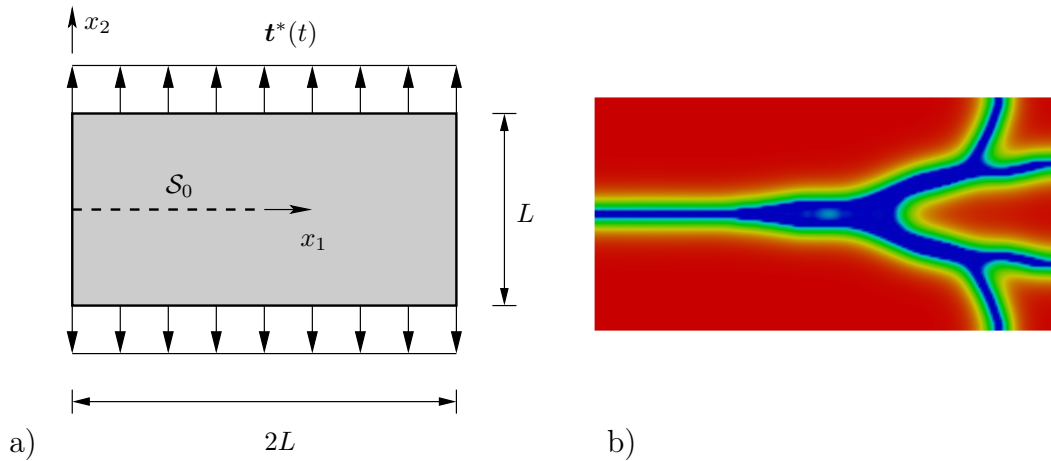


Figure 5.5: a) Setup for the crack branching benchmark: specimen with an initial crack, subjected to a tensile stress and b) plot of the phase field at $t = 6.0\Delta t_{cfl}$ computed by S6.

After the reflection of the pulse at the right end of the bar takes place, see Fig. 5.3 c), the differences between the various scheme become more obvious, but have the same trends. Now, the main pulse is positive, i.e. a tensile stress is prevalent. Thus, the wave will be reflected at the crack. Up to this point, only S2/S5 display significant oscillations. The strategies S6 and S1/S4 show no or minor oscillations respectively, as well as no notable decrease of the amplitude.

Nonetheless, significant oscillations can be observed for all strategies except S3 after reflection of the tensile pulse at the crack, see Fig. 5.3 d). Furthermore, the shape of the original pulse is not retained.

Fig. 5.4 shows the runtimes for a simulation of the fractured bar in the time interval $0 \leq t \leq 4.0\frac{L}{c}$ that were obtained on a laptop computer with a 2.3 GHz Intel Core i7 processor. The monolithic schemes S1/S2 perform distinctly better than their staggered counterparts S4/S5. Thus, the algorithmic decoupling of the equation of motion and the phase field evolution equation does not hold any advantages for the implicit schemes in this example. This may be explained by the fact that, due to the subcritical load, the solution of the phase field equation is stationary and hence a strong coupling of the phase field equation to the displacements does not exist.

Nonetheless, the staggered algorithm performs significantly better if explicit time integration of the equation of motion is employed (S6). Although twice the number of time steps is required for S6, it outperforms all other strategies except the monolithic Euler strategy S3. In light of the shortcomings of S3 mentioned above and the close match between S6 and the analytic solution in the first stages of the simulation, the performance of S6, which has to be attributed to the efficiency

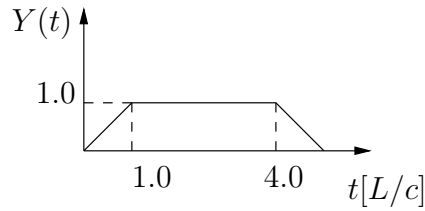


Figure 5.6: Temporal distribution of the applied load $Y(t)$.

of the central difference scheme in solving the equation of motion, is even more impressive.

The second benchmark problem considers a tension loaded specimen with an initial crack as displayed in Fig. 5.5 a). Unlike in the first problem, the load is large enough to cause crack growth. The final crack pattern computed by S6 with $\Delta t = 0.95\Delta t_{cfl}$ is displayed in Fig. 5.5 b). This benchmark allows to evaluate the performance of the different solution strategies in a more complex scenario. Plane strain conditions are assumed, i.e. the displacements have the form $\mathbf{u} = u_1(x_1, x_2)\mathbf{e}_1 + u_2(x_1, x_2)\mathbf{e}_2$. The Lamé parameters have identical values, i.e. $\lambda = \mu$. An initial crack is defined, by specifying appropriate initial conditions $s_0(\mathbf{x}_{\text{crack}}, 0) = 0$. The body is again loaded by a traction boundary condition $\mathbf{t}^* = \sigma_0 Y(t)\mathbf{e}_2$, with $\sigma_0 = 2.0\sqrt{2\mu\mathcal{G}_c/L}$ at the upper boundary and $\sigma_0 = -2.0\sqrt{2\mu\mathcal{G}_c/L}$ at the lower boundary and

$$Y(t) = \begin{cases} v_0 \cdot t & \text{if } 0 \leq t \leq 1.0\frac{L}{c}, \\ 1.0 & \text{if } 1.0\frac{L}{c} \leq t \leq 4.0\frac{L}{c}, \\ 1.0 - v_0 \cdot t & \text{if } 4.0\frac{L}{c} \leq t \leq 5.0\frac{L}{c}, \\ 0.0 & \text{if } 5.0\frac{L}{c} \leq t, \end{cases} \quad (5.4)$$

where $v_0 = 1.0\frac{c}{L}$ and $c = \sqrt{\frac{2\mu}{\rho}}$, see also Fig. 5.6. The domain is spatially discretized by a regular mesh of 200×100 quadrilateral finite elements with bilinear shape functions, i.e. the element edge length is $h = 0.01L$. The length-scale parameter is chosen to be $l = 0.02L$. In this numerical benchmark, use is made of the automatic time step control mentioned above (S1, S2, S3) and the staggered convergence criterion (B.78) is employed for S4 and S5. The maximum number of staggered iterations is set to $k_{max} = 200$. The initial and maximum time step sizes for the monolithic solution strategies (S1, S2, S3) are varied from $1\Delta t_{cfl}$ to $40\Delta t_{cfl}$ but the time step can of course be decreased by the automatic time step control. For the implicit staggered strategies (S4, S5) the fixed time step is varied from $1\Delta t_{cfl}$ to $40\Delta t_{cfl}$, whereas for S6 time steps in the range $0.2\Delta t_{cfl}$ to $1.0\Delta t_{cfl}$ are chosen.

Convergence with respect to the time step size is obtained when the solution is insensitive to a further decrease of the time step.

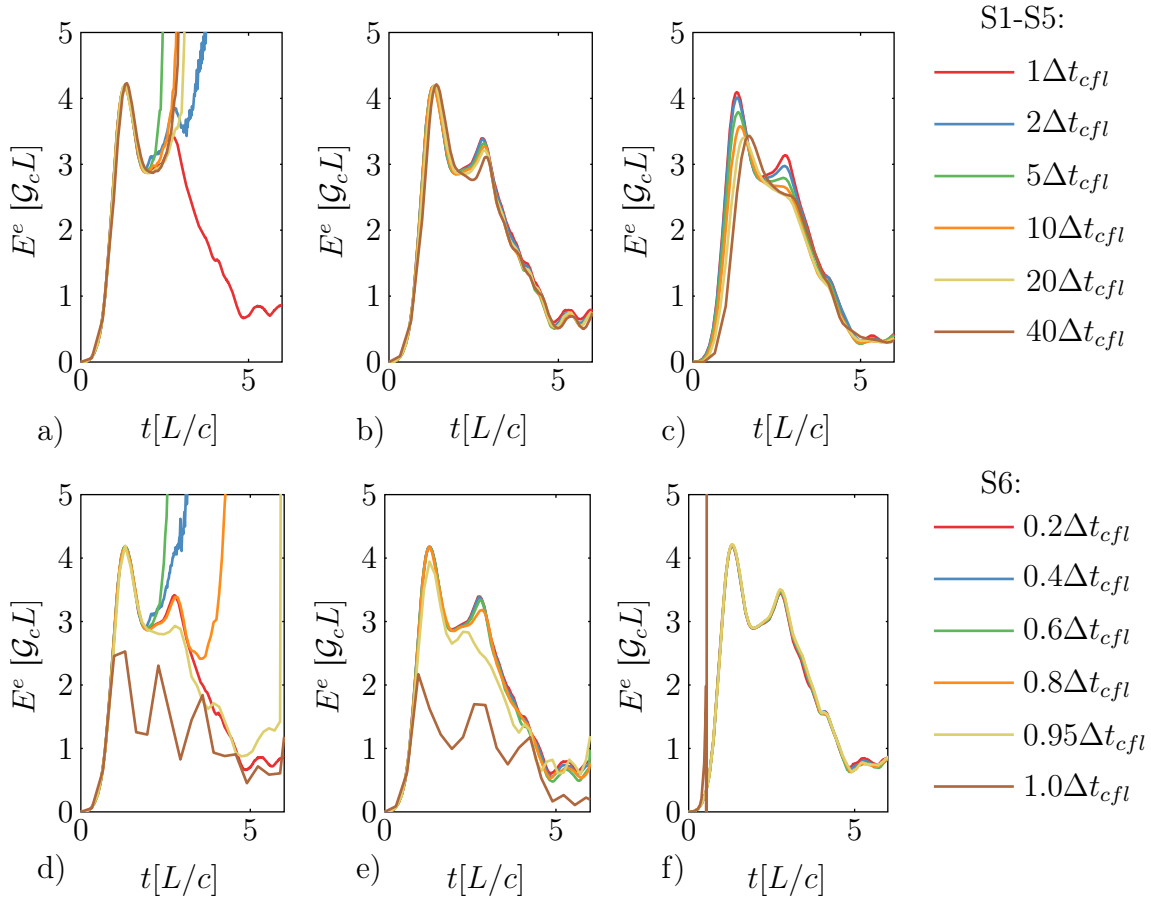


Figure 5.7: Time step convergence study for the different schemes: plots of the global elastic energy in dependence of the specified time step limit a): S1, b): S2, and c): S3) and fixed time step d): S4, e): S5, and f): S6).

Fig. 5.7 shows the elastic energy $E^e = \int_{\Omega} \psi^e dV$, computed by the different solution strategies. The scheme S1 fails to converge for times larger than $t \approx 2.7 \dots 3.5 \frac{L}{c}$ except for the smallest time step limit $1\Delta t_{cfl}$, see Fig. 5.7 a). The elastic energy increases significantly for the computations that do not converge. Thus, only a maximum time step of $1\Delta t_{cfl}$ produces a meaningful result if S1 is used. The monolithic solution strategy with a modified Newmark scheme (S2) is less sensitive to the choice of the upper bound of the time step, see Fig. 5.7 b). All time step limits yield useful results. Nevertheless, there are minor differences, such that for our purposes simulations with a time step limit of $5\Delta t_{cfl}$ or smaller are considered as converged. The remaining monolithic solution strategy S3 only yields a converged

solution for the smallest time step limit due to the severe numerical dissipation of the Euler scheme. In contrast to S1, however, the simulations are in reasonable agreement with the converged solution, quantitatively and qualitatively, see Fig. 5.7 c).

The staggered strategies with implicit time integration S4 and S5 show similar behaviour as their monolithic counterparts, see Fig. 5.7 d) and e). S4 yields reasonable results only for the smallest time step and again the strategy with the modified Newmark scheme for time integration S5 allows to use larger time steps. If S5 is chosen, useful results are obtained for time steps $\Delta t \leq 5\Delta t_{cfl}$. The staggered scheme with explicit time integration of the equation of motion S6 yields converged results for all chosen time step sizes except for $1.0\Delta t_{cfl}$, see Fig. 5.7 f). Thus, in this example, the maximum admissible time step for S6 is $0.95\Delta t_{cfl}$.

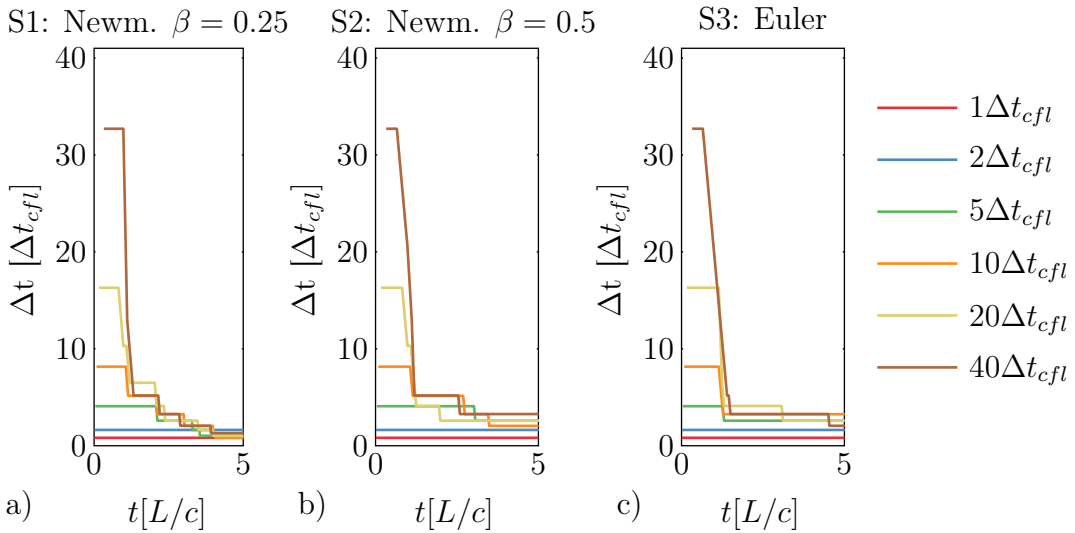


Figure 5.8: Actual time step sizes chosen by the automatic time step control for the strategies a) S1, b) S2, and c) S3.

Fig. 5.8 displays the actual time step chosen by the automatic time step control of the three monolithic solution strategies S1-S3. Initially, the time step is constant and has the value of the prescribed maximum admissible time step size. Just as the crack starts to grow the time step size is reduced step-wise and by a significant amount in all schemes. Exceptions to this are the two smallest time step limits $1\Delta t_{cfl}$ and $2\Delta t_{cfl}$ for which the time step is kept constant by the control algorithm throughout the whole course of the simulation. Eventually, none of the strategies allows for an actual time step larger than $5\Delta t_{cfl}$ in the later stages of the numerical experiment. Recall, that we considered the simulation with a time step limit of $10\Delta t_{cfl}$ to be converged for S2. Interestingly, a final time step size of $\approx 3\Delta t_{cfl}$ seems to be sufficient for S2, see the yellow line in Fig. 5.8 b). Nevertheless, if S1 is

employed, an even smaller time step $2\Delta t_{cfl}$ fails to produce a converged solution, see the red lines in Fig. 5.8 a) and Fig. 5.7 a).

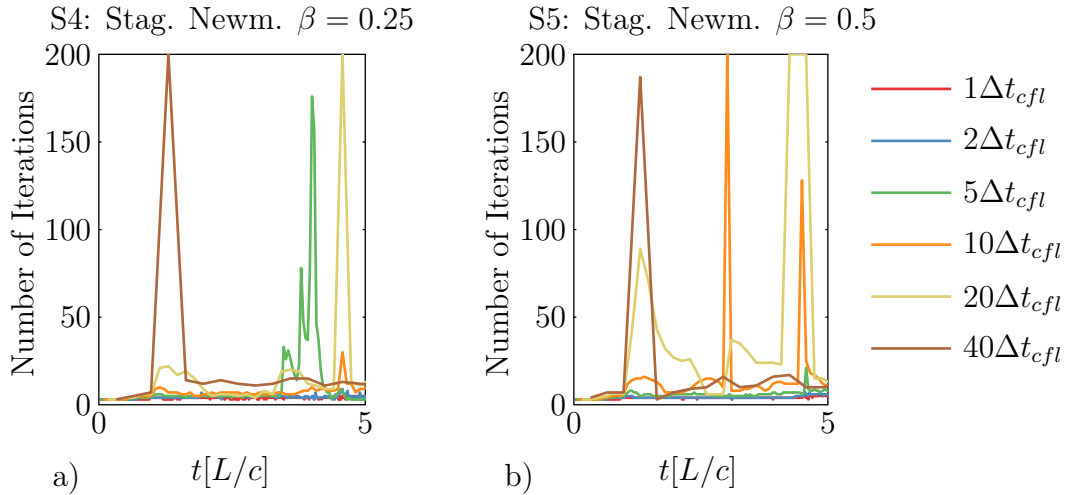


Figure 5.9: Number of iterations of the staggered algorithm for the strategies a) S4 and b) S5.

Fig. 5.9 displays the number of iterations needed for the different strategies to converge for S4 and S5. Since the maximum number of staggered iterations is set to $k_{\max} = 200$, the staggered algorithm is assumed to have not converged for all computations reaching this limit. For S4, this is the case for the largest two time steps $20\Delta t_{cfl}$ and $40\Delta t_{cfl}$, see Fig. 5.9 a). Intriguingly, the computation with the largest time step does not fail to converge for S5, see Fig. 5.9 b), but the simulations with $10\Delta t_{cfl}$ and $20\Delta t_{cfl}$ do. However, for the time step sizes $1\Delta t_{cfl}$ (S4) and $5\Delta t_{cfl}$ (S5) which are considered to be converged in the sense of an insensitivity of the solution to a further decrease of the time step size, the staggered algorithm also converges. The average, maximum and total number of iterations of the staggered algorithm for these two cases are summarized in Table 5.1. S5 needs a larger number of iterations in order to converge but allows for a larger time step as well. Thus, the total number of iterations is significantly smaller for S5.

Table 5.1: Quantitative analysis of the staggered strategies S4 and S5.

strategy, Δt	av. stag. it.	max. stag. it.	sum stag. it
S4, $1\Delta t_{cfl}$	3.77	6	2769
S5, $5\Delta t_{cfl}$	6.1	21	890

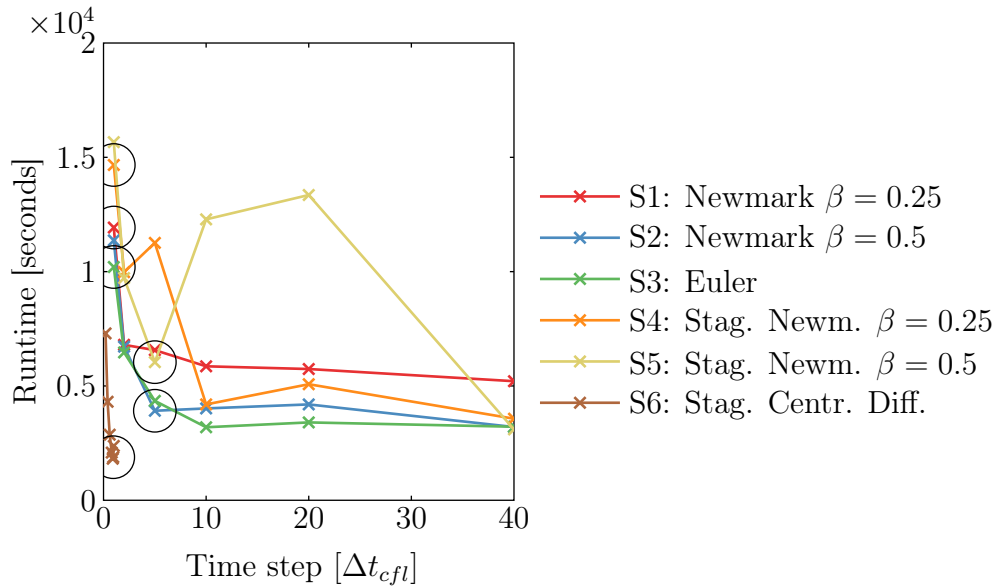


Figure 5.10: Runtimes of the different schemes for the second benchmark versus the prescribed time step limit (S1, S2, S3) and fixed time step (S4, S5, S6), respectively.

Fig. 5.10 displays the obtained runtime of the different strategies versus the prescribed time step (S4, S5, S6), or time step limit (S1, S2, S3), respectively. The runtime of the largest time step that yields a converged solution, in the sense that the solution is insensitive to a further decrease of the time step, is marked by a black circle. As in the previous benchmark, the performance of S6 is remarkable. Although the time step is much smaller than for the other strategies, the total runtime is around half the value of the next best performing scheme, i.e. S2.

Further insight can be gained by the quantitative analysis presented in Table 5.2 which shows the average and maximum number of residual and tangent computations per time step as well as their total number. These operations together with the solution of the linear systems of equations that appear in every Newton iteration - their number is the same as the number of tangent computations - determine the computational effort and thus the runtime. Nevertheless, it has to be kept in mind, that the residual computations, tangent computations and solving operations for the staggered algorithms are performed for the relatively small decoupled subproblems, whereas the same operations in the monolithic scheme are performed for the full coupled problem and consequently are more computationally expensive. Thus, the number of operations is naturally larger for the staggered algorithm, but this does not necessarily imply that the computational effort is also higher.

Considering only the monolithic schemes S1-S3, it is found that S2 performs best, because of the larger time step that can be chosen. S2 is only outperformed by

the staggered strategy with explicit time integration S6. Interestingly, S6 requires more tangent and residual computations as well as solves of a system of linear equations than S2. However, as mentioned above, these operations are performed for the decoupled evolution equation (B.94), which reduces the computational effort significantly compared to the respective operations for the fully coupled problem (B.84).

Table 5.2: Analysis of the average number per time step, the maximum number per time step, and the sum of residual and tangent computations of the different strategies.

strategy, Δt	av. rs.	mx. rs.	sum rs.	av. tg.	mx. tg.	sum tg.	runtime
S1, $1\Delta t_{cfl}$	4.58	5	2808	4.58	5	2808	$1.19 \cdot 10^4$ s
S2, $5\Delta t_{cfl}$	6.48	9	979	6.48	9	979	$3.92 \cdot 10^3$ s
S3, $1\Delta t_{cfl}$	4.38	6	2685	4.38	6	2685	$1.02 \cdot 10^4$ s
S4, $1\Delta t_{cfl}$	24.86	37	15242	21.13	31	12954	$1.47 \cdot 10^4$ s
S5, $5\Delta t_{cfl}$	48.88	176	6012	42.11	155	5303	$6.04 \cdot 10^3$ s
S6, $0.9\Delta t_{cfl}$	4.90	7	3162	3.90	6	2517	$1.88 \cdot 10^3$ s

6 Simulations of Dynamic Brittle Fracture

A number of numerical experiments is discussed in this chapter in order to improve the understanding of the present phase field model and to illustrate its capabilities to reproduce complex features of dynamic fracturing. The finite element implementation described in Appendix B is used to solve the initial boundary value problem from Section 4.2 numerically. Furthermore, the monolithic solution strategy with implicit time integration by a modified Newmark scheme, i.e. the strategy S2 from Section 5, is chosen. All subsequent 2D examples assume plane strain conditions. Unless otherwise specified, the maximal allowable time step is set to $\Delta t = 2\Delta t_{cfl}$.

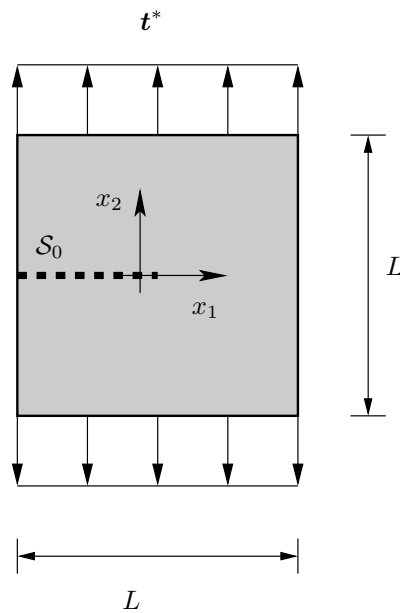


Figure 6.1: Quadratic specimen with an initial crack of length $L/2$ subjected to uniaxial traction load.

6.1 Stationary Cracks and the Effect of the Tension-Compression Asymmetry Formulations

At first, only stationary cracks are studied. This means that the phase field evolution in the simulations is negligible in a way that already existing cracks do not propagate and no new cracks nucleate inside undamaged material. The analysis of such a scenario reveals and confirms interesting features of the asymmetry formulations from Section 4.4.

6.1.1 Quasi-Static Load

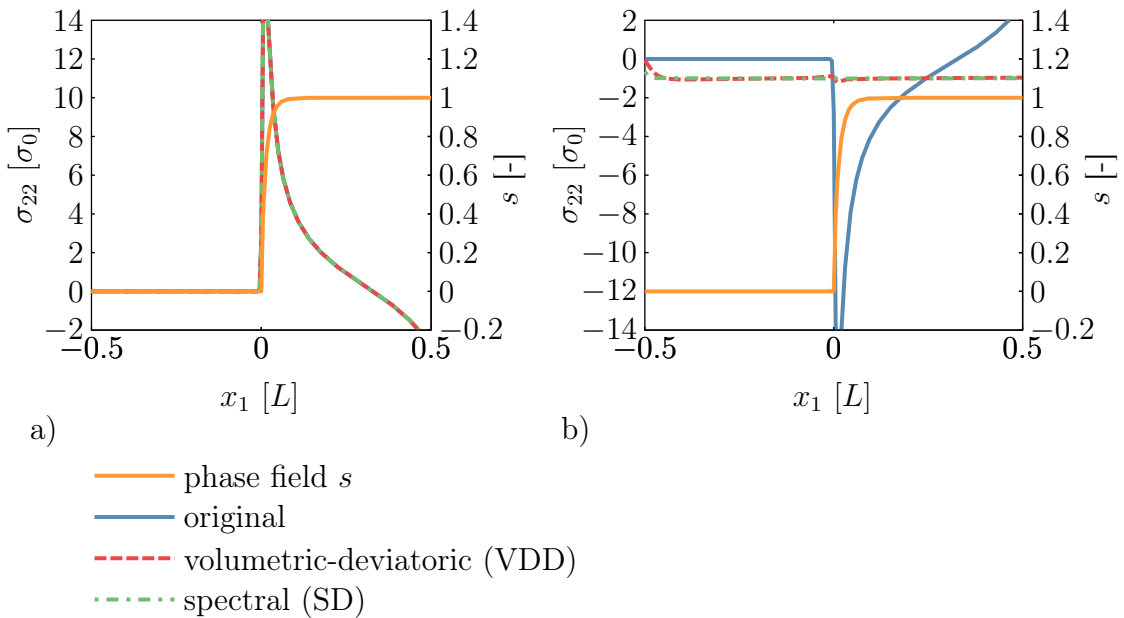


Figure 6.2: Stress $\sigma_{22}(x_2 = 0)$ and phase field $s(x_2 = 0)$ for a) tensile load $\sigma_0 > 0$ and b) compressive load $\sigma_0 < 0$. The crack is modelled by specifying initial conditions $s = 0$ at two vertically successive rows of nodes. The parameter of the degradation function is set to $a = 0.1$.

Consider a quadratic specimen as depicted in Fig. 6.1. The body is subjected to an uniaxial load $\mathbf{t}^* = \pm\sigma_0\mathbf{e}_2$, $\sigma_0 = \frac{1}{10}\sqrt{2\mu\mathcal{G}_c/L}$. In this example, inertial effects are neglected meaning $\rho = 0$ and the Lamé parameters have an identical value, $\lambda = \mu$. The load is chosen small enough so that the phase field is stationary with respect to time. The body is spatially discretized by a regular mesh of 200×200 quadrilateral finite elements with bilinear shape functions resulting in an element edge length of $h = 0.005L$. The length-scale parameter is $l = 0.01L$. The initial crack is modelled

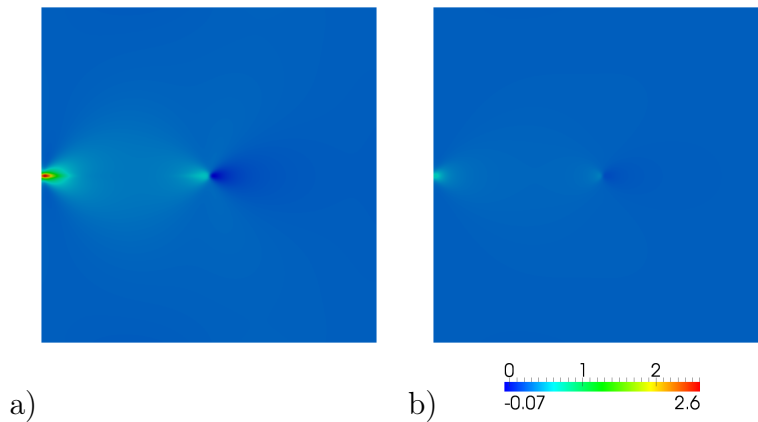


Figure 6.3: Contour plot of the volume dilatation $\varepsilon_1 + \varepsilon_2 = \varepsilon_V \left[\sqrt{\mathcal{G}_c/2\mu L} \right]$ a) for the volumetric-deviatoric formulation of the strain energy density and b) the spectrally decomposed formulation of the strain energy density. The crack is modelled by specifying initial conditions $s = 0$ of two vertically successive rows of nodes. The parameter of the degradation function is set to $a = 0.1$.

by prescribing Dirichlet boundary conditions $s(x_1 \leq 0, x_2 = 0) = 0$ for either one row of nodes or two vertically successive rows of nodes. The latter definition of an initial crack causes the phase field to be zero also in the interior of the finite elements – in particular at the integration points – whereas for the former variant this is not the case.

Figure 6.2 displays $\sigma_{22}(x_2 = 0)$ in blue for the original formulation of the strain energy density (4.8), in red for the volumetric-deviatorically decomposed formulation VDD (4.42) and in green for the spectral decomposition SD (4.47). Additionally, the phase field $s(x_2 = 0)$ is depicted in orange.

A ‘two row’ approximation of the crack is chosen and the parameter of the degradation function is set to $a = 0.1$.

It appears in Fig. 6.2 a) that for tension with $\sigma_0 > 0$ all formulations yield virtually identical stress distributions which is in agreement with the considerations made in Section 4.4. A physically sound stress concentration at the crack tip at $x_1 = 0$ can be observed. In a compressive load state $\sigma_0 < 0$, however, the modified formulations constitute a significant improvement over the unphysical behaviour of the original formulation. From a physical point of view, the crack should close causing a uniform stress distribution $\sigma_{22} = \sigma_0 < 0$. This is predicted reasonably well by both modified formulations. The original formulation on the contrary results in an unrealistic stress distribution where no stress is transmitted across the crack and a stress concentration forms at the crack similar to the tensile case.

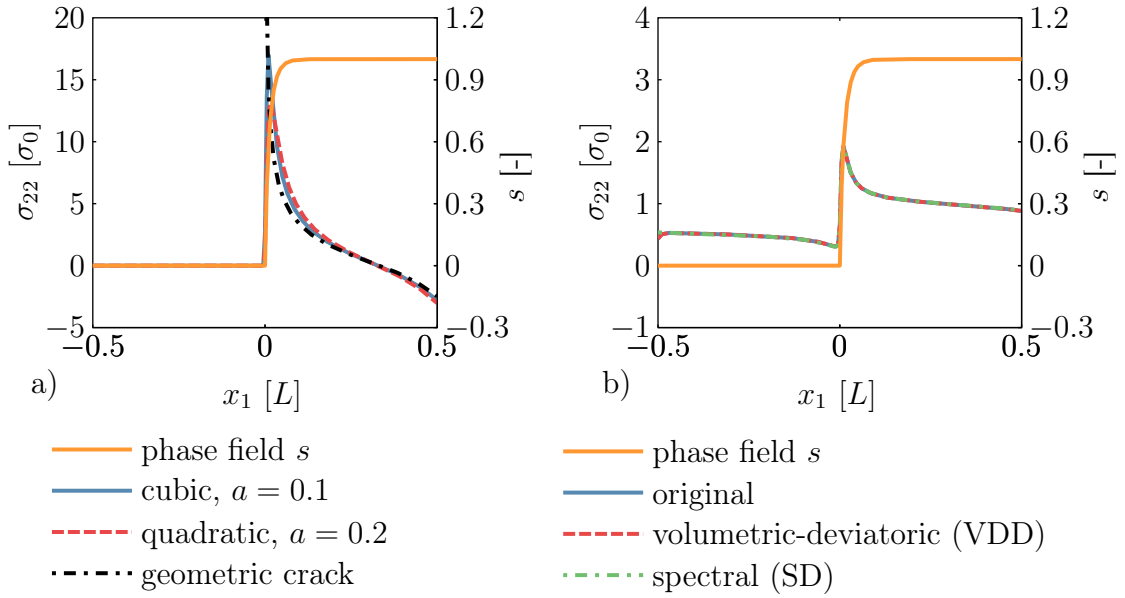


Figure 6.4: a) Stress $\sigma_{22}(x_2 = 0)$ and phase field $s(x_2 = 0)$ for different choices of the degradation function and a geometric representation of the crack. The crack is modelled by specifying initial conditions $s(x_1 \leq 0, x_2 = 0) = 0$ of two vertically successive rows of nodes. b) Stress $\sigma_{22}(x_2 = 0)$ and phase field $s(x_2 = 0)$ for different choices of the degradation function and for a phase field crack that is modelled by specifying initial conditions $s(x_1 \leq 0, x_2 = 0) = 0$ at one row of nodes. The parameter of the degradation function is set to $a = 0.1$.

Interestingly, it can be observed that even for the modified formulations the stress is not perfectly homogeneous in x_1 -direction. At the far left boundary ($x_1 = -0.5L$) crack opening is detected and thus the stress is degraded. This degradation is slightly stronger for the VDD formulation than for SD, cf. the value of σ_{22} at the left boundary $x_1 = -0.5L$ in Fig. 6.2 b). It appears that in both cases the dilatation is indeed positive at $x_1 = -0.5L$ and $x_2 = 0$, see Figs. 6.3 a) and b). This can be explained due to the facts that the deformation in x_1 -direction is not constrained by surrounding material at the boundary and the stiffness is degraded at the crack. Thus, a large positive strain ε_{11} eventually causes the dilatation to be positive and crack closure to be detected incorrectly. As a consequence, the stress is fully degraded in the VDD formulation, see (4.42). The effect is reduced in the SD formulation since the crack closure detection and the degradation of the stress do not completely rely on the sign of the dilatation but also on the sign of the principal strains that can be negative at the far left boundary.

Figure 6.4 a) compares the stress distributions obtained from simulations using a phase field approximation of the crack to the stress distribution computed for a geometric representation of the crack under tensile loading conditions. The

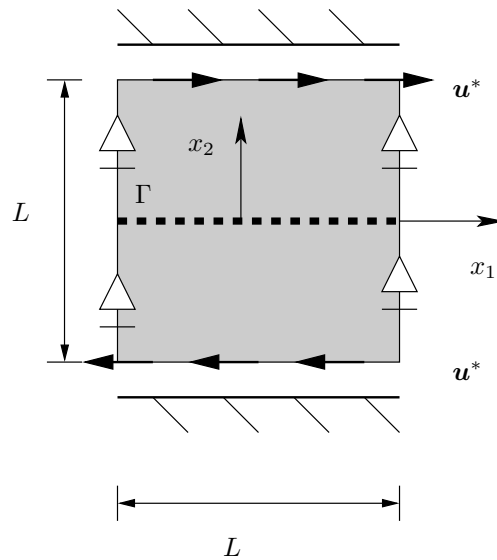


Figure 6.5: Quadratic specimen with an initial crack of length L subjected to simple shear.

geometric representation of the crack is mesh-based, i.e. for each node along the crack there is a second node at the opposite crack face with identical position that is not connected to the first node. One can expect that in the limit $l \rightarrow 0$, the phase field results converge to the results obtained for the geometric crack, cf. Section 4.1. Additionally, two variants $a = 2$ and $a = 0.1$ of the degradation function are used in Fig. 6.4 a) for the phase field simulations. Both phase field formulations are in fairly good agreement with the geometric results for the chosen length-scale $l = 0.01L$. Nonetheless, the solution for the cubic ($a = 0.1$) degradation function, yields a steeper gradient and higher maximum stress value at the crack tip with a lower stress level away from the crack and thus matches the solution for the geometric crack slightly better.

Figure 6.4 b) displays the stress distribution for a tensile loaded ‘one row’ crack with the degradation function characterized by $a = 0.1$. Just as in Fig. 6.2 a), the stress distribution is identical for all formulations of the strain energy density. Dissimilarly to the two row crack situation, however, for a one row crack the stress is not fully reduced at the crack, i.e. $\sigma_{22}(x_1 < 0, x_2 = 0) \neq 0$. This can be explained by recalling that in the finite element scheme the constitutive law is evaluated at the integration points of each element, which do not have identical positions as the element nodes, cf. Section B.2. Thus, the phase field is unequal to zero at the integration points, if a ‘one row’ crack is considered. Hence, the stress at the integration points and also the projected nodal stress obtained by means of (B.67) are also not fully degraded, i.e. they are in general different from

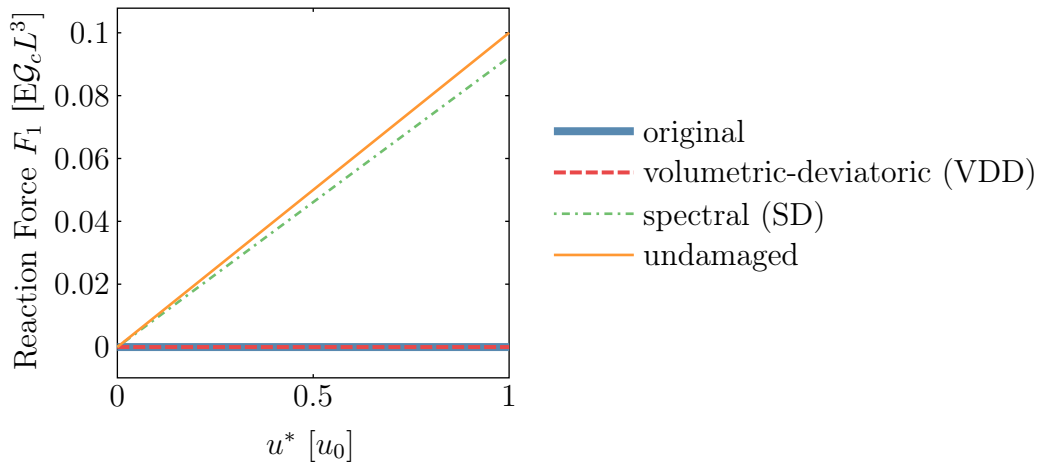


Figure 6.6: Sum of nodal forces F_1 at the top edge for the shear test.

zero. Some improvement can be achieved by using a finer mesh $h \ll l$. However, the crack needs to be at least one element wide for a physically correct modelling of the crack boundary conditions. Nonetheless, this conflicts with the objective to predict the fracture surface energy correctly. As pointed out in Strobl and Seelig (2016), the surface energy will be overestimated more severely by the two row crack formulation.

Next, the performance of the different tension-compression formulations is studied for a shear loading of the crack as discussed in Strobl and Seelig (2016). Strobl and Seelig (2016) considered a fully broken specimen see Fig. 6.5, where a displacement load is applied at the top and bottom boundary edge. This load is incrementally increased from zero to its final value $\mathbf{u}^*(x_2 = \pm \frac{L}{2}) = \pm u_0 \mathbf{e}_1$ with $u_0 = 0.1 \sqrt{G_c L / 2\mu}$. The vertical displacement at the left and right boundary is set to zero meaning $u_2^*(x_1 = \pm \frac{L}{2}) = 0$. The mesh, the material and the phase field parameters remain unchanged compared to the previous example. A ‘two row’ representation of the crack is chosen, the parameter of the degradation function is set to $a = 0.1$, and again quasi-static conditions are assumed. If there is no friction or adhesion between the crack faces, such a load would not cause any stress response and a Mode II sliding motion of the crack faces can be expected.

Fig. 6.6 displays the sum of the x_1 -components of all nodal forces at the top edge. It appears that the original formulation and the volumetric-deviatoric decomposition yield a reaction force of approximately zero, in other words there is no stiffness to the sliding motion of the crack faces. As pointed out in Strobl and Seelig (2016) and mentioned in Section 4.4, the SD formulation causes a significant residual stiffness of the crack, i.e. the reaction force is linearly dependent on the

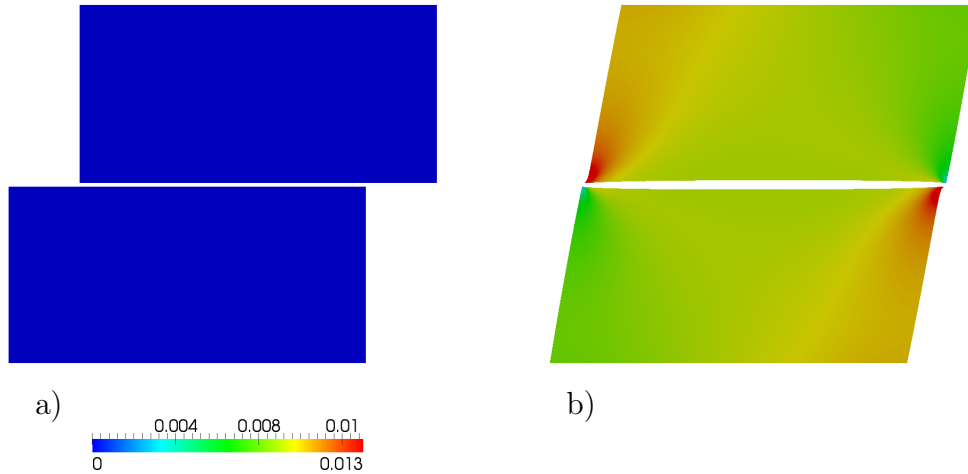


Figure 6.7: Contour plots of the shear stress $\sigma_{12} \left[\sqrt{2\mu\mathcal{G}_c/L} \right]$ a) for the volumetric-deviatoric and b) spectral decomposition of the strain energy density. Regions where $s < 0.1$ are rendered invisible in order to illustrate the crack. The deformation is scaled by a factor of $\sqrt{2\mu L/\mathcal{G}_c}$.

applied displacement load. In fact, the slope of the force-displacement curve – and consequently the material stiffness – is only slightly smaller than for an undamaged body.

Figure 6.7 displays the deformed geometry and the resulting shear stress distribution for VDD, see Fig. 6.7 a), and SD, see Fig. 6.7 b). The former formulation allows the Mode II sliding motion of the crack faces without a deformation of the bulk material. Consequently, also the shear stress vanishes. The spectral decomposition on the contrary causes an unrealistic residual stiffness of the crack. Thus, the shear stress is non-zero and the sliding motion of a frictionless crack without adhesion is not predicted correctly.

Concerning the two quasi-static examples discussed above one can draw the conclusion that the volumetric-deviatoric formulation should be preferred if it is the goal to model Mode II fracture without friction or adhesion between the crack faces. Furthermore, the normal contact and the impenetrability of crack faces is predicted rather accurately by the volumetric-deviatoric as well as the spectral decomposition of the strain energy density. Consequently, both formulations constitute a significant improvement over the original one. In addition, a cubic

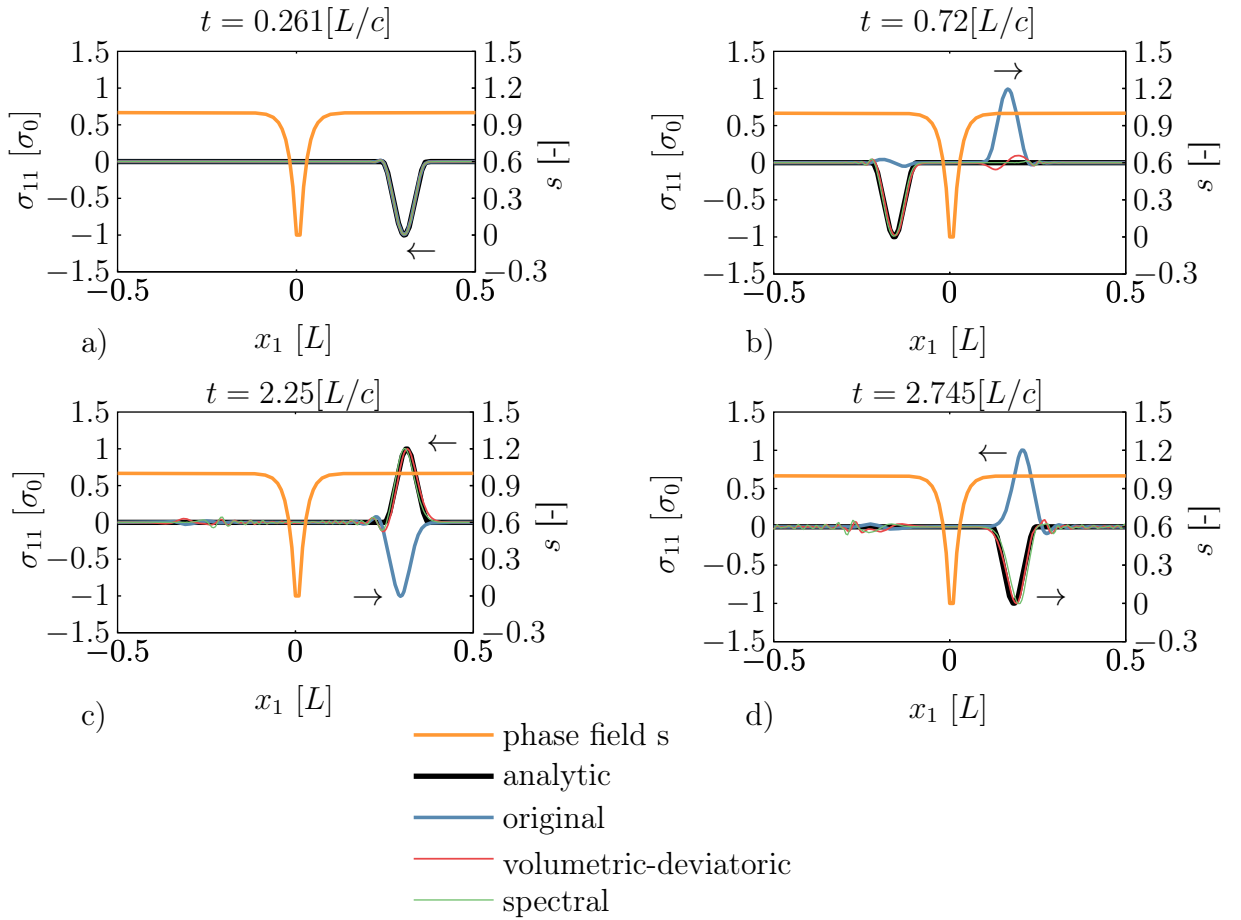


Figure 6.8: Stress σ_{11} and phase field s for different formulations of the strain energy density at different times.

degradation function with $a = 0.1$ yields a slightly better agreement with the stress distribution obtained for a geometric representation of the crack than the quadratic degradation function with $a = 2$.

6.1.2 Wave Interaction with a Phase Field Crack

The previous section discussed how well the phase field model captures the behaviour of stationary cracks under quasi-static situations when inertial effects are neglected. In the dynamic case, however, it is of particular interest to understand how stress waves interact with a crack which is approximated by a phase field formulation.

To this end, the 1D problem depicted in Fig. 5.2 is considered again. All parameters are kept the same as in Chapter 5 but, similar to the previous section, the

formulation of the strain energy is varied. Hence, the performances of the original formulation (4.8), the volumetric-deviatoric decomposition (4.42), and the spectral decomposition (4.47) are compared to each other. As a numerical solution strategy, the monolithic scheme with implicit time integration by a modified Newmark scheme S2 is used, whereupon a fixed time step of $0.2\Delta t_{cfl}$ is chosen.

Initially, the generated stress wave propagates towards the crack at $x_1 = 0$ and all formulations are in good agreement with the analytical solution, see Fig. 6.8 a). This changes after the stress pulse passes the crack. Both modified formulations predict a physically sound transmission of the stress wave across the crack, whereas the original formulation (4.8) falsely claims that the pulse is reflected at the crack in the form of a tensile wave, see Fig. 6.8 b). Later on, the wave approaches the crack once more as a tensile ($\sigma_{11} > 0$) pulse for the modified formulations, see Fig. 6.8 c). In this situation, reflection at the crack as a compressive pulse is the correct response which is governed by both modified formulations, see Fig. 6.8 d). Thus, the modified formulations can also be considered as a significant improvement over the original formulation with respect to the correct prediction of wave interaction with the crack in the dynamic case. Moreover, in the dynamic case a guess whether the loading of the crack will be purely tensile or not is often not as straightforward to make as in the quasi-static case. While in the quasi-static case one can forecast reasonably well if the original formulation is sufficient, i.e. the situation at the crack is crack opening, this might not be feasible in the dynamic case where elastic waves are reflected at the boundary and interact with the crack. Similar numerical experiments have been discussed in Schlüter et al. (2014b) and Steinke et al. (2016), which confirmed that the volumetric-deviatoric as well as the spectral decomposition govern the reflection of elastic waves and clearly represent an improvement over the original formulation.

6.2 Crack Nucleation

Classical theories of fracture based on Irwin's stress intensity factor criterion or Griffith's energetic criterion require an initial singularity of order $1/\sqrt{r}$, with r the radial distance from the crack tip, to predict the initiation of crack propagation see Fig. 3.1. Since such a singularity typically exists only at crack tips, crack nucleation in undamaged material cannot be predicted by these original theories for weaker singularities or for stress concentrations without a singular behaviour. On the contrary, phase field models for brittle fracture combine an energetic criterion that is closely related to Griffith's theoretical approach with a critical stress criterion for crack nucleation, as discussed in Kuhn (2013) and also outlined for the quasi-static 1D case in Section 4.6.1. The ability of phase field models to simulate crack nucleation in undamaged material has been thoroughly discussed for the quasi-

static case in Kuhn (2013). Kuhn described that in 1D as well as 2D situations certain stress measures which depend only on the stiffness of the material λ, μ , the specific fracture energy \mathcal{G}_c and the length-scale parameter l , cf. (4.93) and (4.94), can be interpreted as critical stress levels at which cracks nucleate if they are reached in sufficiently large regions (estimated at $\sim 10l$).

Crack nucleation in the dynamic case has been discussed, among others, in a replication of the Kalthoff-Winkler experiment in Hofacker and Miehe (2012), in Schlüter et al. (2014b) for several 1D, 2D and 3D situations and in Dally and Weinberg (2017) as a replication of the split Hopkinson bar experiment. It has been discovered that also in the dynamic case the phase field model is suitable to describe crack nucleation. The following numerical simulations further illustrate the capability of the phase field approach to reproduce crack nucleation in undamaged material for scenarios in which the propagation of elastic waves has major impact on the results.

6.2.1 1D-Hopkinson Wire

The first example treats an experiment that was performed by Hopkinson (1872). In his experiments J. Hopkinson loaded steel wires by a falling weight. The majority of specimens broke near the fixed end of the wire. Hopkinson argued that a tensile stress pulse travels along the wire and is reflected at the fixed end. The incoming stress pulse is then superimposed by the reflected stress pulse which leads to a local increase of the stress amplitude and finally to failure of the wire. The

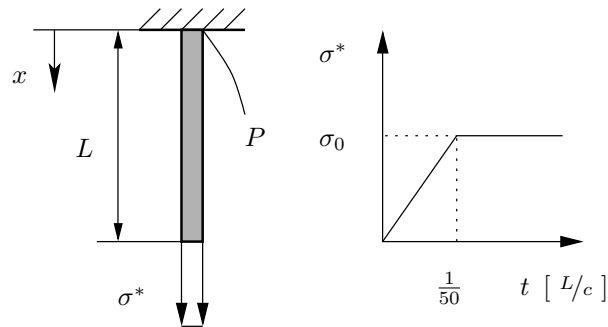


Figure 6.9: Dynamic crack nucleation set-up.

setup in Fig. 6.9 is intended to reproduce this experiment. The problem is reduced to the one-dimensional set of equations (4.58) under isothermal conditions. The body is fixed at the top edge meaning that the boundary condition $u = 0$ is specified at point P. The length-scale parameter is chosen to be $l = 0.01L$. The computational domain is meshed by 200 homogeneously distributed elements of size $h = 0.5l$. The falling weight is modelled by a load $\sigma^*(t)$ that grows rapidly

from $\sigma^*(0) = 0$ to $\sigma^*(\tau) = \sigma_0$ in a time interval of $\tau = 1/50 \frac{L}{c}$, and afterwards the load is kept constant. According to the considerations made in Section 4.6.1, material failure is expected at loads larger than σ_c or σ_c^* depending on the chosen degradation function. At first, the degradation function given by (4.94) with $a = 0.1$ is considered. Since the goal of this numerical example is to investigate fracture due to a stress amplitude doubling after reflection at the fixed boundary, the load is only set to $\sigma_0 = 0.6\sigma_c$ in the first simulation and $\sigma_0 = 0.4\sigma_c$ in the second simulation. In both cases, the applied traction is too small to break the wire if inertia effects are neglected. From the analytical solution of the wave equation it is known that the stress wave should be reflected at the fixed boundary at time $t = 1.0 \frac{L}{c}$. In the first case, $\sigma_0 = 0.6\sigma_c$, it is expected that the computed stress exceeds the material strength while for the second case, $\sigma_0 = 0.4\sigma_c$, the expected maximum stress is smaller than the material strength.

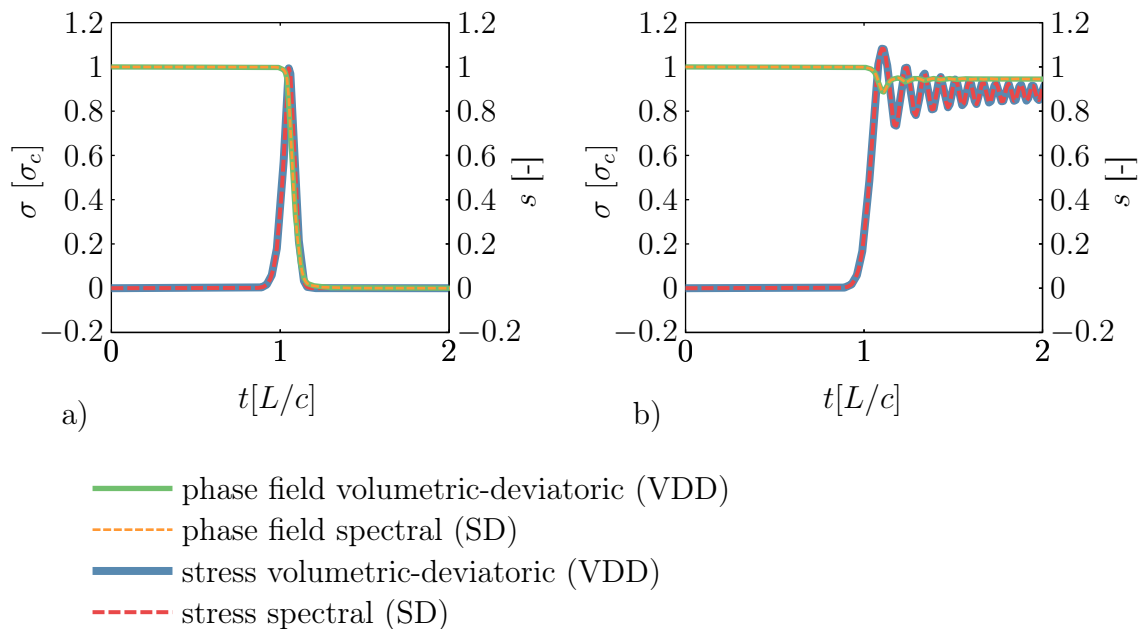


Figure 6.10: Stress $\sigma(t)$ and phase field $s(t)$ at point P for a) $\sigma_0 = 0.6\sigma_c$ and b) $\sigma_0 = 0.4\sigma_c$. The parameter of the degradation function is $a = 0.1$.

Figure 6.10 a) shows the stress and phase field values at the fixed boundary for a load of $\sigma_0 = 0.6\sigma_c$. Both variants of the tension-compression asymmetry formulations are considered but yield virtually identical results as expected in this 1D situation. The pulse indeed reaches the point P at time $t = \frac{L}{c}$ and hence the stress rapidly increases to σ_c , a value that is distinctly above the applied load σ_0 . Precisely when the peak stress is reached, the phase field value drops to zero

and a crack nucleates at P which causes the stress to rapidly go to zero as well. Subsequently, the irreversibility constraint (4.31) prevents a recovery of the phase field. For a smaller load $\sigma_0 = 0.4\sigma_c$, see Fig. 6.10 b), the stress does not reach the material strength and the mean final value is $\sigma = 0.8\sigma_c$. In this second simulation, the phase field at the fixed boundary is only reduced to $s \approx 0.94$, which means that the material is still undamaged.

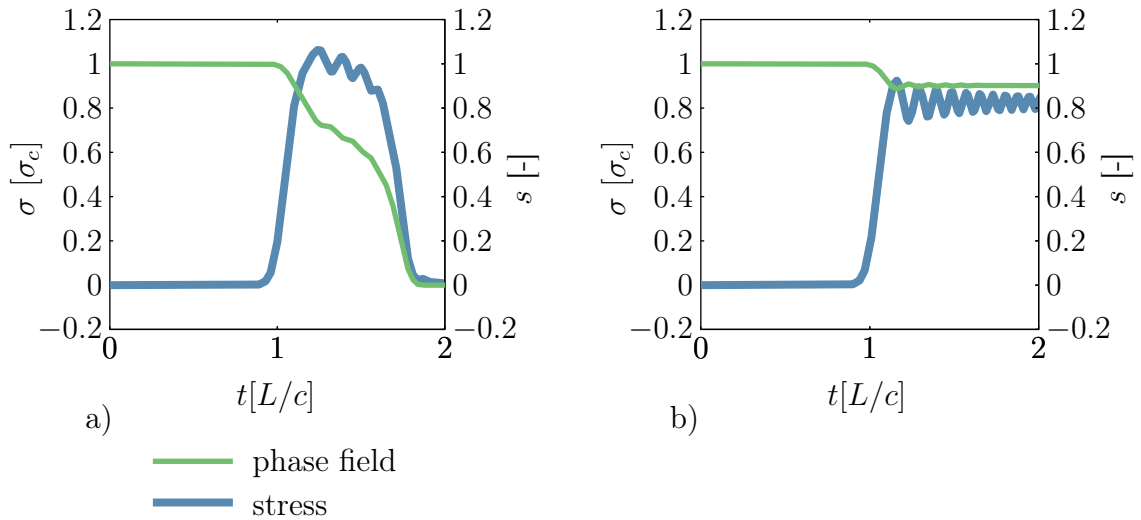


Figure 6.11: Stress $\sigma(t)$ and phase field $s(t)$ at point P a) for $\sigma_0 = 0.6\sigma_c$ and b) $\sigma_0 = 0.4\sigma_c$. The parameter of the degradation function is $a = 2$ and only the volumetric-deviatoric decomposition of the strain energy density is considered.

Figure 6.11 shows the numerical results for the same problem but using the quadratic degradation function ($a = 2$) which have already been reported in Schlüter et al. (2014b) and Schlüter (2013). The stress loads are rescaled to fit the reduced material strength σ_c^* , i.e. $\sigma_0 = 0.4\sigma_c^*$ for the smaller load level and $\sigma_0 = 0.6\sigma_c^*$ for the higher load case. While the subcritical case yields qualitatively similar results, compare Fig. 6.10 b) to Fig. 6.11 b), the results for the critical case strongly depend on the chosen degradation function. The crack nucleation process for the quadratic degradation function is not at all a brief event compared to the fracture behaviour displayed in Fig. 6.10 a). It lasts from the point of time when the maximum stress σ_c^* is attained at a time slightly larger than $t = 1.0\frac{L}{c}$ to the final reduction of the phase field to zero at time $t \approx 1.85\frac{L}{c}$. Two phases can be identified for the quadratic degradation function. The initial decrease of the phase field parameter to $s \approx 0.75$ happens in a rather short time interval. At this point, the stiffness of the material is severely degraded and the critical load is reached. Nonetheless, final fracture is delayed and the decrease of s in the second phase is

less rapidly. From a physical standpoint fracture should happen immediately as soon as the critical stress is reached and thus, the formulation with $a = 0.1$ should be preferred. The example highlights that the phase field model is indeed capable to reproduce dynamic crack nucleation as observed in Hopkinson's experiments.

6.2.2 2D-Crack Nucleation Hopkinson Plate

A problem that is similar to the previous wire example can be investigated in 2D. An experiment performed by B. Hopkinson as described in Hopkinson (1921) serves as an example. B. Hopkinson subjected steel plates to a compressive pulse P^* by applying an explosive, see Fig. 6.12. He observed that for thin specimens such a load simply punched a hole into the plate and thus ductile failure was caused due to the induced shear stress. Thicker specimens, however, showed a different crack pattern. In that case, a spherical crack formed at the opposite plate side, like it is indicated in Fig. 6.12. B. Hopkinson argued that the applied pressure pulse caused a stress wave that was reflected as a tensile pulse at the free boundary. Since the material is much stronger in compression than it is in tension, a crack was only nucleated after reflection of the compressive pulse at the free boundary.

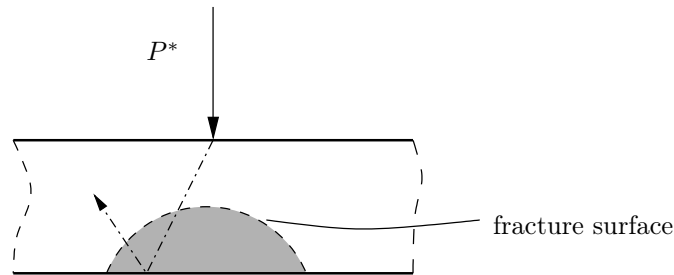


Figure 6.12: Dynamically loaded plate. The shaded region illustrates the experimentally observed crack-pattern from Hopkinson (1921). The dashed-and-dotted line shows the propagation and reflection of the emitted elastic wave.

The experiment is reproduced by the finite element setting illustrated in Fig. 6.13 (left). The quadratic formulation of the degradation function is used and the amplitude of the stress pulse $\mathbf{t}^* = -\sigma^* \mathbf{e}_2$ is set to $\sigma_0 = 3.0483\sigma_c^*$. This value is fully applied at time $t_1 = 0.002236 \frac{L}{c}$ and starts to decrease at time $t_2 = 0.044721 \frac{L}{c}$, see Fig. 6.13 (right). The rate of the load application and the subsequent decrease of the load are identical. The elastic parameters are chosen to be equal, i.e. $\lambda = \mu$. The geometry is discretized by 500×140 homogeneously distributed rectangular elements, where the length-scale parameter is $l = 0.01L$. This results in an element edge length of $h_1 = l$ in x_1 -direction and an element edge length of $h_2 = 0.5l$ in x_2 -direction. Furthermore, the boundary conditions at the left and at the right

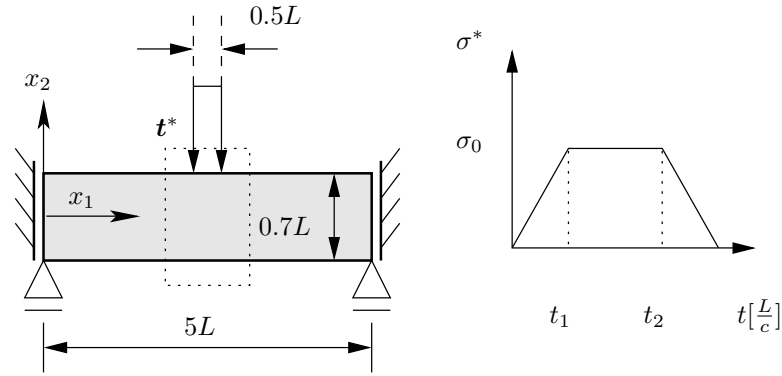


Figure 6.13: Finite element setup of a dynamically loaded plate. The dotted square indicates the section of the body that is also displayed in Fig. 6.14

side of the specimen are

$$u_1(x_1 \in \{0, 5L\}, x_2, t) = 0 \quad (6.1)$$

and

$$u_2(x_1 \in \{0, 5L\}, -0.35L, t) = 0. \quad (6.2)$$

Both modified formulations of the strain energy are considered and the quadratic degradation function with $a = 2$ is used. The results for the VDD formulation have already been reported in Schlüter (2013) and Schlüter et al. (2014b). Fig. 6.14 shows the hydrostatic stress

$$\sigma_H(\mathbf{x}, t) = \frac{\sigma_{11} + \sigma_{22}}{2} \quad (6.3)$$

and the associated phase field $s(\mathbf{x}, t)$ for both formulations of the strain energy density as snapshots at certain points in time. At time t_2 , a considerable decrease in the phase field can be observed next to the application point of the pressure load for the volumetric-deviatoric formulation of the strain energy density. This phenomenon can only be found in regions where the material is mainly subjected to shear stress. For the spectral decomposition formulation such a significant degradation of the phase field cannot be noticed. This is consistent with the considerations made in Section 4.4, which predicted the shear resistance to be higher for SD than for the VDD formulation. Subsequently, the wave front spreads out in the specimen. However, the main pulse propagates almost parallel to the upper surface and does not extend radially, since the applied load has been modelled as a distributed traction load instead of a discrete force. This behaviour can be detected for both formulations, see the plots at time $t = 7.5t_2$ in Fig. 6.14 a) and Fig. 6.14 b).

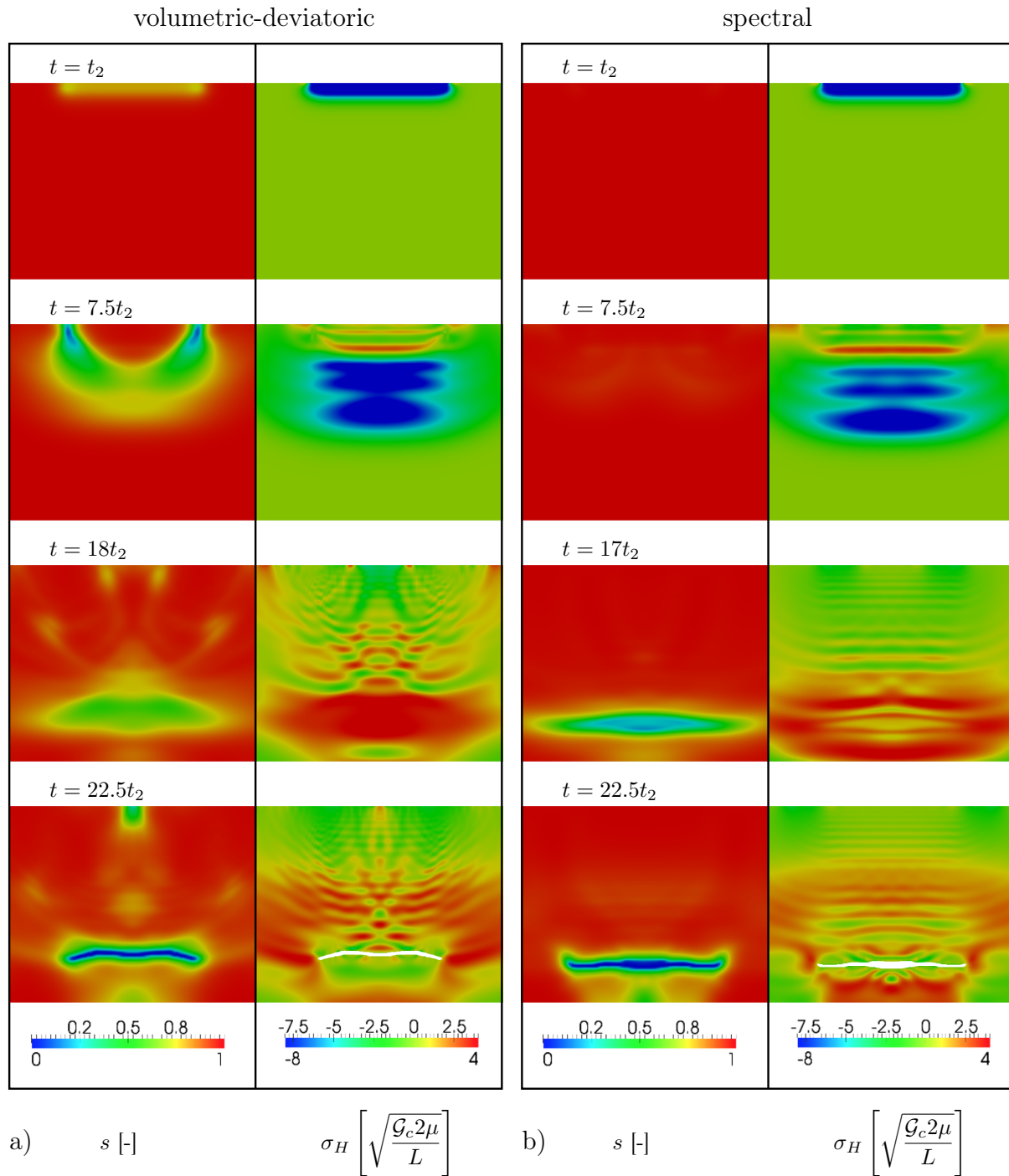


Figure 6.14: Contour plots of the phase field s and of the hydrostatic stress for the volumetric-deviatoric a) and spectral b) decompositions of the strain energy density for the dynamically loaded plate. Elements where $s < 0.1$ are not depicted in the stress plots in order to illustrate the crack. Only a section of the body is displayed, see also Fig. 6.13.

The compressive pulse approximately reaches the stress free lower boundary at time $t \approx 12.78t_2$, where it is reflected as a tensile pulse. The snapshots recorded at time $t = 16t_2$ for the VDD formulation of the strain energy density and $t = 17t_2$ for the SD formulation show that the positive volumetric stress σ_H leads to a significant decrease of the phase field parameter some distance away from the lower boundary. Furthermore, it can be noticed that for the VDD formulation the phase field has recovered at the upper boundary. Eventually the reflected tensile pulse triggers fracturing for VDD as well as SD which is observable in the snapshots recorded at time $t = 22.5t_2$. The final fracture pattern is similar for both formulations, i.e. there is a nearly horizontally oriented crack some distance away from the bottom edge. The offset from the bottom edge is slightly smaller for the SD formulation of the strain energy density and fracture also occurs a bit earlier. The observed crack pattern resembles the experimental observations by Hopkinson but the crack is more parallel to the free surface compared to the observations in the experiments. This can be explained as a consequence of defining the load as a distributed load instead of a more concentrated force. However, the present phase field model seems to be capable to qualitatively reproduce the results of the plate experiments of Hopkinson.

Figure 6.15 shows the phase field $s(2.5L, x_2, t)$ and the normal stress in x_2 -direction $\sigma_{22}(2.5L, x_2, t)$ for both formulations of the strain energy density in the middle of the plate at $x_1 = 2.5L$. At time $t = t_2$, a compressive pulse of a magnitude of $\sigma_{22} \approx \sigma_0$ travels towards the free boundary, see Fig. 6.15 a). While the stress is virtually identical for both variants of the strain energy density, a significant drop of the phase field can be detected for the VDD formulation that does not occur for the SD formulation. The amplitude of the VDD stress wave decreases as it spreads out in the body, see Fig. 6.15 b). At this point in time, differences are notable in the stress distribution where the SD predicted stress has a slightly larger amplitude. Again, a considerable drop of the phase field variable is only detected for the VDD formulation. Nevertheless, the phase field does not localize until the pulse is reflected as a tensile pulse at the free boundary. In Fig. 6.15 c), the stress for VDD can be observed to exceed the theoretical stress limit at time $t = 18t_2$ in an extended region. Simultaneously, the phase field drops to values of $s \approx 0.75$. Localization of the crack field is even more progressed for the SD formulation at this point in time. The plot shows the situation directly after the stress has exceeded the theoretical stress limit σ_c^* . At the last point in time, $t = 22.5t_2$, a crack has already been formed with $s = 0$ at some distance away from the bottom boundary, see Fig. 6.15 d). Although the stress σ_{22} exceeds the theoretical limit at $x_2 \approx 0$ at this point in time, in particular for VDD, the fracture field does not localize. This agrees with the observations made in Kuhn (2013), where it was found that the average stress needs to exceed the stress limit

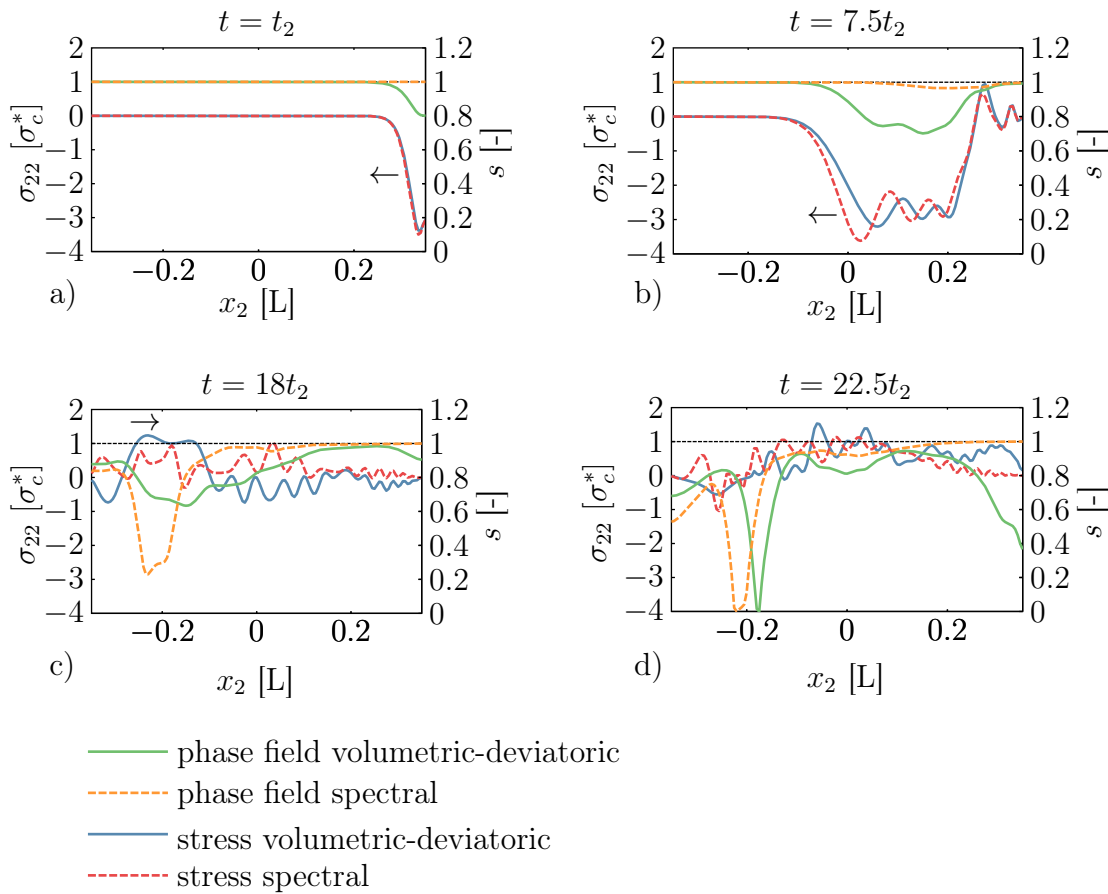


Figure 6.15: Stress σ_{22} ($x_1 = 2.5L$) and phase field s ($x_1 = 2.5L$). The horizontal dashed black line represents the theoretical stress limit σ_c^* .

in an extended region in order for crack nucleation to occur. Nonetheless, the exceedance of the critical stress limit is restricted to narrow regions at this stage of the simulation and thus, fracturing of the material does not occur except for the already existing horizontal crack.

This example demonstrates that the present phase field model is a suitable tool to model dynamic crack nucleation also in a more complex 2D setting. Furthermore, it displays the usefulness of the decompositions of the strain energy density to prohibit unphysical fracture in compressive load states. In addition, some qualitative differences between the two formulations have been detected that are in agreement with the theoretical considerations made in Section 4.4. These differences can mainly be noticed in shear-dominated load cases. Here, the VDD formulation does yield a significant decrease of the phase field parameter whereas the SD formulation does not. However, the decrease of the phase field parameter is larger for VDD also in mainly compressive load states, cf. Fig. 6.14 a) and b) at

time $t = t_2$. This is mainly attributed to the fact that the deviatoric part of the strain energy density is fully factored into the crack driving energy source term ψ_e^+ in this variant. The maximum positive stress is significantly lower than the absolute value of the applied pressure load but nonetheless leads to final failure with $s = 0$ at time $t = 22.5t_2$, see Fig. 6.15 d). Figure 6.15 c) shows that the maximum magnitude of the tensile pulse just before localization agrees well with the theoretical stress limit, see (4.93).

6.2.3 Crack Nucleation in a CT Specimen

In this section, crack nucleation at the notch ground of a compact tension (CT) specimen, see Fig. 6.16, is investigated. The setup is the same as for the analysis of the quasi-static case in Kuhn (2013) and Kuhn et al. (2015). At first, the global

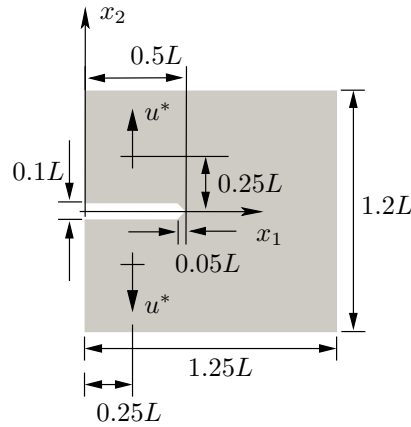


Figure 6.16: Computational domain for the CT-specimen examples.

effect of the choice of the degradation function on the constitutive behaviour of the specimen is considered. To this end, quasi-static conditions are assumed. In other words

$$\operatorname{div} \boldsymbol{\sigma} = \mathbf{0} \quad (6.4)$$

is solved instead of (4.24). Furthermore, different choices of the degradation function are investigated. The Lamé parameters are set so that they have equal value, meaning that $\lambda = \mu$. The length-scale parameter is $l = 0.01L$ with the element size along the expected crack path chosen accordingly, i.e. $h = 0.005L$. For the quasi-static simulations, the viscous approximation of the phase field evolution equation (B.74) is used instead of (4.26). The body is subjected to a linearly increasing displacement load $u^* = u_0 t$. In the quasi-static model, the characteristic time scale of the problem, cf. (4.65), is determined by the applied loading

rate u_0 . Consequently, the characteristic time scale is given by $T = (\sqrt{\mathcal{G}_c L / 2\mu}) / u_0$. The mobility parameter is set to

$$M = 2 \cdot 10^5 u_0 \sqrt{\frac{2\mu L}{\mathcal{G}_c^3}}. \quad (6.5)$$

A monolithic strategy with a backward Euler scheme for time integration is used for the quasi-static computations. In all phase field fracture simulations, a crack nucleates at a certain load level and subsequently propagates along the x_1 -axis. The time step chosen by the automatic time step size control during the period of crack nucleation is $\Delta t_{stat} = 2.96 \cdot 10^{-6} \sqrt{\mathcal{G}_c L / 2\mu} / u_0$. Thus, the load increment per time step at this important stage of the simulation is

$$\Delta u_{stat}^* = \Delta t_{stat} u_0 = 2.96 \cdot 10^{-6} \sqrt{\frac{\mathcal{G}_c L}{2\mu}}. \quad (6.6)$$

Figure 6.17 displays the simulated load displacement curves for the purely linear elastic case without any fracturing as well as results of phase field fracture simulations with different degradation functions. The linear elastic case shows a perfectly linear constitutive response of the structure as expected. The phase field simulations that allow for fracture display qualitatively very similar behaviour when compared to each other. Here, the reaction force increases up to a maximum level at which a crack nucleates. The consequence is a rapid reduction of the reaction force. Subsequently, a phase of stable crack growth can be observed. The peak reaction force is higher for the $a = 0.1$ degradation function. This behaviour is expected since the maximum 1D stress response is also higher than for $a = 2$, see (4.93) and (4.94). The graph for the quadratic degradation function initially agrees with the purely elastic simulation but a significant deviation from the elastic curve can be noticed well before the peak stress response is reached. Nonetheless, this nonlinear material response is less pronounced than for the 1D simulations, cf. Fig. 4.13, because the degraded region is confined to the notch ground. The degradation function with $a = 0.1$ constitutes a significant improvement over the quadratic degradation function. In this case, the curve matches the purely elastic response perfectly almost up to the peak load, where the reaction force drops again due to crack nucleation. Thus, it can be concluded that the $a = 0.1$ degradation function also results in a better approximation of linear elastic material behaviour – and thus brittle fracture – for general 2D situations.

In a next step, the load is still applied in a quasi-static manner. In other words the displacement rate is low compared to the wave speeds of the material. However, in the following, the material's inertia is accounted for, i.e. (4.24) is solved instead of (6.4) and (4.26) is solved instead of (B.74). Since an initial crack

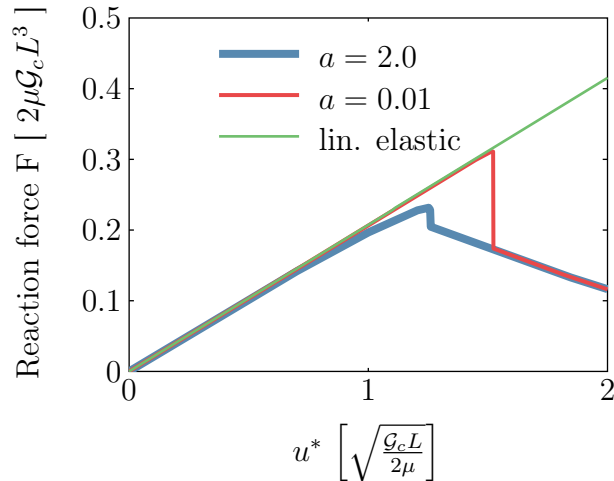


Figure 6.17: Reaction forces for the CT-specimen under quasi-static conditions for different choices of the degradation function and linear elastic response without fracture.

forms rapidly even if the load is applied in a quasi-static manner, dynamic effects certainly play a role in a crack nucleation scenario. In the following, the question how the dynamic solution compares to the quasi-static case is studied. While the backward Euler scheme is still employed for the quasi-static simulations, a staggered scheme with the central difference method (strategy S6 from Section 5) is used to solve the dynamic problem. The time step in the dynamic simulations is set to $\Delta t_{dyn} = 0.4\Delta t_{cfl}$ and the cubic degradation function with $a = 0.1$ is utilized. The applied normalized loading rate, cf. (4.79), is

$$r = \frac{u_0}{c} = 0.005\sqrt{\frac{\mathcal{G}_c}{2\mu L}}, \quad (6.7)$$

i.e. the load increment per time step in the dynamic case follows as

$$\Delta u_{dyn}^* = u_0\Delta t_{dyn} = 0.002h_{min}\sqrt{\frac{\mathcal{G}_c}{2\mu L}} \approx 9.3750 \cdot 10^{-6}\sqrt{\frac{\mathcal{G}_c L}{2\mu}}. \quad (6.8)$$

Figure 6.18 displays the computed strain energy E^e , kinetic energy \mathcal{K} (only for the dynamic case) and fracture energy E^s for the quasi-static as well as for the dynamic simulations. As one can observe in Fig. 6.18 a), the loading speed is small enough so that the evolution of the elastic energy in the dynamic simulations before crack nucleation is virtually identical to the evolution of the elastic energy of the quasi-static simulations. At this subcritical load level, the material is practically undamaged and consequently the body behaves in a linear elastic manner. This involves that the strain energy rises quadratically with the applied

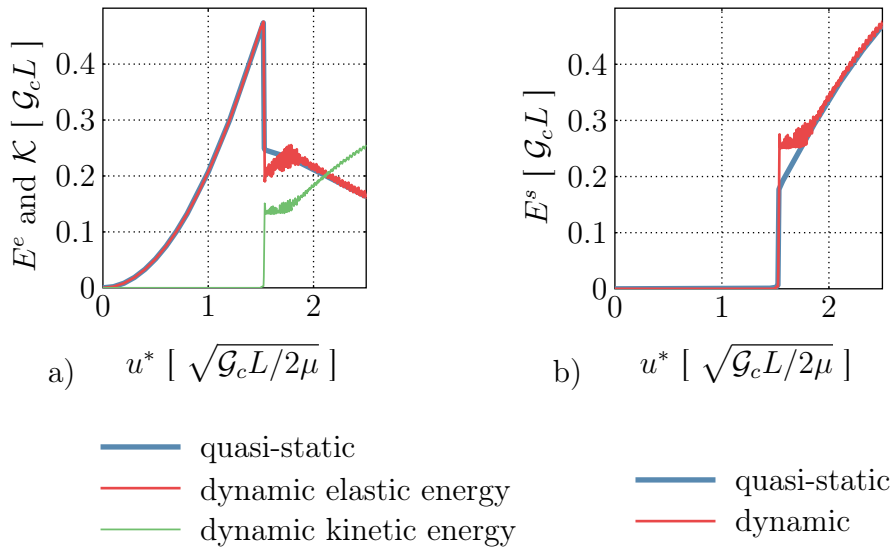


Figure 6.18: a) Plot of the kinetic energy and the elastic energy and b) the fracture energy.

displacement load. At the onset of crack nucleation, a large amount of elastic energy is released in a discontinuous manner and therefore the strain energy drops considerably. This happens at an almost identical point of time for the quasi-static and the dynamic simulations. Interestingly, the drop of the strain energy is larger for the dynamic case, signifying that more energy is released initially if inertial effects are considered. In the quasi-static simulations, a phase of stable crack growth directly follows crack nucleation, meaning that the crack further propagates only when the load is increased. In this phase, the strain energy decreases monotonously. In contrast, the strain energy rises for increased displacements in the dynamic simulation after crack nucleation and the associated initial release of strain energy. This suggests that the crack does not propagate in this phase. In addition, oscillations of the various energy components can be observed which are results of elastic waves originating from the crack nucleation event. As the simulation progresses, the mean value of the elastic energy for the dynamic simulation approaches the curve obtained from the quasi-static simulations. Due to the low loading velocity, the kinetic energy is initially negligible but substantially rises upon crack nucleation, see the green line in Fig. 6.18 a). This displays, that due to brutal crack nucleation large amounts of material are accelerated away from the passing crack. Apart from oscillations, the kinetic energy remains constant shortly after crack nucleation during the period of crack arrest. In the subsequent phase of stable crack propagation more and more material is accelerated and thus the kinetic energy rises steadily. The plot of the fracture energy supports these findings,

see Fig. 6.18 b). Indeed, the fracture energy is higher for the dynamic simulation shortly after crack nucleation, showing that a longer initial crack nucleates than in the quasi-static case. Furthermore, a period of approximately constant fracture energy can be observed that directly follows crack nucleation. This also illustrates that the crack arrests after crack nucleation and only later on resumes stable crack growth.

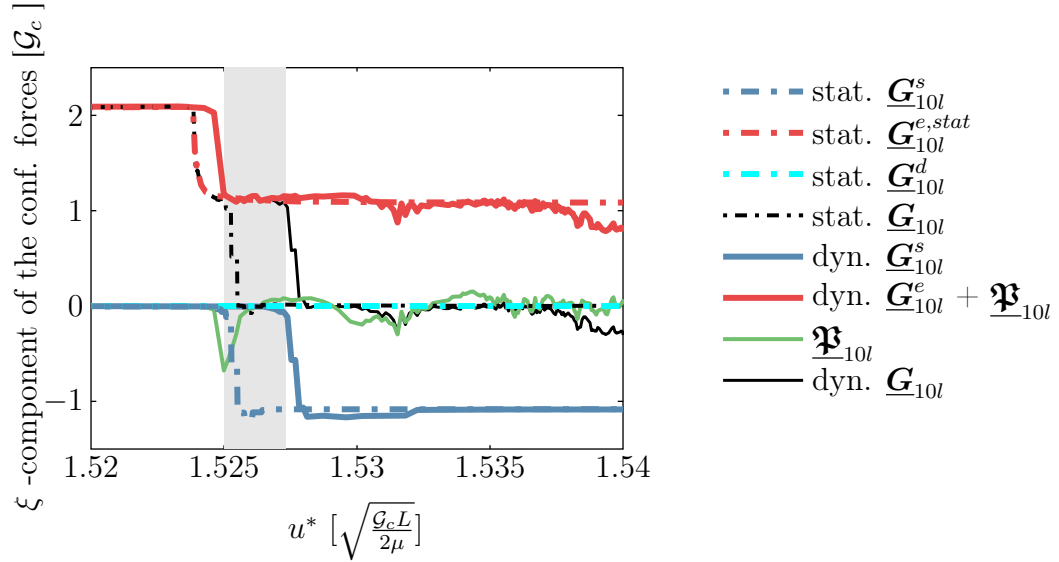


Figure 6.19: Configurational force components in ξ -direction for the quasi-static and dynamic simulations for the period of crack nucleation.

Further insight can be gained by considering the configurational force balances that were introduced in Section 4.6.2. In the quasi-static model, the crack-driving elastic configurational force is given by

$$\mathbf{G}_{D_\delta}^{e,stat} = \int_{D_\delta} \operatorname{div}(\psi^e \mathbf{1} - (\operatorname{grad} \mathbf{u})^T \boldsymbol{\sigma}) \, dV, \quad (6.9)$$

whereas the cohesive configurational force is identical to that of the dynamic formulation (4.124). Analogously to the dynamic situation, a total configurational force can be defined for the quasi-static model as

$$\mathbf{G}_{D_\delta}^{stat} = \mathbf{G}_{D_\delta}^{e,stat} + \mathbf{G}_{D_\delta}^s, \quad (6.10)$$

where the additional dissipative contribution mentioned in Kuhn (2013)

$$\mathbf{G}^d = \int_{D_\delta} \frac{\dot{s}}{M} \nabla_s \, dV \quad (6.11)$$

is negligible small because M is chosen large enough such that \mathbf{G}^d is of negligible size compared to all other configurational forces, cf. Fig. 6.19. Figure 6.19 shows the various configurational force components in ξ -direction – which coincides with the x_1 -direction in this example – that were evaluated for a tip disc control volume of the type (4.119) with a radius of $\delta = 10l$. The figure shows a section of the narrow loading range in which crack nucleation takes place. To be precise, the depicted loading range is $1.52\sqrt{\mathcal{G}_c L/2\mu} \leq u^* \leq 1.54\sqrt{\mathcal{G}_c L/2\mu}$, cf. Fig. 6.18. Prior to crack nucleation, the numerically evaluated ξ -component of the quasi-static elastic configurational force is larger than $2\mathcal{G}_c$ but drops discontinuously to \mathcal{G}_c as the crack nucleates. The positive sign indicates that $\underline{\mathbf{G}}^{e,stat}$ is indeed a crack driving force. The drop of the cohesive configurational force to $\underline{G}_\xi^s \approx -\mathcal{G}_c$ is delayed, since $\underline{\mathbf{G}}_{D_\delta}^s$ is zero as long as the whole phase field crack is contained in D_δ , cf. the considerations that lead to (4.128). As soon as the part of the crack is outside D_δ , the resulting configurational force assumes a value slightly smaller than $-\mathcal{G}_c$, which is in agreement with (4.128). The slight overestimation of the absolute value of the fracture energy and consequently also of the cohesive configurational force is typical for finite element discretizations of the phase field equations, see also Kuhn (2013) and Borden (2012). As discussed in Section 4.6.2, the cohesive configurational force provides a resistant force to crack propagation which manifests in its negative sign. In situations in which the cohesive configurational force actually represents the resistance to crack propagation at the crack tip, implying that a part of the crack is outside D_δ , the total configurational force is zero. This reflects the connection of the quasi-static phase field model to the Griffith condition for crack propagation, which is fulfilled if $\underline{\mathbf{G}}_{D_\delta}^{stat} = \mathbf{0}$, see Kuhn (2013).

The configurational forces evaluated in the dynamic model show the same patterns. Here, the sum $\underline{\mathbf{G}}_{D_\delta}^e + \underline{\mathfrak{P}}_{D_\delta}$ can be identified as the crack driving force that is related to the energy release rate, cf. Section 4.6.2. The value of $\underline{G}_\xi^e + \underline{\mathfrak{P}}_\xi$ agrees very well with $\underline{G}_\xi^{e,stat}$ prior to fracture, which shows that the loading rate is indeed chosen small enough so that inertial effects represented by $\underline{\mathfrak{P}}_\xi$ are not significant at this stage. It can be detected that in the dynamic simulation, the drop of the crack driving force appears at a slightly higher applied displacement load. This might be an effect of the chosen time step size. Indeed, the load increment applied in a time step of the staggered scheme (6.8) is significantly larger than the respective load increment in the quasi-static simulation, (6.6) during the regarded time interval. The cohesive configurational force behaves just as in the quasi-static case and assumes its eventual value of $\underline{G}_\xi^s \approx -\mathcal{G}_c$ in a delayed fashion. The dynamic configurational force or pseudo-momentum $\underline{\mathfrak{P}}_\xi$ is approximately zero until the crack nucleates. Upon crack nucleation, however, a relatively large inertial resistance is displayed as a peak dynamic configurational force of size $\underline{\mathfrak{P}}_\xi \sim -0.5\mathcal{G}_c$. Subsequently, the sign of $\underline{\mathfrak{P}}_\xi$ fluctuates between positive (crack driving) and negative

(crack decelerating) values. The total configurational force given by (4.118) is approximately zero during crack propagation as in the quasi-static case, demonstrating that - also in the dynamic situation - the fracture behaviour in the simulations is related to the Griffith condition. Nevertheless, as long as the crack is completely contained in D_δ the cohesive configurational force on D_δ does not represent the material resistance to crack propagation at the crack tip. As a consequence of (4.118) the total configurational force does not represent the complete energetic force which acts on crack tip in this situation. The result is that although the phase field is suspected to evolve according to a balance of fracture and elastic energy that is closely related to the Griffith criterion, the non-zero total configurational force does not reflect this as long as the complete crack is contained in D_δ . The respective period for the dynamic simulation is indicated by the grey shaded region in Fig. 6.19. In contrast to the quasi-static simulation the total configurational force indeed assumes a subcritical value $\underline{G}_\xi < 0$ after the initial phase of crack nucleation. Thus - while crack nucleation is directly followed by stable crack nucleation if inertial effects are neglected - the dynamic simulations predict crack arrest at $u^* \approx 1.5375 \sqrt{\frac{\mathcal{G}_c L}{2\mu}}$.

This numerical example demonstrates that even in quasi-static loading situations inertial effects play a role during brutal crack nucleation and cannot be neglected in general. Thus, even if the dynamic results converge to those of the quasi-static model in some situations, e.g. stable crack growth, there are significant differences in these critical situations.

6.2.4 Crack Initiation in an Infinite Elastic Body

In this section, a numerical simulation employing the present phase field model is compared to an analytic solution for an abstract crack nucleation scenario. At first, the analytic solution from Freund (1990) is presented which considers a half plane crack in an unbounded elastic body on the plane $x_2 = 0, x_1 \leq z_0$ under plane strain conditions, see Fig. 6.20. Concentrated forces $\mathbf{p}^* = \pm p^* \mathbf{e}_2$ act on the crack faces at $x_1 = 0$ as shown in the figure. The crack tip is assumed to be blunted, meaning that the crack only nucleates at an excessive energy release rate of $\mathcal{G}_{n_0} = n_0 \mathcal{G}_c$, where $n_0 > 1$. The load p^* is gradually increased until \mathcal{G}_{n_0} is reached and afterwards kept constant. At the critical load level \mathcal{G}_{n_0} , the crack is assumed to grow according to the Griffith condition (3.28). The equilibrium stress intensity factor for this situation is

$$K_I = p^* \sqrt{\frac{2}{\pi z_1}}, \quad (6.12)$$

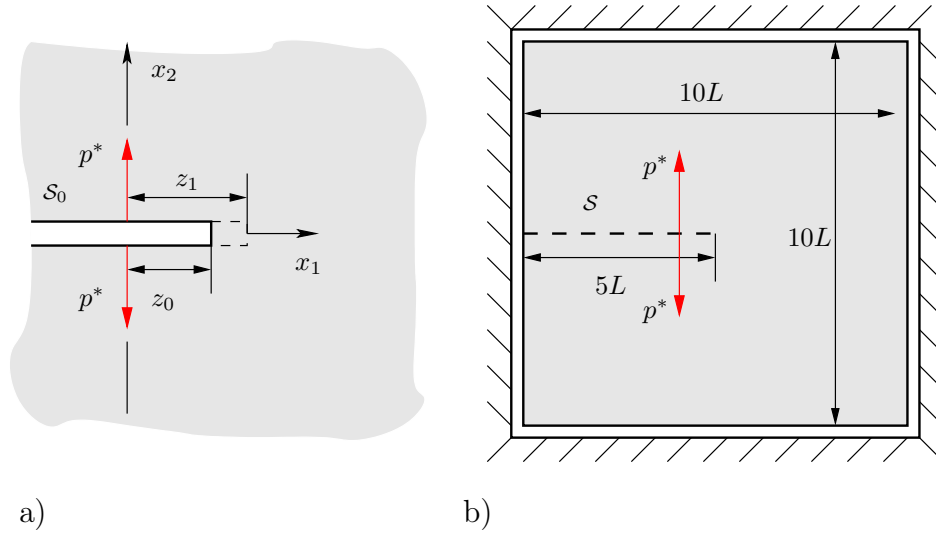


Figure 6.20: a) Unbounded elastic body subjected to concentrated forces and b) the respective finite element setup.

where z_1 is the current tip position, which - provided that the load is applied in a quasi-static manner - yields at crack nucleation

$$\mathcal{G} = \frac{1 - \nu^2}{E} K_I^2 = \frac{1 - \nu^2}{E} K_I^2 \frac{2p^{*2}}{\pi z_1} = n_0 \mathcal{G}_c. \quad (6.13)$$

Consequently, the load required for crack nucleation and the phase of subsequent crack propagation is

$$p^* = \sqrt{\frac{n_0 \mathcal{G}_c E \pi z_0}{2(1 - \nu^2)}}. \quad (6.14)$$

By substituting (6.14) into (6.12) and recalling (3.33), the crack tip equation of motion (3.35) is obtained as

$$\frac{z_1}{n_0 z_0} \approx 1 - \frac{\dot{z}_1}{c_r}, \quad \text{where } z_1(0) = z_0, \quad (6.15)$$

which directly yields the initial speed of the crack tip as $\dot{z}_1(0) = c_r(n_0 - 1)/n_0$. By integration, the crack tip trajectory is given as

$$z_1(t) = z_0 \left[n_0 - (n_0 - 1) \exp\left(\frac{-c_r t}{n_0 z_0}\right) \right]. \quad (6.16)$$

In other words, the crack decelerates and arrests at its final length of $l = n_0 l_0$, which is also the equilibrium length of a sharp crack subjected to the same load.

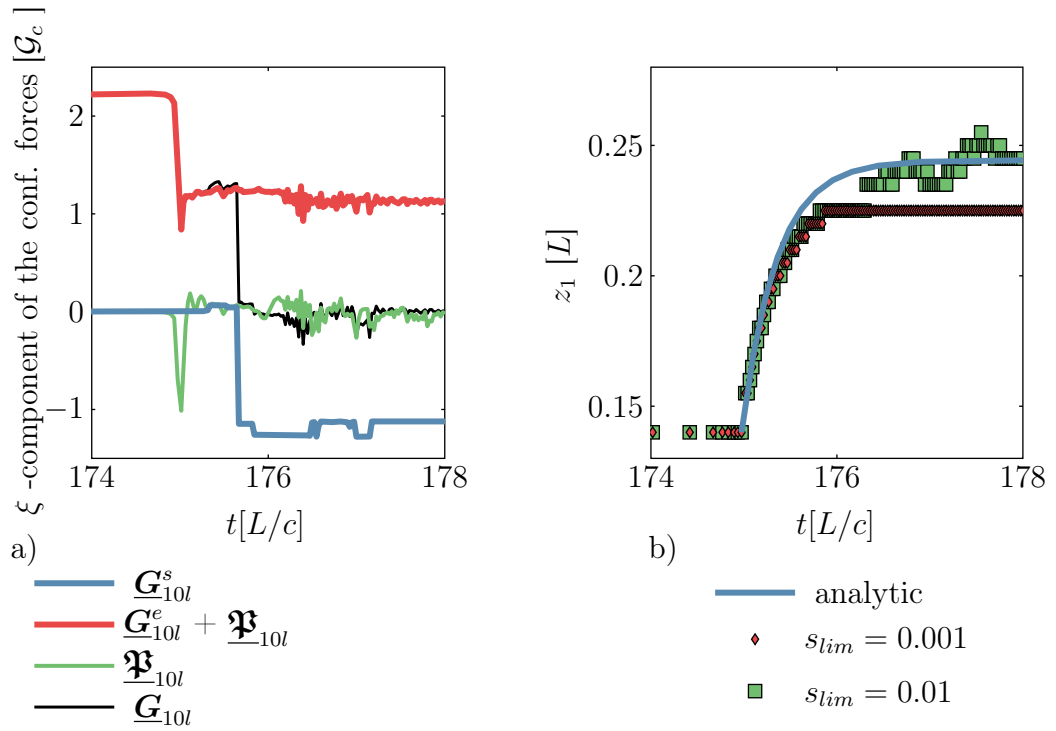


Figure 6.21: a) Configurational force components in ξ -direction and b) analytic solution for the crack tip trajectory as well as the computed crack tip trajectory for different values of s_{lim} .

The numerical simulation considers the domain depicted in Fig. 6.20 b). The initial crack is modelled as a geometric notch of width $0.02L$, where the element size at the crack path is $h = 2l$ with $l = 0.005L$. The distance from the point of load application to the initial crack tip is $z_0 = 0.14L$. Furthermore, the displacements that are normal to the boundary are set to zero. The load is linearly increased at a rate of

$$p_0 = 0.005\sqrt{\mu\mathcal{G}_cL^3}\frac{c}{L} \quad (6.17)$$

to the final value of $p^* = 0.875\sqrt{\mu\mathcal{G}_cL^3}$ which is reached at $t = 175\frac{L}{c}$, i.e. at the point of crack nucleation. The time step size is $\Delta t = 2\Delta t_{cfl}$ and the parameter of the degradation function is chosen as $a = 0.1$.

Figure 6.21 a) shows the configurational force components in ξ/x_1 -direction, which display the same characteristics as already discussed for crack nucleation for the CT-specimen, see Section 6.16. The evaluation allows to estimate the

parameter n_0 that characterizes the excess energy release rate prior to fracture as

$$n_0 \approx \frac{\max \left| \underline{G}_{10l,\xi}^e + \underline{\mathfrak{B}}_{10l,\xi} \right|}{\max \left| \underline{G}_{10l,\xi}^s \right|} = 1.7451 \quad (6.18)$$

if the interpretation of the configurational forces (4.123) and (4.128) are recalled. Figure 6.21 b) shows the resulting analytic solution for the crack tip trajectory as well as the computed crack tip positions for different values of the crack tip defining limit value s_{lim} , see (B.103). For $s_{lim} = 0.001$, the crack tip position is monotonously increasing, i.e. the crack tip position reflects that crack growth is strictly irreversible. One can notice that for this choice of s_{lim} , the analytic solution initially agrees well with the simulation. However, the final crack length is not predicted correctly. If $s_{lim} = 0.01$ is chosen as the value that defines the crack tip position, a better agreement between the simulation and the analytic solution is found for $t > 176 \frac{L}{c}$. This limit does not strictly comply with the irreversibility feature of cracks, and in Fig. 6.21 b) it can be detected that the crack tip position oscillates in the later stages of the simulation for $s_{lim} = 0.01$.

6.3 Crack Speed Limits and Inter-sonic Fracture

As discussed in Section 3.4, the maximum crack velocities in brittle materials are theoretically limited by inertial effects. These analytically derived limits are in agreement with experimental findings to a certain extent, cf. Section 3.4. This section is concerned with the question whether numerical simulations relying on the present phase field model yield crack speed limits that are consistent with theory and experiment. The discussion presented in this section is published in Schlüter et al. (2016b).

For all simulations of this section, the quadratic formulation of the degradation function is employed. Since a particular focus is on the modelling of Mode II fracture, the volumetric-deviatoric formulation of the strain energy density (4.42) is chosen. The first numerical experiment of this section is motivated by a molecular dynamic simulation described in Gao et al. (2001). Its purpose is to study the effect of the mode of crack tip loading on the observed maximum crack speed. The elastic Lamé parameters are set up so that the Poisson ratio is $\nu = \frac{1}{3}$. The considered domain includes an initial crack and a weak plane with reduced fracture resistance that is intended to prescribe the crack path and prevent the crack from branching or kinking. Such a modification keeps the material homogeneous with respect to its dynamic properties and thus, the theoretically derived crack speed limits, which are independent of \mathcal{G}_c , still apply. The initial crack is modelled by setting $s(\boldsymbol{x}, t_0) = 0$ at the respective nodes and the weak plane is implemented

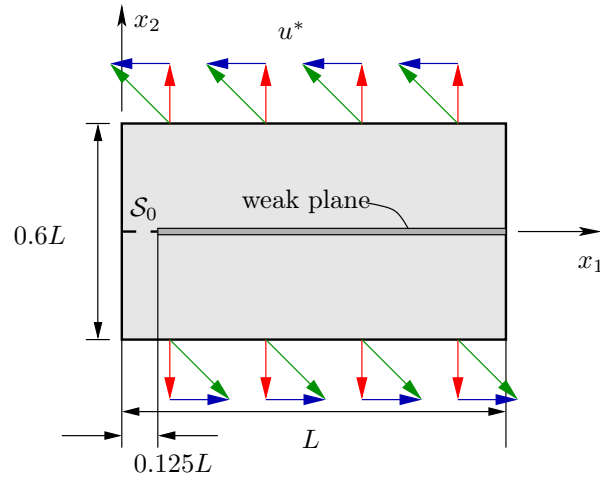


Figure 6.22: Finite element setup. A rectangular domain containing an initial crack (dashed line) and a weak plane is subjected to Mode I (red arrows), Mode II (blue arrows) and Mixed Mode (green arrows) loading.

by replacing the fracture resistance $\mathcal{G}_{c,\text{bulk}}$ in a small strip, see Fig. 6.22, with a reduced value $\mathcal{G}_{c,\text{wp}} = 0.01 \dots 0.3 \mathcal{G}_{c,\text{bulk}}$. The strip is $4l$ wide. In order to properly resolve the phase field in the proximity of the crack, the regular mesh is set up in such a way that the element edge length is $h = 0.5l$ in the weak strip, where $l = 10^{-4}L$. In contrast to previous simulations, the residual stiffness is non-zero, i.e. $\eta^s = 10^{-9}$. The specimen is loaded by prescribing a constant displacement rate at the upper and at the lower edge. Mode I loading is achieved by setting the displacement rate in x_2 -direction to $\dot{u}_2 = 2.284 \sqrt{\mathcal{G}_c/\rho L^3}$, whereas Mode II loading is applied by enforcing a displacement rate of $\dot{u}_1 = 11.419 \sqrt{\mathcal{G}_c/\rho L^3}$ in x_1 -direction. For the Mixed Mode simulations both displacement rates are applied simultaneously.

The Mode I results for varying fracture resistance $\mathcal{G}_{c,\text{wp}}$ of the weak plane are shown as the red lines in Fig. 6.23. The analysis reveals that decreasing fracture resistance in the weak plane shifts the initiation of crack growth to smaller times, i.e. also to lower crack tip loading. Furthermore, it can be observed that the maximum crack speed indeed approaches - but never exceeds - the Rayleigh wave speed c_r for small fracture resistances $\mathcal{G}_{c,\text{wp}}$ which is in good agreement with the theoretically predicted crack speed limits and experimental findings summarized in Section 3.4. As Section 6.4 will demonstrate, a traction loaded crack under Mode I conditions has the tendency to branch symmetrically if the weak plane is lacking. Furthermore, the crack speed without the weak plane does not exceed $0.6c_r$, see Fig. 6.28 b). Thus, the results from Section 6.4 in conjunction with the present results support the theory that dynamic instability phenomena like branching limit the maximum observable crack tip velocity if a preferred crack

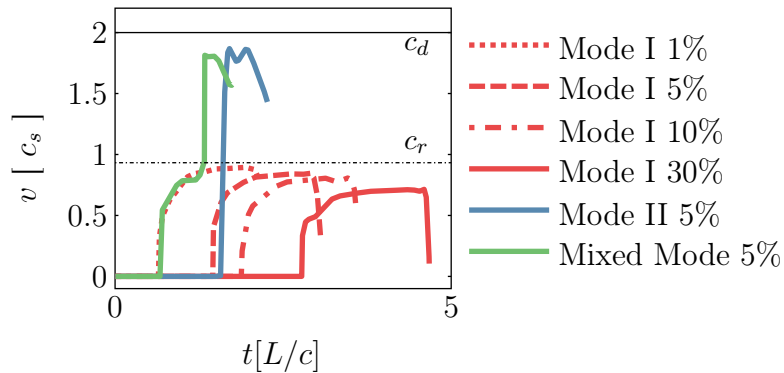


Figure 6.23: Crack speed for varying fracture toughness $\mathcal{G}_{c,wp}$ of the weak plane and varying mode of crack tip loading. The graphs show the crack speed records for different modes of crack tip loading and different values of the weak plane fracture resistance $\mathcal{G}_{c,wp}$ ranging from 1% to 30% of the bulk value $\mathcal{G}_{c,bulk}$. The horizontal dashed line indicates the Rayleigh wave speed.

growth direction, e.g. a weak plane, is missing.

Next, the mode of crack tip loading is changed from pure Mode I to pure Mode II. The resulting crack speed record is shown as a blue line in Fig. 6.23. It can be detected that the crack starts to grow a little bit later than the Mode I crack with the same fracture resistance of the weak plane. In contrast to the Mode I case, the Mode II crack exceeds c_s and accelerates rapidly to an intersonic crack speed of $\sim 1.8c_s$. Eventually, the crack velocity decays to $\sim 1.5c_s$ at the point of complete fragmentation of the body.

For Mixed Mode loading, the crack speed record is again different. Here, crack initiation is triggered much earlier, i.e. at $t \approx 0.7348 \frac{L}{c}$, see the green line in Fig. 6.23. Furthermore, there are also considerable qualitative differences compared to the two loading modes discussed above. At first, the crack starts to propagate subsonically and approaches a crack speed that is close to c_r . There is no rapid acceleration to this speed limit. In fact, the crack speed seems to converge to c_r just like in the Mode I case. The σ_{12} -stress field depicted in Fig. 6.24 a) shows no shock waves at this time. At $t = \frac{1.5 \cdot 0.6L}{c_s} = 1.2728 \frac{L}{c}$, reflected shear waves arrive at the crack tip and the crack accelerates to the intersonic crack speed regime. This transition occurs rapidly, as the crack speed crosses the ‘forbidden’ speed range $c_r < v < c_s$, cf. Section 3.4. This rather discontinuous increase of the crack speed is very similar to the abrupt crack acceleration found in the Mode II simulation. The maximum crack speed of $\sim 1.8c_s$ is also similar to the one that is observed for pure Mode II loading. Nonetheless, the predicted crack speed is significantly lower than the maximum crack speeds close to c_d reported in Gao et al. (2001). During the period of intersonic crack growth, a shock wave can be observed that emanates from the crack tip, see Fig. 6.24 c) and d) and a bulge can be identified that trails

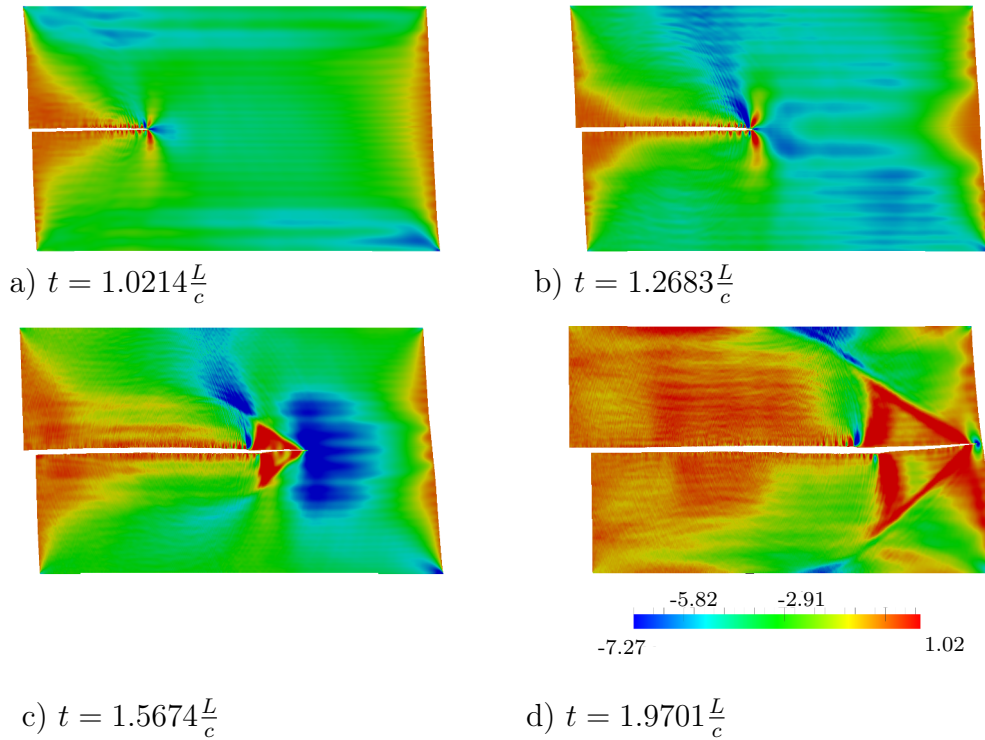


Figure 6.24: Post-processed contour plots of $\sigma_{12} \left[\sqrt{2\mu\mathcal{G}_{c,wp}/L} \right]$. Regions where $s = 0$ are rendered invisible in order to show the crack. The deformation is exaggerated.

behind the crack tip at the Rayleigh wave speed. However, the mother-daughter crack mechanism, reported in Gao et al. (2001), who argue that an intersonically growing daughter crack nucleates some distance ahead of the original subsonic (mother) crack, could not be verified in the simulations. This may be due to the smearing effects inherent in the regularized crack representation which prevent the detection of crack features at scales smaller than the parameter l .

Since the present phase field model stems from the energy based Griffith criterion of fracture mechanics, it is worthwhile to analyze the different energy contributions that are present in the body. Figure 6.25 plots the elastic E^e , fracture E^s and kinetic energy \mathcal{K} for all three loading types. In all cases, the elastic energy rises in the first part of the simulations and continues to do so even when the crack starts to grow. As soon as the point of crack initiation is reached, the fracture energy also increases, see Fig. 6.25. Fracture is furthermore accompanied by a sharp rise of the kinetic energy, which can be explained by the fact that material is accelerated away from the ligament once the crack has passed. The elastic and kinetic energy peak values for Mixed Mode and especially for pure Mode II are almost ten times higher than for Mode I loading. On the one hand this is a conse-

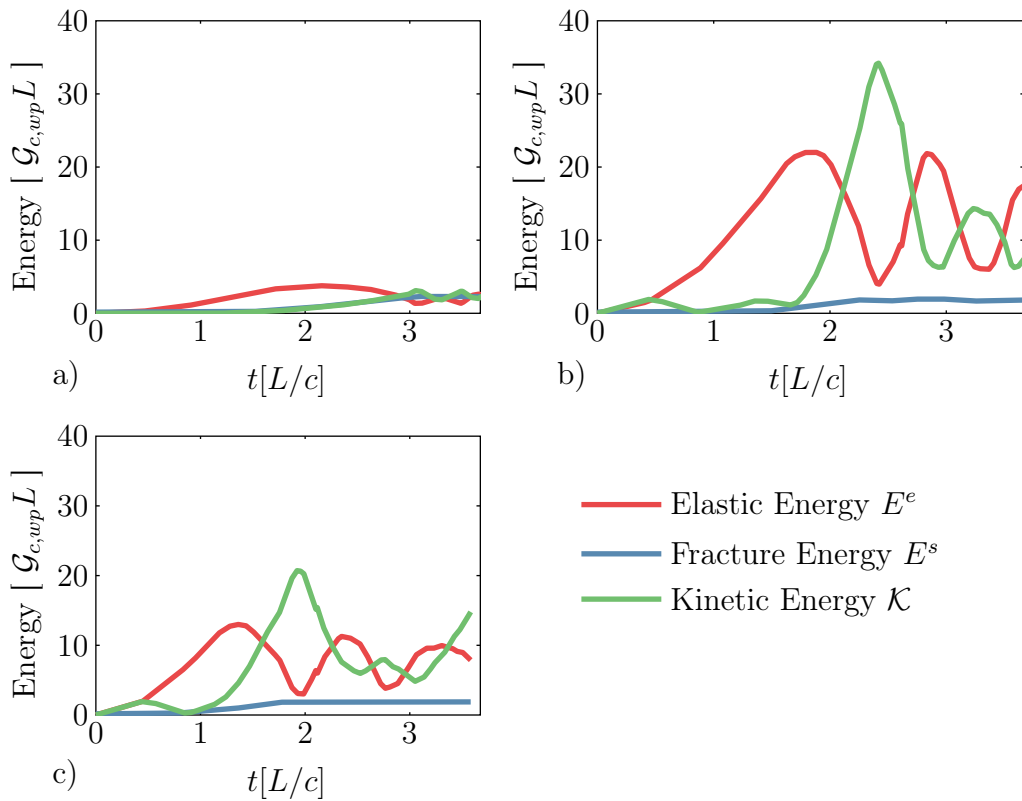


Figure 6.25: Energy plots of the elastic energy E^e , the fracture energy E^s and the kinetic energy \mathcal{K} for a) Mode I, b) Mode II and c) Mixed Mode loading. The fracture resistance of the weak plane is $\mathcal{G}_{c,wp} = 0.05\mathcal{G}_{c,bulk}$.

quence of the prescribed Mode II opening rate \dot{u}_2 is five times the Mode I opening rate \dot{u}_1 , on the other hand the characteristics of the fracture process possibly also play a role. The peak energies are highest for pure Mode II loading. In this case, the crack grows intersonically from the start and initiates much later than in the Mixed Mode case. Therefore, a lot of elastic energy can build up in the body, that is rapidly released in fracture energy and kinetic energy during the phase of fast intersonic fracture. After full fragmentation of the specimen, the total energy $E^t = E^e + E^s + \mathcal{K}$ is approximately constant. At this stage, it is possible to observe the conversion of elastic energy into kinetic energy and vice versa as phase shifted oscillations in the energy records, see Fig. 6.25 b) for $t > 2.2045\frac{L}{c}$ and Fig. 6.25 c) for $t > 1.8371\frac{L}{c}$. This is typical for oscillating elastic bodies. The fracture energy is small compared to the elastic and kinetic energies and is therefore hard to detect in Fig. 6.25. Hence, a rescaled record of the fracture energies for all three loading modes is displayed in Fig. 6.26. The irreversible part of E^s can be interpreted as the fracture energy. This energy component is proportional to the crack surface, i.e. to the crack length in 2D. Thus, the slope of E^s is approximately

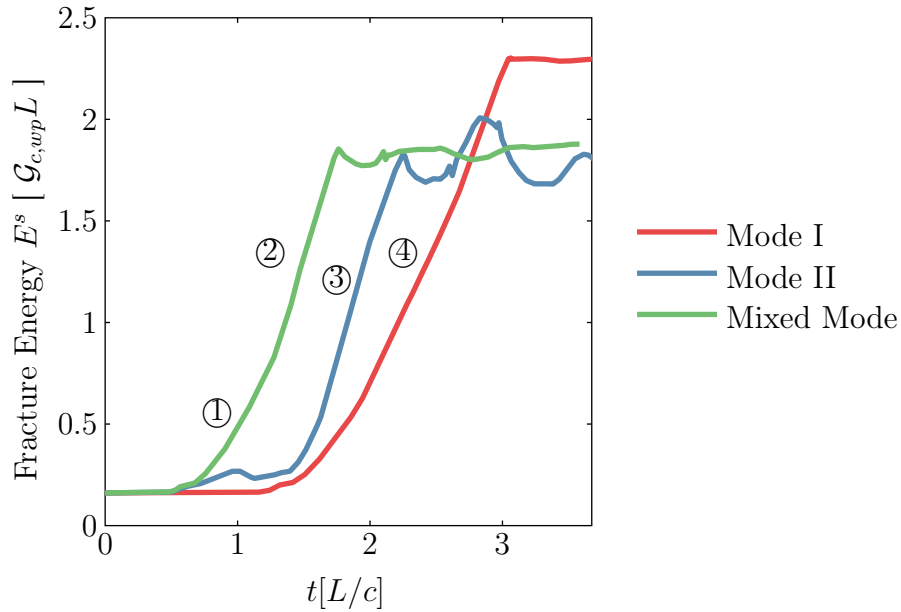


Figure 6.26: Fracture energy E^s for Mode I, Mode II and Mixed Mode loading. The fracture resistance of the weak plane is $\mathcal{G}_{c,wp} = 0.05\mathcal{G}_{c,bulk}$.

proportional to the crack speed v if only one crack tip propagates which is the case in the present simulations. All three E^s -records show parts with a nearly constant slope, i.e. an approximately constant crack speed. The mixed mode crack initiates earlier than both the Mode I and Mode II crack and consequently the Mixed Mode fracture energy is also the first to increase. In the first phase ①, see Fig. 6.26, the slope of E^s is nearly constant and the curve is close to parallel to the curve for pure Mode I loading ④. At this stage, the crack grows subsonically at a velocity just below c_r . Then a kink can be observed and E^s increases at a steeper slope ② that is similar to the slope for pure Mode II loading ③. The fracture energy reaches its maximum value when the crack has separated the specimen completely. Subsequently, E^s oscillates around a mean final value. Here, it becomes clear that E^s does not exclusively represent the irreversible part of the fracture energy. The final values of E^s are about the same for Mode II and Mixed Mode loading but the Mode I crack reaches a significantly higher final fracture energy E^s . Consequently, the Mode I crack has to be wider than the other two cracks since the final crack length is the specimen length L in all three cases. This may be explained by the tendency of Mode I cracks to branch at high crack speeds, cf. the numerical branching experiment reported in Schlüter et al. (2014b) and Section 6.4. In the present simulations, crack branching is prevented by the introduction of a weak plane and thus, the directional instability is only allowed to manifest as bulging and widening of the phase field crack inside the weak strip. The width of the strip

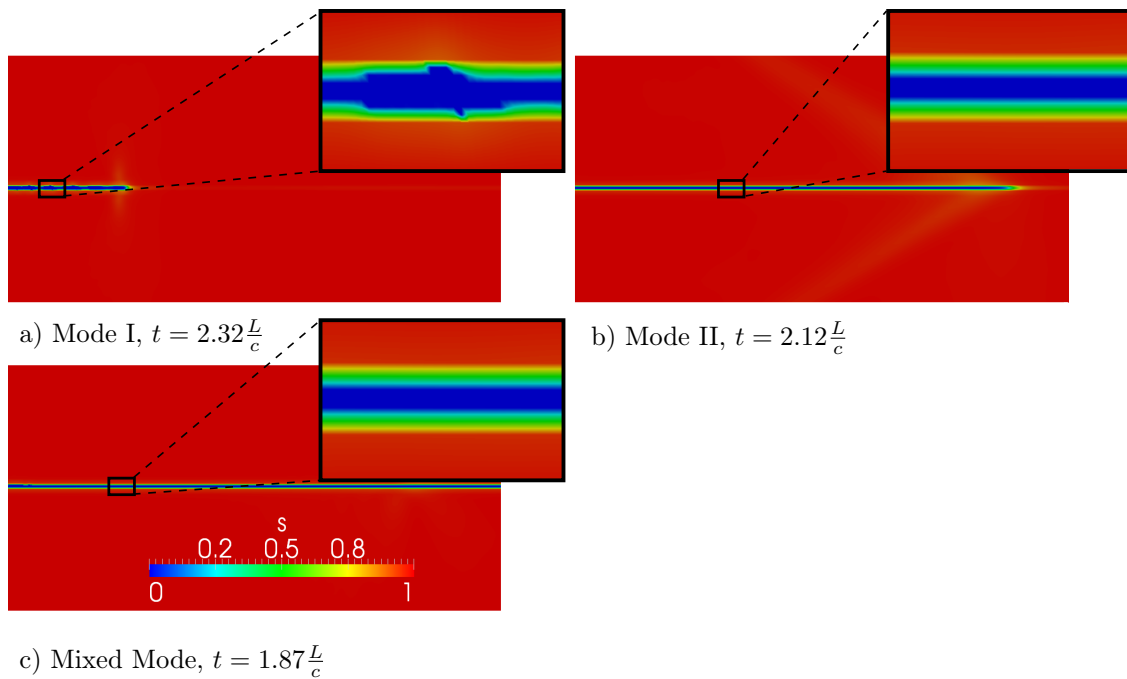


Figure 6.27: Section of a contour plot of s for a) Mode I , b) Mode II and c) Mixed Mode .

is $4l$. Thus, crack widening is possible to a certain extent, see Fig. 6.27 a). Crack bulging or widening does not occur for Mode II and Mixed Mode loading, see also Fig. 6.27 b) and c).

The numerical results presented in this section suggest that the derived model is able to predict the maximum crack speed in agreement with experimental data and theory. For symmetric crack opening, i.e. Mode I, it is shown that the Rayleigh wave speed is an upper limit for the crack speed which only can be reached if dynamic branching instabilities are avoided by prescribing the crack path. Mode II cracks are found to be able to propagate at a speed above the shear wave speed but below the dilatational wave speed. In this case, it is also necessary to trigger the crack to grow along a prescribed path by introducing a weak strip of reduced specific fracture energy to avoid kinking of the crack. For combined Mode I and Mode II loading, the crack starts to propagate subsonically and then jumps to the intersonic speed regime when reflected waves arrive at the crack tip. The results are in agreement with molecular dynamic simulations reported in Gao et al. (2001). Nonetheless, the mother-daughter crack mechanism as observed in Gao et al. (2001) could not be verified in the simulations.

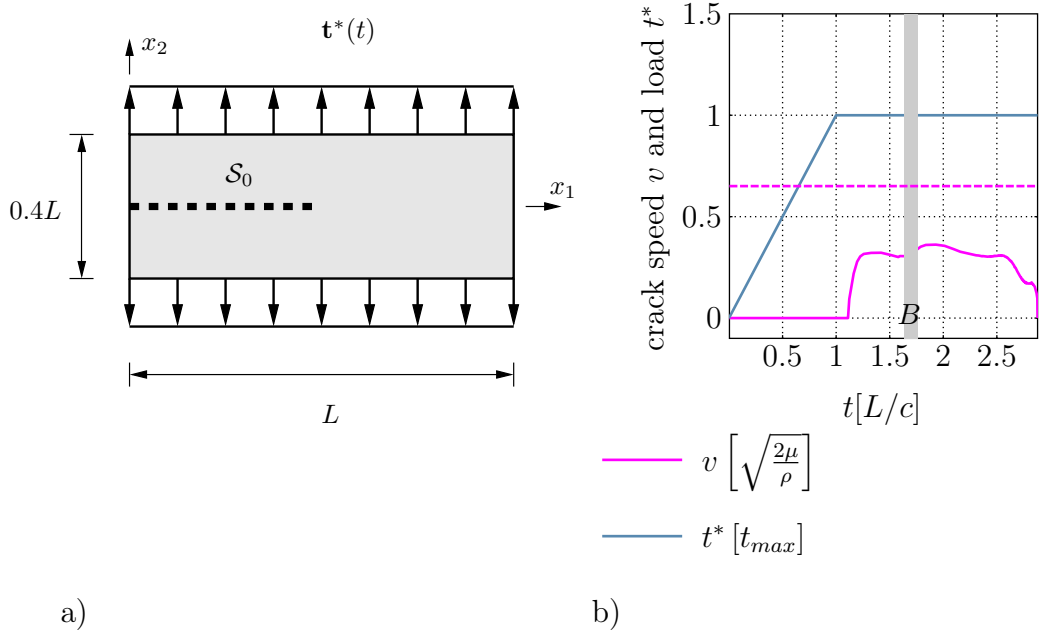


Figure 6.28: a) Setup for the branching problem and b) crack speed v and applied traction load t^* . The period of crack branching B is indicated by the grey region. The Rayleigh wave speed is indicated by the magenta dashed line.

6.4 Dynamic Crack Branching

The theoretical aspects and experimental findings concerning the phenomenon of dynamic crack branching of rapidly propagating Mode I cracks were briefly discussed in Section 3.5. Among the possible causes for dynamic branching are an excessive energy supply at the crack tip as well as a directional instability at high crack speeds. The argument states that this instability limits the experimentally observed crack speeds to velocities that are smaller than the theoretical limit value c_r . In the previous section, the directional instability mechanism has been removed by the introduction of a weak strip. Indeed, the associated phase field simulations have revealed that the maximum obtainable Mode I crack speed in phase field simulations converges to c_r as the fracture resistance of the weak strip goes to zero. Furthermore, previous studies reported promising results of phase field simulations of dynamic crack branching under symmetric Mode I loading conditions, see e.g. Borden (2012), Hofacker and Miehe (2013) and Schlüter et al. (2014b). In Hofacker and Miehe (2013) it is observed that the rate of E^s , cf. (4.1), as-

sumes a critical value prior to branching. On the other hand, Borden (2012) and Schlüter et al. (2014b) examine the relation between branching and the crack tip velocity and show a good agreement with the analytical results of Katzav et al. (2007), see Section 3.5.

This section is also concerned with numerical simulations of dynamic crack branching by means of the discussed phase field model. In order to get a deeper understanding of the energetic driving mechanisms involved in crack branching, a special focus is on the analysis of the configurational forces which act on a crack tip control volume of the type (4.119). A body with an initial crack as depicted in Fig. 6.28 a) is considered. The Lamé parameters of the material have identical values $\lambda = \mu$ and a regular mesh with an element size of $h = 2l$ is used. The length-scale parameter is set to $l = 0.005L$ and the parameter of the degradation function is specified as $a = 0.1$. The applied traction load $\mathbf{t}^* = \pm t^* \mathbf{e}_2$ is increased linearly to its maximum value of $t_{max} = 1.0 \sqrt{2\mu G_c/L}$ and afterwards held constant, cf. Fig. 6.28 b). Initially, the crack propagates in x_1 -direction and eventually branches, see Fig. 6.29. The crack speed – recorded for the lower branch – reaches its maximum value of $v \approx 0.56c_r$ right after branching occurs.

Figure 6.29 displays the hydrostatic stress as a contour plot. Furthermore, two crack tip control volumes of different size D_{10l} and D_{20l} as well as the respective crack driving configurational forces $\mathbf{G}_{D_\delta}^e + \mathfrak{B}_{D_\delta}$ and the cohesive configurational forces $\mathbf{G}_{D_\delta}^s$ are depicted. Before crack initiation, the cohesive configurational forces are the only ones of significant size and they have virtually the same value for both control volumes, see Fig. 6.29 a). Upon crack initiation, the crack does not branch immediately but initially the single crack tip propagates in x_1 -direction. During this period, the configurational forces acting on the two control volumes are approximately identical and the crack driving configurational forces are almost of the same size as the cohesive configurational forces, see Fig. 6.29 b). This involves that the Griffith criterion is fulfilled in the sense of (4.129). As the crack branches, the size of the control volume has significant impact on the computed configurational forces. To illustrate this fact, Fig. 6.29 c) depicts a situation in which only the lower crack tip is included in the smaller control volume, but the larger control volume still contains both crack tips. While for the smaller control volume the crack driving and cohesive configurational forces are of comparable size and opposed to each other, this is not the case for the larger control volume. Instead, the crack driving configurational force is considerably larger than the cohesive configurational force. In this situation, the evaluated configurational forces for the larger control volume D_{20l} do not represent the energetic state at the crack tip and the violation of the Griffith condition by a positive ξ -component of the total configurational force, cf. (4.129), should be considered as an effect of the finite size of the control volume. The state in which two crack tips are included in a

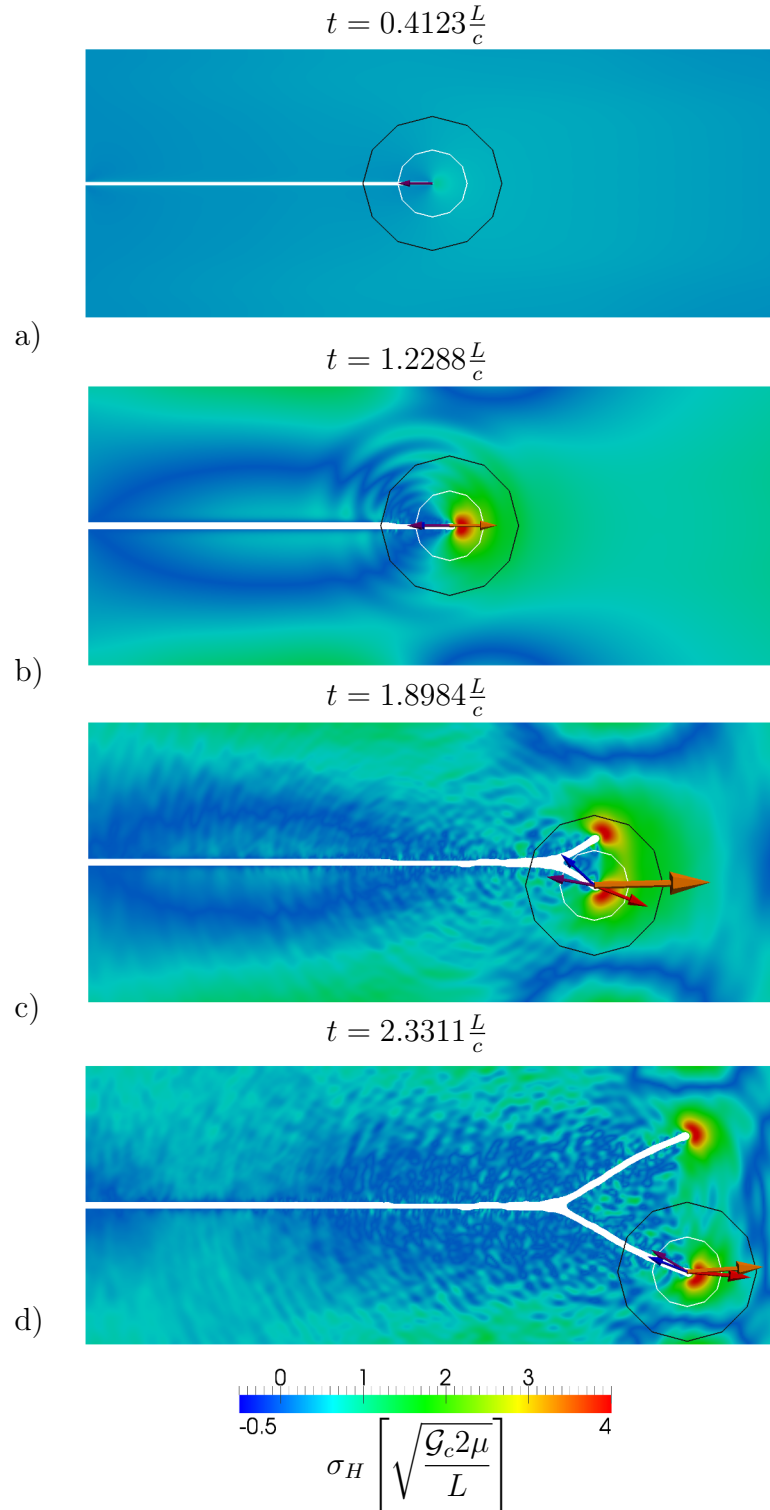


Figure 6.29: Contour plots of the hydrostatic stress $\sigma_H = \sigma_{11} + \sigma_{22} / 2$ at different times. Tip disc control volumes D_{10l} (white circles) and D_{20l} (black circles). Cohesive configurational forces $\underline{\mathbf{G}}_{D_{10l}}^s$ (blue arrows) and $\underline{\mathbf{G}}_{D_{20l}}^s$ (purple arrows). Crack driving configurational force $\underline{\mathbf{G}}_{D_{10l}}^e + \underline{\mathfrak{P}}_{D_{10l}}^s$ (red arrows) and $\underline{\mathbf{G}}_{D_{20l}}^e + \underline{\mathfrak{P}}_{D_{20l}}^s$ (orange arrows). Regions where $s < 0.2$ are rendered invisible in order to represent the crack. The length of the arrows representing the configurational forces is proportional to their absolute values.

crack tip control volume is unavoidable because a certain size of D_δ compared to the length-scale l is necessary, see assumption B in Section 4.6.2. However, the occurrence of a positive ξ -component of the total configurational force – which is caused by the presence of a second crack tip in D_δ – can be taken as an early indication for crack branching. Eventually, only the lower crack tip is contained in the crack tip control volume, see Fig. 6.29 d) and a better agreement of the computed configurational forces between both control volumes can be detected. Furthermore, at this point the cohesive configurational forces and the crack driving configurational forces tangential to the crack approximately balance each other so that the connection to the Griffith condition is established again.

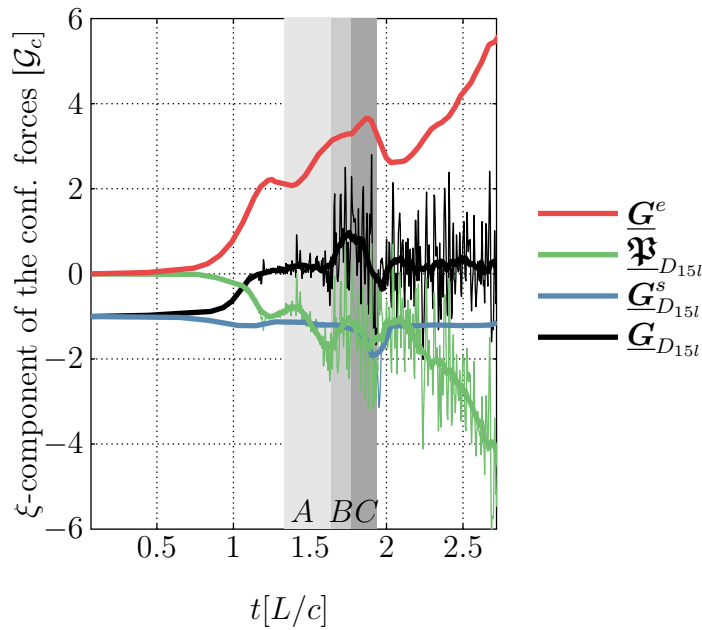


Figure 6.30: ξ -components of the configurational forces for a tip disc control volume with a radius of $\delta = 15l$ (thin lines) and corresponding moving average filtered data (thick lines). The stages of branching A , B , C are indicated by regions of different shades of grey.

It is not possible to unambiguously determine the moment of branching since the diffuse phase field representation of the crack surface does not allow to identify distinct crack tips in the very early stages of the branching process. Instead, branching is announced by a period A of crack widening during which bulges form along the crack as well, see Fig. 6.30. This indicates the directional instability of the crack. Subsequently, pronounced bulging of the crack tip initiates the actual crack branching and eventually two distinct crack tips can be identified. This branching period is denoted as B and lasts from $t = 1.63\frac{L}{c}$ until $t = 1.76\frac{L}{c}$. A

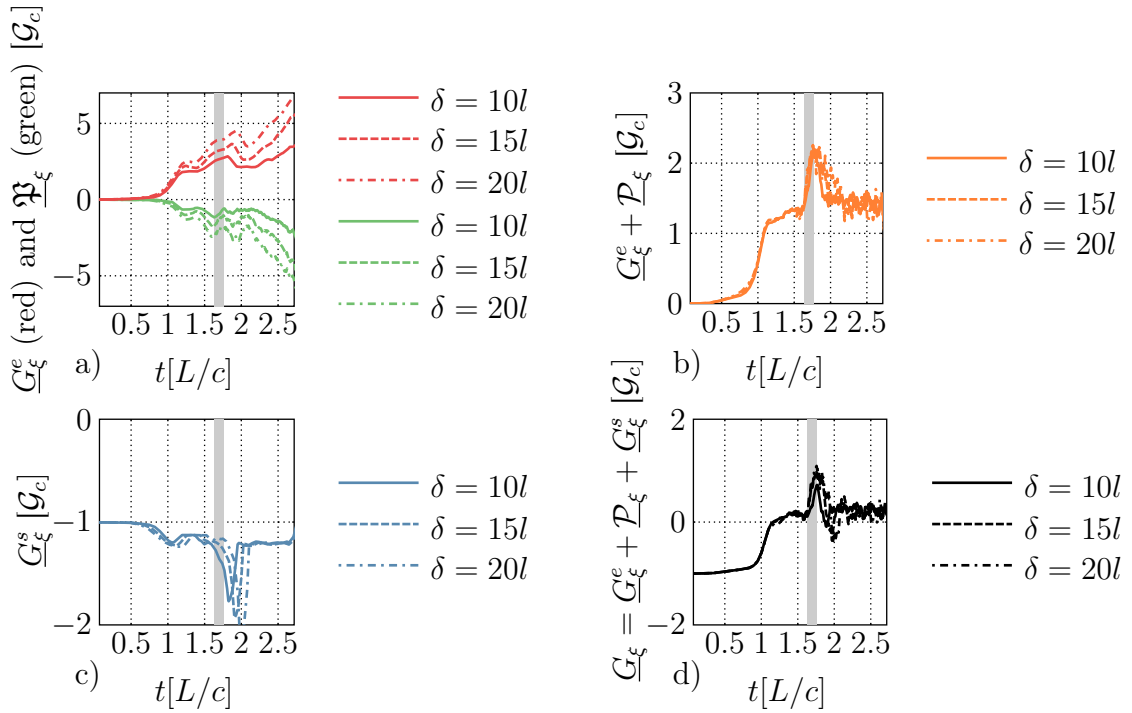


Figure 6.31: Configurational force components for different radii of the tip disc: a) the elastic part \underline{G}_ξ^e (red) and the pseudo-momentum $\underline{\mathfrak{P}}_\xi$ (green), b) the sum of the elastic part and the pseudo-momentum $\underline{G}_\xi^e + \underline{\mathfrak{P}}_\xi$, c) the cohesive configurational force \underline{G}_ξ^s , and d) the total configurational force \underline{G}_ξ . The branching period B is indicated by the grey region.

third characteristic period may be defined as the period C , where branching already took place but both crack tips are still contained in the considered crack tip control volume D_δ . The configurational force components acting on a control volume of size $\delta = 15l$ are displayed in Fig. 6.30. In addition to the computed data (thin lines) the corresponding moving average filtered data sets (thick lines) are plotted. The filtered data corresponds to the unweighted mean of the data of the last 30 time steps. Furthermore, the resulting lag is corrected. These post-processing steps are necessary to make the strongly oscillating configurational forces more accessible to interpretation. Initially, only the cohesive configurational force – which represents the material resistance to crack propagation – is non-zero and its ξ -component agrees well with $-\mathcal{G}_c$ as can be presumed from (4.128). Over the course of the simulation this does not change significantly, except for a slight increase of $|\underline{G}_\xi^s|$ well before crack initiation and a distinct peak just at the end of period C that lasts from $t = 1.76\sqrt{L^2\rho/2\mu}$ to $t \leq 1.94\sqrt{L^2\rho/2\mu}$. The elastic component of

the configurational force $\underline{G}_\xi^e > 0$ is the crack driving force, whereas and $\underline{\mathfrak{P}}_\xi < 0$ represents the inertial resistance to crack propagation.

For small times, the total configurational force is $\underline{G}_\xi \approx -\mathcal{G}_c$, since the crack tip is unloaded, and thus $\underline{G}_\xi^e = 0$ and $\underline{\mathfrak{P}}_\xi = 0$ but the material's resistance $\underline{G}_\xi^s = -\mathcal{G}_c$ is non-zero. A negative ξ -component of the total configurational force implies that the resulting energetic driving force on the crack tip favors a recession of the crack, i.e. crack healing. Hence, an according evolution of the order parameter should take place in this subcritical load state. However, such an evolution of s is prevented by the irreversibility constraint (4.31). The irreversibility constraint counteracts the crack closing energetic driving force \underline{G}_ξ^s in subcritical load states but – since the antagonistic irreversibility force is not accounted for in the configurational force balances (4.112) and (4.118) – a net configurational force $\underline{G}_\xi \approx -\mathcal{G}_c \neq 0$ follows.

As in previous examples, see e.g. Fig. 6.19, the ξ -component of the total configurational force also assumes distinctly positive values. \underline{G}_ξ is slightly larger than zero in the phase of notable crack widening A , and shows peak averaged values of around $\underline{G}_\xi \approx 1.0 \mathcal{G}_c$ during crack branching, i.e. phase B . This suggests that a second crack tip has already formed inside D_{15l} which is also reflected in a steep increase of the crack driving force \underline{G}^e . The limited change of $|\underline{G}_\xi^s|$ during periods A and B is consistent with the considerations of Section 4.6.2, since the net value of \underline{G}_ξ^s is given by (4.128) and thus, only the cohesive configurational stress on the boundary segment traversing the crack $\partial D_{\delta, B \rightarrow A}$ is decisive. Consequently, no information about the cohesive effects in the interior of D_{15l} is available through \underline{G}_ξ^s during crack branching. Note, that the cohesive configurational force \underline{G}_ξ^s peaks significantly later than \underline{G}_ξ , i.e. at the end of C , which drives the total configurational force \underline{G}_ξ back to approximately zero.

The various components of the tip configurational force are displayed in Fig. 6.31 for different sizes of the crack tip control volume that range from $\delta = 10l$ to $\delta = 20l$. As expected, the elastic configurational force \underline{G}_ξ^e and the pseudo-momentum $\underline{\mathfrak{P}}_\xi$ taken in isolation are clearly dependent on the size of the control volume. Their graphs (quantitatively) vary significantly for different size δ , see Fig. 6.31 a). The sum $\underline{G}_\xi^e + \underline{\mathfrak{P}}_\xi$ on the contrary is less sensitive to the size of the control volume, see Fig. 6.31 b), which is in good agreement with the considerations that led to (4.132). A significant difference in the graphs of $\underline{G}_\xi^e + \underline{\mathfrak{P}}_\xi$ can, however, be noted directly after crack branching. This is a result of the fact that the second crack tip may still be contained in a larger control volume while it is not located in a smaller control volume anymore. The presence of a second crack tip in D_δ violates the assumptions that lead to (4.132) and thus, domain independence of the crack driving configurational force is not given in the branched case.

The cohesive configurational forces show pronounced peak values, see Fig. 6.31 c).

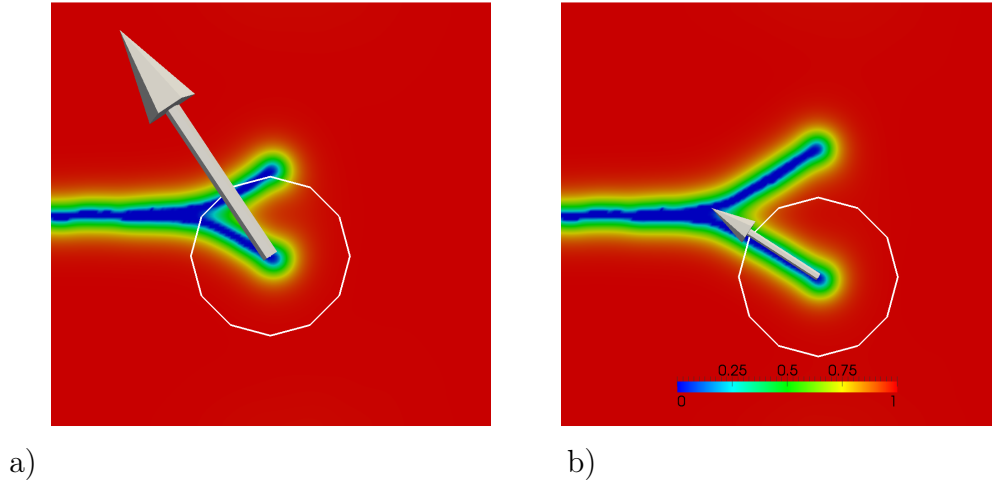


Figure 6.32: Cohesive configurational force $\underline{G}_{D_\delta}^s$ (arrows) a) at the end of period C and b) shortly after period C . The size of the arrows is proportional to the absolute value of $\underline{G}_{D_\delta}^s$. The circle indicates the considered control volume D_δ .

The magnitude of the peaks as well as the time of their occurrence is also clearly dependent on δ . The peaks appear right before the second crack leaves the respective control volume completely. In this situation, the boundary ∂D_δ touches a significant segment of the secondary branch, see Fig. 6.32 a), which leads to an increase of \underline{G}_ξ^s , cf. also (4.128). Since the period C in which both crack tips are contained in the control volume lasts longer for a larger control volume, the characteristic maximum of \underline{G}_ξ^s is delayed for larger control volumes as well. Furthermore, sizeable control volumes also contain a substantial part of the second crack at the end of period C . Hence, the respective peak value of \underline{G}_ξ^s for increasing δ is larger as well. Briefly after period C the cohesive configurational force again assumes a value that is slightly smaller than \mathcal{G}_c , see also Fig. 6.32 b).

The total configurational force \underline{G}_ξ shows a low sensitivity on δ . All graphs in Fig. 6.31 d) have a significant peak during crack branching in common. Its magnitude ranges from $\underline{G}_\xi \approx 0.7\mathcal{G}_c$ for $\delta = 10l$ to $\underline{G}_\xi \approx 1.0\mathcal{G}_c$ for $\delta = 20l$.

It is concluded that the interpretation of the configurational forces during crack branching needs to be done carefully. In particular the cohesive configurational force does not represent the material resistance to crack propagation if two crack tips are contained in the considered control volume. As a result of this, it is observed that an excessive crack driving configurational force $\underline{G}_\xi^e + \mathfrak{P}_\xi$ – which manifests in a positive ξ -component of the total configurational force $\underline{G}_\xi > 0$ – goes along with dynamic crack branching. Although the observation of a distinctly positive $\underline{G}_\xi > 0$ may be considered as counterintuitive of the configurational

force approach for post-processing purposes, it enables the identification of crack branching even before two distinct crack tips can be observed in contour plots of the phase field variable. In addition, the simulation shows that the energy release rate $\mathcal{G} \approx \underline{G}_\xi^e + \underline{\mathfrak{P}}_\xi$, the cohesive configurational force \underline{G}_ξ^s and the total configurational force \underline{G}_ξ are less sensitive to the size of the crack tip control volume than \underline{G}_ξ^e and $\underline{\mathfrak{P}}_\xi$, which is in good agreement with the considerations made in Section 4.6.2.

7 Application to Thermoelastic Fracture Problems

This chapter presents two examples of how the phase field approach to dynamic brittle fracture can be applied to thermoelastic fracture problems. In contrast to the previous numerical examples, the temperature is considered as an additional field in order to model fracturing induced by a laser beam in Section 7.1 and heavy-ion irradiation in Section 7.2. The numerical strategy S2, c.f. Section 5, as well as the quadratic formulation of the degradation function with $a = 2$, see (4.85), are chosen for the simulations presented in this chapter. Furthermore, the VDD formulation of the strain energy density is employed except for the simulations presented in Section 7.1 which were performed utilizing the SD formulation.

7.1 Laser-Cutting of Ceramic Substrates

Lasers have been widely used to cut ceramics and glasses, either by scribing the work piece in order to control and facilitate subsequent fracturing due to mechanical loads, see Garibotti (1963), or by sole use of a laser, see eg. Lumley (1969) and Lambert et al. (1976). In some cases an additional coolant is used to induce thermal stresses, see e.g. Kondratenko (1997). All mentioned techniques aim at directing a cutting path by means of a laser, whereas full material separation is eventually due to brittle fracture caused by mechanical loads or thermoelastic effects. Process effectiveness, i.e. power consumption and quality of the cutting surface, can be enhanced by a modification of the technique by Lambert et al. (1976), as it is claimed in Tsai and Chen (2003). The work of Tsai and Chen (2003) analyzes the process in detail and even provides a finite element analysis of the thermoelastic problem that enhances the understanding of the mechanics behind the fracture process. However, actual fracturing was not described in these simulations. A more recent discussion of the laser-aided controlled fracture technique for glass, which comprises experiments as well as finite element simulations, can be found in Nisar et al. (2009). Nonetheless, the simulations presented in this

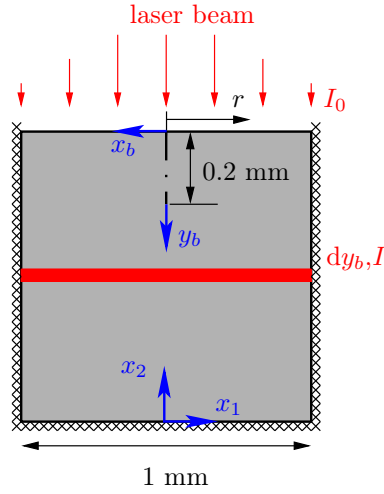


Figure 7.1: Computational model and illustration of the Beer-Lambert law. The initial crack is indicated by a dash-dotted line.

work also do not model the separation of the material.

This section discusses a phase field fracture model as a means to simulate the laser-aided manufacturing process presented in Tsai and Chen (2003) and follows the results published in Schlüter et al. (2017). As a first step, the details of the model of the laser-substrate interaction are introduced. Afterwards, the analysis of a simplified laser-cutting scenario is presented. This part also discusses the influence of two basic process parameters, i.e. the applied laser power and the size of an initial groove in the material on the quality of the manufacturing process.

7.1.1 Modelling of the Laser Beam

In order to describe the effect of a laser beam on the solid, the Beer-Lambert law is employed. It has been extensively used to describe laser-solid interaction e.g. in Zohdi (2014). In order to illustrate the Beer-Lambert law, a setup as depicted in Fig. 7.1 is considered. The power per unit area of the beam cross section that enters the solid and is not reflected at the surface is denoted as the surface intensity $I(x_b, y_b = 0, t) = I_0(x_b, t)$, where x_b is the lateral distance from the center of the beam and y_b measures the penetration depth of the beam. The Beer-Lambert law states that the loss of intensity of the beam, i.e. the energy that is absorbed by a slice of thickness dy_b of the solid material, is proportional to dy_b and $I(x_b, y_b, t)$, i.e.

$$dI = -\alpha I(x_b, y_b, t) dy_b \quad (7.1)$$

where α is the attenuation coefficient. Integration results in

$$I(x_b, y_b, t) = I_0 \exp(-\alpha y_b) \quad (7.2)$$

which can be substituted in (7.1) to yield the absorbed energy

$$-\frac{dI}{dy_b} = \alpha I_0 \exp(-\alpha y_b) = s^\theta. \quad (7.3)$$

The heat source determined by (7.3) enters the energy balance (4.30).

7.1.2 Simulation of Laser-Cutting of Ceramic Substrates by a Controlled Fracture Technique

The simulations that are discussed in this section are motivated by the experiments described in Tsai and Chen (2003). Tsai and Chen presented a cutting process for relatively thick, up to 10 mm, ceramic substrates that is driven by two lasers - a focused Nd:YAG laser and a defocused CO₂ laser. The main purpose of the Nd:YAG laser is to melt and evaporate an approximately 0.5 mm deep groove on the surface of the substrate. Simultaneously, the second laser induces the additional thermal stress that extends this initial crack and eventually breaks the substrate. The evaporation and melting due to the Nd:YAG laser is not explicitly included in the phase field simulations, since the model presented in Chapter 4 does not account for possible phase changes of the material. Instead, the effect of the Nd:YAG laser is modelled by defining an initial crack, see Fig. 7.1. The analysis is limited to straight laser paths in order to be able to reduce the model to 2D. The computational model, which is depicted in Fig. 7.1, assumes plane strain conditions, i.e. the out of plane displacement is zero, $u_3 = 0$, and the in-plane displacements depend only on x_1 and x_2 , i.e. $u_1 = \hat{u}_1(x_1, x_2)$ and $u_2 = \hat{u}_2(x_1, x_2)$, which also implies that the absorbed laser intensity of the second laser is assumed to be independent of the x_3 -coordinate, i.e. $I_0 = \hat{I}_0(x_1, x_2, t)$. This is certainly a simplifying assumption because it differs from the real situation, where the effect of the laser resembles a point heat source moving on the surface of the substrate. However, the assumption is deemed necessary to reduce the computational effort of the simulations. The boundary of the computational domain is assumed to be stress free. Furthermore, there is no heat flux across the boundaries except for the absorbed laser energy. Following the above mentioned assumptions the local intensity of the non-reflected part of the beam on the surface can be expressed as

$$I_0(x_1, t) = I_{0,\max} X(x_1) T(t), \quad (7.4)$$

where $I_{0,\max}$ is the intensity in the center of the beam spot, $X(x_1)$ is the lateral distribution of the intensity and $T(t)$ describes a possible dependence of the intensity on the time. It is

$$X(x_1) = \exp\left(-\left(\frac{x_1}{x_0}\right)^2\right). \quad (7.5)$$

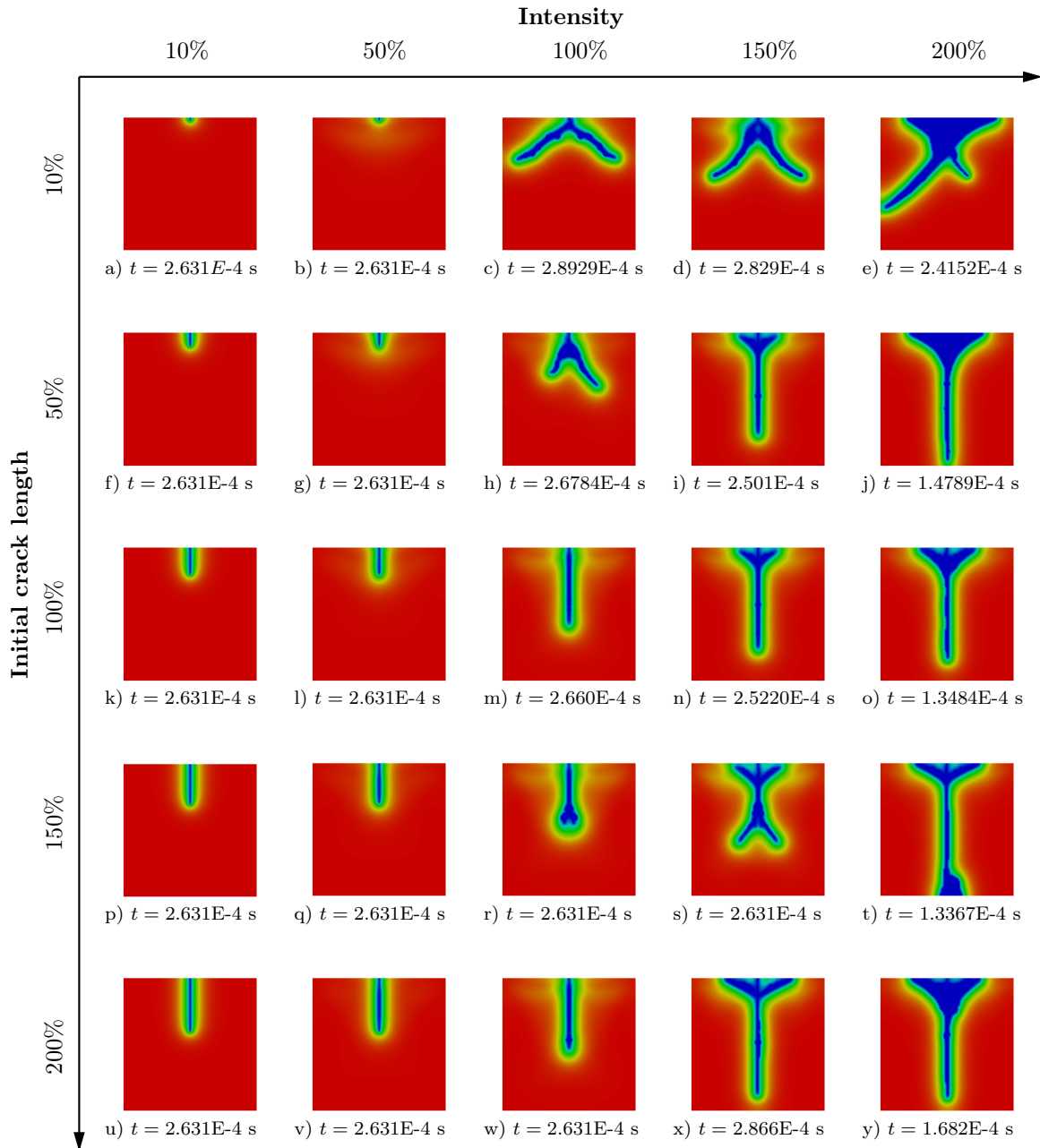


Figure 7.2: Contour plots of the order parameter $s(\mathbf{x}, t)$ for all investigated parameter sets $(l_{\text{crack}}, I_{0, \text{max}})$.

Table 7.1: Material and model parameters. Except for the specific fracture energy \mathcal{G}_c and the length-scale parameter l the values of the material parameters are the same as in Tsai and Chen (2003).

mechanical	phase field	thermal
$\lambda = 138.51 \cdot 10^9 \frac{\text{N}}{\text{m}^2}$	$l = 0.25 \cdot 10^{-4} \text{ m}$	$\alpha_T = 8.2 \cdot 10^6 \frac{1}{\text{K}}$
$\mu = 162.6 \cdot 10^9 \frac{\text{N}}{\text{m}^2}$	$\mathcal{G}_c = 0.379 \frac{\text{N}}{\text{m}}$	$\kappa = 33.5 \frac{\text{W}}{\text{m K}}$
$\rho = 3960 \frac{\text{kg}}{\text{m}^3}$		$c_\theta = 780 \frac{\text{J}}{\text{kg K}}$

and

$$T(t) = \begin{cases} 0.0 & \text{if } t < 0.0 \\ 1.0 & \text{if } t \geq 0.0 \end{cases}. \quad (7.6)$$

In conjunction with (7.3), the equations (7.4) - (7.6) allow to model the laser. The beam parameters are $x_0 = 0.373 \cdot 10^{-3} \text{ m}$, $I_{0,\max} = 0.538\text{E}8 \text{ J/m}^2\text{s}$ and $\alpha = 522260.0 \text{ 1/m}$. As in Tsai and Chen (2003) the considered substrate material is a Al_2O_3 ceramic. The mechanical and thermal properties used in the simulations are shown in Table 7.1.

In the following, the problem is investigated for varying initial crack lengths and varying intensities of the laser beam. The reference values, i.e. 100%, are a groove crack depth of $l_{\text{crack}} = 0.2 \text{ mm}$ and a beam intensity of $I_{0,\max} = 0.538 \cdot 10^8 \text{ J/m}^2\text{s}$ respectively. The input parameters are varied to be 10%, 50%, 100%, 150% and 200% of the reference values. A total number of 25 simulations has been performed to cover the permutations of input pairs $(l_{\text{crack}}, I_{0,\max})$. All simulations were aimed to last $0.25\text{E-}4 \text{ s}$. Due to early abortion of the computations, this could not be achieved for all pairs $(l_{\text{crack}}, I_{0,\max})$.

The computed crack patterns are illustrated in Fig. 7.2 as contour plots of the order parameter $s(\mathbf{x}, t)$. It can be observed that lower intensities, i.e. 10% and 50% of the reference value, do not lead to crack extension at all, and apart from the initial crack no further fracturing occurs. This changes for higher intensities that are equal to or larger than the reference intensity. In this case, crack growth takes place for all initial crack lengths. Nonetheless, large differences in the topology of the cracks can be observed. For 10% l_{crack} , crack branching seems to be likely, see Fig. 7.2 c)-e). This tendency can also be observed for simulations with larger initial crack lengths, see e.g. Fig. 7.2 h), r), and s). No branching occurs for 100% and 200% l_{crack} . In the case of higher intensities, the material near the upper surface, i.e. material that is directly hit by the laser, fails and a large region of cracked

material can be found, see e.g. 7.2 e), j), and y). Full separation occurs only for the combination (150% l_{crack} , 200% $I_{0,\text{max}}$), see e.g. Fig. 7.2 t). Since the problem is completely symmetric, the asymmetric crack patterns displayed in Fig. 7.2 e), h), and t) have to be attributed to small numerical fluctuations that eventually trigger the simulation to converge to a non-symmetric solution.

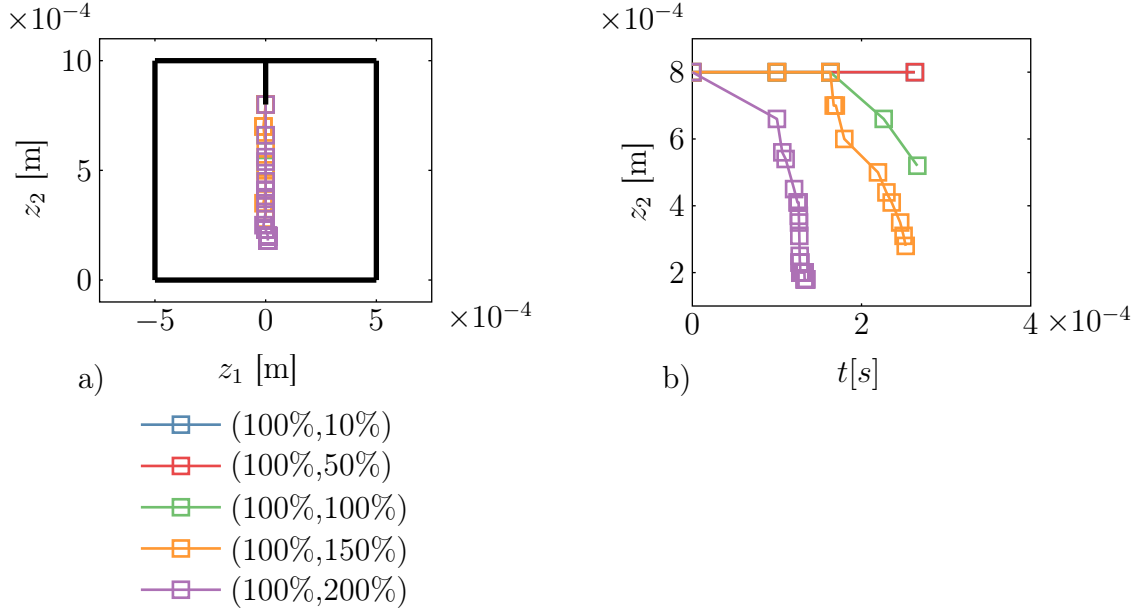


Figure 7.3: a) Successive crack tip positions and b) x_2 -coordinate of the crack tip. In this plot the initial crack length is kept constant at 100% l_{crack} and only the intensity $I_{0,\text{max}}$ is varied.

In the following, the combinations (100% l_{crack} , 10% - 200% $I_{0,\text{max}}$), i.e. Fig. 7.2 k) - o), are examined in more detail. Figure 7.3 a) shows the successive crack tip positions for all combinations (100% l_{crack} , 10% - 200% $I_{0,\text{max}}$). The crack tip mainly grows in negative x_2 -direction. Thus, the x_2 -coordinate of the crack tip position z is plotted versus the simulation time in Fig. 7.3 b). Not surprisingly, the higher the intensity of the laser beam, the earlier a critical level of strain energy is reached at which the crack extends. Furthermore, the crack speed indicated by the slope of the curves in Fig. 7.3 is largest for the highest intensities. Eventually, the final crack length, i.e. the extent to which the specimen is separated, also reaches a maximum for the largest intensity. Due to the energy-based character in the present model, it is worthwhile to take a closer look at the energies that control fracturing. Plots of the total elastic energy E^e and the total fracture energy E^s are depicted in Fig. 7.4 a) and b), respectively. Due to the laser beam the temperature rises and thermo-mechanical coupling leads to a global rise of the stored elastic

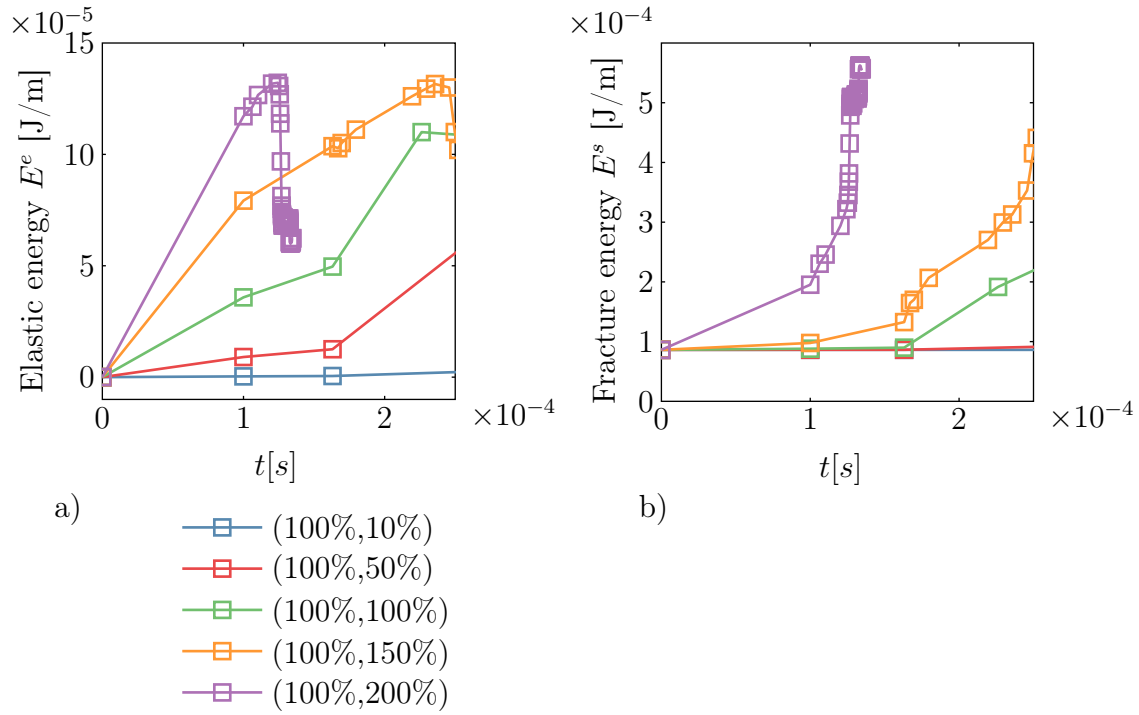


Figure 7.4: a) Elastic energy E^e and b) fracture Energy E^s per unit thickness. In this plot the initial crack length is kept constant at 100% l_{crack} and only the intensity $I_{0,\text{max}}$ is varied.

energy. In case of the two highest intensities, a part of the elastic energy is released due to fracturing. Interestingly, the maximum value of the global elastic energy appears to be the same for these two simulations. The rate of the fracture energy also increases for larger intensities as can be observed in Fig. 7.4 b). Additionally, more damage is inflicted by the higher intensities, c.f. Fig. 7.2, which manifests in a larger final value of the fracture energy.

The goal of the regarded manufacturing process is to cut the substrate without unnecessarily damaging the material. Ideally, the laser should extend the initial crack through the whole body whereas secondary cracks that diminish the surface quality are to be avoided. Consequently, a possible figure of merit of process parameters could be the final crack length divided by the total fracture energy i.e.

$$\bar{l}_{\text{crack}} = \frac{l_{\text{crack,final}} - l_{\text{crack}}}{E^s}, \quad (7.7)$$

where $l_{\text{crack,final}} = 1 \text{ mm} - z_2(t_{\text{max}})$ is the final crack length computed from the x_2 -coordinate of the crack tip position $z_2(t_{\text{max}})$, c.f. Fig. 7.1. From (7.7) it can be concluded that an effective parameter set results in a large effective crack length \bar{l}_{crack} .

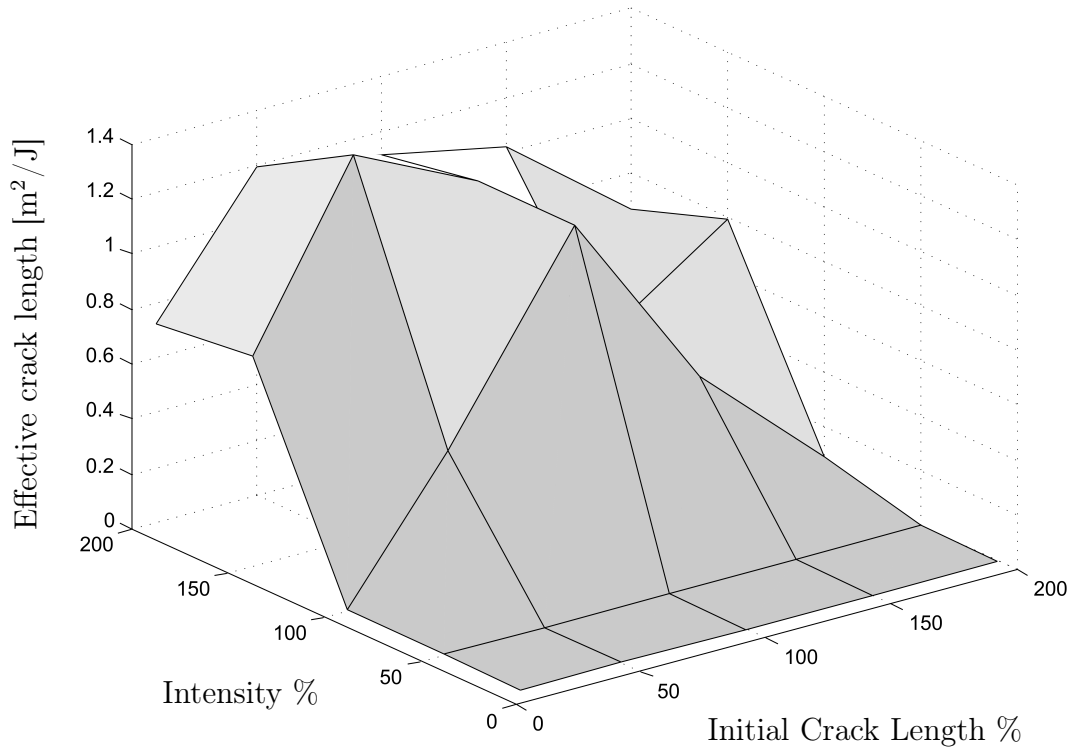


Figure 7.5: Effective crack length \bar{l}_{crack} as a function of the beam intensity $I_{0,\text{max}}$ and the initial crack length l_{crack} .

A plot of \bar{l}_{crack} is displayed in Fig. 7.5. Of course \bar{l}_{crack} for the lowest intensities is zero, since $l_{\text{crack,final}} = l_{\text{crack}}$, see also Fig. 7.1. The maximum of \bar{l}_{crack} , i.e. the optimal process parameters out of the given set of simulations, results from the input parameters (50% l_{crack} , 150% $I_{0,\text{max}}$).

This section demonstrates that the present phase field model is indeed a viable tool to simulate the laser cutting process of ceramics, as described in Tsai and Chen (2003). However, the present 2D simulations cannot capture all effects that govern the laser cutting process described in Tsai and Chen (2003). Hence 3D simulations are certainly necessary in the future to precisely predict the outcome of the process and therefore to be able to accurately optimize process parameters.

7.2 Phase Field Modelling of Thermal Fracture in the Context of Irradiation Damage

This section is about modelling thermoelastic fracturing due to relativistic particle beams, e.g. heavy ion beams. Such beams are able to almost instantaneously deposit a huge amount of energy (> 1 GeV) into the considered solid. Induced energy densities as high as 12 kJ/g result in a rapid temperature rise in a spatially limited region. Thermoelastic effects finally lead to a highly dynamic expansion of the material. This induces elastic waves into the body that may cause failure due to brittle fracture.

For new high-power accelerator facilities such as the future facility for antiprotons and ion research (FAIR) in Darmstadt and other existing or planned neutrino factories, it is of utmost interest to develop reliable models that can predict dynamic fracture under the mentioned loading conditions. In particular, computer-aided calculations are required to identify critical operating conditions for the components and for optimized engineering of devices to be exposed to intense particle beams. A hydrodynamic model has been proposed to simulate the propagation of shock waves in Tahir et al. (2007) and finite element simulations of the mechanical response of a solid target triggered by heavy-ion beams have been reported in Plate (2008) and Nguyen (2013). Nevertheless, none of these studies actually modelled material separation. A phase field model has been considered for the simulation of dynamic brittle fracture due to heavy-ion beams in Schlüter et al. (2017) for the first time. This section presents the findings from Schlüter et al. (2017).

The phase field model presented in this work is designed to predict brittle fracture in solids. Hence, it is not capable of modelling other causes of failure like phase changes or plastic deformation. It should therefore be considered as a tool to predict fracture in basically two situations:

- The particle beam is of relatively low intensity and the final temperature is significantly lower than the melting or sublimation temperature of the target material. Thus, the whole body can be assumed to be linearly elastic with constant material parameters.
- The particle beam is of high intensity but causes inelastic behaviour (plastic deformation, phase changes, etc.) only in a confined region of the target. Hence, elastic waves triggered by the beam, propagate in regions of the body that can be assumed to consist of linear elastic material with constant material parameters.

In the latter case the results in the vicinity of the beam-spot are not reliable but

the model can be used to predict brittle fracture in the remaining parts of the target.

If a solid is exposed to an intense beam of energetic heavy ions, a large amount of energy is absorbed by the material within a short time span. The temperature increases rapidly and strains and stresses are induced in the body due to thermoelastic expansion which is constrained by the surrounding material. Under these loading conditions, dynamic effects caused by elastic waves in the material are expected to be decisive for failure processes. Compared to the speed of elastic waves, thermoelastic effects due to heat conduction are much slower for the considered materials and consequently heat conduction is negligible regarding the short time intervals that will be considered. Thus, the heat equation (4.30) is not solved but the temperature is prescribed as an external stationary field of defined spatial distribution.

An axisymmetric finite element formulation of the phase field model from Chapter 4 is employed in the simulations. This means all fields \mathbf{u} , s and θ are assumed to be independent of the angular coordinate φ in a cylindrical r, φ, z -coordinate system, see Fig. 7.6. For this reason, not only the geometry but also the loading and boundary conditions are not allowed to break the axial symmetry. These assumptions reduce the computational effort significantly. However, the formation of cracks in radial direction cannot be captured by the reduced model and needs to be addressed in future 3D simulations.

7.2.1 Fracturing of a Cylinder

A cylindrical body that is subjected to a particle beam is considered, see Fig. 7.6. Since the problem is axisymmetric, it is sufficient to reduce the model to the shaded rectangular area that is also shown in Fig. 7.6. The temperature load θ^* is assumed to be independent of the z - and φ -coordinate and can be expressed as

$$\theta^*(r, t) = \theta_{\max} R(r) T_0(t), \quad (7.8)$$

where $R(r)$ is a function of the radial coordinate and $T(t)$ is a function of the time. A temperature field θ^* that is nearly independent of the penetration depth of the particles is a reasonable assumption if the target-beam configuration is set up in such a way that the peak energy deposition, the so-called Bragg peak, lies outside the target geometry, see e.g. Tahir et al. (1999). The highest increase of temperature is expected in the center of the beam, i.e. at $r = 0$ mm, whereas the outer parts of the cylinder will not be hit directly. Hence an exponential distribution

$$R(r) = \exp\left(-\left(\frac{r}{r_0}\right)^2\right) \quad (7.9)$$

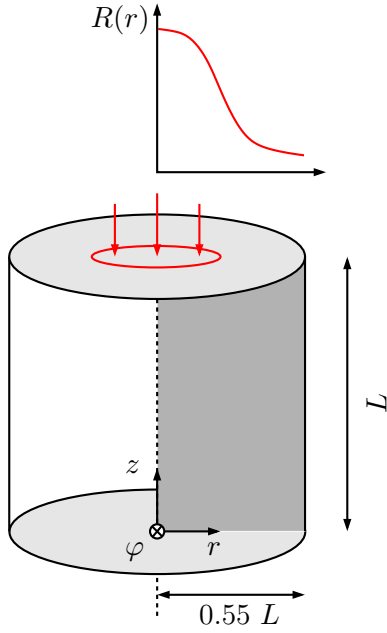


Figure 7.6: Cylindrical specimen subjected to a particle beam.

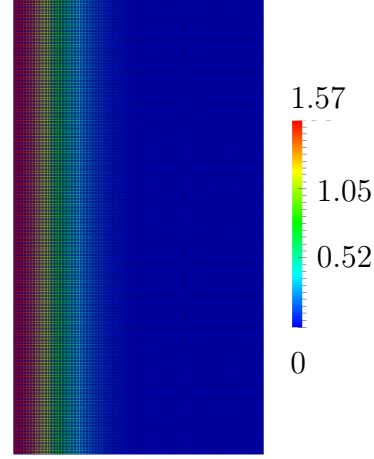


Figure 7.7: Finite element mesh and contour plot of the temperature field θ [$\mathcal{G}_c/\rho c_\theta L$] for $g(t) = 1.0$ and $\theta_{\max} = 1.57$ [$\mathcal{G}_c/\rho c_\theta L$].

is chosen. The length parameter is $r_0 = 0.086L$. The temperature increases rapidly when the beam hits the body. This is described by the function

$$T_0(t) = \begin{cases} 0.0 & \text{if } t < t_1 \\ \sin^2\left(\frac{\pi}{2} \frac{t - t_1}{t_e}\right) & \text{if } t_1 \leq t \leq t_1 + t_e \\ 1.0 & \text{if } t \geq t_1 + t_e \end{cases} \quad (7.10)$$

which is illustrated in Fig. 7.8. The loading time scale is $t_e = 0.2199 \frac{L}{c}$ and it is $t_1 = 0$. The mesh consists of 165×300 square finite elements with an edge length of $h = 1/300L$. Since the element size is the same for the whole mesh, the computed crack pattern will not be influenced by any mesh-inhomogeneities. The boundaries of the body are all stress free and the phase field is set to $s_0 = 1$ at all nodes, so the material is originally undamaged. The coefficient of thermal expansion is

$$\alpha_T = 6.4293 \sqrt{\frac{\rho^2 c_\theta^2 L}{\mathcal{G}_c 2\mu}}. \quad (7.11)$$

The Poisson ratio is set to $\nu = 0.3$ and the characteristic length is specified as $l = 0.005L$.

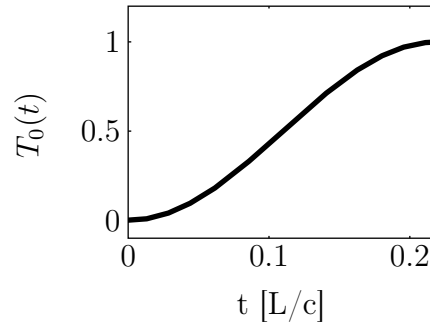


Figure 7.8: Function $T_0(t)$ for $t_e = 0.2199L/c$.

Figure 7.9 shows the results of the simulation. The contour plots display the hoop stress σ_φ , see (3.37). Regions in which the phase field is lower than a threshold of $s < 0.1$ are rendered invisible in order to illustrate the crack. Furthermore, the stress field is plotted on the deformed body, while the deformation is exaggerated by a factor of 30.

The temperature load has reached its final value, i.e. $T(t) = 1.0$, at time $t_e = 0.2199\frac{L}{c}$. During the heating process, the material starts to expand and a bulge forms at the top and the bottom edge of the specimen. In the interior body, however, inertia forces resist the expansion. Consequently, a compressive stress results in the center of the specimen, see Fig. 7.9 a). This maximum compressive stress decreases over time as the material further expands. Simultaneously, elastic waves are emitted towards the circumferential surface of the cylinder and the first cracks can be observed, see Fig. 7.9 c). These cracks nucleate at the upper and lower boundary of the cylinder in regions that experience high shear stress σ_{rz} . This is consistent with the formulation of the elastic energy density (4.42), that allows for crack propagation under deviatoric or shear load states. At time $t = 1.7611\frac{L}{c}$ further cracks form, see Fig. 7.9 d). In contrast to the primary shear cracks, the material now breaks within the interior of the body. These cracks grow and branch several times, see Fig. 7.9 e). The reflection of elastic waves at the boundaries and at the cracks leads to a rather complicated stress field. The final crack pattern is restricted to the region around the axis of the cylinder, which is shattered to pieces, see Fig. 7.9 f). Note that the absolute value of the peak compressive, i.e. negative stress, is much larger than the material strength estimate σ_c^* but the positive tensile stress does not exceed this limit significantly. This is also a feature of the formulation (4.42), which models a resistance against crack growth in compression.

Failure of heavy-ion irradiated copper cylinders has been reported in Richter et al. (2011). The cylinders were irradiated by a uranium beam along their axis similar to the situation that is shown in Fig. 7.6. In the experiments, damage

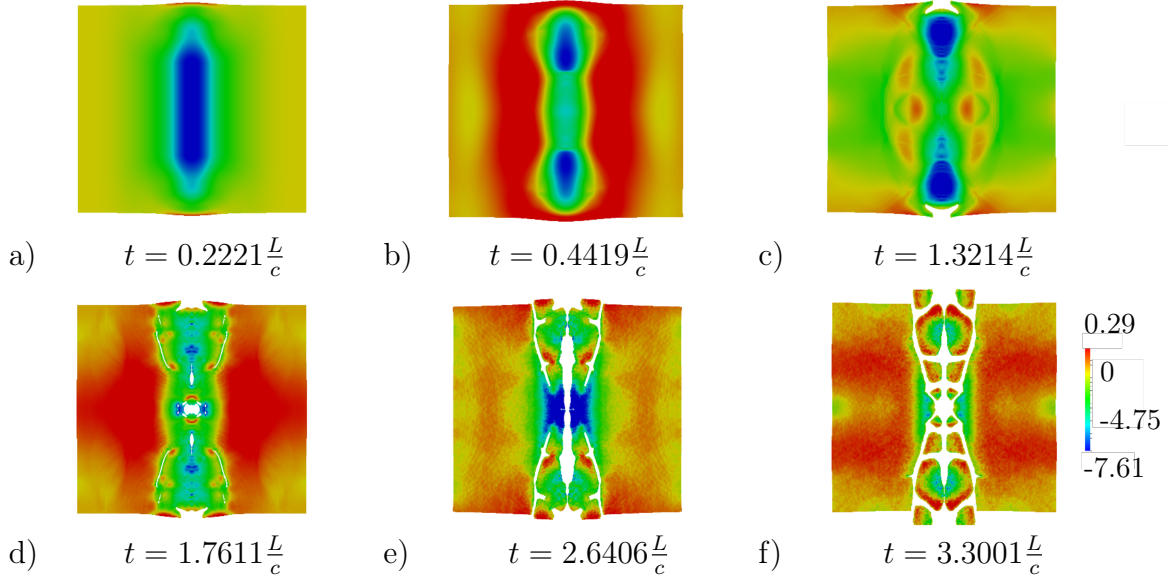


Figure 7.9: Hoop stress $\sigma_\varphi \left[\sqrt{G_c 2\mu/L} \right]$. Although the finite element model only covers one half of the model, the whole body is restored in a post processing step to enhance the visualization of the results.

was also confined to the region around the cylinder's axis and the beam cut a 3.8 mm deep hole in the target. However, failure was probably not solely due to fracture. Additional experiments, using thin disc targets subjected to a heavy-ion beam have been conducted at the GSI Helmholtz Centre for Heavy Ion Research in fall 2014. Although most specimens failed due to melting or did not fail at all because of the low beam intensity, a copper-diamond specimen showed different signs of damage, see Fig. 7.10. Here, the beam cut a hole into the specimen and brittle fracture possibly may have played a role in the failure process.

7.2.2 Fracturing of a Disc

The second numerical example of this section studies a circular disk. The disc is subjected to an annular particle beam as it is shown in Fig. 7.11.

The setup can also be interpreted as a fast rotating disc, in which the angular velocity ω advects thermal energy much faster than heat conduction takes place. Nevertheless, inertia effects due to fast rotation are neglected in the simulations. The loading and the geometry are again axisymmetric, so the model can be reduced to the shaded area. The temperature load is expressed in the form

$$\theta^*(r, t) = \theta_{\max} R(r) T_0(t). \quad (7.12)$$

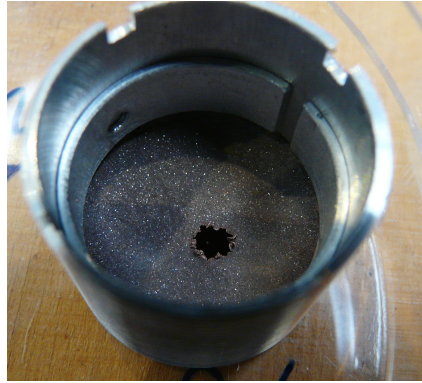


Figure 7.10: Beam induced damage in a thin disc made of a copper-diamond composite caused by a short pulse, 125 MeV/u 238U beam with an intensity of 10^{10} ions/pulse. The disc had a thickness of $200 \mu\text{m}$ and a diameter of 20 mm. The picture is taken from Schlüter et al. (2017).

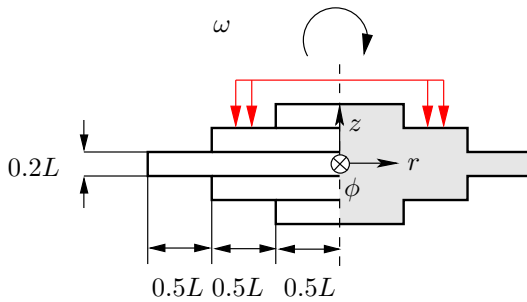


Figure 7.11: Disc subjected to a particle beam.

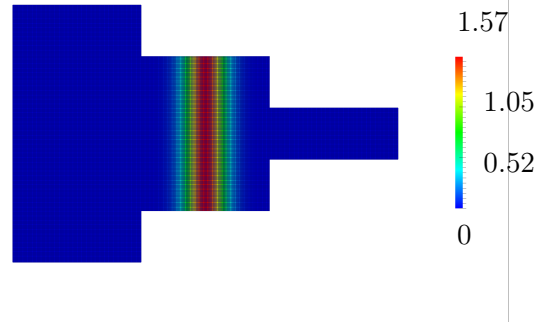


Figure 7.12: Finite element mesh and contour plot of the temperature field $\theta [G_c/\rho c_\theta L]$ for $g(t) = 1.0$ and $\theta_{\max} = 1.57 [G_c/\rho c_\theta L]$.

In this example, the radial distribution $R(r)$ is set to

$$R(r) = \exp\left(-\left(\frac{r - 0.75L}{r_0}\right)^2\right), \quad (7.13)$$

where $r_0 = 0.06L$. The temperature profile is also shown in Fig. 7.12 and the function $T(t)$ is the same as in Section 7.2.1. The regular mesh consists of 81000 quadratic elements. Again, all boundaries are stress free and the material parameters remain unchanged to the previous example.

The results are shown in Fig. 7.13 as contour plots of the phase field variable s . At first, the phase field drops considerably in regions where the temperature load is applied, see Fig. 7.13 a). Subsequently, several cracks form in the interior of

the body and cracks nucleate at the surfaces of the disc as well. Note the crack nucleation at a number of corners which suggests some kind of a notch effect of these geometric features, see Fig. 7.13 b). The maximum temperature load is reached at $t_e = 0.2199 \frac{L}{c}$. Dilatational waves start to reach the center of the disc at time $t_c \approx \frac{0.75L}{c_d} + t_e \approx 0.4507 \frac{L}{c}$. Shortly after that one can once again observe a significant drop of the phase field in a large region, see Fig. 7.13 c). In contrast to the initial cracks, however, final damage, i.e. $s = 0$, is not restricted to thin cracks. Instead, a large region is completely broken material and several thin cracks emerge from this region, see Fig. 7.13 d) and Fig. 7.13 e). Here, it can be assumed that the internal length l is too large to resolve a number of very close thin cracks. Hence, the result is not a set of small cracks but one large region of completely damaged material. The final crack pattern is shown in Fig. 7.13 f). The two simulations

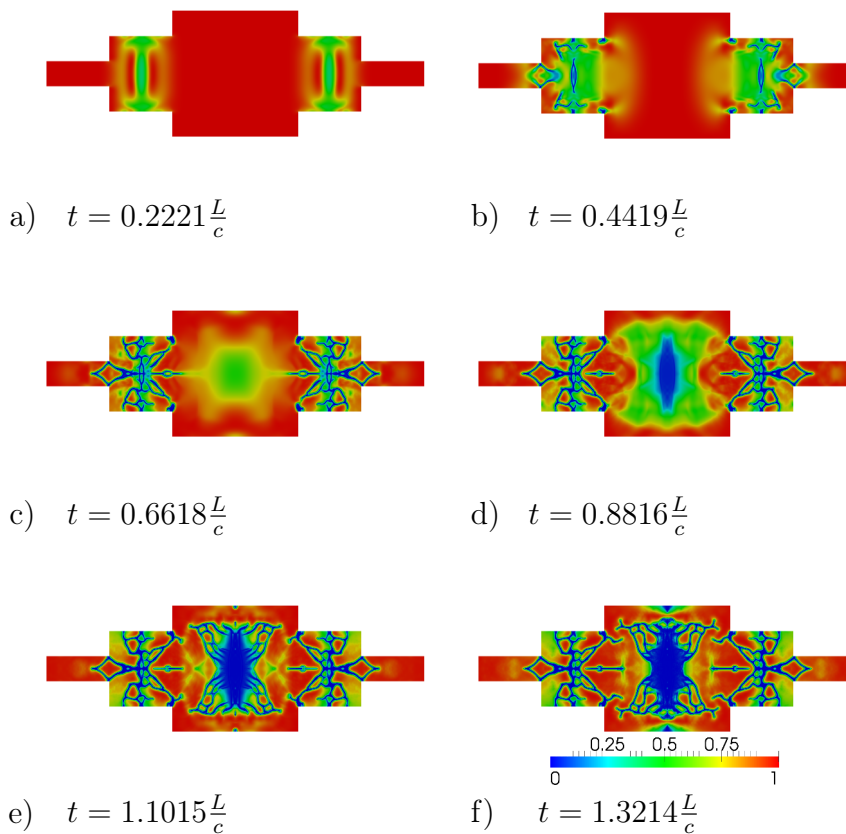


Figure 7.13: Contour plots of the phase field s . Although the finite element model only covers one half of the model, the whole body is restored in a post processing step to enhance the visualization of the results.

presented in this section illustrate the application of the phase field approach to

the coupled phenomenon of dynamic thermal fracture. Nonetheless, the relevance of the model for predicting structural failure caused by heavy-ion beams could not yet be validated by comparison to experimental results, which is considered to be an important next step. Since the current facility in Darmstadt cannot deliver beams of sufficient intensity to actually cause fracture in most situations, high-power lasers have to be used until FAIR is in service. Furthermore, the temperature-dependence of critical material parameters like the Young's modulus should be taken into account in the future in order to capture the possibly large changes that occur in material which is hit directly by the beam.

8 Conclusion and Outlook

In this work, a phase field model of dynamic brittle fracture has been investigated. The model originates from the variational formulation of brittle fracture of Francfort and Marigo (1998) which may be interpreted as a generalization of the classical Griffith condition for crack growth of linear elastic fracture mechanics. An additional scalar field, the so-called phase field, provides a smooth regularized representation of the cracks which also allows to express the fracture energy and the strain energy as functionals of the displacement field and the phase field. Since brittle materials are considered, this work assumes linear elastic material behaviour. Following the idea of the variational formulation of brittle fracture, the crack evolution is determined from local minimization of the combined fracture and strain energy with respect to the displacement and phase fields. This postulate on crack growth is stated in the framework of Hamilton's variational principle and it yields a set of coupled partial differential equations as necessary conditions. These equations describe the local evolution of the primary fields. The first field equation is the equation of motion which is coupled to the phase field via a degradation function that describes the loss of stiffness in broken material. A second field equation governs the evolution of the phase field, i.e. crack growth. This relation is referred to as the phase field evolution equation and it contains a specific part of the strain energy density which acts as a source term that drives the local evolution of the phase field. Apart from the displacement and the phase field, the temperature is considered as a third primary field. However, a corresponding field equation is not obtained from a variational principle but it is stated as a separate postulate of the balance of energy, i.e. the first law of thermodynamics. This implements the capability to reproduce thermal loading situations into the model. Although, the derived set of governing field equations is able to describe the spatial and temporal evolution of the three primary fields, modifications are necessary to govern certain physical features of fracture. Special attention has to be given to the irreversibility of fracturing, which is modelled by prescribing adequate homogeneous Dirichlet boundary conditions on the phase field as proposed in Kuhn (2013). Additionally, in reality, cracks behave differently in tensile situations than they do in compressive mechanical states. This tension-

compression asymmetry concerns the resistance to crack nucleation in undamaged material, as well as the correct modelling of the boundary conditions at already existing cracks. In particular, the impenetrability of the material and the contact of the crack faces during crack closure need to be implemented. The approach to include the tension-compression asymmetry into the model relies on a decomposition of the strain energy density in positive, i.e. crack driving, and negative, i.e. not crack driving, components. Two common ways to implement this decomposition are the volumetric-deviatoric decomposition by Amor et al. (2009) and the spectral decomposition first introduced by Miehe et al. (2010b). It is found that both methods significantly improve the unphysical behaviour of the unmodified formulation. Nonetheless, considerable differences exist between the two modifications in particular under shear loads. In this situation, the spectral decomposition predicts a higher resistance to crack nucleation in originally undamaged material. Furthermore, a residual stiffness remains for a sliding motion of the crack faces of a phase field crack. Consequently, the spectral approach is not recommended to model Mode II crack propagation.

The constitutive behaviour of the material up to fracture is strongly influenced by the choice of the degradation function. In this work, a general cubic degradation function that has originally been proposed by Borden (2012) is employed. The effect of the choice of the degradation function is investigated analytically for a simplified 1D situation that follows the approach explained in Kuhn et al. (2015) as well as in numerical simulations. It is shown that the general cubic degradation function better models brittle material behaviour than the rather common quadratic degradation function. In this context, the well-known effect of the regularization length-scale on the effective material strength is also demonstrated.

The concept of configurational forces can be used to describe the energetic change due to modifications of a solid body's material configuration, e.g. a translation of a crack tip. Thus, the concept is very close to the energetically driven phase field model for dynamic brittle fracture. It is demonstrated that the configurational forces acting on the crack tip of a phase field crack are related to the classical Griffith condition for crack growth. Furthermore, the potential of the configurational forces as a post-processing tool is highlighted in numerical simulations of complex fracture scenarios such as crack branching.

Apart from the implementation of the irreversibility constraint, the numerical treatment of the phase field model by a finite element scheme is straightforward. Nonetheless, efficiency of the chosen solution strategy is an issue with phase field simulations of dynamic brittle fracture since the computational effort can become large. Thus, different staggered and monolithic solution strategies are presented and compared to each other in two benchmark problems. A staggered scheme with explicit time integration by the central difference method is found to be partic-

ularly accurate and efficient. Alternatively, a monolithic solution strategy with time integration by a modified Newmark method also performs well in the benchmarks. The discussed solution strategies allow to conduct a number of numerical experiments that demonstrate features and capabilities of the phase field model to describe cracks and fracturing in different situations. An analysis of stationary cracks for instance displays the effect of the tension-compression asymmetry formulations in static and dynamic situations. In addition, the simulation of dynamic crack nucleation scenarios shows the model's capability to handle this complicated situation. Numerical experiments motivated by the works of Hopkinson (1872) and Hopkinson (1921) display that the dynamic model clearly can predict fracture in situations in which wave reflection at the body's boundaries has major impact on the results, whereas the study of crack nucleation in the notch ground of a CT specimen highlights the difference between quasi-static and dynamic phase field formulations of brittle fracture in a crack nucleation scenario. The dynamic model predicts a considerably longer initial crack than the quasi-static model. In contrast to the quasi-static model, crack arrest appears after the initial phase of rapid crack extension in the dynamic case. The analysis of the configurational forces acting on the crack tip reveals that the configurational forces do not represent the state at the crack tip as long as the whole crack is contained in the considered control volume. Nevertheless, if the crack tip lies within the control volume and the crack intersects the boundary of the control volume the connection of the phase field model to the Griffith condition is confirmed by the computed configurational forces. Subsequently, an analytical solution for crack nucleation is compared to the results obtained from a phase field simulation and a reasonable agreement is found. The next part of this work deals with the effect of the mode of crack tip loading on the maximum obtainable crack speed in phase field simulations. Indeed, the phase field model is able to predict crack speeds that agree with theoretical results, experiments and molecular dynamic simulations. For Mode I loading the limit speed is for instance the Rayleigh wave speed of the material which can only be achieved if the directional instability of such a crack is removed by prescribing the crack path. This is accomplished by introducing a thin strip of weakened material with reduced specific fracture energy into the bulk material. Such a modification is necessary for Mode II as well in order to prevent the kinking of the crack. In the Mode II case, crack speeds in the intersonic speed regime, i.e. crack velocities that are larger than the speed of equivoluminal waves but smaller than the characteristic velocity of irrotational waves, can be observed.

Dynamic crack branching is treated as well. Here, the focus lies on the evaluation of the configurational forces acting on a crack tip control volume for post-processing purposes. It is shown that during crack branching the size of the chosen control volume has a significant effect on the computed configurational forces. As

long as both crack tips are contained in the control volume, the configurational forces do not comply with the Griffith condition for crack propagation, which can in fact be used to identify a branching event even before it can be noticed in the spatial distribution of the phase field.

The application of the present phase field model to thermoelastic fracture problems is demonstrated by means of two examples. In this part of the work, the temperature is considered as an additional field in the simulations meaning that the thermoelastic formulation is employed. First, a manufacturing process for the cutting of ceramic substrates is studied. The work of Tsai and Chen (2003) describes such a process which makes use of two lasers. Initially, a focused laser melts a groove in the substrate which is extended by the thermal stress induced by the second defocused laser. In this work, only the second laser is explicitly accounted for by prescribing an adequate heat source. The groove melted by the first laser is modelled by defining an initial crack. The results are analyzed and an approach is proposed to use the computational model to find optimal process parameters. As a second application scenario, dynamic brittle fracture in a structure that is subject to heavy-ion beams is investigated. Such a situation appears in new high-power accelerator facilities like for instance the future facility for antiprotons and ion research (FAIR) at Darmstadt. The ion beam instantaneously deposits a huge amount of energy in the interior of the regarded solid and thus, the temperature increases rapidly. Since the resulting thermoelastic expansion of the irradiated material and the subsequent propagation of elastic waves are much faster than effects of heat conduction, the temperature is not considered as a free field variable but is prescribed in the simulations. It is demonstrated that the present phase field model is, in principle, a viable tool to predict this kind of structural failure.

In summary, it can be concluded that the phase field model at hand is indeed capable of reproducing critical features of dynamic fracturing. Its sound physical basis which lies in the classic Griffith condition can also be verified in the simulations by evaluating the configurational forces acting on a crack tip as well as by the comparison of numerical simulations with analytical results and experimental data. Furthermore, the approach is suitable for solving engineering problems that involve desired or unwanted material separation due to brittle fracture.

The application of the present model to engineering problems certainly has great potential, and thus should be a future topic of research. Regarding manufacturing processes, the approach can be utilized as a design tool to safeguard against unwanted structural failure or, as demonstrated in laser cutting example in this work, as a means to simulate desired material separation that is part of the manufacturing process.

In order to make the phase field approach to brittle fracture amenable to more complicated geometric situations, which consequently require computation-

ally more expensive simulations, further effort must be expended in improving the efficiency of numerical solution strategies.

Often, fracture in technical devices is not triggered by a unique impact load but by a cyclically recurrent load pattern. This situation eventually results in the formation of a fatigue crack. Apart from the implementation of more complex material models, the description of such types of fracturing is also a promising research direction that has rarely been addressed so far.

Lastly, the common tension-compression asymmetry formulations, that were discussed in this work, face several problems. Improvement of this aspect of phase field models for fracture is key to a more realistic description of crack behaviour under compressive loads. Furthermore, a mathematical proof of convergence of these formulations to a discrete crack model is still missing.

A Notation and Mathematical Preliminaries

The position of points is described in a right-handed rectangular coordinate frame with unit base vectors $\mathbf{e}_1, \mathbf{e}_2, \mathbf{e}_3$ in a three dimensional Euclidean space \mathbb{E}^3 as

$$\mathbf{x} = x_1\mathbf{e}_1 + x_2\mathbf{e}_2 + x_3\mathbf{e}_3 = x_i\mathbf{e}_i. \quad (\text{A.1})$$

In (A.1) Einsteins summation convention has been introduced for the last term which means that repeated indices in a term indicate a summation over this index. The quantities x_1, x_2, x_3 are the rectangular coordinates of \mathbf{x} . As a convention, bold-face letters are used for vector and tensor quantities, whereas normal font letters denote scalars. Components of vectors and tensors are represented by normal letters with subscripts, i.e.

$$a_i = \mathbf{a} \cdot \mathbf{e}_i, \quad A_{ij} = \mathbf{e}_i \cdot \mathbf{A}\mathbf{e}_j \quad (\text{A.2})$$

for vectors \mathbf{a} and second-order tensors \mathbf{A} , respectively. The dot operator "." denotes the inner product operator of two vectors. The identity tensor of second order is abbreviated by $\mathbf{1} = \delta_{ij}\mathbf{e}_i \otimes \mathbf{e}_j$, where

$$\delta_{ij} = \begin{cases} 1 & \text{if } i = j \\ 0 & \text{else} \end{cases} \quad (\text{A.3})$$

is the Kronecker delta. Several matrix notations of identity tensors are introduced to illustrate the numerical implementation in Appendix B. The identity tensor of second order in Voigt notation in the two-dimensional case for example is given by

$$\underline{\mathbf{1}}^{2 \times 1} = \begin{bmatrix} 1 \\ 1 \\ 0 \end{bmatrix}, \quad (\text{A.4})$$

whereas the full matrix notation

$$\underline{\mathbf{1}}^{k \times k} = [\delta_{ij}], \quad i, j = 1, 2, \dots, k \quad (\text{A.5})$$

is also required. In many cases, the differential operator

$$\nabla(*) = \frac{\partial(*)}{\partial x_i} \mathbf{e}_i = (*),_i \mathbf{e}_i \quad (\text{A.6})$$

is used, which when viewed as a vector, motivates generalizations of the gradient and divergence operations. The gradient of a vector field $\mathbf{a}(\mathbf{x}, t)$ for example is

$$\text{grad} \mathbf{a} = \frac{\partial \mathbf{a}}{\partial \mathbf{x}} = \mathbf{a} \otimes \nabla = \frac{\partial a_i}{\partial x_j} \mathbf{e}_i \otimes \mathbf{e}_j = a_{i,j} \mathbf{e}_i \otimes \mathbf{e}_j, \quad (\text{A.7})$$

where the operator ‘ \otimes ’ indicates the dyadic product of two vectors. Similarly, the gradient of a second-order tensor field $\mathbf{A}(\mathbf{x}, t)$ is

$$\text{grad} \mathbf{A} = \frac{\partial \mathbf{A}}{\partial \mathbf{x}} = \mathbf{A} \otimes \nabla = \frac{\partial A_{ij}}{\partial x_k} \mathbf{e}_i \otimes \mathbf{e}_j \otimes \mathbf{e}_k. \quad (\text{A.8})$$

In an analogous way, the divergence of vectors and tensors are

$$\text{div} \mathbf{a} = \mathbf{a} \cdot \nabla = \frac{\partial a_i}{\partial x_i} \quad (\text{A.9})$$

and

$$\text{div} \mathbf{A} = \mathbf{A} \cdot \nabla = \frac{\partial A_{ij}}{\partial x_j} \mathbf{e}_i \quad (\text{A.10})$$

respectively.

Gauss’s divergence theorem is also an essential ingredient for many derivations that are presented in this work. Assume that $R \subset \mathbb{E}^3$ is a regular bounded region, i.e. R is a closed region with piecewise smooth boundary ∂R of finite size. The quantities $a(\mathbf{x}, t)$, $\mathbf{a}(\mathbf{x}, t)$ and $\mathbf{A}(\mathbf{x}, t)$ are sufficiently smooth scalar, vector and second order tensor fields defined on $R \times (t_1, t_2)$. The divergence theorem relates the flux of a vector field or a tensor field through ∂R to its behaviour inside R , i.e.

$$\begin{aligned} \int_{\partial R} a \mathbf{n} \, dA &= \int_R \text{grad} a \, dV, \\ \int_{\partial R} \mathbf{a} \cdot \mathbf{n} \, dA &= \int_R \text{div} \mathbf{a} \, dV, \\ \int_{\partial R} \mathbf{A} \mathbf{n} \, dA &= \int_R \text{div} \mathbf{A} \, dV, \end{aligned} \quad (\text{A.11})$$

with the outward normal vector \mathbf{n} of the boundary ∂R . Another important integral theorem is the transport theorem. In this case, the boundary ∂R is explicitly considered to move with velocity $\mathbf{v}_{\partial R}$. The amounts of the previously defined scalar and vector valued fields inside the control volume $R(t)$ are

$$\mathcal{A}(t) = \int_{R(t)} a(\mathbf{x}, t) \, dV \quad \text{and} \quad \mathcal{A}(t) = \int_{R(t)} \mathbf{a}(\mathbf{x}, t) \, dV. \quad (\text{A.12})$$

The rate of change of these quantities is

$$\begin{aligned} \frac{d\mathcal{A}}{dt} &= \int_{R(t)} \frac{\partial a}{\partial t} \, dV + \int_{\partial R(t)} a \mathbf{n} \cdot \mathbf{v}_{\partial R} \, dA, \\ \frac{d\mathcal{A}}{dt} &= \int_{R(t)} \frac{\partial \mathbf{a}}{\partial t} \, dV + \int_{\partial R(t)} \mathbf{a}(\mathbf{v}_{\partial R} \cdot \mathbf{n}) \, dA. \end{aligned} \quad (\text{A.13})$$

In the special case when ∂R is a material surface, i.e. $\mathbf{v}_{\partial R}$ is equal to the velocity of the particles $\dot{\mathbf{u}}$ on ∂R , the theorem (A.13) is called Reynolds transport theorem. In the more general case, when $\mathbf{v}_{\partial R}$ is arbitrary, (A.13) is referred to as the generalized transport theorem.

B Finite Element Implementation

B.1 Spatial Discretization and Linearization

At first, the weak forms of the equation of motion (4.24), the phase field evolution equation (4.26) and the energy balance (4.30) are derived. By means of partial integration, the boundary conditions (4.9), (4.10), the fact that the otherwise arbitrary test functions $\boldsymbol{\eta}^u$, η^s and η^θ vanish on the respective Dirichlet boundary, and the divergence theorem (A.11) the respective weak forms can be expressed as

$$\int_{\Omega} (-\rho \ddot{\mathbf{u}} \cdot \boldsymbol{\eta}^u - \boldsymbol{\sigma} : \nabla \boldsymbol{\eta}^u) \, dV + \int_{\partial\Omega_t} \mathbf{t}^* \cdot \boldsymbol{\eta}^u \, dA = 0, \quad (\text{B.1})$$

$$\int_{\Omega} \left(\left[g'(s) \psi_+^e - \mathcal{G}_c \frac{1-s}{2l} \right] \eta^s + 2l \mathcal{G}_c \nabla s \cdot \nabla \eta^s \right) \, dV = 0, \quad (\text{B.2})$$

and

$$- \int_{\Omega} \left(\left[\rho c_\theta \dot{\theta} - \boldsymbol{\sigma} : \dot{\boldsymbol{\varepsilon}} - s^\theta \right] \eta^\theta - \mathbf{q}^\theta \cdot \nabla \eta^\theta \right) \, dV - \int_{\partial\Omega_{\mathbf{q}^\theta}} \mathbf{q}^\theta \cdot \mathbf{n} \, \eta^\theta \, dA = 0. \quad (\text{B.3})$$

Standard isoparametric, four node finite elements are utilized to represent the continuum Ω as the union of all finite elements $\Omega_d \approx \Omega$ in a discretized form. The primary fields \mathbf{u} , s , θ and the test functions $\boldsymbol{\eta}^u$, η^s , η^θ are interpolated between the element nodes by means of the nodal values $\underline{\mathbf{u}}_I, s_I, \theta_I, \underline{\boldsymbol{\eta}}_I^u, \eta_I^s, \eta_I^\theta$ and the scalar bilinear shape functions N_I

$$\underline{\mathbf{u}}_h = \sum_{I=1}^N N_I \underline{\mathbf{u}}_I, \quad s_h = \sum_{I=1}^N N_I s_I, \quad \theta_h = \sum_{I=1}^N N_I \theta_I, \quad (\text{B.4})$$

and

$$\underline{\boldsymbol{\eta}}_h^u = \sum_{I=1}^N N_I \underline{\boldsymbol{\eta}}_I^u, \quad \eta_h^s = \sum_{I=1}^N N_I \eta_I^s, \quad \eta_h^\theta = \sum_{I=1}^N N_I \eta_I^\theta, \quad (\text{B.5})$$

where N is the total number of nodes. In a two dimensional setting, the spatial derivatives in (B.1) and (B.2) can be expressed by means of the matrices

$$\underline{\mathbf{B}}_I^u = \begin{bmatrix} N_{I,1} & 0 \\ 0 & N_{I,2} \\ N_{I,2} & N_{I,1} \end{bmatrix} \quad \text{and} \quad \underline{\mathbf{B}}_I^s = \underline{\mathbf{B}}^\theta = \begin{bmatrix} N_{I,1} \\ N_{I,2} \end{bmatrix}. \quad (\text{B.6})$$

In these matrices $N_{I,1}$ and $N_{I,2}$ denote the differentiation of the shape functions with respect to the coordinates x_1 and x_2 . This way, it is possible to express the required derivatives of the primary fields and the test functions as

$$\underline{\boldsymbol{\varepsilon}}_h = \text{sym}(\nabla \underline{\mathbf{u}}_h) = \begin{bmatrix} \varepsilon_{11h} \\ \varepsilon_{22h} \\ 2\varepsilon_{12h} \end{bmatrix} = \sum_{I=1}^N \underline{\mathbf{B}}_I^u \underline{\mathbf{u}}_I, \quad \nabla s_h = \sum_{I=1}^N \underline{\mathbf{B}}_I^s s_I, \quad \nabla \theta_h = \sum_{I=1}^N \underline{\mathbf{B}}_I^\theta \theta_I, \quad (\text{B.7})$$

and

$$\nabla \underline{\boldsymbol{\eta}}_h^u = \sum_{I=1}^N \underline{\mathbf{B}}_I^u \underline{\boldsymbol{\eta}}_I^u, \quad \nabla \eta_h^s = \sum_{I=1}^N \underline{\mathbf{B}}_I^s \eta_I^s, \quad \nabla \eta_h^\theta = \sum_{I=1}^N \underline{\mathbf{B}}_I^\theta \eta_I^\theta \quad (\text{B.8})$$

in matrix notation. By means of these relations, the governing equations can be reformulated in their spatially discretized forms as

$$\sum_{i=1}^N \left[\underline{\boldsymbol{\eta}}_i^u \right]^T \underline{\mathbf{R}}_i^u = 0, \quad (\text{B.9})$$

$$\sum_{i=1}^N \eta_i^s R_i^s = 0, \quad (\text{B.10})$$

and

$$\sum_{i=1}^N \eta_i^\theta R_i^\theta = 0, \quad (\text{B.11})$$

where

$$\underline{\mathbf{R}}_I^u = - \int_{\Omega_d} \left([\underline{\mathbf{B}}_I^u]^T \underline{\boldsymbol{\sigma}}_h + \rho N_I \underline{\ddot{\mathbf{u}}}_h \right) dV + \int_{\partial\Omega_d^t} N_I \underline{\mathbf{t}}_h^* dA, \quad (\text{B.12})$$

$$R_I^s = - \int_{\Omega_d} \left([\underline{\mathbf{B}}_I^s]^T 2l \mathcal{G}_c \nabla s_h + N_I \left(g'(s_h) \psi_{h+}^e - \frac{\mathcal{G}_c}{2l} (1 - s_h) \right) \right) dV, \quad (\text{B.13})$$

and

$$R_I^\theta = - \int_{\Omega_d} \left(N_I c_\theta \rho \dot{\theta}_h - N_I \underline{\sigma}_h^T \dot{\underline{\epsilon}}_h - [\underline{\mathbf{B}}_I^{\theta}]^T \underline{\mathbf{q}}_h^\theta \right) dV + \int_{\Omega_d} N_I s_h^\theta dV - \int_{\partial\Omega_d^q} \underline{\mathbf{q}}_h^{\theta*T} \underline{\mathbf{n}} N_I dA. \quad (\text{B.14})$$

The derived quantities $\underline{\sigma}_h$, $\underline{\mathbf{q}}_h^\theta$ and ψ_{h+}^e must be determined from the constitutive laws (4.25), (4.29) and (4.42), (4.47) or (4.8), respectively. The derivatives with respect to time are calculated as

$$\dot{\underline{\mathbf{u}}}_h = \sum_{I=1}^N N_I \dot{\underline{\mathbf{u}}}_I, \quad \dot{\theta}_h = \sum_{I=1}^N N_I \dot{\theta}_I \quad \text{and} \quad \dot{\underline{\epsilon}}_h = \sum_{I=1}^{N_e} \underline{\mathbf{B}}_I^u \dot{\underline{\mathbf{u}}}_I. \quad (\text{B.15})$$

Usually, the residuals are computed element-wise and assembled later on in order to obtain the global representations (B.12), (B.13) and (B.14). The contribution of the element e to the residuals of node I are

$$\underline{\mathbf{R}}_{I,e}^u = - \underbrace{\left(\sum_{J=1}^{N_e} \underline{\mathbf{M}}_{IJ,e}^{uu} \dot{\underline{\mathbf{u}}}_J + \underbrace{\int_{\Omega_e} ([\underline{\mathbf{B}}_I^u]^T \underline{\sigma}_h) dV}_{=P_{I,e}^u} \right)}_{=I_{I,e}^u} + \underbrace{\int_{\partial\Omega_e^t \cap \partial\Omega^t} N_I \underline{\mathbf{t}}_h^* dA}_{=F_{I,e}^u}, \quad (\text{B.16})$$

$$R_{I,e}^s = -I_{I,e}^s = -P_{I,e}^s = - \int_{\Omega_e} \left([\underline{\mathbf{B}}_I^s]^T 2l \mathcal{G}_c \nabla s_h + N_I \left(g'(s_h) \psi_{h+}^e - \frac{\mathcal{G}_c}{2l} (1 - s_h) \right) \right) dV \quad (\text{B.17})$$

and

$$R_{I,e}^\theta = - \underbrace{\left(\sum_{J=1}^{N_e} D_{IJ,e}^{\theta\theta} \dot{\theta}_J + \sum_{J=1}^{N_e} \underline{\mathbf{D}}_{IJ,e}^{\theta u} \dot{\underline{\mathbf{u}}}_J - \underbrace{\int_{\Omega_e} (\underline{\mathbf{B}}_I^{\theta T} \underline{\mathbf{q}}_h^\theta) dV}_{=P_{I,e}^\theta} \right)}_{=I_{I,e}^\theta} + \underbrace{\int_{\Omega_e} N_I s_h^\theta dV - \int_{\partial\Omega_e^q \cap \partial\Omega_d^q} \underline{\mathbf{q}}_h^{\theta*T} \underline{\mathbf{n}} N_I dA}_{=F_{I,e}^\theta}, \quad (\text{B.18})$$

where

$$\underline{\mathbf{M}}_{IJ,e}^{uu} = \int_{\Omega_e} N_I \rho N_J dV \mathbf{1}^{2 \times 2}, \quad D_{IJ,e}^{\theta\theta} = \int_{\Omega_e} N_I \rho c_\theta N_J dV \quad (\text{B.19})$$

and

$$\underline{\mathbf{D}}_{IJ,e}^{\theta u} = - \int_{\Omega_e} N_I \underline{\boldsymbol{\sigma}}_h^T \underline{\mathbf{B}}_J^u \, dV. \quad (\text{B.20})$$

The components and constituents of the nodal residual may also be rearranged in the forms

$$\underline{\mathbf{R}}_{I,e} = \left[(\underline{\mathbf{R}}_{I,e}^u)^T \quad R_{I,e}^s \quad R_{I,e}^\theta \right]^T, \quad (\text{B.21})$$

$$\underline{\mathbf{I}}_{I,e} = \left[(\underline{\mathbf{I}}_{I,e}^u)^T \quad I_{I,e}^s \quad I_{I,e}^\theta \right]^T, \quad \underline{\mathbf{P}}_{I,e} = \left[(\underline{\mathbf{P}}_{I,e}^u)^T \quad P_{I,e}^s \quad P_{I,e}^\theta \right]^T, \quad (\text{B.22})$$

and

$$\underline{\mathbf{F}}_{I,e} = \left[(\underline{\mathbf{F}}_{I,e}^u)^T \quad 0 \quad F_{I,e}^\theta \right]^T. \quad (\text{B.23})$$

The arrays of all unknowns at node I and the nodal values of the test functions are denoted as

$$\underline{\mathbf{d}}_I = [\underline{\mathbf{u}}_I^T, s_I, \theta_I]^T, \quad \underline{\boldsymbol{\eta}}_I = \left[(\underline{\boldsymbol{\eta}}_I^u)^T, \eta_I^s, \eta_I^\theta \right]^T, \quad (\text{B.24})$$

which allows to express the contribution of the element e to the residual of node I also as

$$\underline{\mathbf{R}}_{I,e} = - \sum_{J=1}^{N_e} \underline{\mathbf{M}}_{IJ,e} \ddot{\mathbf{d}}_J - \sum_{J=1}^{N_e} \underline{\mathbf{D}}_{IJ,e}(\underline{\mathbf{d}}_h) \dot{\mathbf{d}}_J - \underline{\mathbf{P}}_{I,e}(\underline{\mathbf{d}}_h) + \underline{\mathbf{F}}_{I,e}, \quad \underline{\mathbf{d}}_h = \sum_{I=1}^{N_e} N_I \underline{\mathbf{d}}_I, \quad (\text{B.25})$$

with the nodal contributions to the mass and damping matrix of the element e given by

$$\underline{\mathbf{M}}_{IJ,e} = \begin{bmatrix} \underline{\mathbf{M}}_{IJ,e}^{uu} & \underline{\mathbf{0}}^{2 \times 1} & \underline{\mathbf{0}}^{2 \times 1} \\ \underline{\mathbf{0}}^{1 \times 2} & 0 & 0 \\ \underline{\mathbf{0}}^{1 \times 2} & 0 & 0 \end{bmatrix} \quad \text{and} \quad \underline{\mathbf{D}}_{IJ,e} = \begin{bmatrix} \underline{\mathbf{0}}^{2 \times 2} & \underline{\mathbf{0}}^{2 \times 1} & \underline{\mathbf{0}}^{2 \times 1} \\ \underline{\mathbf{0}}^{1 \times 2} & 0 & 0 \\ \underline{\mathbf{D}}_{IJ,e}^{\theta u} & 0 & D_{IJ,e}^{\theta\theta} \end{bmatrix}, \quad (\text{B.26})$$

where

$$\underline{\mathbf{0}}^{k \times l} = [0_{(ij)}], \quad i = 1, \dots, k, \quad j = 1, 2, \dots, l \quad (\text{B.27})$$

represents the $k \times l$ -zero matrix. The element mass and damping matrices are composed of all nodal contributions of the respective element e , i.e

$$\underline{\mathbf{M}}_e = \begin{bmatrix} \underline{\mathbf{M}}_{11,e} & \underline{\mathbf{M}}_{12,e} & \cdots & \underline{\mathbf{M}}_{1N^e,e} \\ \underline{\mathbf{M}}_{21,e} & \underline{\mathbf{M}}_{22,e} & & \vdots \\ \vdots & & \ddots & \vdots \\ \underline{\mathbf{M}}_{N^e 1,e} & \cdots & \cdots & \underline{\mathbf{M}}_{N^e N^e,e} \end{bmatrix}, \quad \underline{\mathbf{D}}_e = \begin{bmatrix} \underline{\mathbf{D}}_{11,e} & \underline{\mathbf{D}}_{12,e} & \cdots & \underline{\mathbf{D}}_{1N^e,e} \\ \underline{\mathbf{D}}_{21,e} & \underline{\mathbf{D}}_{22,e} & & \vdots \\ \vdots & & \ddots & \vdots \\ \underline{\mathbf{D}}_{N^e 1,e} & \cdots & \cdots & \underline{\mathbf{D}}_{N^e N^e,e} \end{bmatrix}. \quad (\text{B.28})$$

The sums of the contributions of all adjacent elements \mathcal{E}_I to the considered node I yield

$$\underline{\mathbf{R}}_I = \sum_{e \in \mathcal{E}_I} \underline{\mathbf{R}}_{I,e}, \quad \underline{\mathbf{I}}_I = \sum_{e \in \mathcal{E}_I} \underline{\mathbf{I}}_{I,e}, \quad \underline{\mathbf{F}}_I = \sum_{e \in \mathcal{E}_I} \underline{\mathbf{F}}_{I,e}. \quad (\text{B.29})$$

With this notation, (B.9)-(B.11) can be written in a more compact form as

$$\underline{\boldsymbol{\eta}}^T \underline{\mathbf{R}} = 0, \quad \text{where } \underline{\mathbf{R}} = [\underline{\mathbf{R}}_1, \dots, \underline{\mathbf{R}}_N]^T \quad \text{and} \quad \underline{\boldsymbol{\eta}} = [\underline{\boldsymbol{\eta}}_1, \dots, \underline{\boldsymbol{\eta}}_N]^T. \quad (\text{B.30})$$

Since the nodal values of the test functions can take on arbitrary values, it follows

$$\underline{\mathbf{R}} = \underline{\mathbf{F}} - \underline{\mathbf{I}} = \underline{\mathbf{0}}, \quad (\text{B.31})$$

where

$$\underline{\mathbf{F}} = [\underline{\mathbf{F}}_1, \dots, \underline{\mathbf{F}}_N] \quad \text{and} \quad \underline{\mathbf{I}} = [\underline{\mathbf{I}}_1, \dots, \underline{\mathbf{I}}_N]. \quad (\text{B.32})$$

By means of

$$\underline{\mathbf{M}} = \bigcup_{e=1}^{n_e} \underline{\mathbf{M}}_e, \quad \underline{\mathbf{D}} = \bigcup_{e=1}^{n_e} \underline{\mathbf{D}}_e, \quad (\text{B.33})$$

with the total number of elements n_e , the set of equations (B.9)-(B.10) can be reformulated as

$$\underline{\mathbf{R}} = \underline{\mathbf{F}} - \underline{\mathbf{M}} \ddot{\underline{\mathbf{d}}} - \underline{\mathbf{D}}(\underline{\mathbf{d}}) \dot{\underline{\mathbf{d}}} - \underline{\mathbf{P}}(\underline{\mathbf{d}}) = \underline{\mathbf{0}}, \quad \text{where } \underline{\mathbf{d}} = [\underline{\mathbf{d}}_1, \dots, \underline{\mathbf{d}}_N]^T, \quad (\text{B.34})$$

or in a notation that is more suitable to introduce a staggered algorithm as

$$\begin{aligned} \begin{bmatrix} \underline{\mathbf{R}}^u \\ \underline{\mathbf{R}}^s \\ \underline{\mathbf{R}}^\theta \end{bmatrix} &= \begin{bmatrix} \underline{\mathbf{M}}^{uu} & \underline{\mathbf{0}} & \underline{\mathbf{0}} \\ \underline{\mathbf{0}} & \underline{\mathbf{0}} & \underline{\mathbf{0}} \\ \underline{\mathbf{0}} & \underline{\mathbf{0}} & \underline{\mathbf{0}} \end{bmatrix} \begin{bmatrix} \ddot{\underline{\mathbf{u}}} \\ \ddot{\underline{\mathbf{s}}} \\ \ddot{\underline{\boldsymbol{\theta}}} \end{bmatrix} + \begin{bmatrix} \underline{\mathbf{0}} & \underline{\mathbf{0}} & \underline{\mathbf{0}} \\ \underline{\mathbf{0}} & \underline{\mathbf{0}} & \underline{\mathbf{0}} \\ \underline{\mathbf{D}}^{\theta u}(\underline{\mathbf{d}}) & \underline{\mathbf{0}} & \underline{\mathbf{D}}^{\theta\theta} \end{bmatrix} \begin{bmatrix} \dot{\underline{\mathbf{u}}} \\ \dot{\underline{\mathbf{s}}} \\ \dot{\underline{\boldsymbol{\theta}}} \end{bmatrix} \\ &+ \begin{bmatrix} \underline{\mathbf{P}}^u(\underline{\mathbf{d}}) \\ \underline{\mathbf{P}}^s(\underline{\mathbf{d}}) \\ \underline{\mathbf{P}}^\theta(\underline{\boldsymbol{\theta}}, \underline{\mathbf{s}}) \end{bmatrix} - \begin{bmatrix} \underline{\mathbf{F}}^u \\ \underline{\mathbf{0}} \\ \underline{\mathbf{F}}^\theta \end{bmatrix} = \underline{\mathbf{0}}, \end{aligned} \quad (\text{B.35})$$

where

$$\underline{\mathbf{R}}^u = [\underline{\mathbf{R}}_1^u, \dots, \underline{\mathbf{R}}_N^u]^T, \quad \underline{\mathbf{R}}^s = [R_1^s, \dots, R_N^s]^T, \quad \underline{\mathbf{R}}^\theta = [R_1^\theta, \dots, R_N^\theta]^T, \quad (\text{B.36})$$

$$\underline{\mathbf{P}}^u = [\underline{\mathbf{P}}_1^u, \dots, \underline{\mathbf{P}}_N^u]^T, \quad \underline{\mathbf{P}}^s = [P_1^s, \dots, P_N^s]^T, \quad \underline{\mathbf{P}}^\theta = [P_1^\theta, \dots, P_N^\theta]^T \quad (\text{B.37})$$

and

$$\underline{\mathbf{F}}^u = [\underline{\mathbf{F}}_1^u, \dots, \underline{\mathbf{F}}_N^u]^T, \quad \underline{\mathbf{R}}^\theta = [R_1^\theta, \dots, R_N^\theta]^T. \quad (\text{B.38})$$

The problem (B.34) or in alternative form (B.35) is a set of nonlinear ordinary differential equations. Thus, its numerical solution requires a linearization with respect to the nodal unknowns meaning that

$$\underline{\mathbf{R}}(\underline{\mathbf{d}} + \Delta \underline{\mathbf{d}}) = \underline{\mathbf{R}}(\underline{\mathbf{d}}) + \frac{d\underline{\mathbf{R}}}{d\underline{\mathbf{d}}} \Delta \underline{\mathbf{d}} = \underline{\mathbf{0}}, \quad (\text{B.39})$$

needs to be evaluated. Here, it has been assumed that the first and second order derivatives of the nodal unknowns w.r.t time can be approximated by functions of the nodal unknowns themselves as

$$\dot{\underline{\mathbf{d}}} = \dot{\underline{\mathbf{d}}}(\underline{\mathbf{d}}), \quad \ddot{\underline{\mathbf{d}}} = \ddot{\underline{\mathbf{d}}}(\underline{\mathbf{d}}). \quad (\text{B.40})$$

The global tangent matrix is defined as

$$\underline{\mathbf{S}} = -\frac{d\underline{\mathbf{R}}}{d\underline{\mathbf{d}}} = \frac{d\underline{\mathbf{I}}}{d\underline{\mathbf{d}}}. \quad (\text{B.41})$$

With (B.34) the tangent matrix takes on the form

$$\underline{\mathbf{S}} = \underline{\mathbf{M}} \frac{\partial \ddot{\underline{\mathbf{d}}}}{\partial \underline{\mathbf{d}}} + \underline{\mathbf{D}} \frac{\partial \dot{\underline{\mathbf{d}}}}{\partial \underline{\mathbf{d}}} + \underline{\mathbf{K}}, \quad (\text{B.42})$$

where $\underline{\mathbf{M}}$ and $\underline{\mathbf{D}}$ are the global mass and damping matrices introduced in (B.33) and

$$\underline{\mathbf{K}} = \frac{\partial \underline{\mathbf{I}}}{\partial \underline{\mathbf{d}}} \quad (\text{B.43})$$

is the global stiffness matrix. The derivatives

$$\frac{\partial \ddot{\underline{\mathbf{d}}}}{\partial \underline{\mathbf{d}}}, \quad \text{and} \quad \frac{\partial \dot{\underline{\mathbf{d}}}}{\partial \underline{\mathbf{d}}} \quad (\text{B.44})$$

are determined by the chosen time integration scheme, see Section B.5. The computation of the stiffness matrix is usually also performed on the element level as well. The global stiffness matrix

$$\underline{\mathbf{K}} = \bigcup_{e=1}^{n_e} \underline{\mathbf{K}}_e, \quad (\text{B.45})$$

is assembled subsequently, where

$$\underline{\mathbf{K}}_e = \begin{bmatrix} \underline{\mathbf{K}}_{11,e} & \underline{\mathbf{K}}_{12,e} & \cdots & \underline{\mathbf{K}}_{1N^e,e} \\ \underline{\mathbf{K}}_{21,e} & \underline{\mathbf{K}}_{22,e} & & \vdots \\ \vdots & & \ddots & \vdots \\ \underline{\mathbf{K}}_{N^e1,e} & \cdots & \cdots & \underline{\mathbf{K}}_{N^eN^e,e} \end{bmatrix} \quad (\text{B.46})$$

and

$$\underline{\mathbf{K}}_{IJ,e} = \begin{bmatrix} \underline{\mathbf{K}}_{IJ,e}^{uu} & \underline{\mathbf{K}}_{IJ,e}^{us} & \underline{\mathbf{K}}_{IJ,e}^{u\theta} \\ \underline{\mathbf{K}}_{IJ,e}^{su} & K_{IJ,e}^{ss} & K_{IJ,e}^{s\theta} \\ \underline{\mathbf{K}}_{IJ,e}^{\theta u} & K_{IJ,e}^{\theta s} & K_{IJ,e}^{\theta\theta} \end{bmatrix}. \quad (\text{B.47})$$

The individual components of the element stiffness matrices are given by

$$\begin{aligned} \underline{\mathbf{K}}_{IJ,e}^{uu} &= \frac{\partial \underline{\mathbf{I}}_{I,e}^u}{\partial \underline{\mathbf{u}}_J} = \int_{\Omega_e} [\underline{\mathbf{B}}_I^u]^T \frac{\partial \underline{\boldsymbol{\sigma}}_h}{\partial \underline{\boldsymbol{\varepsilon}}_h} \left[\frac{\partial \underline{\boldsymbol{\varepsilon}}_h}{\partial \underline{\mathbf{u}}_J} \right] dV \\ &= \int_{\Omega_e} [\underline{\mathbf{B}}_I^u]^T \underline{\mathbb{C}} [\underline{\mathbf{B}}_J^u] dV, \end{aligned} \quad (\text{B.48})$$

$$\begin{aligned} \underline{\mathbf{K}}_{IJ,e}^{us} &= \frac{\partial \underline{\mathbf{I}}_{I,e}^u}{\partial s_J} = \int_{\Omega_e} [\underline{\mathbf{B}}_I^u]^T \frac{\partial \underline{\boldsymbol{\sigma}}_h}{\partial s_h} \frac{\partial s_h}{\partial s_J} dV \\ &= \int_{\Omega_e} [\underline{\mathbf{B}}_I^u]^T g'(s_h) \left[\frac{\partial \psi_{h+}^e}{\partial \underline{\boldsymbol{\varepsilon}}_h} \right]^T N_J dV, \end{aligned} \quad (\text{B.49})$$

$$\begin{aligned} \underline{\mathbf{K}}_{IJ,e}^{u\theta} &= \frac{\partial \underline{\mathbf{I}}_{I,e}^u}{\partial \theta_J} = \int_{\Omega_e} [\underline{\mathbf{B}}_I^u]^T \frac{\partial \underline{\boldsymbol{\sigma}}_h}{\partial \theta_h} \frac{\partial \theta_h}{\partial \theta_J} dV \\ &= \int_{\Omega_e} [\underline{\mathbf{B}}_I^u]^T \underline{\mathbb{C}} (-\alpha_T \mathbf{1}^{n \times 1}) N_J dV, \end{aligned} \quad (\text{B.50})$$

$$\begin{aligned} \underline{\mathbf{K}}_{IJ,e}^{su} &= \frac{\partial \underline{\mathbf{I}}_{I,e}^s}{\partial \underline{\mathbf{u}}_J} = \int_{\Omega_e} N_I g'(s_h) \left[\frac{\partial \psi_{h+}^e}{\partial \underline{\boldsymbol{\varepsilon}}_h} \right]^T \left[\frac{\partial \underline{\boldsymbol{\varepsilon}}_h}{\partial \underline{\mathbf{u}}_J} \right] dV \\ &= \int_{\Omega_e} N_I g'(s_h) \left[\frac{\partial \psi_{h+}^e}{\partial \underline{\boldsymbol{\varepsilon}}_h} \right]^T [\underline{\mathbf{B}}_J^u] dV, \end{aligned} \quad (\text{B.51})$$

$$\begin{aligned}
K_{IJ,e}^{ss} &= \frac{\partial I_{I,e}^s}{\partial s_J} = \int_{\Omega_e} \left([\underline{\mathbf{B}}_I^s]^T [2\mathcal{G}_c l] \frac{\partial \nabla s_h}{\partial s_J} + N_I \left(g''(s_h) \psi_{h+}^e + \frac{\mathcal{G}_c}{2l} \right) \frac{\partial s_h}{\partial s_J} \right) dV \\
&= \int_{\Omega_e} \left([\underline{\mathbf{B}}_I^s]^T [2\mathcal{G}_c l] \underline{\mathbf{B}}_J^s + N_I \left(g''(s_h) \psi_{h+}^e + \frac{\mathcal{G}_c}{2l} \right) N_J \right) dV,
\end{aligned} \tag{B.52}$$

$$\begin{aligned}
K_{IJ,e}^{s\theta} &= \frac{\partial I_{I,e}^s}{\partial \theta_J} = \int_{\Omega_e} N_I g'(s_h) \frac{\partial \psi_{h+}^e}{\partial \underline{\boldsymbol{\varepsilon}}_h^e} \frac{\partial \underline{\boldsymbol{\varepsilon}}_h^e}{\partial \theta_J} dV \\
&= \int_{\Omega_e} N_I g'(s_h) \left[\frac{\partial \psi_{h+}^e}{\partial \underline{\boldsymbol{\varepsilon}}_h^e} \right]^T (-\alpha_T \mathbf{1}^{n \times 1}) N_J dV,
\end{aligned} \tag{B.53}$$

$$\begin{aligned}
\underline{\mathbf{K}}_{IJ}^{\theta u} &= \frac{\partial I_{I,e}^\theta}{\partial \underline{\mathbf{u}}_J} = \int_{\Omega_e} N_I \dot{\underline{\boldsymbol{\varepsilon}}}_h^T \frac{\partial \underline{\boldsymbol{\sigma}}_h}{\partial \underline{\boldsymbol{\varepsilon}}_h^e} \frac{\partial \underline{\boldsymbol{\varepsilon}}_h^e}{\partial \underline{\mathbf{u}}_J} dV \\
&= \int_{\Omega_e} N_I \dot{\underline{\boldsymbol{\varepsilon}}}_h^T \underline{\mathbb{C}} \underline{\mathbf{B}}_J^u dV,
\end{aligned} \tag{B.54}$$

$$\begin{aligned}
\underline{\mathbf{K}}_{IJ}^{\theta s} &= \frac{\partial I_{I,e}^\theta}{\partial s_J} = \int_{\Omega_e} N_I \dot{\underline{\boldsymbol{\varepsilon}}}_h^T \frac{\partial \underline{\boldsymbol{\sigma}}_h}{\partial s_h} \frac{\partial s_h}{\partial s_J} dV \\
&= \int_{\Omega_e} N_I g'(s) \dot{\underline{\boldsymbol{\varepsilon}}}_h^T \left[\frac{\partial \psi_{h+}^e}{\partial \underline{\boldsymbol{\varepsilon}}_h^e} \right]^T N_J dV,
\end{aligned} \tag{B.55}$$

$$\begin{aligned}
K_{IJ}^{\theta\theta} &= \frac{\partial I_{I,e}^\theta}{\partial \theta_J} = - \int_{\Omega_e} [\underline{\mathbf{B}}_I^\theta]^T \frac{\underline{\mathbf{q}}_h^\theta}{\partial \theta_J} dV - \int_{\Omega_e} N_I \dot{\underline{\boldsymbol{\varepsilon}}}_h^T \frac{\partial \underline{\boldsymbol{\sigma}}_h}{\partial \theta_h} \frac{\partial \theta_h}{\partial \theta_J} dV \\
&= \int_{\Omega_e} \kappa [\underline{\mathbf{B}}_I^\theta]^T \underline{\mathbf{B}}_J^\theta dV + \int_{\Omega_e} N_I \dot{\underline{\boldsymbol{\varepsilon}}}_h^T \underline{\mathbb{C}} \mathbf{1}^{n \times 1} \alpha_T N_J dV.
\end{aligned} \tag{B.56}$$

The material tangent

$$\underline{\mathbb{C}}(\lambda, \mu, s_h, \underline{\boldsymbol{\varepsilon}}_h, \theta_h) = \frac{\partial \underline{\boldsymbol{\sigma}}_h}{\partial \underline{\boldsymbol{\varepsilon}}_h^e} \tag{B.57}$$

is in general dependent on the elastic parameters, the fields $\underline{\mathbf{u}}_h, s_h, \theta_h$ and on the chosen decomposition of the strain energy density, see Section 4.4. If the volumetric-deviatoric decomposition (4.42) is applied, $\underline{\mathbb{C}} = \underline{\mathbb{C}}^{VDD}$ is given by

$$\underline{\mathbb{C}}^{VDD} = \begin{bmatrix} \mathbb{C}_{11} & \mathbb{C}_{12} & 0 \\ \mathbb{C}_{12} & \mathbb{C}_{11} & 0 \\ \mathbb{C}_{12} & \mathbb{C}_{12} & 0 \\ 0 & 0 & \frac{1}{2}(\mathbb{C}_{11} - \mathbb{C}_{12}) \end{bmatrix}, \tag{B.58}$$

where

$$\begin{aligned} \mathbb{C}_{11} &= \frac{\partial \langle \text{tr}(\underline{\boldsymbol{\varepsilon}}_h^e) \rangle_-}{\partial \text{tr}(\underline{\boldsymbol{\varepsilon}}_h^e)} K_n + g(s_h) \left(\frac{\partial \langle \text{tr}(\underline{\boldsymbol{\varepsilon}}_h^e) \rangle_+}{\partial \text{tr}(\underline{\boldsymbol{\varepsilon}}_h^e)} K_n + \mu \right), \\ \mathbb{C}_{12} &= \frac{\partial \langle \text{tr}(\underline{\boldsymbol{\varepsilon}}_h^e) \rangle_-}{\partial \text{tr}(\underline{\boldsymbol{\varepsilon}}_h^e)} K_n + g(s_h) \left(\frac{\partial \langle \text{tr}(\underline{\boldsymbol{\varepsilon}}_h^e) \rangle_+}{\partial \text{tr}(\underline{\boldsymbol{\varepsilon}}_h^e)} K_n - \mu \right). \end{aligned} \quad (\text{B.59})$$

The derivative of the positive part of the strain energy with respect to the strain is given by

$$\begin{aligned} \frac{\partial \psi_{h+}^e}{\partial \underline{\boldsymbol{\varepsilon}}_h}{}^{VDD} &= K_n \langle \text{tr}(\underline{\boldsymbol{\varepsilon}}_h^e) \rangle_+ \frac{\partial \langle \text{tr}(\underline{\boldsymbol{\varepsilon}}_h^e) \rangle_+}{\partial \underline{\boldsymbol{\varepsilon}}_h} + \mu \frac{\partial (\underline{\boldsymbol{\varepsilon}}_h^{eT} \underline{\boldsymbol{\varepsilon}}_h^e)}{\partial \underline{\boldsymbol{\varepsilon}}_h} \\ &= K_n \langle \text{tr}(\underline{\boldsymbol{\varepsilon}}_h^e) \rangle_+ \mathbf{1}^{n \times 1} + 2\mu \underline{\boldsymbol{\varepsilon}}_h^e, \end{aligned} \quad (\text{B.60})$$

where

$$\underline{\boldsymbol{\varepsilon}}_h^e = \begin{bmatrix} e_{11_h}^e \\ e_{22_h}^e \\ 2e_{12_h}^e \end{bmatrix} \quad \text{and} \quad \tilde{\underline{\boldsymbol{\varepsilon}}}_h^e = \begin{bmatrix} e_{11_h}^e \\ e_{22_h}^e \\ e_{12_h}^e \end{bmatrix} \quad (\text{B.61})$$

are representations of the deviatoric part of the elastic strain.

The numerical treatment of the spectral decomposition is much more complex. It is helpful to first define the mappings of the elastic strain onto their positive and negative elastic parts, cf. (4.48) and (4.49), as

$$\underline{\mathbb{P}}^+ = \frac{\partial \underline{\boldsymbol{\varepsilon}}_{h+}^e}{\partial \underline{\boldsymbol{\varepsilon}}_h^e} \quad \text{and} \quad \underline{\mathbb{P}}^- = \frac{\partial \underline{\boldsymbol{\varepsilon}}_{h-}^e}{\partial \underline{\boldsymbol{\varepsilon}}_h^e}. \quad (\text{B.62})$$

These mappings can be computed according to the algorithms described in Miehe (1998) and Miehe and Lambrecht (2001). The material tangent defined by (B.57) follows from (4.47) and (B.62) as

$$\underline{\mathbb{C}}^{SD} = \frac{\partial \langle \text{tr}(\underline{\boldsymbol{\varepsilon}}_h^e) \rangle_-}{\partial \text{tr}(\underline{\boldsymbol{\varepsilon}}_h^e)} \lambda \mathbf{1}^{3 \times 3} + 2\mu \underline{\mathbb{P}}^- + g(s_h) \left(\frac{\partial \langle \text{tr}(\underline{\boldsymbol{\varepsilon}}_h^e) \rangle_+}{\partial \text{tr}(\underline{\boldsymbol{\varepsilon}}_h^e)} \lambda \mathbf{1}^{3 \times 3} + 2\mu \underline{\mathbb{P}}^+ \right) \quad (\text{B.63})$$

and the derivative of the positive part of the strain energy with respect to the strain as

$$\frac{\partial \psi_{h+}^e}{\partial \underline{\boldsymbol{\varepsilon}}_h^e}{}^{SD} = \lambda \langle \text{tr}(\underline{\boldsymbol{\varepsilon}}_h^e) \rangle_+ \mathbf{1}^{2 \times 1} + 2\mu \underline{\boldsymbol{\varepsilon}}_{h+}^e. \quad (\text{B.64})$$

B.2 Isoparametric Concept and Numerical Quadrature

There is a number of ways to implement the interpolation of the fields (B.4) and the approximation of the geometry $\Omega_d \approx \Omega$. In this work, the so-called isoparametric concept is utilized, which approximates the geometry and the primary fields in the same manner. The 2D four node elements that are used for most of the simulations

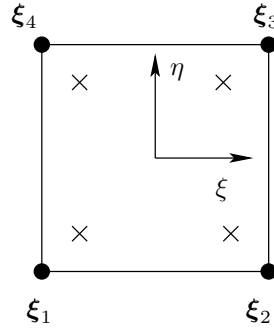


Figure B.1: Natural configuration Ω_{ref} of a four node quadrilateral element. The crosses illustrate the location of the integration points.

in this work use bilinear shape functions of the type

$$N_I(\xi, \eta) = \frac{1}{2}(1 + \xi_I \xi) \frac{1}{2}(1 + \eta_I \eta). \quad (\text{B.65})$$

The parameters $\xi_I = (\xi_I, \eta_I)$ denote the nodal coordinates in the natural coordinate system of the element, see Fig. B.1. For the four node element, the natural configuration is given by the nodal coordinates

$$\xi_1 = (-1, -1) \quad \xi_2 = (1, -1) \quad \xi_3 = (1, 1) \quad \xi_4 = (-1, 1). \quad (\text{B.66})$$

Following the isoparametric concept, the spatial coordinates $\underline{\mathbf{x}}_e$ inside the element are computed in the same manner as the fields, i.e.

$$\underline{\mathbf{x}}_e = \sum_{I=1}^{N_e} N_I \underline{\mathbf{x}}_I. \quad (\text{B.67})$$

The shape functions (B.65) are defined as functions of the natural coordinates ξ . However, the derivatives with respect to $\underline{\mathbf{x}}_e$ are required in $\underline{\mathbf{B}}_I^u$, $\underline{\mathbf{B}}_I^s$ and $\underline{\mathbf{B}}_I^\theta$. These derivatives can be found by means of the chain rule as

$$\left[\frac{\partial N_I}{\partial \xi} \right]^T = \left[\frac{\partial \underline{\mathbf{x}}_e}{\partial \xi} \right]^T \left[\frac{\partial N_I}{\partial \underline{\mathbf{x}}_e} \right]^T, \quad (\text{B.68})$$

where

$$\mathbf{J}_e = \left[\frac{\partial \mathbf{x}_e}{\partial \boldsymbol{\xi}} \right]^T \quad (\text{B.69})$$

is the Jacobian matrix of the element e . An illustration of the transformation (B.68) of the configuration of the finite element in the physical space to its natural configuration is depicted in Fig. B.2. By means of (B.67) the Jacobian matrix may

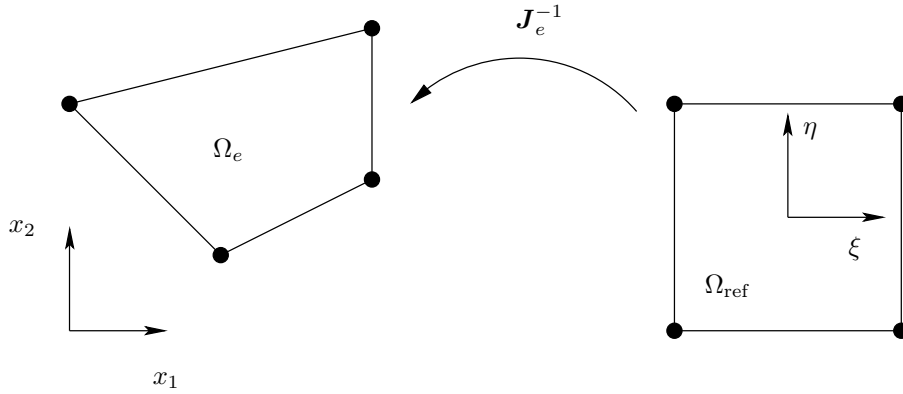


Figure B.2: Transformation of the finite element e in its natural configuration Ω_{ref} to its configuration in physical space Ω_e .

also be expressed as

$$\mathbf{J}_e = \sum_I^{N_e} \left[\mathbf{x}_I \frac{\partial N_I}{\partial \boldsymbol{\xi}} \right]^T. \quad (\text{B.70})$$

The coordinate transformation (B.67) allows to map the integrals that appear in the residuals and the tangent matrix to the natural configuration Ω_{ref} , i.e

$$\int_{\Omega_e} f(\mathbf{x}_h) dV = \int_{\Omega_{\text{ref}}} \hat{f}(\boldsymbol{\xi}) \det(\mathbf{J}_e) dV_{\text{ref}}. \quad (\text{B.71})$$

The integration is performed by a Gaussian quadrature rule

$$\int_{\Omega_{\text{ref}}} \hat{f}(\boldsymbol{\xi}) \det(\mathbf{J}_e) dV_{\text{ref}} \approx \sum_{p=1}^{n_p} f(\xi_p, \eta_p) \det(\mathbf{J}_e(\boldsymbol{\xi}_p^i)) \omega_p. \quad (\text{B.72})$$

The number n_p is the total number of integration points per element, $\boldsymbol{\xi}_p^i$ denotes the coordinates of the integration points in the natural coordinate system and w_p is their weight factor. For the four node element with bilinear shape functions (B.65) all weights are chosen to be $w_p = 1$ and the coordinates of the integration

points are given by

$$\begin{aligned}\boldsymbol{\xi}_1^i &= \left(-\frac{1}{\sqrt{3}}, -\frac{1}{\sqrt{3}} \right), & \boldsymbol{\xi}_2^i &= \left(-\frac{1}{\sqrt{3}}, -\frac{1}{\sqrt{3}} \right), \\ \boldsymbol{\xi}_3^i &= \left(-\frac{1}{\sqrt{3}}, -\frac{1}{\sqrt{3}} \right), & \boldsymbol{\xi}_4^i &= \left(-\frac{1}{\sqrt{3}}, -\frac{1}{\sqrt{3}} \right).\end{aligned}\tag{B.73}$$

B.3 Staggered Solution Strategy

For the solution of the coupled phase field fracture problem (B.34), or in alternative notation (B.35), two basic strategies exist. The first option is a staggered approach, where the solution is decomposed into three stages (the staggers) that are solved consecutively, see Fig. B.3.

- Set initial values $(\underline{\mathbf{u}}^0, \underline{\mathbf{s}}^0, \underline{\theta}^0)$
- Start loop $k = 0, 1 \dots k_{\max}$
 - 1: Solve $\underline{\mathbf{M}}^{uu} \dot{\underline{\mathbf{u}}}^{k+1} + \underline{\mathbf{P}}^u(\underline{\mathbf{u}}^{k+1}, \underline{\mathbf{s}}^k, \underline{\theta}^k) - \underline{\mathbf{F}}^u = \underline{\mathbf{0}}$ for $\underline{\mathbf{u}}^{k+1}$
 - 2: Solve $\underline{\mathbf{P}}^s(\underline{\mathbf{u}}^{k+1}, \underline{\mathbf{s}}^{k+1}, \underline{\theta}^k) = \underline{\mathbf{0}}$ for $\underline{\mathbf{s}}^{k+1}$
 - 3: Solve $\underline{\mathbf{D}}^{\theta\theta} \dot{\underline{\theta}}^{k+1} + \underline{\mathbf{D}}^{\theta u} \dot{\underline{\mathbf{u}}}^{k+1} + \underline{\mathbf{P}}^\theta(\underline{\mathbf{s}}^{k+1}, \underline{\theta}^{k+1}) - \underline{\mathbf{F}}^\theta = \underline{\mathbf{0}}$ for $\underline{\theta}^{k+1}$
 - 4: Check for convergence
- Exit loop if convergence or $k = k_{\max}$
- $(\underline{\mathbf{u}}^*, \underline{\mathbf{s}}^*, \underline{\theta}^*) = (\underline{\mathbf{u}}^{k+1}, \underline{\mathbf{s}}^{k+1}, \underline{\theta}^{k+1})$ is the solution of (B.35)

Figure B.3: Staggered solution of the spatially discretized phase field fracture problem.

One advantage of this staggered algorithm is that it results in three possibly linear subproblems. The equation of motion is nonlinear with respect to the displacements due to the split of the strain energy (4.2) meaning that the stress is nonlinearly dependent on the strain state. Hence, the equation of motion is linear, whenever $\psi_-^e = 0$ or $\psi_+^e = 0$. The phase field equation on the other hand is linear w.r.t. s if $g'(s)$ is linear, meaning that $g(s)$ is a polynomial of order two at most. The heat equation is linear in θ anyway. Even if some of the above nonlinear features occur, the solution of the decoupled subproblems is more robust than the solution of the fully coupled problem since additional nonlinear features, see for

example (4.2), are removed by freezing one of the fields. Furthermore, efficient explicit time integration schemes can be used to solve the second order spatially discretized equation of motion. This is not possible for the coupled equations because of the lack of a time derivative in the discretized evolution equation (B.10). In principle, a viscous approximation

$$\frac{\dot{s}}{M} + g'(s)\psi_e^+ - \mathcal{G}_c \left[2\epsilon\Delta s + \frac{1-s}{2l} \right] = 0, \quad (\text{B.74})$$

with the mobility parameter $M > 0$ could be utilized. This formulation is typically found in quasi-static phase field models for brittle fracture, e.g. in Kuhn (2013) and could be used instead of the stationary phase field equation (4.26). Such a modification would introduce a time derivative of s into the phase field evolution equation and thus enable an explicit solution. However, explicit time integration of the coupled system would still be impractical because of the strict stability requirements. For a first order equation such as (B.74), it is required that the time step obeys $\Delta t \leq \Delta t_{\max} \sim h^2$, where h is a characteristic length of the smallest element, see textbooks like Zienkiewicz and Taylor (2000). Compared to the larger time step size $\Delta t_{\max} = \Delta t_{cfl} \sim h$ which is allowed to integrate the second order equation of motion, cf. (B.93), this would increase the computational effort unnecessarily.

The accuracy of one iteration of the staggered algorithm depends on how well $\underline{\mathbf{s}}^k$ and $\underline{\boldsymbol{\theta}}^k$ approximate $\underline{\mathbf{s}}^{k+1}$ and $\underline{\boldsymbol{\theta}}^{k+1}$, respectively. If the assumed fields $\underline{\mathbf{s}}^k, \underline{\boldsymbol{\theta}}^k$ are close to the final fields $\underline{\mathbf{s}}^{k+1}$ and $\underline{\boldsymbol{\theta}}^{k+1}$, the displacements $\underline{\mathbf{u}}^{k+1}$ will also be a good approximation of the correct solution. Thus, one staggered iteration might be enough to find an accurate solution whenever the time step is small. In general, however, several iterations of the staggered algorithm need to be performed until the algorithm converges. In Ambati et al. (2015) it is proposed that the staggered algorithm can be assumed to be converged for the quasi-static and isothermal case if the solution is insensitive to further iterations. Ambati et al. (2015) propose the total energy $E^c + E^s$ as a quantitative measure to judge the change of the solution per staggered iteration. This work pursues the idea presented in Ambati et al. (2015) but suggests the contribution of inertial and internal forces to the global residual $\underline{\mathbf{I}}$, see (B.32), as a global convergence measure. For the isothermal case, the algorithm can be stated as follows. First, the change of $\underline{\mathbf{I}}$ in the current staggered iteration is normalized by the total change of $\underline{\mathbf{I}}$ in all previous staggered iterations at the current time, i.e.

$$\Delta I_{norm}^k = \frac{\|\underline{\mathbf{I}}(\underline{\mathbf{u}}^{k+1}, \underline{\mathbf{s}}^{k+1}) - \underline{\mathbf{I}}(\underline{\mathbf{u}}^k, \underline{\mathbf{s}}^k)\|}{\|\underline{\mathbf{I}}(\underline{\mathbf{u}}^{k+1}, \underline{\mathbf{s}}^{k+1}) - \underline{\mathbf{I}}(\underline{\mathbf{u}}^0, \underline{\mathbf{s}}^0)\|}. \quad (\text{B.75})$$

The number of iterations is normalized as well

$$l^k = \frac{k}{k+1}. \quad (\text{B.76})$$

Eventually, the quantity

$$\gamma^{k+1} = \arctan \left(\frac{\Delta I_{norm}^k}{l^{k+1} - l^k} \right) \frac{180^\circ}{\pi} \quad (\text{B.77})$$

can be computed to judge convergence in the form of the criterion

$$\gamma^{k+1} \leq \gamma^{tol}, \quad (\text{B.78})$$

where γ^{tol} is chosen to be 1° . The proposed criterion requires at least three stag-

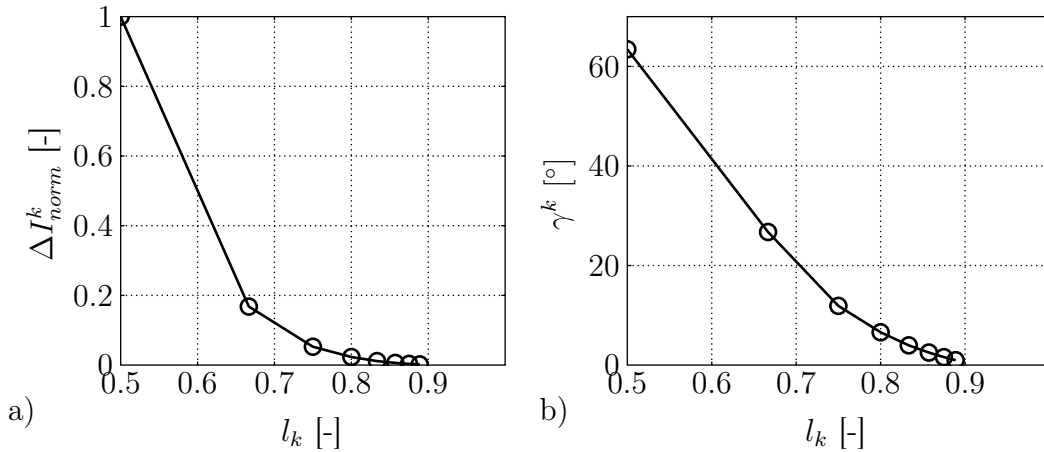


Figure B.4: a) Normalized change of the contribution of internal and inertial forces to the residual ΔI_{norm}^k versus the normalized number of staggered iterations l_k and b) convergence measure γ^k versus l_k .

gered iterations per time step, because information of the previous iteration is needed, i.e. there is no convergence check in the first iteration, and convergence cannot be achieved in the second iteration, where $\Delta I_{norm}^2 = 1.0$. Typical graphs of ΔI_{norm}^k and γ^k are shown in Fig. B.4.

B.4 Monolithic Solution Strategy

Alternatively to the staggered strategy, the complete nonlinear system (B.34) may be solved in a single step for \underline{d} . In this case, the fully coupled problem has to be handled and implicit time integration is most practical. Consequently, the computational effort per time step of this strategy is larger than for each of the subproblems in the staggered scheme. Utilizing an adequate time integration scheme, the monolithic algorithm can be set up so that it is unconditionally stable meaning that formally there are no stability bounds for the chosen time step size. However, a larger time step has still to be justified physically. The time discretization needs

to be fine enough to properly resolve wave propagation and possibly fast crack growth. The monolithic algorithm is also not as robust as the staggered algorithm because the Newton algorithm (B.5) will not necessarily find a solution if the time step and therewith the changes in the computed quantities are too substantial. Hence, it is reasonable to introduce an adaptive time step size control to enhance the robustness of the scheme in situations where a small time step is necessary, e.g. during fast crack propagation, and to exploit the numerical efficiency of larger time steps whenever possible.

B.5 Time Integration

For both the monolithic as well as the staggered strategy time discrete approaches are considered. Thus, discrete time steps are introduced recursively as

$$t_{n+1} = t_n + \Delta t, \quad (\text{B.79})$$

where t_n , t_{n+1} and Δt are the previous discrete time, the current discrete time and the current time step size, respectively. Evaluating (B.35) or (B.34) at time t_{n+1} yields

$$\begin{aligned} \begin{bmatrix} \underline{\mathbf{R}}^u \\ \underline{\mathbf{R}}^s \\ \underline{\mathbf{R}}^\theta \end{bmatrix} &= \begin{bmatrix} \underline{\mathbf{M}}^{uu} & \underline{\mathbf{0}} & \underline{\mathbf{0}} \\ \underline{\mathbf{0}} & \underline{\mathbf{0}} & \underline{\mathbf{0}} \\ \underline{\mathbf{0}} & \underline{\mathbf{0}} & \underline{\mathbf{0}} \end{bmatrix} \begin{bmatrix} \underline{\ddot{\mathbf{u}}}_{n+1} \\ \underline{\ddot{\mathbf{s}}}_{n+1} \\ \underline{\ddot{\boldsymbol{\theta}}}_{n+1} \end{bmatrix} + \begin{bmatrix} \underline{\mathbf{0}} & \underline{\mathbf{0}} & \underline{\mathbf{0}} \\ \underline{\mathbf{0}} & \underline{\mathbf{0}} & \underline{\mathbf{0}} \\ \underline{\mathbf{D}}^{\theta u}(\underline{\mathbf{d}}_{n+1}) & \underline{\mathbf{0}} & \underline{\mathbf{D}}^{\theta\theta} \end{bmatrix} \begin{bmatrix} \underline{\dot{\mathbf{u}}}_{n+1} \\ \underline{\dot{\mathbf{s}}}_{n+1} \\ \underline{\dot{\boldsymbol{\theta}}}_{n+1} \end{bmatrix} \\ &+ \begin{bmatrix} \underline{\mathbf{P}}^u(\underline{\mathbf{d}}_{n+1}) \\ \underline{\mathbf{P}}^s(\underline{\mathbf{d}}_{n+1}) \\ \underline{\mathbf{P}}^\theta(\underline{\boldsymbol{\theta}}_{n+1}, \underline{\mathbf{s}}_{n+1}) \end{bmatrix} - \begin{bmatrix} \underline{\mathbf{F}}^u \\ \underline{\mathbf{0}} \\ \underline{\mathbf{F}}^\theta \end{bmatrix} = \underline{\mathbf{0}} \end{aligned} \quad (\text{B.80})$$

or

$$\underline{\mathbf{M}} \underline{\ddot{\mathbf{d}}}_{n+1} + \underline{\mathbf{D}}(\underline{\mathbf{d}}_{n+1}) \underline{\dot{\mathbf{d}}}_{n+1} + \underline{\mathbf{P}}(\underline{\mathbf{d}}_{n+1}) - \underline{\mathbf{F}} = \underline{\mathbf{0}} \quad (\text{B.81})$$

respectively. The introduction of time integration schemes further reduces the number of unknowns by establishing relations between the nodal unknowns and their first and second order derivatives w.r.t. time. In this work, one-step time integration schemes are considered for the implicit time integration schemes that are used in the monolithic solution strategies. These schemes only require information on quantities from the previous time step and not of even earlier time steps.

As mentioned before, implicit time integration schemes are the adequate choice, if the monolithic solution strategy is used, but can be used in a staggered solution strategy as well. Two different implicit time integration schemes are examined. The Newmark method introduces the approximations

$$\begin{aligned}\underline{\mathbf{d}}_{n+1} &= \underline{\mathbf{d}}_n + \Delta t \underline{\dot{\mathbf{d}}}_n + \frac{(\Delta t^2)}{2} \left[(1 - 2\beta) \underline{\ddot{\mathbf{d}}}_n + 2\beta \underline{\ddot{\mathbf{d}}}_{n+1} \right], \\ \underline{\dot{\mathbf{d}}}_{n+1} &= \underline{\dot{\mathbf{d}}}_n + \Delta t \left[(1 - \gamma) \underline{\ddot{\mathbf{d}}}_n + \gamma \underline{\ddot{\mathbf{d}}}_{n+1} \right],\end{aligned}\tag{B.82}$$

with parameters $0 < 2\beta \leq 1$, $0 \leq \gamma \leq 1$ for time integration. In Wood (1990) the amplitude error and stability of the Newmark scheme have been investigated for linear problems. The amplitude error of linear problems is zero if $\gamma = 0.5$. In the presence of damping effects the amplitude error is of order $\mathcal{O}(\Delta t^2)$. Stability is ensured for $2\beta \geq \gamma \geq 0.5$ for linear problems.

The first order accurate fully implicit Euler scheme uses the approximations

$$\begin{aligned}\underline{\mathbf{d}}_{n+1} &= \underline{\mathbf{d}}_n + \Delta t \underline{\dot{\mathbf{d}}}_{n+1} \\ \underline{\dot{\mathbf{d}}}_{n+1} &= \underline{\dot{\mathbf{d}}}_n + \Delta t \underline{\ddot{\mathbf{d}}}_{n+1}\end{aligned}\tag{B.83}$$

and is unconditionally stable. Nonetheless, this time integration scheme involves severe numerical dissipation for larger time steps.

The equations gained from time integration (B.82) or (B.83) can be substituted in (B.81) to yield a nonlinear system of algebraic equations for the current unknowns

$$\underline{\mathbf{R}}(\underline{\mathbf{d}}_{n+1}) = \underline{\mathbf{0}}.\tag{B.84}$$

This system is solved with the Newton-Raphson algorithm summarized in Fig. B.5. The computational effort of the Newton algorithm per iteration is dictated by the computation of the residual, the computation of the tangent matrix, i.e. step 1, and the solution of a set of linear equations, i.e. step 2. Furthermore, the number of necessary Newton iterations is determined by the nonlinear features of the phase field fracture problem. In addition, an automatic time step control is implemented that adjusts the time step according to the number of iterations that is needed for the Newton algorithm to converge. If the number of Newton iterations of the previous time step exceeds eight, a bisection of the time step is performed. On the contrary, if the number of Newton iterations falls below four, the time step size is doubled for the next time step.

Due to the reasons explained above, explicit time integration schemes may only be used in a staggered solution strategy as a means to solve the equation of motion. The most popular explicit time integration method in structural mechanics is the

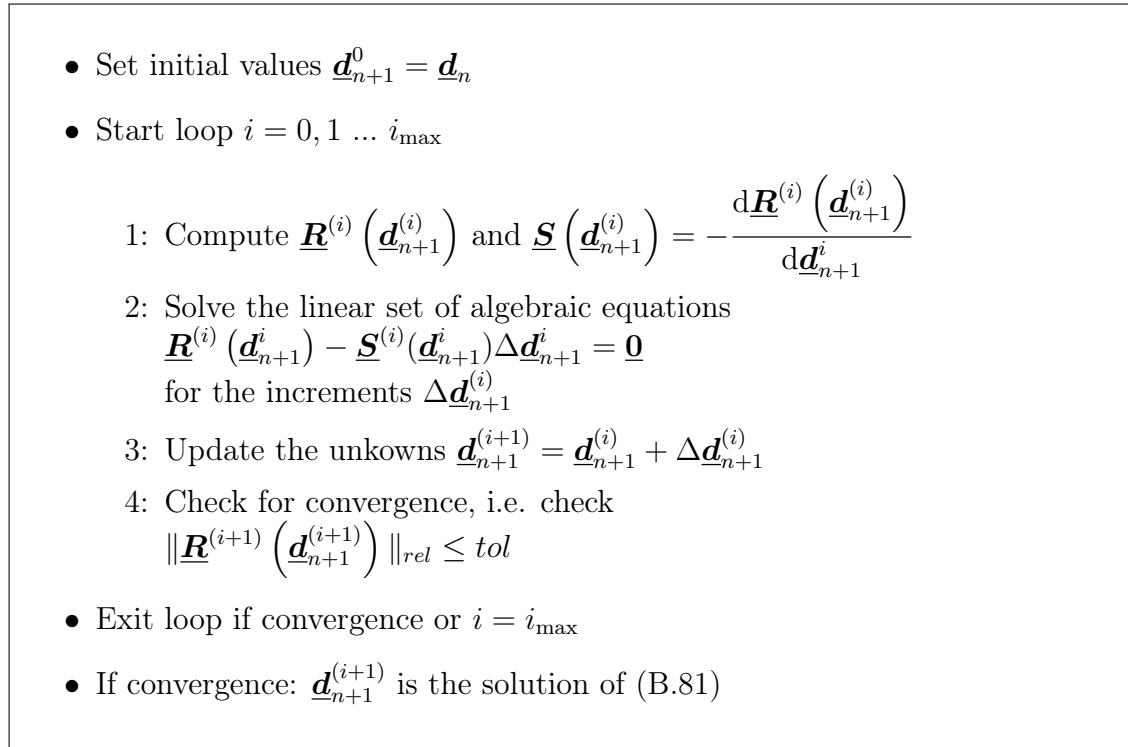


Figure B.5: Newton-Raphson algorithm. The residual norm $\|*\|_{rel}$ is a relative quantity that allows the tolerance tol to be chosen independently of the problem size. For the solution of linear systems of algebraic equations (step 2) several established methods exist and hardware acceleration of this operation is feasible as shown in Schlüter et al. (2013).

central difference scheme which uses the approximations

$$\dot{\underline{\mathbf{u}}}_n = \frac{\underline{\mathbf{u}}_{n+1} - \underline{\mathbf{u}}_{n-1}}{2\Delta t}, \quad (\text{B.85})$$

$$\ddot{\underline{\mathbf{u}}}_n = \frac{\underline{\mathbf{u}}_{n+1} - 2\underline{\mathbf{u}}_n + \underline{\mathbf{u}}_{n-1}}{\Delta t^2}. \quad (\text{B.86})$$

Evaluating (B.80)₁ at time t_n and substituting (B.86), results in the explicit relation

$$\underline{\mathbf{M}}^{uu}\underline{\mathbf{u}}_{n+1} = (\Delta t)^2 [\underline{\mathbf{F}}_n^u - \underline{\mathbf{P}}^u(\underline{\mathbf{u}}_n)] + \underline{\mathbf{M}}^{uu}(2\underline{\mathbf{u}}_n - \underline{\mathbf{u}}_{n-1}) \quad (\text{B.87})$$

for the current unknowns $\underline{\mathbf{u}}_{n+1}$. In the first time step, the quantity $\underline{\mathbf{u}}_{-1}$ has to be initialized as

$$\underline{\mathbf{u}}_{-1} = \underline{\mathbf{u}}_0 - \Delta t \dot{\underline{\mathbf{u}}}_0 + \frac{(\Delta t)^2}{2} \ddot{\underline{\mathbf{u}}}_0, \quad (\text{B.88})$$

where

$$\ddot{\underline{\mathbf{u}}}_0 = (\underline{\mathbf{M}}^{uu})^{-1} [-\underline{\mathbf{P}}^u(\underline{\mathbf{u}}_0) + \underline{\mathbf{F}}_0^u]. \quad (\text{B.89})$$

Solving (B.87) is trivial if $\underline{\mathbf{M}}^{uu}$ has a diagonal structure, which can be achieved by so called lumping strategies. A diagonalized, lumped approximation of the consistent element mass matrix (B.28) that retains the element mass

$$M_e = \int_{\Omega_e} \rho \, d\Omega_e \quad (\text{B.90})$$

is achieved by the approach

$$\underline{\mathbf{M}}_{II,e}^{\text{lump}} = \frac{M_{II,e}}{\sum_{J=1}^{N_e} M_{JJ,e}} M_e \mathbf{1}^{2 \times 2}, \quad \text{where} \quad M_{II,e} = \int_{\Omega_e} N_I^2 \rho \, d\Omega_e. \quad (\text{B.91})$$

The resulting element mass matrix is

$$\underline{\mathbf{M}}_e^{uu} = \begin{bmatrix} \underline{\mathbf{M}}_{11,e}^{\text{lump}} & \underline{\mathbf{0}} & \underline{\mathbf{0}} & \underline{\mathbf{0}} \\ \underline{\mathbf{0}} & \underline{\mathbf{M}}_{22,e}^{\text{lump}} & \underline{\mathbf{0}} & \underline{\mathbf{0}} \\ \underline{\mathbf{0}} & \underline{\mathbf{0}} & \underline{\mathbf{M}}_{33,e}^{\text{lump}} & \underline{\mathbf{0}} \\ \underline{\mathbf{0}} & \underline{\mathbf{0}} & \underline{\mathbf{0}} & \underline{\mathbf{M}}_{44,e}^{\text{lump}} \end{bmatrix}, \quad (\text{B.92})$$

as described in Wriggers (2009) and Hinton et al.. In this work, such a lumped mass matrix is used whenever the central difference method is employed. The central difference scheme is not unconditionally stable. As mentioned in Zienkiewicz and Taylor (2000) and Wriggers (2009), the critical time step for the second order problem (B.80)₁ is governed by

$$\Delta t \leq \delta \frac{h}{c_d} = \delta \Delta t_{cfl}, \quad (\text{B.93})$$

where c_d is the dilatational wave speed and h is the characteristic length of the smallest element. The factor δ further reduces the allowable time step and accounts for nonlinear effects. The quantity $\Delta t_{cfl} = \frac{h}{c_d}$ which is determined by the physics of the problem and the spatial discretization may be referred to as the Courant Friedrichs Lewy (CFL) time step in analogy to the stability condition described in Lewy et al. (1928). The amplitude error of the central difference scheme is also of second order, see Wriggers (2009).

From (B.93) it follows that the central difference scheme requires small time steps for stability reasons. On the other hand, the staggered approach depends upon small time steps as well in order to achieve sufficient accuracy. These observations motivate a combination of both methods.

In a staggered approach, the decoupled phase field equation reduces to a non-linear set of algebraic equations i.e. time integration is not necessary and the Newton-Raphson algorithm, see Fig. B.5, is used to solve

$$\underline{\mathbf{P}}^s(\underline{\mathbf{u}}_{n+1}^{k+1}, \underline{\mathbf{s}}_{n+1}^{k+1}, \underline{\boldsymbol{\theta}}_{n+1}^k) = \underline{\mathbf{0}} \quad (\text{B.94})$$

for $\underline{s}_{n+1}^{k+1}$, i.e. to perform step 2 of the staggered algorithm displayed in Fig. B.3. The solution of the energy balance even reduces to a linear set of equations

$$\underline{D}^{\theta\theta}\dot{\underline{\theta}}^{k+1} + \underline{D}^{\theta u}\dot{\underline{u}}^{k+1} + \underline{P}^\theta(\underline{s}^{k+1}, \underline{\theta}^{k+1}) - \underline{F}^\theta = \underline{0} \quad (\text{B.95})$$

that requires only a single Newton iteration in order to obtain a solution.

B.6 Implementation of the Irreversibility Constraint

As proposed in Kuhn (2013), the irreversibility of crack growth is modelled by defining homogeneous Dirichlet boundary conditions for the phase field $s(\mathbf{x}, t)$ once a value of $s \leq s_{tol}$ with $s_{tol} = 10^{-8}$ is reached at the considered location for the first time meaning that

$$s_{I,n+1} = 0 \quad \text{if} \quad s_{I,n} \leq s_{tol}. \quad (\text{B.96})$$

This is accomplished by a reformulation of the residual and the tangent matrix on the element level rather than changing global boundary conditions in order to achieve

$$\Delta s_{I,n+1}^{(i)} = -s_{I,n+1}^{(i)} \quad (\text{B.97})$$

in every Newton iteration. Such an increment causes the phase field to remain zero in all subsequent iterations and time steps, i.e.

$$s_{I,n+1}^{(i+1)} = s_{I,n+1}^{(i)} + \Delta s_{I,n+1}^{(i)} = s_{I,n+1}^{(i)} - s_{I,n+1}^{(i)} = 0, \quad (\text{B.98})$$

see also step 3 in Fig. B.5. The result (B.97) is enforced by a modification of

$$\underline{R}_{e,n+1}^{(i)} = \underline{S}_{e,n+1}^{(i)} \Delta \underline{d}_{e,n+1}^{(i)} \quad (\text{B.99})$$

on the element level.

- In a first step, the column $\underline{S}_{e,n+1}^{(i)} [: , s_I]$ of the element tangent matrix is multiplied by $s_{I,n+1}^{(i)}$ and added to the residual

$$\underline{R}_{e,n+1}^{(i)} \leftarrow \underline{R}_{e,n+1}^{(i)} + s_{I,n+1}^{(i)} \underline{S}_{e,n+1}^{(i)} [: , s_I]. \quad (\text{B.100})$$

- Then the corresponding residual entry to s_I is replaced by $-s_{I,n+1}^{(k)}$, i.e.

$$R_{e,n+1}^{(k)} [s_I] = -s_{I,n+1}^{(k)}. \quad (\text{B.101})$$

- Finally, the row $\underline{S}_{e,n+1}^{(i)} [s_I, :]$ and the column $\underline{S}_{e,n+1}^{(i)} [: , s_I]$ are set to zero and the entry $\underline{S}_{e,n+1}^{(i)} [s_I, s_I]$ is set to

$$\underline{S}_{e,n+1}^{(i)} [s_I, s_I] = 1. \quad (\text{B.102})$$

B.7 Computation of the Crack Tip Position and of the Crack Velocity

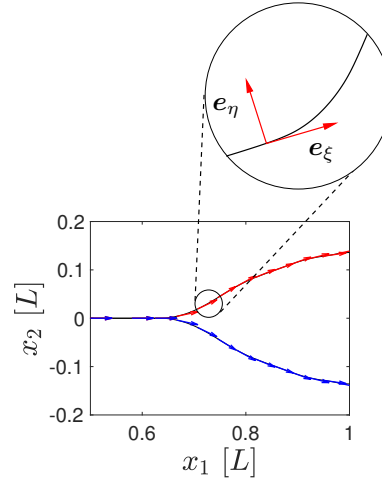


Figure B.6: Representation of a (branched) 2D crack pattern by successive crack tip positions $\tilde{\mathbf{z}}$ (black lines), tangential vectors \mathbf{e}_ξ for the lower (blue arrows) and upper (red arrows) branch, illustration of the ξ - η -coordinate system (magnified view).

The crack tip position $\mathbf{z}(t)$ is identified with the position \mathbf{x}_J of the node J that is the most progressed on the computed crack path – which is available for post-processing purposes – and fulfills

$$s_J < s_{lim}, \quad \text{with} \quad s_{lim} \ll 1 \quad (\text{B.103})$$

at time t . A regression analysis of the successive discrete crack tip positions yields a continuous representation of the crack tip position

$$\tilde{\mathbf{z}}(t) \approx \mathbf{z}(t), \quad (\text{B.104})$$

cf. Fig. B.6, that allows to define a crack tip velocity

$$\mathbf{v}(t) = \frac{d\tilde{\mathbf{z}}(t)}{dt} \quad (\text{B.105})$$

and the tangential vector at the crack tip as

$$\mathbf{e}_\xi = \frac{\mathbf{v}}{|\mathbf{v}|}. \quad (\text{B.106})$$

B.8 Finite Element Discretization of the Configurational Force Balance

The configurational forces can be evaluated numerically from the primary fields that are available from the necessary preceding finite element simulation. Starting from the weak form of the configurational force balance

$$\int_{\Omega} (-\mathbf{g} + \operatorname{div}\Sigma - \dot{\mathbf{p}}) \cdot \boldsymbol{\eta}^g \, dV = 0, \quad (\text{B.107})$$

where $\boldsymbol{\eta}^g$ is a test function that vanishes on $\partial\Omega$, it is by means of the identity

$$\operatorname{div}\Sigma \cdot \boldsymbol{\eta}^g = \operatorname{div}(\Sigma^T \boldsymbol{\eta}^g) - \Sigma : \operatorname{grad}\boldsymbol{\eta}^g \quad (\text{B.108})$$

and the divergence theorem (A.11)

$$\int_{\Omega} (-\mathbf{g} \cdot \boldsymbol{\eta}^g - \Sigma : \operatorname{grad}\boldsymbol{\eta}^g - \dot{\mathbf{p}} \cdot \boldsymbol{\eta}^g) \, dV = 0. \quad (\text{B.109})$$

The geometry is discretized as explained in Section B.1 and the test functions employ the same ansatz as the primary fields (B.4)

$$\underline{\boldsymbol{\eta}}_h^g = \sum_{I=1}^N N_I \underline{\boldsymbol{\eta}}_I^g. \quad (\text{B.110})$$

The gradients of the test function are approximated by

$$\nabla \underline{\boldsymbol{\eta}}_h^g = \sum_{I=1}^N \underline{\boldsymbol{\eta}}_I^g [\underline{\mathbf{B}}_I^\eta]^T, \quad (\text{B.111})$$

where

$$\underline{\mathbf{B}}_I^\eta = \begin{bmatrix} \partial N_I \\ \partial \underline{\mathbf{x}}_e \end{bmatrix}^T. \quad (\text{B.112})$$

The configurational stress is expressed as

$$\underline{\boldsymbol{\Sigma}}_h^e = (\psi_h^e - k_h) \mathbf{1}^{n \times n} - [\nabla \underline{\mathbf{u}}_h^{\text{full}}]^T \underline{\boldsymbol{\sigma}}_h^{\text{full}} \quad (\text{B.113})$$

and

$$\underline{\boldsymbol{\Sigma}}_h^s = \psi_h^s \mathbf{1}^{n \times n} - 2\mathcal{G}_c l \nabla \underline{\boldsymbol{s}}_h \nabla \underline{\boldsymbol{s}}_h^T, \quad (\text{B.114})$$

where

$$\underline{\boldsymbol{\sigma}}_h^{\text{full}} = [\sigma_{ijh}] \quad \text{and} \quad \nabla \underline{\mathbf{u}}_h^{\text{full}} = \begin{bmatrix} \partial u_{ih} \\ \partial x_j \end{bmatrix}, \quad (\text{B.115})$$

imply the full matrix notation of the stress tensor and the gradient of the displacement. The momentum is given by

$$\underline{\mathbf{p}}_h = \sum_{I=1}^N N_I \dot{\underline{\mathbf{u}}}_I. \quad (\text{B.116})$$

Consequently, the rate of the pseudo-momentum is

$$\dot{\underline{\mathbf{p}}}_h = - [\nabla \underline{\mathbf{u}}_h^{\text{full}}]^T \dot{\underline{\mathbf{p}}}_h - [\nabla \dot{\underline{\mathbf{u}}}_h^{\text{full}}]^T \underline{\mathbf{p}}_h. \quad (\text{B.117})$$

These relations are used to express the weak form of the configurational force

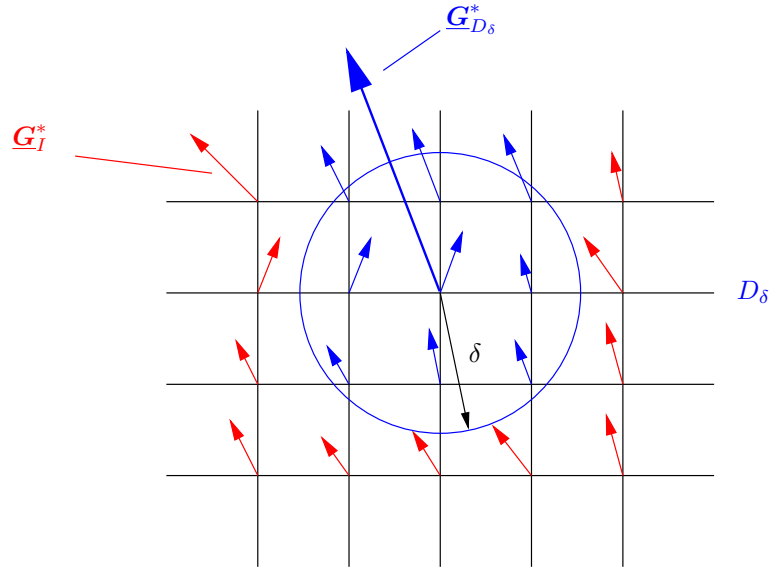


Figure B.7: Illustration of the numerical evaluation of the configurational force acting on a crack tip control volume D_δ .

balance as

$$\sum_{I=1}^N [\underline{\boldsymbol{\eta}}_I^g]^T \left[\int_{\Omega_d} \left(-\underline{\mathbf{g}}_h N_I - \underline{\boldsymbol{\Sigma}}_h^e \underline{\mathbf{B}}_I^\eta - \underline{\boldsymbol{\Sigma}}_h^s \underline{\mathbf{B}}_I^\eta - \dot{\underline{\mathbf{p}}}_h N_I \right) dV \right] = 0. \quad (\text{B.118})$$

Since the test functions are – apart from the restriction $\underline{\boldsymbol{\eta}}_h^g = \underline{\mathbf{0}}$ on $\partial\Omega_d$ – arbitrary, it is

$$\int_{\Omega_d} \left(-\underline{\mathbf{g}}_h - \underline{\boldsymbol{\Sigma}}_h^e \underline{\mathbf{B}}_I^\eta - \underline{\boldsymbol{\Sigma}}_h^s \underline{\mathbf{B}}_I^\eta - \dot{\underline{\mathbf{p}}}_h N_I \right) dV = \underline{\mathbf{0}}. \quad (\text{B.119})$$

The nodal configurational forces are defined as

$$\underline{\mathbf{G}}_I^e = - \int_{\Omega_d} \underline{\boldsymbol{\Sigma}}_h^e \underline{\mathbf{B}}_I^\eta dV, \quad (\text{B.120})$$

$$\underline{\mathbf{G}}_I^s = - \int_{\Omega_d} \underline{\boldsymbol{\Sigma}}_h^s \underline{\mathbf{B}}_I^\eta \, dV, \quad (\text{B.121})$$

$$\underline{\mathfrak{P}}_I = - \int_{\Omega_d} \underline{\dot{\mathbf{p}}}_h N_I \, dV \quad (\text{B.122})$$

and

$$\underline{\mathbf{G}}_I = \int_{\Omega_d} \underline{\mathbf{g}}_h N_I \, dV, \quad (\text{B.123})$$

which allows to write the discrete configurational force balance for a particular node I as

$$\underline{\mathbf{G}}_I = \underline{\mathbf{G}}_I^e + \underline{\mathbf{G}}_I^s + \underline{\mathfrak{P}}_I. \quad (\text{B.124})$$

The configurational force components $\underline{\mathbf{G}}_{D_\delta}^*$, $\underline{\mathfrak{P}}_{D_\delta}$ acting on a crack tip control volume D_δ are determined by adding the nodal configurational forces inside that respective control volume

$$\underline{\mathbf{G}}_{D_\delta}^* \approx \sum_{I \in \mathcal{E}} \underline{\mathbf{G}}_I^*, \quad \underline{\mathfrak{P}}_{D_\delta} \approx \sum_{I \in \mathcal{E}} \underline{\mathfrak{P}}_I, \quad \mathcal{E} = \{I : \mathbf{x}_I \in D_\delta\}, \quad (\text{B.125})$$

as illustrated in Fig. B.7.

Bibliography

- M. Adda-Bedia. Brittle fracture dynamics with arbitrary paths. II. Dynamic crack branching under general antiplane loading. *J. Mech. Phys. Solid.*, 52(6):1407 – 1420, 2004.
- M. Adda-Bedia. Brittle fracture dynamics with arbitrary paths III. The branching instability under general loading. *J. Mech. Phys. Solid.*, 53(1):227 – 248, 2005.
- M. Ambati, T. Gerasimov, and L. Lorenzis. A review on phase-field models of brittle fracture and a new fast hybrid formulation. *Comput. Mech.*, 55(2):383–405, 2015.
- L. Ambrosio and A. Braides. Energies in SBV and variational models in fracture mechanics. In *Homogenization and applications to material sciences*, pages 1–22, 1995.
- L. Ambrosio and V. M. Tortorelli. Approximation of functional depending on jumps by elliptic functional via γ -convergence. *Commun. Pure Appl. Maths*, 43(8):999–1036, 1990.
- H. Amor, J.-J. Marigo, C. Maurini, and N. K. Pham. Stability analysis and numerical implementation of non-local damage models via a global variational approach. In *WCCM8 - ECCOMAS 2008*, 2008.
- H. Amor, J.-J. Marigo, and C. Maurini. Regularized formulation of the variational brittle fracture with unilateral contact: Numerical experiments. *J. Mech. Phys. Solid.*, 57(8):1209–1229, 2009.
- I. S. Aranson, V. A. Kalatsky, and V. M. Vinokur. Continuum field description of crack propagation. *Phys. Rev. Let.*, 85(1):118–121, 2000.
- R. J. Archuleta and S. M. Day. Dynamic rupture in a layered medium: The 1966 Parkfield earthquake. *Seismol. Soc. Am., Bull.*, 70(3):671–689, 1980.
- C. Atkinson and J. D. Eshelby. The flow of energy into the tip of a moving crack. *International Journal of Fracture Mechanics*, 4(1):3–8, 1968.

- G. I. Barenblatt. The mathematical theory of equilibrium cracks in brittle fracture. In H. L. Dryden, T. von Kármán, G. Kuerti, F. H. van den Dungen, and L. Howarth, editors, *Advances in Applied Mechanics*, volume 7 of *Adv. Appl. Mech.*, pages 55–129. Elsevier, 1962.
- W. Becker and D. Gross. *Mechanik elastischer Körper und Strukturen*. Mechanical Engineering Series. Springer, 2002.
- A. Benallal and J.-J. Marigo. Bifurcation and stability issues in gradient theories with softening. *Modell. Simul. Mater. Sci. Eng.*, 15(1):283–295, 2007.
- W. J. Boettinger, J. A. Warren, C. Beckermann, and A. Karma. Phase-field simulation of solidification. *Annual Review of Materials Research*, 32(1):163–194, 2002.
- M. J. Borden. *Isogeometric analysis of phase-field models for dynamic brittle and ductile fracture*. PhD thesis, The University of Texas at Austin, 2012.
- M. J. Borden, C. V. Verhoosel, M. A. Scott, T. J. R. Hughes, and C. M. Landis. A phase-field description of dynamic brittle fracture. *Comput. Meth. Appl. Mech. Eng.*, 217–220:77–95, 2012.
- B. Bourdin. *Une méthode variationnelle en mécanique de la rupture*. PhD thesis, Université Paris-Nord, 1998.
- B. Bourdin and A. Chambolle. Implementation of an adaptive finite-element approximation of the Mumford-Shah functional. *Numer. Mat.*, 85:609–646, 2000.
- B. Bourdin, G. Francfort, and J.-J. Marigo. The variational approach to fracture. *J. Elasticity*, 91(1):5–148, 2008.
- B. Bourdin, C. Larsen, and C. Richardson. A time-discrete model for dynamic fracture based on crack regularization. *Int. J. Fract.*, 168:133–143, 2011.
- B. Bourdin, J. J. Marigo, C. Maurini, and P. Sicsic. Morphogenesis and propagation of complex cracks induced by thermal shocks. *Phys. Rev. Lett.*, 112:014301, 2014.
- K. Broberg. *Cracks and Fracture*. Elsevier Science, 1999.
- K. B. Broberg. The near-tip field at high crack velocities. *Int. J. Fract.*, 39(1):1–13, 1989.
- R. Burridge. An influence function for the intensity factor in tensile fracture. *IJES*, 14(8):725 – 734, 1976.

- A. Chambolle. A density result in two-dimensional linearized elasticity, and applications. *Arch. Rat. Mech. Anal.*, 167:211–233, 2003.
- A. Chambolle. An approximation result for special functions with bounded deformation. *J. Math. Pure Appl.*, 83(7):929–954, 2004.
- D. R. Curran, D. A. Shockey, and S. Winkler. Crack propagation at supersonic velocities. *Int. J. Fract.*, 6(3):271–278, 1970.
- T. Dally and K. Weinberg. The phase-field approach as a tool for experimental validations in fracture mechanics. *Commun. Numer. Meth. Engng*, 29(4):947–956, 2017.
- L. O. Eastgate, J. P. Sethna, M. Rauscher, T. Cretegnny, C.-S. Chen, and C. R. Myers. Fracture in Mode I using a conserved phase-field model. *Phys. Rev. E*, 65(3):036117, 2002.
- A. Ehrlacher. Path independent integral for the calculation of the energy release rate in elastodynamics. *Advances in fracture research*, 5:2187–2195, 1981.
- F. Erdogan and G. C. Sih. On the crack extension in plates under plane loading and transverse shear. *J. Basic Engineering*, 85(4):519–525, 1963.
- J. D. Eshelby. The force on an elastic singularity. *Phil. Trans. Roy. Soc. Lond. A*, 244(877):87–112, 1951.
- J. D. Eshelby. *Energy Relations and the Energy-Momentum Tensor in Continuum Mechanics*, pages 82–119. Springer Berlin Heidelberg, Berlin, Heidelberg, 1999. ISBN 978-3-642-59938-5.
- J. Fineberg, S. P. Gross, M. Marder, and H. L. Swinney. Instability in the propagation of fast cracks. *Phys. Rev. B*, 45:5146–5154, Mar 1992.
- G. A. Francfort. Quasistatic brittle fracture seen as an energy minimization movement. *GAMM-Mitt.*, 29(2):172–191, 2006.
- G. A. Francfort and C. J. Larsen. Existence and convergence for quasi-static evolution in brittle fracture. *Commun. Pure Appl. Maths*, 56:1465–1500, 2003.
- G. A. Francfort and J.-J. Marigo. Revisiting brittle fracture as an energy minimization problem. *J. Mech. Phys. Solid.*, 46(8):1319–1342, 1998.
- G. A. Francfort and J.-J. Marigo. Griffith theory of brittle fracture revisited: Merits and drawbacks. *Latin Amer. J. Solids Struct.*, 2:57–64, 2005.

- L. B. Freund. Energy flux into the tip of an extending crack in an elastic solid. *J. Elasticity*, 2(4):341–349, 1972.
- L. B. Freund. *Dynamic Fracture Mechanics*. Cambridge Monographs on Mechanics. Cambridge University Press, 1990.
- H. Gao, Y. Huang, and F. F. Abraham. Continuum and atomistic studies of intersonic crack propagation. *J. Mech. Phys. Solid.*, 49(9):2113 – 2132, 2001.
- D. Garibotti. Dicing of micro-semiconductors, Dec. 3 1963. US Patent 3112850.
- R. V. Goldstein and R. L. Salganik. Brittle fracture of solids with arbitrary cracks. *Int. J. Fract.*, 10:507–523, 1974.
- A. A. Griffith. The phenomena of rupture and flow in solids. *Phil. Trans. Roy. Soc. Lond. A*, 221:163–198, 1921.
- D. Gross and T. Seelig. *Fracture Mechanics: With an Introduction to Micromechanics*. Mechanical Engineering Series. Springer, 2nd edition, 2011.
- S. P. Gross, J. Fineberg, M. Marder, W. D. McCormick, and H. L. Swinney. Acoustic emissions from rapidly moving cracks. *Phys. Rev. Lett.*, 71:3162–3165, Nov 1993.
- M. E. Gurtin. *An Introduction to Continuum Mechanics*. Mathematics in Science and Engineering. Academic Press, 1981.
- M. E. Gurtin. *Configurational forces as basic concepts of continuum physics*. Applied mathematical sciences. Springer, 2000.
- V. Hakim and A. Karma. Laws of crack motion and phase-field models of fracture. *J. Mech. Phys. Solid.*, 57(2):342–368, 2009.
- W. R. Hamilton. Second essay on a general method in dynamics. *Phil. Trans. Roy. Soc. Lond.*, 125:95–144, 1835.
- H. Henry and H. Levine. Dynamic instabilities of fracture under biaxial strain using a phase field model. *Phys. Rev. Lett.*, 93(10):105504, 2004.
- E. Hinton, T. Rock, and O. C. Zienkiewicz. A note on mass lumping and related processes in the finite element method. *Earthq. Eng. Struct. D.*, 4(3).
- M. Hofacker and C. Miehe. Continuum phase field modeling of dynamic fracture: variational principles and staggered FE implementation. *Int. J. Fract.*, 178(1): 113–129, 2012.

- M. Hofacker and C. Miehe. A phase field model of dynamic fracture: Robust field updates for the analysis of complex crack patterns. *Int. J. Numer. Meth. Eng.*, 93(3):276–301, 2013.
- G. A. Holzapfel. *Nonlinear solid mechanics: a continuum approach for engineering*. Wiley, 2000.
- B. Hopkinson. The pressure of a blow. *The Scientific Papers of Bertram Hopkinson*, pages 423–437, 1921.
- J. Hopkinson. On the rupture of iron wire by a blow. *Proc. Manch. Lit. Philos. Soc.*, 11:40–45, 1872.
- M. Hossain, C.-J. Hsueh, B. Bourdin, and K. Bhattacharya. Effective toughness of heterogeneous media. *J. Mech. Phys. Solid.*, 71:15 – 32, 2014.
- T. J. R. Hughes. *The Finite Element Method: Linear Static and Dynamic Finite Element Analysis*. Dover Publications, Inc., Mineola, New York, 2000.
- G. R. Irwin. Analysis of stresses and strains near the end of a crack traversing a plate. *J. Appl. Mech.*, 24:361–364, 1957.
- G. R. Irwin. Fracture mechanics. *Structural Mechanics*, pages 557–591, 1960.
- J. Kalthoff. Modes of dynamic shear failure in solids. *Int. J. Fract.*, 101:1–31, 2000.
- J. F. Kalthoff and S. Winkler. Failure mode transition of high rates of shear loading. *Proc. I. Con. Imp. Load. Dyn. Beh. Mat.*, 1:185–195, 1987.
- A. Karma, D. A. Kessler, and H. Levine. Phase-Field Model of Mode III Dynamic Fracture. *Phys. Rev. Lett.*, 87(4):45501, 2001.
- E. Katzav, M. Adda-Bedia, and R. Arias. Theory of dynamic crack branching in brittle materials. *Int. J. Fract.*, 143:245–271, 2007.
- R. Kienzler and G. Herrmann. *Mechanics in material space: with applications to defect and fracture mechanics*. Engineering online library. Springer, 2000.
- A. S. Kobayashi, B. G. Wade, W. B. Bradley, and S. T. Chiu. Crack branching in homalite-100 sheets. *Off. Nav. Res.*, 13, 1972.
- V. Kondratenko. Method of splitting non-metallic materials, 1997. US Patent 5609284.

- B. V. Kostrov and L. V. Nikitin. Some general problems of mechanics of brittle fracture. *Arch. Mech. Stos.*, 22:749–775, 1970.
- R. Krueger. Virtual crack closure technique: History, approach, and applications. *Appl. Mech. Rev.*, 57(2):109, 2004.
- C. Kuhn. *Numerical and Analytical Investigation of a Phase Field Model for Fracture*. PhD thesis, Technische Universität Kaiserslautern, 2013.
- C. Kuhn and R. Müller. Phase field simulation of thermomechanical fracture. *PAMM*, 9(1):191–192, 2009.
- C. Kuhn and R. Müller. A continuum phase field model for fracture. *Eng. Fract. Mech.*, 77(18):3625–3634, 2010a. Computational Mechanics in Fracture and Damage: A Special Issue in Honor of Prof. Gross.
- C. Kuhn and R. Müller. Configurational forces in a phase field model for fracture. In *18th European Conference on Fracture*. DVM, 2010b.
- C. Kuhn, A. Schlüter, and R. Müller. On degradation functions in phase field fracture models. *Comput. Mater. Sci.*, 108, Part B:374 – 384, 2015.
- E. Lambert, J. Lambert, and B. De Longueville. Severing of glass or vitrocrytalline bodies, Jan. 27 1976. US Patent 3935419.
- C. J. Larsen, C. Ortner, and E. Süli. Existence of solutions to a regularized model of dynamic fracture. *Math. Models Methods Appl. Sci.*, 20(07):1021–1048, 2010.
- H. Lewy, K. Friedrichs, and R. Courant. Über die partiellen Differenzgleichungen der mathematischen Physik. *Math. Ann.*, 100:32–74, 1928.
- T. Li, J. J. Marigo, D. Guilbaud, and S. Potapov. Numerical investigation of dynamic brittle fracture via gradient damage models. *AMSES*, 3(1):26, 2016.
- A. Love. *A Treatise on the Mathematical Theory of Elasticity*. Dover Books on Engineering Series. Dover Publications, 1944. ISBN 9780486601748.
- R. M. Lumley. Controlled separation of brittle materials using a laser. *J. Am. Ceram. Soc.*, 48(4):850–854, 1969.
- G. D. Maso and R. Toader. A model for the quasi-static growth of brittle fractures: existence and approximation results. *Arch. Rat. Mech. Anal.*, 162:101–135, 2002.
- G. A. Maugin. *Material Inhomogeneities in Elasticity*. Applied mathematics and mathematical computation. Taylor & Francis, 1993.

- G. A. Maugin. *Configurational forces: thermomechanics, physics, mathematics, and numerics*. CRC series—modern mechanics and mathematics. Taylor and Francis, 2010.
- G. A. Maugin and C. Trimarco. Pseudomomentum and material forces in nonlinear elasticity: variational formulations and application to brittle fracture. *Acta Mechanica*, 94(1):1–28, 1992.
- M. Mello, H. Bhat, A. Rosakis, and H. Kanamori. Reproducing the supershear portion of the 2002 Denali earthquake rupture in laboratory. *Earth Planet. Sci. Lett.*, 387:89 – 96, 2014.
- C. Miehe. Comparison of two algorithms for the computation of fourth-order isotropic tensor functions. *Comput. Struct.*, 66(1):37 – 43, 1998.
- C. Miehe and E. Gürses. A robust algorithm for configurational-force-driven brittle crack propagation with R-adaptive mesh alignment. *Int. J. Numer. Meth. Eng.*, 72(2):127–155, 2007.
- C. Miehe and M. Lambrecht. Algorithms for computation of stresses and elasticity moduli in terms of Seth - Hill’s family of generalized strain tensors. *Commun. Numer. Meth. Engng*, 17(5):337–353, 2001.
- C. Miehe, M. Hofacker, and F. Welschinger. A phase field model for rate-independent crack propagation: Robust algorithmic implementation based on operator splits. *Comput. Meth. Appl. Mech. Eng.*, 199(45–48):2765–2778, 2010a.
- C. Miehe, F. Welschinger, and M. Hofacker. Thermodynamically consistent phase-field models for fracture: Variational principles and multi-field FE implementations. *Int. J. Numer. Meth. Eng.*, 83(10):1273–1311, 2010b.
- N. Moelans, B. Blainpain, and P. Wollants. An introduction to phase-field modeling of microstructure evolution. *Comput. Coupl. Ph. Diag. Therm.* , 32(1): 268–294, 2008.
- N. Moës, J. Dolbow, and T. Belytschko. A finite element method for crack growth without remeshing. *Int. J. Numer. Meth. Eng.*, 46(1):131–150, 1999.
- D. Mumford and J. Shah. Optimal approximations by piecewise smooth functions and associated variational problems. *Commun. Pure Appl. Maths*, 42(5):577–685, 1989.
- T. Nakamura, C. F. Shih, and L. B. Freund. Computational methods based on an energy integral in dynamic fracture. *Int. J. Fract.*, 27(3):229–243, 1985.

- C. D. C. Nguyen. *Finite Element Analysis of Ion-Irradiated Carbon Foils*. Master thesis, Technische Universität Darmstadt, 2013.
- S. Nisar, M. Sheikh, L. Li, and S. Safdar. Effect of thermal stresses on chip-free diode laser cutting of glass. *Opt. Laser Technol.*, 41(3):318 – 327, 2009.
- K. Özenç, G. Chinaryan, and M. Kaliske. A configurational force approach to model the branching phenomenon in dynamic brittle fracture. *Eng. Fract. Mech.*, 157(Complete):26–42, 2016.
- K. Pham, H. Amor, J.-J. Marigo, and C. Maurini. Gradient damage models and their use to approximate brittle fracture. *Int. J. Damage Mech.*, 20(4):618–652, 2011.
- C. Plate. *Untersuchung von Spannungswellen im Produktionstarget des Super-FRS Fragmentseparators an der Beschleunigeranlage FAIR*. Bachelor thesis, Technische Universität Darmstadt, 2008.
- M. Rahman and T. Michelitsch. A note on the formula for the Rayleigh wave speed. *Wave Motion*, 43(3):272 – 276, 2006.
- M. Ramulu and A. S. Kobayashi. Mechanics of crack curving and branching – a dynamic fracture analysis. *Int. J. Fract.*, 27(3):187–201, 1985.
- K. Ravi-Chandar and W. Knauss. An experimental investigation into dynamic fracture: I. Crack initiation and arrest. *Int. J. Fract.*, 25(4):247–262, 1984a.
- K. Ravi-Chandar and W. Knauss. An experimental investigation into dynamic fracture: II. Microstructural aspects. *Int. J. Fract.*, 26(1):65–80, 1984b.
- K. Ravi-Chandar and W. Knauss. An experimental investigation into dynamic fracture: III. On steady-state crack propagation and crack branching. *Int. J. Fract.*, 26(2):141–154, 1984c.
- K. Ravi-Chandar and W. Knauss. An experimental investigation into dynamic fracture: IV. On the interaction of stress waves with propagating cracks. *Int. J. Fract.*, 26(3):189–200, 1984d.
- J. N. Reddy. Hamilton’s Principle in Continuum Mechanics (A. Bedford). *SIAM Review*, 31(3):512–513, 1989.
- J. R. Rice. A path independent integral and the approximate analysis of strain concentration by notches and cracks. *J. Appl. Mech.*, 35:379–386, 1968.

- H. Richter, H. Aiginger, and E. Noah Messomo. *Simulating Transient Effects of Pulsed Beams on Beam Intercepting Devices*. PhD thesis, Technische Universität Vienna, Vienna, 2011.
- A. J. Rosakis, O. Samudrala, and D. Coker. Intersonic shear crack growth along weak planes. *Mater. Res. Innov.*, 3(4):236–243, 2000.
- M. Sabel, C. C. Sator, and R. Müller. A particle finite element method for machining simulations. *Comput. Mech.*, 54(1):123–131, 2014.
- M. H. Sadd. *Elasticity - Theory, Applications, and Numerics*. Academic Press, second edition, 2009. ISBN 978-0-12-374446-3.
- A. Schlüter. *FE-Implementierung eines dynamischen Phasenfeldmodells für Bruchvorgänge*. Master thesis, Technische Universität Kaiserslautern, 2013.
- A. Schlüter, A. Willenbücher, and C. Kuhn. GPU-accelerated crack path computation based on a phase field approach for brittle fracture. In *Proceedings of the 2nd Young Researcher Symposium (YRS) 2013*, pages 60–65, Kaiserslautern, Germany, 2013. Fraunhofer Verlag.
- A. Schlüter, C. Kuhn, and R. Müller. Phase field approximation of dynamic brittle fracture. *PAMM*, 14(1):143–144, 2014a.
- A. Schlüter, A. Willenbücher, C. Kuhn, and R. Müller. Phase field approximation of dynamic brittle fracture. *Comput. Mech.*, pages 1–21, 2014b.
- A. Schlüter, C. Kuhn, and R. Müller. On configurational forces in a dynamic phase field model for fracturing. *PAMM*, 16(1):171–172, 2016a.
- A. Schlüter, C. Kuhn, R. Müller, and D. Gross. An investigation of intersonic fracture using a phase field model, 2016b.
- A. Schlüter, C. Kuhn, and R. Müller. Simulation of laser-induced controlled fracturing utilizing a phase field model. *J. Comput. Inf. Sci. Eng.*, 12, 2017.
- A. Schlüter, C. Kuhn, R. Müller, M. Tomut, C. Trautmann, H. Weick, and C. Plate. Phase field modelling of dynamic thermal fracture in the context of irradiation damage. *Continuum Mech. Thermodyn.*, 29(4):977–988, 2017.
- A. Schlüter, C. Kuhn, T. Noll, F. Diewald, and R. Müller. Numerical solution strategies for a dynamic phase field fracture model. In *Physical Modeling for Virtual Manufacturing Systems and Processes*, volume 869 of *Applied Mechanics and Materials*, pages 29–49. Trans Tech Publications, 2017.

- A. Schlüter, C. Kuhn, and R. Müller. Configurational forces in a phase field model for dynamic brittle fracture. In *Advanced Structured Materials*. Springer, 2017. A Special Volume in Honor of Prof. Kienzler.
- R. Schmitt, C. Kuhn, R. Müller, and K. Bhattacharya. Crystal plasticity and martensitic transformations - A phase field approach. *Technische Mechanik*, 34(1):23–38, 2014.
- E. Sharon and J. Fineberg. Microbranching instability and the dynamic fracture of brittle materials. *Phys. Rev. B*, 54:7128–7139, Sep 1996.
- E. Sharon and J. Fineberg. The dynamics of fast fracture. *Advanced Engineering Materials*, 1(2):119–122, 1999.
- E. Sharon, S. P. Gross, and J. Fineberg. Local crack branching as a mechanism for instability in dynamic fracture. *Phys. Rev. Lett.*, 74:5096–5099, 1995.
- J.-H. Song, H. Wang, and T. Belytschko. A comparative study on finite element methods for dynamic fracture. *Comput. Mech.*, 42(2):239–250, 2008.
- C. Steinke, K. Özenç, G. Chinaryan, and M. Kaliske. A comparative study of the r-adaptive material force approach and the phase-field method in dynamic fracture. *Int. J. Fract.*, 201(1):97–118, 2016.
- M. Strobl and T. Seelig. A novel treatment of crack boundary conditions in phase field models of fracture. *PAMM*, 15(1):155–156, 2015.
- M. Strobl and T. Seelig. On constitutive assumptions in phase field approaches to brittle fracture. *Procedia Structural Integrity*, 2:3705 – 3712, 2016.
- M. Strobl, L. Morand, and T. Seelig. Simulation of Hertzian cone cracks using a phase field description for fracture. *PAMM*, 16(1):177–178, 2016.
- N. Tahir, V. Kim, a. Matvechev, A. Ostriker, I. V. Lomonosov, A. R. Piriz, J. L. Cela, and D. Hoffmann. Numerical modeling of heavy ion induced stress waves in solid targets. *Laser Part. Beams*, 25(4):523–540, 2007.
- N. A. Tahir, D. H. Hoffmann, J. A. Maruhn, P. Spiller, and R. Bock. Heavy-ion-beam-induced hydrodynamic effects in solid targets. *Phys. Rev. E*, 60:4715–4724, 1999.
- R. L. Taylor. FEAP - Finite Element Analysis Program, 2014.
- C.-H. Tsai and H.-W. Chen. Laser cutting of thick ceramic substrates by controlled fracture technique. *J. Mater. Process. Technol.*, 136(1–3):166 – 173, 2003.

- P. D. Washabaugh and W. G. Knauss. A reconciliation of dynamic crack velocity and Rayleigh wave speed in isotropic brittle solids. *Int. J. Fract.*, 65:97–114, 1994.
- W. Wood. *Practical Time-stepping Schemes*. Clarendon Press, 1990.
- P. Wriggers. *Computational Contact Mechanics*. Springer-Verlag, Berlin, Heidelberg, 2006.
- P. Wriggers. *Nonlinear Finite Element Methods*. Springer-Verlag, Berlin, Heidelberg, 2009.
- C. W. Wu. Maximum energy release rate criterion. *J. Elasticity*, 8:2235–2257, 1978.
- X.-P. Xu and A. Needleman. Numerical simulations of fast crack growth in brittle solids. *J. Mech. Phys. Solid.*, 42(9):1397 – 1434, 1994.
- E. H. Yoffe. LXXV. The moving griffith crack. *Philos. Mag.*, 42(330):739–750, 1951.
- O. C. Zienkiewicz and R. L. Taylor. *The Finite Element Method*. Butterworth-Heinemann, Oxford, Auckland, Boston, Johannesburg, Melbourne, New Delhi, 5th edition, 2000.
- T. Zohdi. Additive particle deposition and selective laser processing-a computational manufacturing framework. *Comput. Mech.*, 54(1):171–191, 2014.

Curriculum Vitae

Name: Alexander Schlüter

Geburtsort: Koblenz

-
- 09.1993 - 07.1997 Grundschule in Hilgert
- 09.1997 - 03.2006 Gymnasium im Kannenbäckerland in Höhr-Grenzhausen
- 03.2007 - 05.2010 Bachelorstudium in Product Development and Design
an der Fachhochschule Koblenz
- Bachelorarbeit:
*Vergleichende Untersuchung zum Versagensverhalten
von Faserverbund-Bauteilen mit der FEM*
Abschluss: Bachelor of Engineering
- 10.2010 - 04.2013 Masterstudium in Computational Engineering
and der Technischen Universität Kaiserslautern
- Masterarbeit:
*FE-Implementierung eines dynamischen
Phasenfeldmodells für Bruchvorgänge*
Abschluss: Master of Science
- 05.2013 - 12.2013 Promotionsstipendiat
am Lehrstuhl für Computational Mechanics,
Fachbereich Maschinenbau und Verfahrenstechnik,
der Technischen Universität Kaiserslautern
- 01.2014 - 07.2017 Wissenschaftlicher Mitarbeiter
am Lehrstuhl für Technische Mechanik,
Fachbereich Maschinenbau und Verfahrenstechnik,
der Technischen Universität Kaiserslautern